Transactions of the ASME, Journal of Heat Transfer (ISSN 0022-1481) is published monthly by The American Society of Mechanical Engineers, Three Park Avenue, New York, NY 10016. Periodicals postage paid at New York, NY and additional mailing offices. POSTMASTER: Send address changes to Transactions of the ASME, Journal of Heat Transfer, c/o THE AMERICAN SOCIETY OF MECHANICAL ENGINEERS, 22 Law Drive, Box 2300, Fairfield, NJ 07007-2300. **CHANGES OF ADDRESS** must be received at Society headquarters seven weeks before they are to be effective. Please send old label and new address. **STATEMENT from By-Laws.** The Society shall not be responsible for statements or opinions advanced in papers or ... printed in its publications (B7.1, Para. 3).

Journal of Heat Transfer

Published Monthly by ASME

VOLUME 129 • NUMBER 6 • JUNE 2007(pp. 685-767)

TECHNICAL PAPERS

TECHNICAL BRIEFS

(Contents continued on inside back cover)

This journal is printed on acid-free paper, which exceeds the ANSI Z39.48-1992 specification for permanence of paper and library materials. ♾™
♻ 85% recycled content, including 10% post-consumer fibers.

Journal of Heat Transfer **Volume 129, Number 6** **JUNE 2007**

The ASME Journal of Heat Transfer is abstracted and indexed in the following:

Applied Science and Technology Index, Chemical Abstracts, Chemical Engineering and Biotechnology Abstracts (Electronic equivalent of Process and Chemical Engineering), Civil Engineering Abstracts, Compendex (The electronic equivalent of Engineering Index), Corrosion Abstracts, Current Contents, E & P Health, Safety, and Environment, Ei EncompassLit, Engineered Materials Abstracts, Engineering Index, Enviroline (The electronic equivalent of Environment Abstracts), Environment Abstracts, Environmental Engineering Abstracts, Environmental Science and Pollution Management, Fluidex, Fuel and Energy Abstracts, Index to Scientific Reviews, INSPEC, International Building Services Abstracts, Mechanical & Transportation Engineering Abstracts, Mechanical Engineering Abstracts, METADEX (The electronic equivalent of Metals Abstracts and Alloys Index), Petroleum Abstracts, Process and Chemical Engineering, Referativnyi Zhurnal, Science Citation Index, SciSearch (The electronic equivalent of Science Citation Index), Theoretical Chemical Engineering

Computation of Flow and Heat Transfer in Rotating Rectangular Channels (AR=4:1) With Pin-Fins by a Reynolds Stress Turbulence Model

Guoguang Su
Turbine Heat Transfer Laboratory,
Department of Mechanical Engineering,
Texas A&M University,
College Station, TX 77843

Hamn-Ching Chen
Ocean Engineering Program,
Department of Civil Engineering,
Texas A&M University,
College Station, TX 77843

Je-Chin Han
Turbine Heat Transfer Laboratory,
Department of Mechanical Engineering,
Texas A&M University,
College Station, TX 77843

Computations with multi-block chimera grids were performed to study the three-dimensional turbulent flow and heat transfer in a rotating rectangular channel with staggered arrays of pin-fins. The channel aspect ratio (AR) is 4:1, the pin length to diameter ratio (H/D) is 2.0, and the pin spacing to diameter ratio is 2.0 in both the stream-wise (S_1/D) and span-wise (S_2/D) directions. A total of six calculations have been performed with various combinations of rotation number, Reynolds number, and coolant-to-wall density ratio. The rotation number and inlet coolant-to-wall density ratio varied from 0.0 to 0.28 and from 0.122 to 0.20, respectively, while the Reynolds number varied from 10,000 to 100,000. For the rotating cases, the rectangular channel was oriented at 150 deg *with respect to the plane of rotation to be consistent with the configuration of the gas turbine blade. A Reynolds-averaged Navier-Stokes (RANS) method was employed in conjunction with a near-wall second-moment turbulence closure for detailed predictions of mean velocity, mean temperature, and heat transfer coefficient distributions.* [DOI: 10.1115/1.2717935]

Keywords: pin-fins, rotating rectangular channels, internal cooling, near-wall Reynolds stress model, chimera grids

Introduction

Gas turbine stages are being designed to operate at increasingly higher inlet temperatures to improve thermal efficiencies. Sophisticated cooling techniques must be employed to cool the components to maintain the performance requirements. One method for cooling the turbine blades is internal cooling. With internal blade cooling, a small amount of air is extracted from the compressor, and the air is injected into the blades. Through forced convection, the coolant air removes heat from the walls of the blade. The narrow trailing edge of the turbine blade poses many challenges from both a cooling and manufacturing view. The trailing edge is very narrow, so the typical cooling techniques of jet impingement and ribbed channels cannot be employed due to manufacturing constraints. Pin-fins provide solutions to these problems. The use of pin-fins to enhance heat transfer in cooling channels has been the focus of many studies throughout the years.

Many experimental investigations have proven that pin-fins perform better in low aspect ratio channels for gas turbine blades. Metzger et al. [1] studied the developing heat transfer of short pin-fins in stationary staggered arrays. They observed that the heat transfer coefficient gradually increases over the first several rows of pins, reaches a maximum around the third row, and gradually decreases through the remaining rows of the array. Metzger and Haley [2] then studied the effects of pin material and pin spacing on heat transfer in staggered arrays. They found that the array-averaged Nusselt number values for the nonconducting pin-fins closely followed the values of the conducting pin-fins. They also showed that as the stream-wise spacing was increased, the Nusselt number values decreased. Later, Metzger et al. [3] examined the row resolved heat transfer variation in pin-fin arrays. VanFossen [4] also investigated stationary cooling channels with pin-fin arrays. The study showed that the heat transfer from an array of short pins is lower than the heat transfer from an array of long pins. It was also found that the heat transfer coefficients on the pin surface were approximately 35% greater than those on the end-wall. In a later study, Brigham and VanFossen [5] investigated the effect of pin-fin length on the heat transfer coefficient and concluded that the pin height-to-diameter ratio is the dominant factor affecting the amount of heat transferred from short pin-fin arrays (end walls included). With the mass transfer technique, Chyu and Goldstein [6] observed the peak distribution of the Sherwood number and concluded that the staggered pin arrangement performs better than inline arrangement.

In more recent studies, Chyu and Hsing [7] investigated the effect of pin shape on heat transfer. They concluded that the cubic pin-fin yields the highest heat transfer (in both staggered and inline arrays), followed by the diamond and then the circular pin-fins. Chyu et al. [8] also studied the heat transfer contribution of pin-fins and end walls in pin-fin arrays. This study found that conducting pin-fins have a significantly higher heat transfer coefficient (10–20%) than the end walls. Uzol and Camci [9] investigated the end wall heat transfer and total pressure loss within various arrays of pin-fins. This investigation used a liquid crystal technique to measure the end wall heat transfer downstream of two rows of fins. This study compared the heat transfer enhancement of circular pins and two elliptical pin-fin arrays. They found that the heat transfer in the wake of circular pins is 25% higher than that of the elliptical arrays. However, the elliptical geometry is viewed as a more desirable configuration due to the relative small pressure drop penalty (when compared to the circular array).

Hwang et al. [10,11] presented experimental heat transfer and

Contributed by the Heat Transfer Division of ASME for publication in the JOURNAL OF HEAT TRANSFER. Manuscript received July 5, 2005; final manuscript received August 17, 2006. Review conducted by Karen Thole.

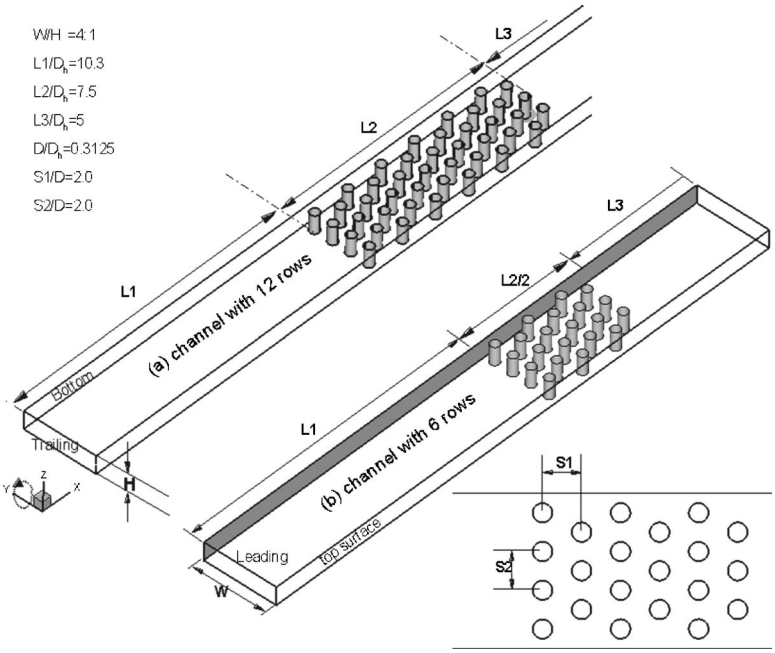

Fig. 1 Geometry and conceptual view of the rotating channel for the rectangular duct (AR=4:1) with pin-fins

pressure drop results for air flows through trapezoidal pin-fin channels with the liquid crystal technique. They concluded that straight wedge duct with a staggered pins array produces the highest heat transfer coefficient enhancement with a moderate pressure drop penalty.

Lau et al. [12] conducted experiments to study the effects of lateral ejection through slots on the local wall heat transfer and the pressure drop for turbulent flow through a pin fin channel. They found that the heat transfer is higher in the vicinity of the ejection slots adjacent to the channel entrance. Lau et al. [13] conducted experiments to study the effects of lateral flow ejection on the overall heat transfer and pressure drops. They found that the overall Nusselt number decreased by as much as 25% as the ejection ratio was increased. Lau et al. [14] also examined the effects of the length of the trailing edge holes on the heat transfer, pressure drops, and mass flow rates in pin fin channels.

In an experiment conducted by Willett and Bergles [15], the heat transfer in rotating channels with conducting pin-fins was studied. They found that the heat transfer enhancement due to rotation and buoyancy was much less than the enhancement observed from their study of a smooth narrow duct [16]. They showed that pin-fins significantly reduce the effect of rotation, but they do not eliminate the effect. Wright et al. [17] studied a staggered array of pins under the rotating condition and found that the heat transfer in a stationary pin-fin channel can be enhanced up to 3.8 times that of a smooth channel, and they confirmed the finding of Willett and Bergles [15] that the effect of rotation is mitigated in the pin-fin channel.

Table 1 Summary of cases studied

Case no.	Ro	$\Delta\rho/\rho$	β (deg)	Re
1	0.00	0.122	⋯	10,000 (12 rows)
2	0.00	0.122	⋯	10,000 (6 rows)
3	0.14	0.122	150	10,000 (6 rows)
4	0.00	0.122	⋯	20,000 (6 rows)
5	0.00	0.122	⋯	100,000 (6 rows)
6	0.14	0.122	150	100,000 (6 rows)
7	0.28	0.2	150	100,000 (6 rows)

Although heat transfer and pressure drop results are available in the open literature for flows through pin-fin channels with staggered and aligned pin-fin arrays, pin-fins of various shapes, full length and partial length pin-fins, and different channel inlet and exit conditions, there are very few data available on the effects of rotation on the heat transfer and flow distributions for pin-fin channels. Furthermore, most of the experimental investigations for rotating pin-fin channels are limited to relatively low rotation number and low Reynolds number conditions and provide only regionally averaged Nusselt number distributions. Therefore, it is desirable to develop advanced numerical methods to facilitate more detailed understanding of the three-dimensional flow and heat transfer characteristics for pin-fin channels under high rotation number, high density ratio, and high Reynolds number conditions.

During the past decade, numerical methods have been used

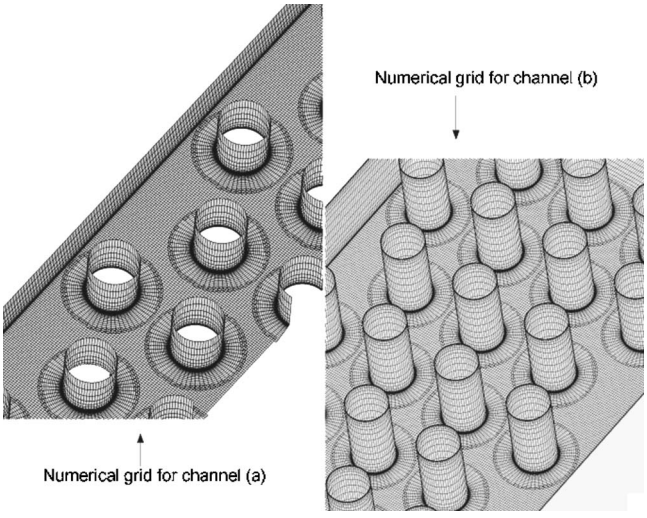

Fig. 2 Numerical grid for (*a*) full channel and (*b*) one-half channel

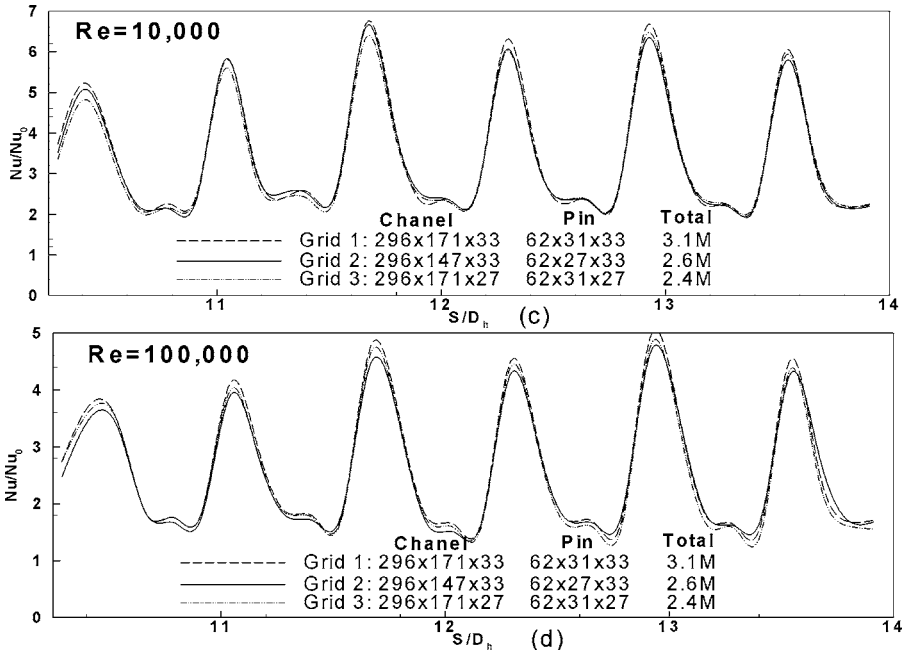

Fig. 3 Grid refinement study for channel B at (*a*) Re=10,000, Ro=0.0 and (*b*) Re =100,000, Ro=0.0

extensively for the prediction of three-dimensional flow and heat transfer in rotating rectangular channels with rib turbulators under various combinations of rotation number, Reynolds number, channel aspect ratio, and channel orientation. However, there are very few numerical studies on the pin-fin channels. Moreover, the few numerical studies in the literature primarily focus on the cooling techniques in electric circuit cooling or the shell and tube heat exchangers. Although there are some similarities with the pin-fin channels in gas turbine blades, these simulation results are not directly applicable for turbine blade cooling applications at high Reynolds number and high rotation number conditions.

Recently, Donahoo et al. [18] employed a Galerkin finite element procedure to perform a 2D study of a staggered cross pin array to determine an optimal row spacing considering both heat dissipation and required pumping power. Subsequently, Donahoo et al. [19] performed a 3D calculation with the k-ε turbulence model to study the same problem including the end wall effects. More recently, Hamilton et al. [20] used the ANSYSTM commercial code to model the incompressible fluid flow in a pin-fin channel using the standard k-ε turbulence model in conjunction with the Van Driest coupling model for the wall region.

The present study is concerned with the numerical prediction of flow and heat transfer characteristics for rectangular pin-fin channels under high Reynolds number, high rotation number, and high density ratio conditions. There are very few numerical studies for cooling channels under high rotation number and high Reynolds number conditions. Recently, Su et al. [21] employed the RANS method of Chen et al. [22] and performed a parametric study of flow and heat transfer in a rectangular cooling channel with V-shaped ribs over a wide range of Reynolds numbers (10,000–500,000), rotation number (0–0.28), and coolant-to-wall density ratio (0.122–0.4). In the present study, the RANS method of Chen et al. [22] is further generalized to incorporate the chimera grid embedding technique of Hubbard and Chen [23] and Chen et al. [24] to facilitate efficient simulation of detailed three-dimensional flow and heat transfer in stationary and rotating pin-fin channels under high Reynolds number and high rotation number conditions. Calculations were performed using both the two-layer k-ε model and the near-wall second-order Reynolds stress model (i.e., second-moment closure) of Chen et al. [22]. However, only the second-moment results are presented since the Reynolds stress model provides significantly more accurate prediction of the heat transfer coefficients. In the second-moment closure model, all six Reynolds stresses are computed directly for accurate resolution of the Reynolds stress anisotropy induced by the horseshoe vortices and channel rotation. It should also be remarked that the Reynolds stress turbulence model requires only 38% more CPU time in comparison with the two-layer k-ε model because the most time-consuming part of the computation is the coupling between the pressure and the mean velocity field, but not the turbulence quantities.

Description of the Problem

A schematic diagram of the pin-fin configuration used in the present study is shown in Fig. 1. This test section shown in Fig.

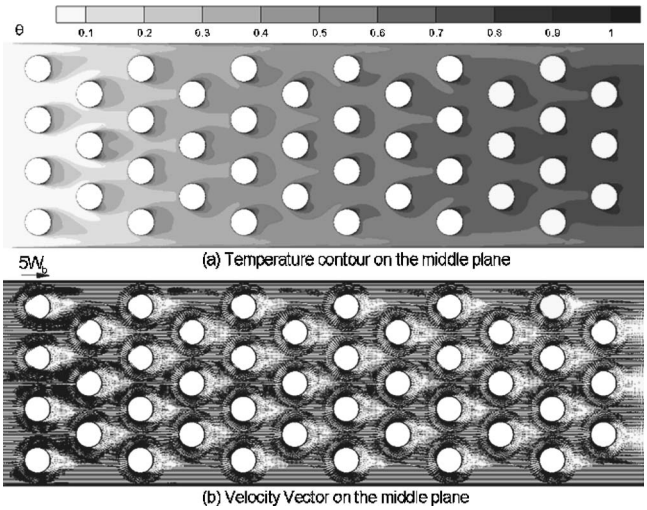

Fig. 4 Velocity vectors and dimensionless temperature [$\theta = (T - T_i)/(T_w - T_i)$] contours in the middle plane of symmetry of the nonrotating channel (Re=10,000, $\Delta\rho/\rho$=0.122)

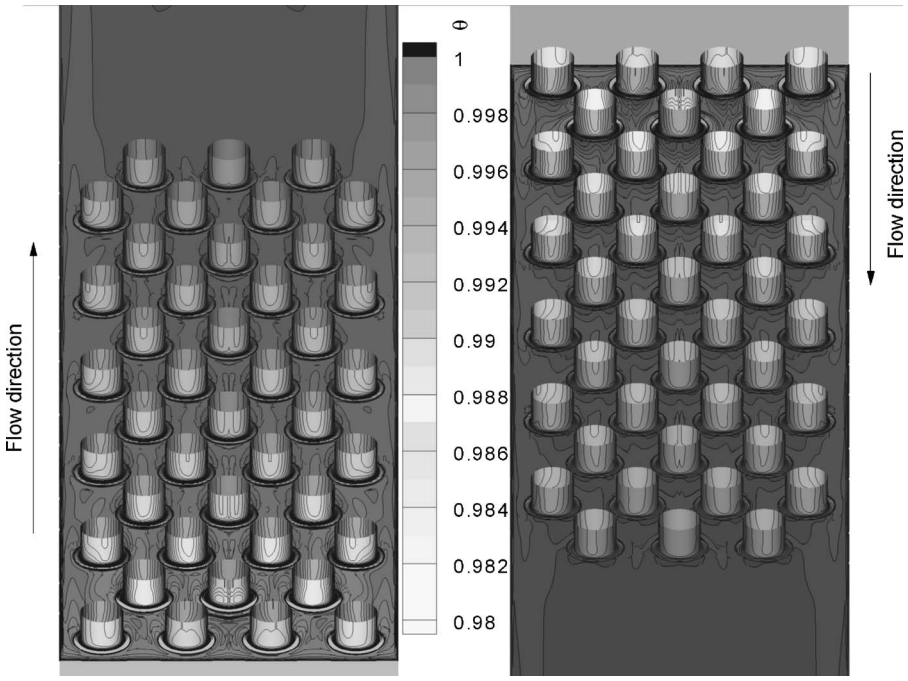

Fig. 5 Dimensionless temperature $[\theta=(T-T_i)/(T_w-T_i)]$ contours close to the pin-fins and the trailing surface of nonrotating channel (Re=10,000, $\Delta\rho/\rho=0.122$)

1(*a*) has 12 rows of pins in the flow direction and is identical to that used by Wright et al. [17] in their experimental investigations. For the nonrotating case, the flow is symmetric with respect to both the y and z coordinates at each longitudinal cross-section. Therefore, it is possible to simulate only one-quarter of the channel cross-section but include all 12 rows of pin-fins. Under rotating conditions, however, the flow is no longer symmetric due to the presence of centrifugal and Coriolis forces induced by the channel rotation. Consequently, it will be necessary to include the full channel cross-section for the rotating pin-fin channels. Due to the limitation in available computer resources, the present rotating channel flow simulations were performed for the full channel cross-section but with only six rows of pin-fins, as shown in Fig. 1(*b*). The channel has a rectangular cross-section with a channel aspect ratio (AR) of 4:1. Of the four side walls, the two in the rotational direction are denoted as the leading and trailing surfaces, while the other two are denoted as the inner and outer surfaces. The channel hydraulic diameter, D_h, is 0.8 in. (2.03 cm). The distance from the inlet of the channel to the axis of rotation is given by $R_r/D_h=20.0$. The channel consists of an unheated smooth starting section ($L_1/D_h=10.3$), a heated section with pins ($L_2/D_h=7.5$ for channel A and $L_2/D_h=3.75$ for channel B in Fig. 1), and an unheated smooth exit section ($L_3/D_h=5.00$). A summary of all six cases studied is given in Table 1.

Computational Procedure

Overview. The Reynolds-averaged Navier-Stokes (RANS) equations in conjunction with a near wall Reynolds stress turbulence model are solved using the chimera RANS method of Chen et al. [22]. The governing equations with the second-moment closure turbulence model for Reynolds stresses and turbulent heat fluxes were described in detail by Chen et al. [22] and will not be repeated here. The flow is considered to be incompressible since the Mach number is quite low. However, the density in the centrifugal force terms is approximated by $\rho=\rho_o T_o/T$ to account for the density variations caused by the temperature differences, where ρ_o and T_o are the density and temperature at the inlet of the cooling channel. In general, the density is also a function of the rotating speed because the centrifugal force creates a pressure gradient along the duct. In the experiments of Wright et al. [17], the maximum pressure variation between the channel inlet and the exit is approximately 0.0113 atm for the highest rotation number of 0.28 (i.e., $\Omega=550$ rpm) considered in the present study. This gives a maximum density variation of approximately 1.1% from the inlet to the exit of the duct at the highest rotation number. Therefore, it is reasonable to omit the density variation caused by the pressure gradients induced by the channel rotation.

Boundary Conditions. For both channels A and B in Fig. 1, a uniform velocity profile was used at the inlet of the duct ($X=0$). The unheated length (L_1) was long enough for the velocity profile to achieve the fully developed turbulent profile before the heating start-point ($X=L_1$). At the exit of the duct, zero-gradient boundary conditions were specified for the mean velocity and all turbulent

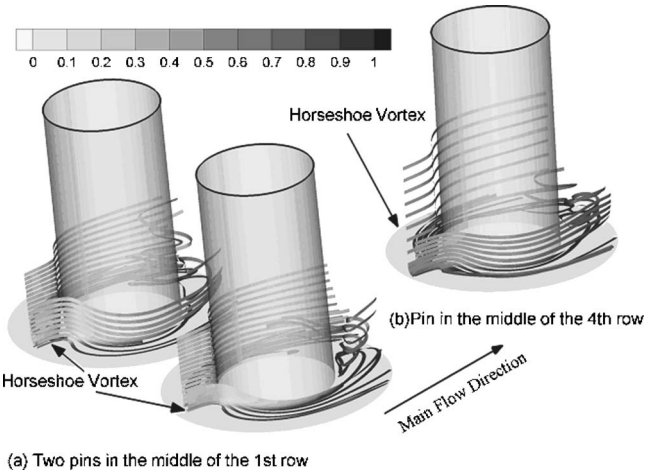

Fig. 6 Horseshoe vortices and dimensionless temperature $[\theta=(T-T_i)/(T_w-T_i)]$ contours around pin-fins in the nonrotating channel (Re=10,000, Ro=0.0, $\Delta\rho/\rho=0.122$)

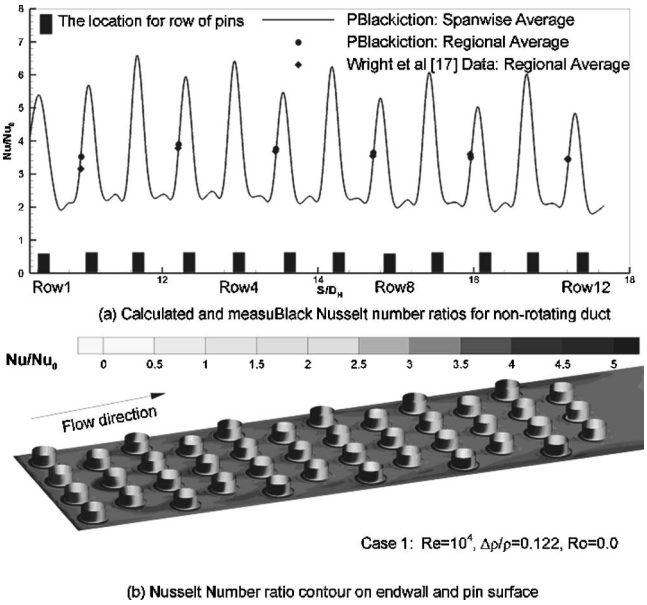

Fig. 7 Comparison between the calculated and measured Nusselt number ratios for the nonrotating duct with 12 rows of pin-fins (Re=10^4, $\Delta\rho/\rho$=0.122)

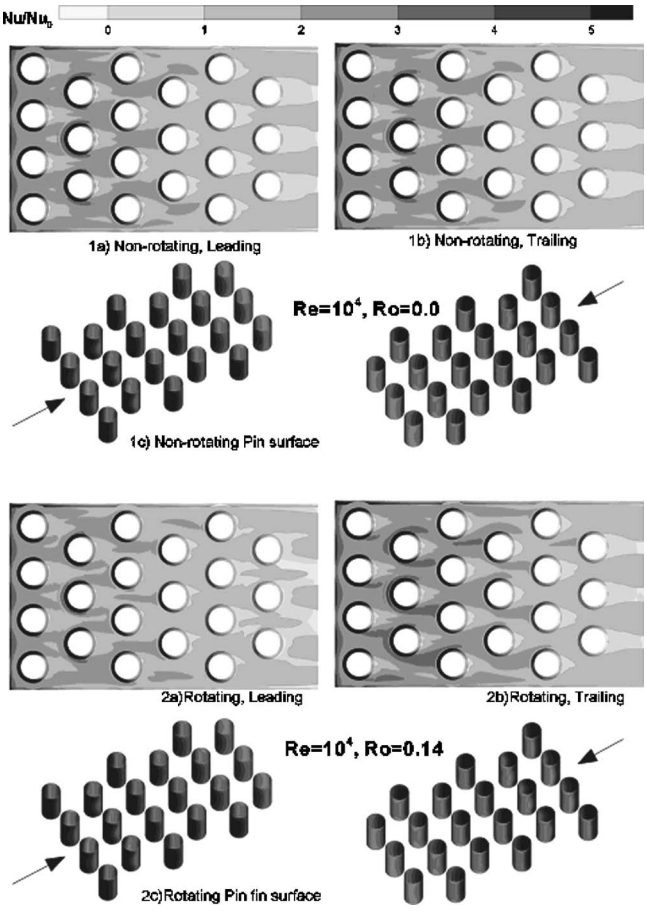

Fig. 8 Nusselt number ratio contours on (*a*) the leading surface, (*b*) the trailing surface, and (*c*) the pin-fin surface for lower Reynolds number (Re=10,000) cases

quantities, while linear extrapolation was used for the pressure field. The coolant fluid at the inlet of the duct is air at uniform temperature $T=T_o$ (i.e., $\theta=(T-T_o)/(T_w-T_o)=0$). The wall temperature of the unheated sections is kept constant at $T=T_o$ ($\theta=0$) while the wall temperature of the heated section (leading, trailing, inner, outer, and wall of pins) is kept constant at $T=T_w$ ($\theta=1$) for channel B. For channel A, the symmetric boundary condition was used on the planes of symmetry in the y and z directions.

Computational Grid Details. Figure 2(*a*) shows the computational grid around the pins that model channel A with the AR =4:1 in Fig. 1(*a*). In this multi-block chimera grid system, the computational domain was divided into 25 overlapping and embedding chimera grid blocks (one block is for the rectangular duct and the other 24 blocks are for the pins) to simplify the grid generation process. Figure 2(*b*) shows the computational grid around the pins that models channel B (Fig. 1(*b*)), which has a total of six rows of pins. In the present chimera domain decomposition approach, the PEGSUS program of Suhs and Tramel [25] was employed to identify the hole points to be blanked out during the computations and determine the interpolation information for the hole fringe points and the block boundary points. Furthermore, the grid-interface conservation technique of Hubbard and Chen [23] was employed to ensure the conservation of mass and momentum in the overlap region between different computational grid blocks. The present chimera grid system also greatly facilitates selective grid refinements in areas of high gradients without significant increase of the overall computing time. To provide adequate resolutions of the viscous sublayer and buffer layer adjacent to a solid surface, the minimum grid spacing for the Re =10,000 cases is maintained at 10^{-3} of the hydraulic diameter, which corresponds to a wall coordinate, y^+, on the order of 0.3; the minimum grid spacing for the Re=100,000 cases is maintained at 2×10^{-5} of the hydraulic diameter, which corresponds to wall coordinate y^+ on the order of 0.3. For the numerical grid (B), the number of grid points in the rectangular duct is $296\times171\times33$ and the number of grid points for each pin is $62\times31\times33$; the identical grid distribution was applied in numerical grid (A). The total number of grid points is just over 3 million. Figures 3(*a*) and 3(*b*) present grid refinement studies for Re=10,000 and 100,000, respectively, which indicates the present simulation results are nearly grid independent. In all calculations, the root-mean-square (rms) and maximum absolute errors for both the mean flow and turbulence quantities were monitored for each computational block to ensure complete convergence of the numerical solutions, and a convergence criterion of 10^{-5} was used for the maximum rms error.

Results and Discussion

Velocity and Temperature Fields. As summarized in Table 1, computations were performed with the Reynolds number (Re) ranging from 10^4 to 10^5, rotation number (Ro) from 0 to 0.28, and inlet coolant to wall density ratio ($\Delta\rho/\rho$) from 0.122 to 0.2, and, for the rotating cases, the channel orientation was fixed at 150 deg.

Figure 4 shows the velocity vector field and dimensionless temperature contours (θ) on the middle plane of symmetry between the leading and trailing surfaces for the nonrotating duct with 12 rows (case 1) of pin-fins. As noted earlier, computations were performed for only one-quarter of the channel since the flow is symmetric with respect to both y and z coordinates. As the flow approaches the first row of pin-fins, it accelerates around the circular pin-fins and boundary layer flow separation is observed downstream of the pin-fins. A pair of counter-rotating vortices are formed on the downstream face of each pin-fin. Due to the narrow span-wise spacing ($S_2/D=2$) between the pin-fins, the mainstream flow accelerates in the gap region before impinging on the leading edge of the second row of pin-fins, which are staggered to the first row pin-fins. In the present staggered pin-fin arrangement, the

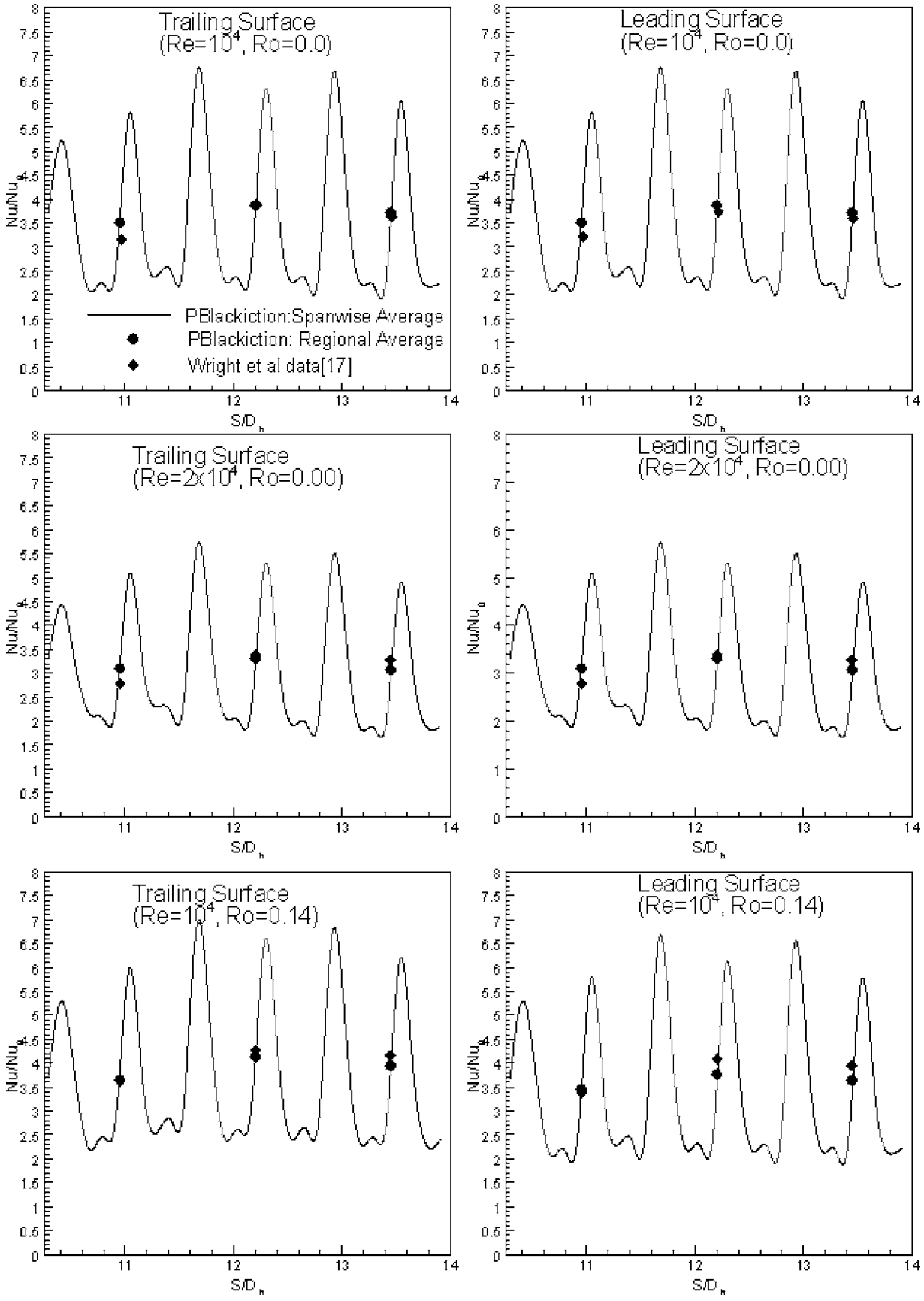

Fig. 9 Comparison between the calculated and measured Nusselt number ratios for the nonrotating and rotating ducts: (*a*) Re=10,000, Ro=0; (*b*) Re=10,000, Ro=0.14; and (*c*) Re=20,000, Ro=0

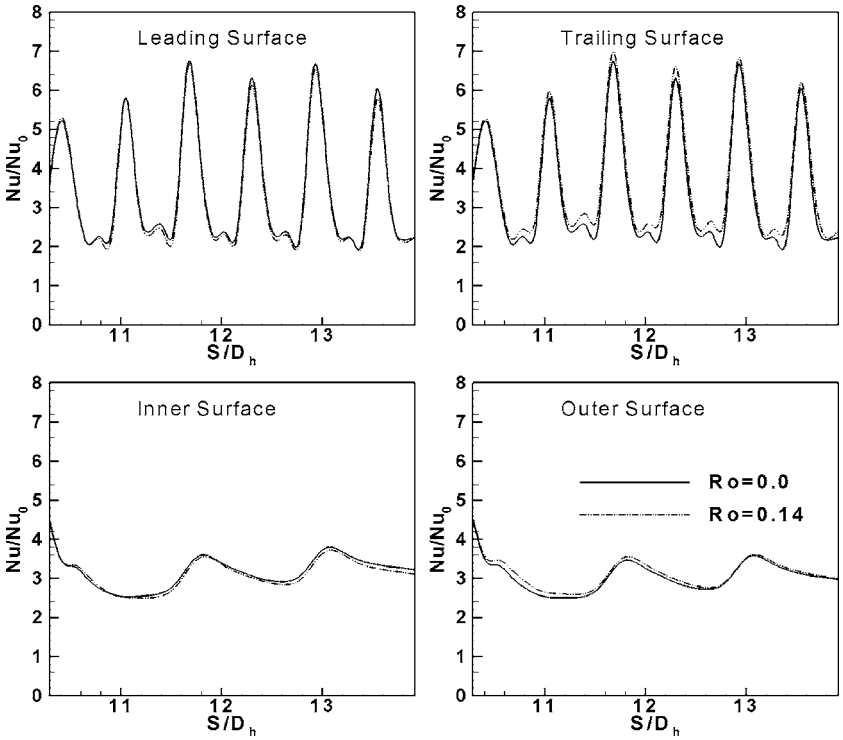

Fig. 10 Effect of rotation on spanwise-averaged Nusselt number ratios for the lower Reynolds number (Re=10,000) cases

coolant accelerates toward the leading edge of each pin and high heat transfer is produced on the front face of the pin-fin surface. As the mainstream flow is directed through the narrow passages between the second row of pin-fins, it also has a desirable effect of accelerating the wake flow behind the first row of pin-fins, and hence reduces the size of the separation bubble behind the first row. The relatively small pin-fin spacing ($S_1/D=2$) in the streamwise direction also limited the longitudinal extent of the upstream pin-fin wakes to less than one pin-fin diameter due to strong mixing between the mainstream flow and the pin-fin wakes.

As the mainstream flow moves around the second row of pin-fins, boundary layer separation occurs again and new wakes are formed downstream of the pin-fins. The mainstream flow is redirected towards the leading edge of the third row pin-fins. The flow pattern around the third row pin-fins is similar to that observed earlier for the second row pin-fins except near the side wall regions. Due to the staggered pin-fin arrangement, there is strong interaction between the pin-fins and side walls for the odd row pin-fins. On the other hand, the side wall effects are negligible for even row pin-fins. It can be clearly seen from both the temperature contours and velocity vector plots that the wakes are skewed behind the odd row pin-fins since the wake flow is only partially blocked by the even row pin-fins in the side wall regions. A detailed examination of the temperature and velocity profiles indicate that the flow is sufficiently mixed with nearly periodic flow patterns beyond the third row pin-fins. It should also be noted that the wakes behind the last row of pin-fins are considerably wider and longer than those observed in previous rows due to the absence of a downstream row of pin-fins.

It is quite clear that the dimensionless temperature contours shown in Fig. 4 are closely related to the mainstream and secondary flow patterns induced by the pin-fins. The temperature is relatively low in the leading edge region of each pin-fin due to the impingement of the cooler mainstream fluid. On the other hand, the temperature is high immediately downstream of each pin-fin due to flow separation in the wake region. Near the side walls, the temperature is relatively low adjacent to odd row pin-fins due to the impingement of cooler mainstream fluid on the end walls.

Figure 5 shows the dimensionless temperature contours on the planes near the trailing (or leading) surface of the nonrotating channel, as well as the pin-fin surfaces ($Y/D=0.001$). Two different views, from upstream and downstream, of the channel are presented to provide a better understanding of the three-dimensional temperature around the leading and trailing edges of the pin-fins. It is clearly seen that the temperature is low on the front face of the pin-fins due to the impingement of the mainstream flow on the pin-fin leading edge. There is also a distinct low temperature region around the junction of each pin and the end wall. This ring-shaped low temperature region is produced by the horseshoe vortices that wrap around the junction of the pin-fin and channel end walls as shown in Fig. 6. The horseshoe vortices bring cooler fluid from the core region of the channel toward the channel end walls and produce high heat transfer on the leading and trailing surfaces of the cooling channel. On the other hand, the temperature on the downstream face of the pin-fins is quite high due to flow separation in the pin-fin wake.

It is interesting to note that the temperature of the second row pin-fins is lower than that of the first row since the mainstream flow accelerates between the first row pin-fins before impinging on the leading edge of the second row pin-fins. After the second row, the coolant temperature increases gradually downstream toward the channel exit. In general, the pin-fins induced strong turbulent mixing between the coolant in the core region and the hotter air near the channel end walls and pin-fins. The heat transfer is also enhanced around the junction of pin-fins and channel end walls due to the horseshoe vortices.

Heat Transfer Coefficient Distribution. The Nusselt numbers presented here are normalized with a smooth tube correlation by Dittus-Boelter for fully developed, turbulent, nonrotating, tube flow:

$$\mathrm{Nu}_o = 0.023\mathrm{Re}^{0.8}\mathrm{Pr}^{0.4} \quad (1)$$

Effect of Rotation on Heat Transfer Coefficient Distribution. Figure 7 shows the local Nusselt number ratio contours on the trailing surface of the channel and the pin-fin surfaces for case 1 with 12 rows of pins. For completeness, the spanwise-averaged Nusselt number distributions were also calculated to provide a better understanding on the heat transfer enhancement due to the pin-fins. The numerical results indicate that the highest Nusselt number ratios are observed on the leading edge region of the pin-fins, while lowest Nusselt number ratios are observed in the wake region on the downstream face of the pin-fins. On the leading and trailing surfaces of the cooling channel, the Nusselt number ratio is high around the junction of the pin-fins and channel end walls due to the presence of the horseshoe vortices. It is also noted that the Nusselt number ratio for the first row pin-fins is quite low since the first row pins are exposed to uniform mainstream flow. In subsequent pin-fin rows, the Nusselt number ratio increases dramatically due to the acceleration of mainstream flow in the narrow gap between the pin-fins and the impingement of mainstream flow on the leading edge of the pin-fins.

It is noted that the spanwise-averaged Nusselt number ratio distribution reaches a maximum value on the third row and reduces only slightly downstream toward the channel exit. This suggests that the coolant is well mixed after the third row and exhibits a nearly periodic flow pattern in subsequent rows. In general, the spanwise-averaged Nusselt number ratio is high ($Nu/Nu_0 = 5-6.6$) around the pin-fins but drops to approximately 2 between two rows of pin-fins. It is also interesting to note that the spanwise-averaged Nusselt number is higher around the odd number rows (except for the first row) since there are four pins on the odd number rows compared to three pins for the even number rows. Finally, it is also worthwhile to note that the calculated regionally averaged (spanwise-averaged over certain S/D_h value) Nusselt number ratios are in close agreement with the experimental data of Wright et al. [17]. This clearly demonstrates the capability of the present near-wall second-order Reynolds stress closure model for accurate prediction of the heat transfer enhancement in pin-fin channels.

After successful validation of the present numerical method for the nonrotating rectangular channel with 12 rows of pin-fins, calculations were then performed for rotating pin-fin channels to investigate the effects of rotation. Since the flow is no longer symmetric with respect to the y and z coordinates under rotating conditions, it is necessary to simulate the full channel configuration in order to correctly resolve the effects of the centrifugal and Coriolis forces. Due to the limitation of available computer resources, it was feasible for us to simulate only six rows of pin-fins for the full channel configurations (i.e., channel B). This is a reasonable simplification since the experimental data of Wright et al. [17] indicates that the Nusselt number ratio changes only slightly after the third row of pin-fins for both the nonrotating and rotating channel configurations. Calculations were performed for six different combinations of rotation number, Reynolds number, and coolant-to-wall density ratios as shown in Table 1 (cases 2–7) for channel B. Note that the simulation for the Re=10,000 nonrotating case (case 2) was repeated with six rows of pin-fins to facilitate a direct comparison on the effects of rotation and Reynolds number for channel B.

Figure 8 shows the local Nusselt number ratio contours on the leading and trailing surfaces of the channel and pin-fin surfaces for the nonrotating and rotating channels with six rows of pins. Figures 8(1*a*) and 8(1*b*) show that the Nusselt number ratio distribution is the same on both the leading and trailing surfaces for the nonrotating case. Similar to those observed in Fig. 7 for 12 rows of pins, the highest Nusselt number ratios are located on the leading edge region of pin-fins, while the lowest Nusselt number ratios are located in the wake region near the leading and trailing surfaces of the nonrotating channel. Also, the Nusselt number ratios on the pin surface of the third and fourth rows of pin-fins are higher than those observed on the other four rows.

In the rotating duct shown in Figs. 8(2*a*) and 8(2*b*), the rotation number is 0.14 while the density ratio is kept at 0.122. Compared to the nonrotating case, it is seen that the channel rotation leads to a small increase in the Nusselt number ratios on the trailing surface while the Nusselt number ratio on the leading surface changes only slightly. It is also noted that the channel rotation has negligible effect on the Nusselt number distributions on the pin-fin surfaces. In general, the combined effects of the centrifugal and Coriolis forces push the cooler fluid toward the trailing surface for the one-pass channel with radially outward flow. However, the rotation-induced secondary flow is not strong enough to change the turbulent mixing pattern around the short and densely spaced pin-fins.

Figures 9(*a*) and 9(*b*) show the spanwise-averaged Nusselt number ratios for the nonrotating (case 2) and rotating (case 3: $\beta=150$ deg) pin-fin channels, respectively, at Re=10,000 and $\Delta\rho/\rho=0.122$. In addition, the spanwise-averaged Nusselt number ratios for the nonrotating (case 4) pin-fin channels at Re=20,000 and $\Delta\rho/\rho=0.12$ are also presented in Fig. 9(*c*). Regionally averaged (spanwise averaged over certain S/D_h value) Nusselt number ratios were also computed and compared to the corresponding experimental data of Wright et al. [17] for the same cases. In general, the numerical predictions are in good agreement with the experimental data for both the rotating and nonrotating cases, except for the inlet of the nonrotating case and the exit of the rotating case. This discrepancy may be partially attributed to the constant wall temperature boundary condition used in the present calculations in comparison with the constant wall heat flux boundary condition used in the measurement.

Figure 10 shows the effect of channel rotation on the numerically predicted spanwise-averaged Nusselt number ratio distributions. It is noted that the spanwise-averaged Nusselt number distributions on both the leading and trailing surfaces show periodic peaks, as those seen earlier in Fig. 7. The two highest peaks correspond to the first and third rows of pin-fins and are caused primarily by the impingement of mainstream flow on the leading edge region of the four pins. The lower peaks are corresponding to the even number rows with three pins, while the lowest Nusselt number ratios are located in the wake region between two rows of pin-fins. As noted earlier, channel rotation leads to a small increase in the Nusselt number on the trailing surface and a very slight decrease in the Nusselt number on the leading surface. The maximum Nusselt number is located at the channel inlet where the thermal boundary layer is very thin. The peak values of the Nusselt number ratio occur next to the odd rows (first, third, and fifth rows) of pin-fins as a result of flow impingement in the narrow gap region between the pin-fins and side walls. The lowest Nusselt number ratios are observed around the second and fourth rows, where the interaction between the pin-fins and side walls is weak. It is also noted that the channel rotation has negligible effects on the magnitude of the spanwise-averaged Nusselt number ratios on side walls.

Effect of High Reynolds Number on Heat Transfer Coefficient Distribution. In addition to the low Reynolds number cases presented above (cases 2, 3, and 4), calculations were also performed for high Reynolds number, high density ratio, and high rotation number cases (i.e., cases 5–7), which are closer to the cooling configurations of power generation turbine blades. In these calculations, the Reynolds number is increased from 10^4 to 10^5, the rotation number is doubled from 0.14 to 0.28, and the density ratio is increased from 0.122 to 0.2.

Figure 11 shows the detailed Nusselt number ratio contours on the leading and trailing surfaces of the channel with six rows of pins for the high Reynolds number cases. Similar to those observed in the low Reynolds number cases, the highest Nusselt number ratios are located on the leading edge region of pin-fins, and the lowest Nusselt number ratios are found in the wake region on the leading and trailing surfaces. The maximum Nusselt number ratio is also attained at the third and fourth rows. A compari-

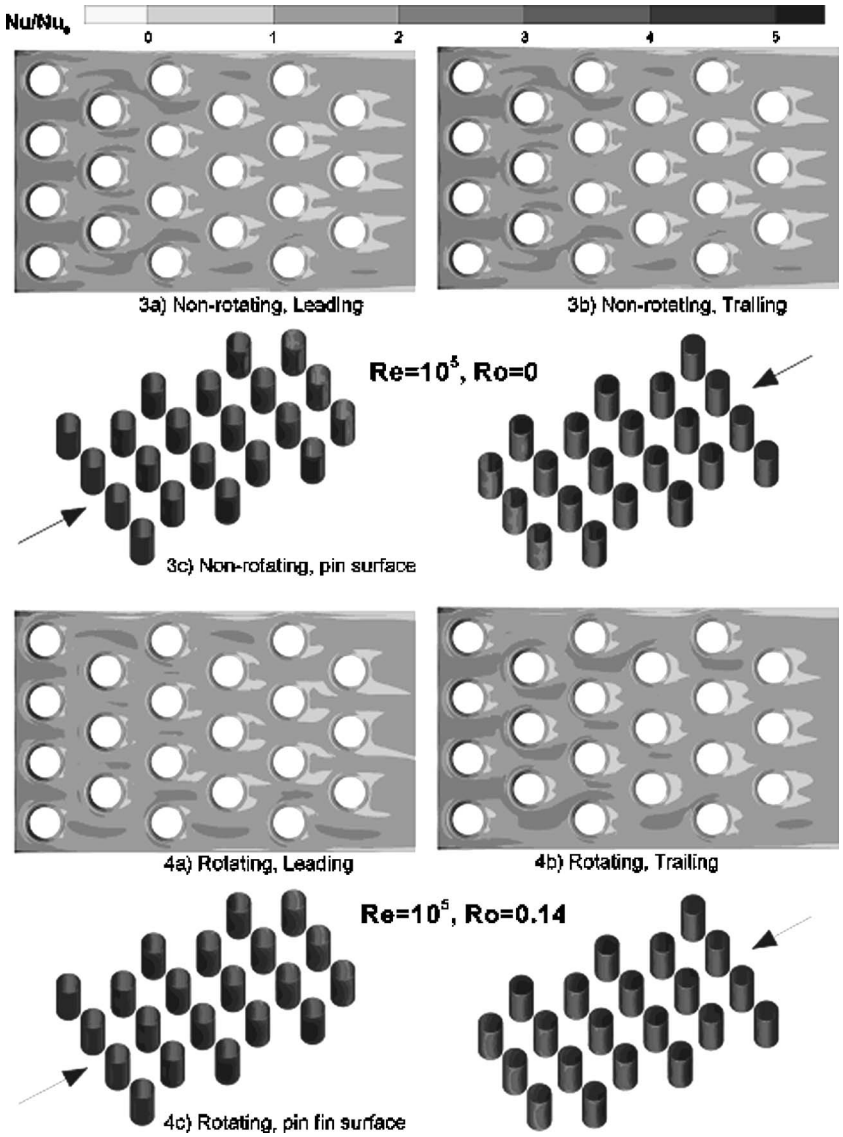

Fig. 11 Nusselt number ratio contours on (*a*) the leading surface, (*b*) the trailing surface, and (*c*) the pin-fin surface for high Reynolds number (Re=100,000) cases

son of the detailed Nusselt number ratio distributions on the leading, trailing, and pin-fin surfaces indicate that the channel rotation has negligible effect on the heat transfer augmentation. This is to be expected since the Nusselt number for a smooth duct (proportional to $Re^{0.8}$) is already very high due to high turbulence and a high temperature gradient in the boundary layer.

Figure 12 shows the spanwise-averaged Nusselt number ratios for the nonrotating duct at three different Reynolds numbers of 10^4, 2×10^4, and 10^5. It is seen that the Nusselt number ratios decrease sharply on all four walls as the Reynolds number increases. This indicates that the pin-fins produce more heat transfer enhancement (in comparison to turbulent flow in a smooth duct) for lower Reynolds number flows. However, the actual Nusselt numbers are much higher for the high Re cases because the Nu_o for the smooth duct (proportional to $Re^{0.8}$) is already very high in these cases due to the high turbulence and high temperature gradient in the boundary layer.

Effect of Rotation and Density Ratio on Heat Transfer Coefficient Distribution. Figure 13 shows a comparison of the spanwise-averaged Nusselt number ratios for high Reynolds number cases under nonrotating (case 5) and rotating with Ro=0.14 (case 6) and Ro=0.28 (case 7) conditions. It is seen that the effect of channel rotation has only minor effects on the heat transfer enhancement even if the rotation number is doubled from 0.14 to 0.28 and the density ratio is increased from 0.122 to 0.20. It is quite obvious that the rotation-induced secondary flow is not strong enough to change the flow and heat transfer characteristics, which are dominated by strong turbulent mixing induced by pin-fins and high Reynolds number boundary layer flow.

Prediction of Flow Friction Factor. Figure 14 shows the spanwise-averaged friction factor ratio C_f/C_{f0} for the heated section of all three nonrotating channels at Re=10,000, 20,000, and 100,000. It is seen that the flow impingement on pin-fins' front surface results in high friction near the leading edge of the pin-fins. Behind the pin-fins, the friction factor ratios are low due to flow separation in the wake region. On the side walls, the friction factors are high adjacent to the odd rows of pin-fins due to strong flow acceleration in the narrow gap between the side walls and the odd-row pin-fins as shown earlier in Fig. 4(*b*). The friction factors

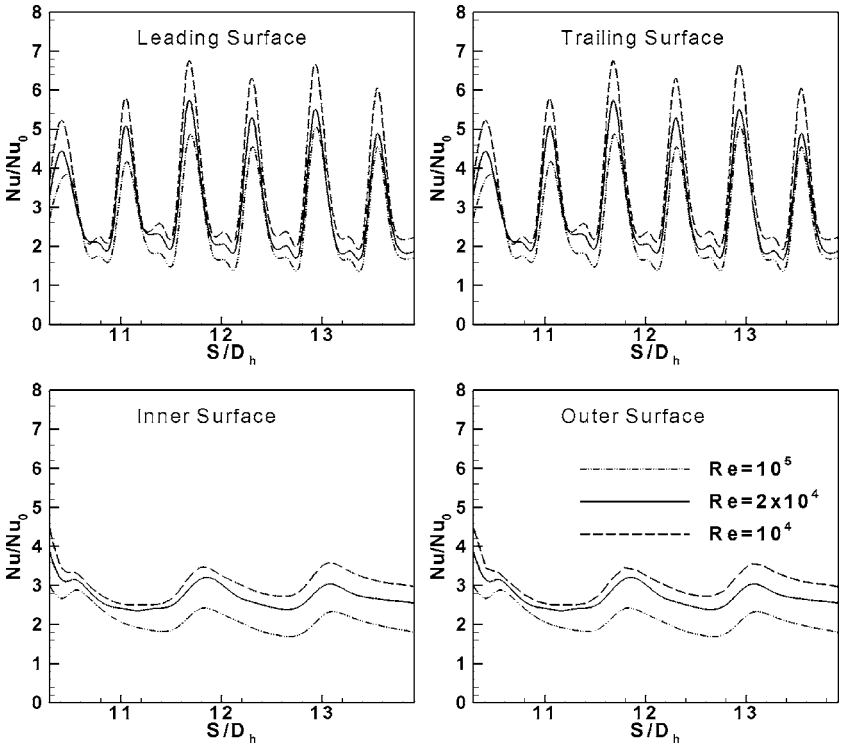

Fig. 12 Effect of Reynolds number on spanwise-averaged Nusselt number ratios for a nonrotating duct (Ro=0.0, $\Delta\rho/\rho$=0.122)

around the even-row pin-fins are considerably lower since those pin-fins are much farther away from the side walls compared to the odd-row pin-fins. Figure 14 also shows the effect of Reynolds number on the spanwise-averaged friction factor ratios for the nonrotating ducts. It is seen that the friction factor ratio reduces when the Reynolds number was increased from 10,000 to 100,000. The actual friction factors are even lower for the higher Reynolds number cases since C_{f0} is proportional to $\mathrm{Re}^{-0.25}$.

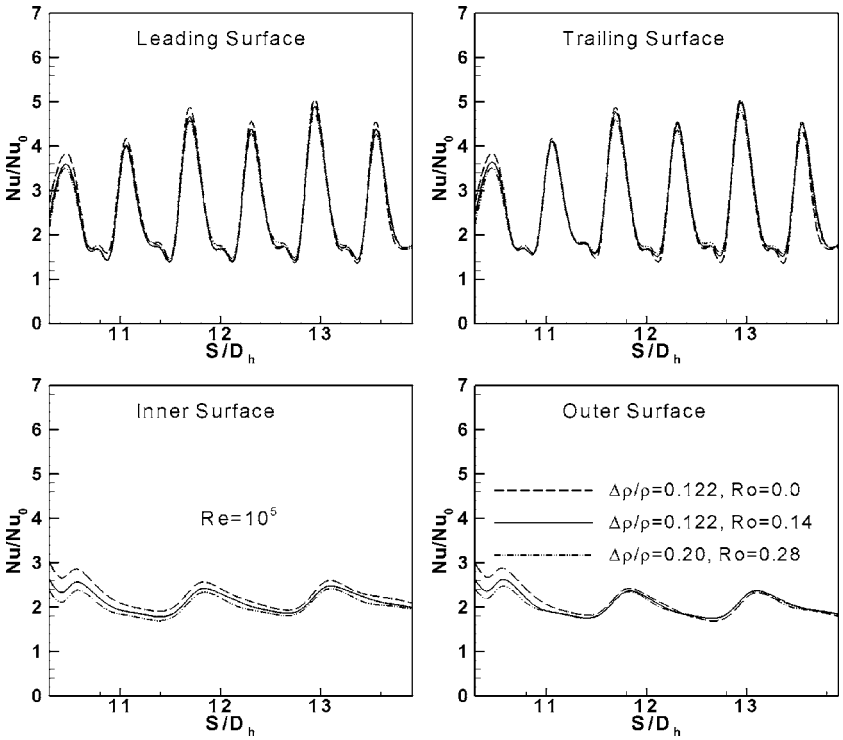

Fig. 13 Effects of rotation and density ratio on spanwise-averaged Nusselt number ratios for high Reynolds number (Re=100,000) cases

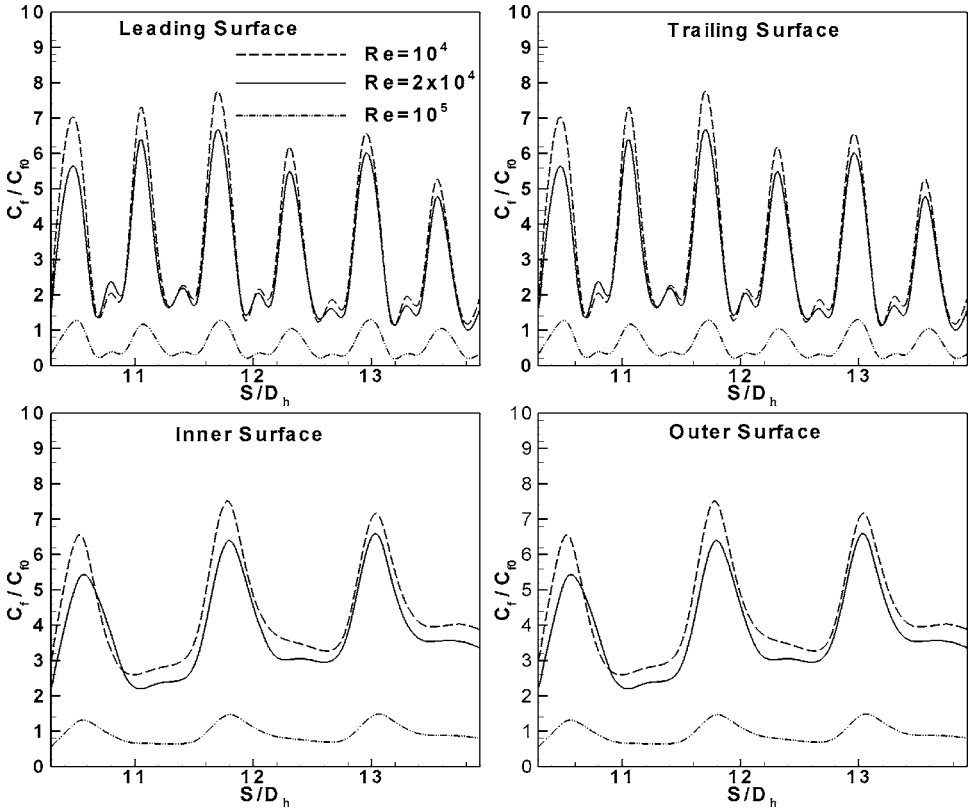

Fig. 14 Effect of Reynolds number on friction factor ratios for nonrotating pin-fin channels

For completeness, the pressure drop across the pin-fin arrays were also evaluated in terms of the friction coefficient as defined in Metzger et al. [26]:

$$f = \frac{\Delta P}{2\rho V_{\max}^2 N}$$

where ΔP is the pressure drop, ρ is the fluid density, $V_{\max}$ is the mean streamwise velocity in the minimum free flow area, and N is the number of pin-fin rows. Since the pressure data are not available in Wright et al. [17], we shall compare the predicted friction coefficients for the present cases with the measurement data and experimental correlations of Metzger et al. [26] as shown in Fig. 15. It should be noted that the experimental correlations of Metzger et al. [26] were obtained for various combinations of spacing ratio and pin height to diameter ratios, and the majority of the experimental data fall within ±15% of the correlation curve. The predicted friction coefficients are about 6% to 14% lower than the correlation curve, which is within the scatter of the experimental data. This clearly demonstrated the capability of the present near-wall Reynolds stress closure model for accurate prediction of the pressure drop in nonrotating pin fin channels.

Conclusions

A multi-block RANS method was employed to predict three-dimensional flow and heat transfer in a rotating rectangular (AR =4:1) channel with pin-fins. It predicted fairly well the complex three-dimensional flow and heat transfer characteristics resulting from the large channel aspect ratio, rotation, centrifugal buoyancy forces, and channel orientation. Main findings from this study are summarized as follows:

1. The Nusselt number ratios predicted by the second moment closure model for both the nonrotating and rotating cases are in good agreement with the measurements in the range of experimental Reynolds number.
2. The pin-fins are very effective in heat transfer enhancement due to turbulent mixing caused by flow separation around the pin-fins and the formation of horseshoe vortices in the junction between the pin-fins and channel walls.
3. The Nusselt number ratio reaches a maximum value around the third row and decreases slightly towards the channel exit.
4. Both the rotation and density ratio have only minor effects on the heat transfer enhancement.
5. High Reynolds numbers tend to reduce the heat transfer enhancement effect of the pin-fins when compared to turbulent flow in a smooth duct.

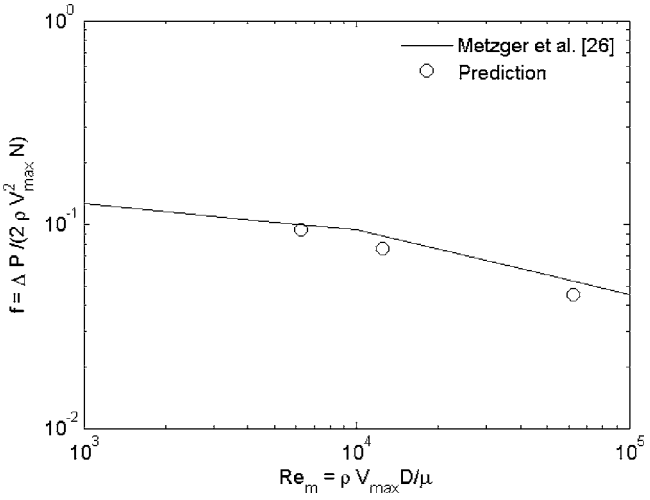

Fig. 15 Comparison of predicted friction coefficients with experimental correlations for nonrotating pin-fin channels

6. The predicted friction coefficients are in good agreement with the experimental correlation curve.

Acknowledgment

This publication was prepared with the support of the U.S. Department of Energy, Office of Fossil Energy, and National Energy Technology Laboratory. However, any opinions, findings, conclusions, or recommendations expressed herein are those of the authors and do not necessarily reflect the views of the DOE. The computations were performed on the SGI Origin 3800 at the Texas A&M Supercomputer Center under a supercomputer research grant. The support of all of the above institutions is greatly appreciated

Nomenclature

AR = channel aspect ratio
C_{f0} = friction factor fully developed turbulent nonrotating tube flow ($=0.078\,\mathrm{Re}^{-0.25}$)
D = pin diameter
D_h = hydraulic diameter, m
D = pin diameter, m
H = pin length, m
h = heat transfer coefficient, $q_w/(T_w-T_b)$, $\mathrm{W/(m^2\,^\circ C)}$
k = thermal conductivity of coolant, $\mathrm{W/(m^2\,^\circ C)}$
L_1 = unheated smooth starting section of the channel, m
L_2 = heated section of the channel, m
L_3 = unheated smooth exit section of the channel, m
Nu = local Nusselt number, hD_h/k
Nu_o = Nusselt number in fully developed turbulent nonrotating tube flow
Pr = Prandtl number
Re = Reynolds number, W_bD_h/ν
Re_m = array Reynolds number, $V_{max}D/\nu$
Ro = rotation number, $\Omega D_h/W_b$
R_r = radius from axis of rotation, m
S = streamwise distance, m
S_1 = pin streamwise spacing
S_2 = pin spanwise spacing
T = local coolant temperature, °C
T_b = bulk mean temperature, °C
T_o = coolant temperature at inlet, °C
T_w = local wall temperature, °C
$V_{\max}$ = average streamline velocity at minimum flow area, m/s
W_b = bulk velocity in streamwise direction, volume flow rate/area, m/s
β = channel orientation measured from direction of rotation
ρ = density of coolant, $\mathrm{kg/m^3}$
$\Delta\rho/\rho$ = inlet coolant-to-wall density ratio, $(T_w-T_o)/T_w$
Ω = rotational speed, rad/s
θ = dimensionless temperature, $(T-T_o)/(T_w-T_o)$

References

[1] Vollertsen, F., 1994, "Mechanisms and Models for Laser Forming," *Laser Assisted Net Shape Engineering, Proceedings of the LANE'94*, Barmberg, Germany, Vol. 1, pp. 345–360.
[2] Mucha, Z., Hoffman, J., Kalita, W., and Mucha, S., 1997, "Laser Forming of Thick Free Plates," *Laser Assisted Net Shape Engineering, Proceedings of the LANE'97*, Barmberg, Germany, Vol. 2, pp. 383–392.
[3] Metzger, D. E., Shepard, W. B., and Haley, S. W., 1986, "Row Resolved Heat Transfer Variations in Pin-Fin Arrays Including Effects of Non-uniform Arrays and Flow Convergence," ASME Paper No. 86-GT-132.
[4] VanFossen, G. J., 1982, "Heat-Transfer Coefficients for Staggered Arrays of Short Pin-Fins," ASME J. Eng. Power, **104**, pp. 268–274.
[5] Brigham, B. A., and VanFossen, G. J., 1984, "Length to Diameter Ratio and Row Number Effects in Short Pin-Fin Heat Transfer," ASME J. Eng. Gas Turbines Power, **106**, pp. 241–245.
[6] Chyu, M. K., and Goldstein, R. J., 1991, "Influence of an Array of Wall-Mounted Cylinders on the Mass Transfer From a Flat Surface," Int. J. Heat Mass Transfer, **34**(9), pp. 2175–2186.
[7] Chyu, M. K., and Hsing, Y. C., 1998, "Convective Heat Transfer of Cubic Fin Arrays in a Narrow Channel," ASME J. Turbomach., **120**, pp. 362–367.
[8] Edwardson, S. P., Watkins, K. G., Abed, E., Bartkowiak, K., and Dearden, G., 2005, "Geometrical Influences on the Bend Angle Rate per Pass During Multi-Pass 2D Laser Forming," *Proc. IWOTE'05*, International Workshop on Thermal Forming, Bremen, Germany, pp. 29–46.
[9] Uzol, O., and Camci, C., 2001, "Elliptical Pin-Fins as an Alternative to Circular Pin-Fins for Gas Turbine Blade Cooling Applications, Part 1: Endwall Heat Transfer and Total Pressure Loss Characteristics," ASME Paper No. 2001-GT-0180.
[10] Hwang, J., and Lui, C., 2001, "Measurement of Endwall Heat Transfer and Pressure Drop in a Pin-Fin Wedge Duct," Int. J. Heat Mass Transfer, **45**, pp. 877–888.
[11] Hwang, J., Lia, D. Y., and Tsia, J. P., 1998, "Heat Transfer and Pressure Drop in Pin-Fin Trapezoidal Ducts," ASME Paper No. 98-GT-110.
[12] Lau, S. C., Kim, Y. S., and Han, J. C., 1987, "Local Endwall Heat/Mass Transfer Distributions in Pin Fin Channels," J. Thermophys. Heat Transfer, **1**, pp. 365–372.
[13] Lau, S. C., Han, J. C., and Kim, Y. S., 1989, "Turbulent Heat Transfer and Friction in Pin Fin Channels With Lateral Flow Ejection," ASME J. Heat Transfer, **111**, pp. 51–58.
[14] Maekwa, K., Shirakashi, T., and Usui, E., 1983, "Flow Stress of Low Carbon Steel at High Temperature and Strain Rate—Part II: Flow Stress Under Variable Temperature and Variable Strain Rate," Bull. Jpn. Soc. Precis. Eng., **17**(3), pp. 167–172.
[15] Willett, F. T., and Bergles, A. E., 2002, "Heat Transfer in Rotating Narrow Rectangular Pin-Fin Ducts," Exp. Therm. Fluid Sci., **25**, pp. 573–582.
[16] Postaciaglu, N., Kapadia, P., and Dowden, J. M., 1997, "Thermal Stresses Generated by a Moving Elliptical Weldpool in the Welding of Thin Metal Sheets," J. Phys. D, **30**(16), pp. 2304–2312.
[17] Wright, L. M., Lee, E., and Han, J. C., 2003, "Effect of Rotation on Heat Transfer In Narrow Rectangular Cooling Channels (AR=8:1 and 4:1) With Pin-Fins," ASME Paper No. GT2003–38340.
[18] Vollertsen, F., and Rodle, M., 1994, "Model for the Temperature Gradient Mechanism of Laser Bending," *Proceedings of the LANE'94*, Bramberg, Germany, Vol. 1, pp. 371–378.
[19] Donahoo, E. E., Camci, C., Kulkarni, A. K., and Belegundu, A. D., 1999, "A Computational Visualization of Three Dimensional Flow: Finding Optimum Heat Transfer and Pressure Drop Characteristics From Short Cross-Pin Arrays and Comparison With Two-Dimensional Calculations," ASME Paper No. 99-GT-257, ASME Turbo Expo 1999, June 7–9, Indianapolis, IN.
[20] Hamilton, L. J., Adametz, D. S., Lind, E. K., and Gropinath, A., 2002, "Numerical Analysis of the Performance of a Staggered Cross-Pin Array Heat Exchanger," 8th AIAA/ASME Joint Thermophysics and Heat Transfer Conference.
[21] Su, G., Chen, H. C., and Han, J. C., 2004, "Flow and Heat-Transfer Computations in Rotating Rectangular Channels With V-Shaped Ribs," J. Thermophys. Heat Transfer, **18**(4), pp. 534–547.
[22] Chen, H. C., Jang, Y. J., and Han, J. C., 2000, "Computation of Heat Transfer in Rotating Two-Pass Square Channels by a Second-Moment Closure Model," Int. J. Heat Mass Transfer, **43**(9), pp. 1603–1616.
[23] Hubbard, B. J., and Chen, H. C., 1994, "A Chimera Scheme for Incompressible Viscous Flows With Applications to Submarine Hydrodynamics," AIAA Paper No. 94–2210, 25th AIAA Fluid Dynamics Conference, Colorado Spring, CO.
[24] Chen, H. C., Liu, T., and Huang, E. T., 2002, "Time-Domain Simulation of Large Amplitude Ship Roll Motions by a Chimera RANS Method," Int. J. Offshore Polar Eng., **12**(2), pp. 206–212.
[25] Suhs, N. E., and Tramel, R. W., 1991, "PEGSUS 4.0 Users Manual," Arnold Eng Dev Center Rep AEDC-TR-91–8, Arnold Air Force Station, TN.
[26] Metzger, D. E., Fan, C. S., and Shepard, W. B., 1982, *Pressure Loss and Heat Transfer Through Multiple Rows of Short Pins*, Heat Transfer 1982, Vol. 3, Hemisphere, Washington, DC, pp. 137–142.

Experimental Model of Temperature-Driven Nanofluid

A. G. Agwu Nnanna
Department of Mechanical Engineering,
Micro- and Nano-scale Heat Transfer Laboratory,
Purdue University Calumet,
Hammond, IN 46323-2094
e-mail: nnanna@calumet.purdue.edu

This paper presents a systematic experimental method of studying the heat transfer behavior of buoyancy-driven nanofluids. The presence of nanoparticles in buoyancy-driven flows affects the thermophysical properties of the fluid and consequently alters the rate of heat transfer. The focus of this paper is to estimate the range of volume fractions that results in maximum thermal enhancement and the impact of volume fraction on Nusselt number. The test cell for the nanofluid is a two-dimensional rectangular enclosure with differentially heated vertical walls and adiabatic horizontal walls filled with 27 nm Al_2O_3–H_2O nanofluid. Simulations were performed to measure the transient and steady-state thermal response of nanofluid to imposed isothermal condition. The volume fraction is varied between 0% and 8%. It is observed that the trend of the temporal and spatial evolution of temperature profile for the nanofluid mimics that of the carrier fluid. Hence, the behaviors of both fluids are similar. Results shows that for small volume fraction, $0.2 \leqslant \phi \leqslant 2\%$ the presence of the nanoparticles does not impede the free convective heat transfer, rather it augments the rate of heat transfer. However, for large volume fraction $\phi > 2\%$, the convective heat transfer coefficient declines due to reduction in the Rayleigh number caused by increase in kinematic viscosity. Also, an empirical correlation for Nu_ϕ as a function of ϕ and Ra has been developed, and it is observed that the nanoparticle enhances heat transfer rate even at a small volume fraction. [DOI: 10.1115/1.2717239]

Keywords: nanofluids, heat transfer, buoyancy, experiments, volume fraction, Nusselt number, Rayleigh number, empirical correlation

1 Introduction

Buoyancy-driven nanofluids are self-propelled nanofluid systems whose motion results from density difference. It has potential applications in the microelectromechanical systems (MEMS) and electronics cooling industry. Nanofluid cooling technology may be used in engines, superconducting magnets, and supercomputers where densely packed chips generate much heat, thermal management of electronics [1], energy supply and production, and transportation [2]. Nanofluid is a mixture of carrier fluid and suspended metallic nanoparticles. Since the thermal conductivity of metallic solids are typically orders of magnitude higher than that of fluids it is expected that a solid/fluid mixture will have higher effective thermal conductivity compared to the carrier fluid. The presence of the nanoparticles changes the transport properties of the fluid, thereby increasing the effective thermal conductivity, which ultimately enhance the heat transfer rate of nanofluid. In addition to the high effective thermal conductivity, the motion of the nanofluid induced by buoyancy force, Brownian motion, ballistic phonon transport, layering at the solid/liquid interface, thermal dispersion, and clustering of nanoparticles also augments the heat transfer rate through convective mechanism. The motion of the nanoparticles will also enhance the rate of heat transfer [3].

Nanofluid has significant advantages over conventional fluid with micron size or even millimeter size metallic particles. Several investigations on solid/fluid mixture containing micro- and/or millimeter sized metallic particles are available in the literature and monographs [4–8]. Reports from numerous studies show that the presence of microsize particles in a micrometer-particle/fluid flow leads to significant loss in pressure, which reduces the heat transfer rate. The particles in the mixture clog microchannels, hence impeding the flow of fluid and heat. Also, the particles tend to coalesce and settle, thereby decreasing the fluid/particle mixing and consequently reducing the heat transfer enhancement capability. Nanofluid does not significantly suffer from any of these limitations. Because of the small size of the nanoparticles, nanofluids incur little or no penalty in pressure drop. Nanofluids are extremely stable and exhibit no significant settling under static conditions, even after weeks or months [9]. Lee et al. [1], in their work on the application of nanofluids in microchannel of only one thousandth of an inch wide, reported significant cooling enhancement without clogging the microchannel. Enhancement of the heat transfer mechanism of nanofluids is attributed to chaotic movement of the ultrafine particles and increase in thermal conductivity due to the suspension of nanoparticles [10].

A review of the literature reveals that most of the research work on nanofluid has focused mainly on the estimation of thermophysical properties, primarily on the effective thermal conductivity. Based on Maxwell theory and average polarization theory, Xue [2] developed a formula for calculating the effective thermal conductivity of nanofluids. Wang et al. [3] performed an experimental investigation on the thermal conductivity of nanoparticle–fluid mixture using the steady-state parallel-plate method. They reported that the motion of particles enhances the heat transfer due to decrease in thermal boundary layer thickness and heat transfer due to conduction between nanoparticles and the wall. Eastman et al. [11] reported higher effective thermal conductivity in copper nanometer-sized particles dispersed in ethylene glycol than pure ethylene glycol containing the same volume fraction of dispersed oxide nanoparticles. Xuan et al. [12] in their work on the aggregation structure and thermal conductivity of nanofluids showed that the thermal conductivity of nanofluids increased with the fluid temperature, and that nanoparticle aggregation and formation of aggregates reduces the efficiency of the energy transport enhancement of the suspended particles. Wang et al. [13] proposed a fractal model for predicting the effective thermal conductivity of liquid with suspension of nanoparticles. Masuda et al. [14] investigated the alteration of thermal conductivity and viscosity of liquid by dispersing ultrafine particles (dispersion γ-Al_2O_3, SiO_2,

Contributed by the Heat Transfer Division of ASME for publication in the JOURNAL OF HEAT TRANSFER. Manuscript received September 6, 2005; final manuscript received September 12, 2006. Review conducted by Yogendra Joshi. Paper presented at the 2004 ASME International Mechanical Engineering Congress (IMECE2004), Anaheim, CA, USA, November 13–19, 2004.

and TiO_2 ultrafine particles). Keblinski et al. [15] explored the mechanisms of heat transfer in nanofluids. From their investigation, they proposed four possible reasons for contribution of the nanosized particles to the increase of the thermal conductivity of the system: Brownian motion of the particles, molecular level layering of the liquid at the liquid/solid interface, the nature of the heat transport in the nanoparticles, and the effects of nanoparticle clustering. The authors believed that there was a synergistic effect of the mechanisms, among which the percolation effect was favored for particles with high or low aspect ratios.

According to the literature search, little or no experimental work has been performed on thermal augmentation of buoyancy-driven nanofluids. Xuan et al. [16] theoretically analyzed the heat transfer performance of nanofluids and derived some functional correlations for predicting convective heat transfer coefficient. As part of their conclusion, they cited that experimental research is needed to improve understanding of the heat transfer enhancement of nanofluids and to assess the effects by its use. Pak et al. [17] investigated the heat transfer enhancement in a circular tube using nanofluids as the flowing medium. In their work, they showed that the Nusselt number increased with volume fraction and Reynolds number. Based on a theoretical investigation of buoyancy-driven nanofluids, Khanafer et al. [18] developed a heat transfer correlation for the average Nusselt number as a function of Grashof number and volume fraction. They concluded that a systematic experimental study is needed to better model nanofluids, and that the Nusselt number increased with Rayleigh number if Nusselt number calculation is based on thermal conductivity of carrier fluid and will decrease if calculation is based on the effective thermal conductivity of nanofluid. A significant amount of experimental and theoretical work have been performed on buoyancy-induced flow in conventional fluids [19–23]. To the author's knowledge, no empirical Nusselt number correlation on buoyancy-driven nanofluids has been cited in the literature. This information is of practical relevance in determining the thermal performance of buoyancy-driven nanofluids, and designing nanofluid heat transfer systems for cooling of electronics and other engineering applications. The objectives of this study are to experimentally investigate the thermal augmentation in buoyancy-driven nanofluids confined in a rectangular enclosure, to correlate the Nusselt number with volume fraction, and to estimate the range of volume fractions that results in maximum thermal enhancement in buoyancy-driven nanofluids.

2 Experimental Facility and Apparatus

2.1 Test Setup. The experimental facility is depicted schematically in Fig. 1. It consists of the test cell, resistive electrical heater, insulation material, nanofluids, power supply, thermocouples, and the data acquisition (DAQ) system. The physical dimensions of the test cell is 35 mm long $\times$ 40.32 mm wide $\times$ 215 mm high, and were determined such that the criterion, $[\mathrm{Ra}=g\beta(T_H-T_L)L^3/\alpha\nu] \geqslant 1708$, for the existence of buoyancy-induced flow in conventional fluids is satisfied. The vertical and horizontal walls are fabricated from aluminum material (6061 T6), and the side walls are made of transparent Plexiglas material. The respective thermal conductivity of the aluminum and Plexiglas materials are 180 W/mK and 1.1 W/mK [21]. The Plexiglas walls are used to visualize the flow patterns of the buoyancy-driven flow. Due to the low thermal conductivity value of Plexiglas, the effect of lateral heat transfer from the sides of the test cell is negligible.

The resistive electrical heater is attached to the vertical wall labeled "3" in Fig. 1 and the opposing wall "7" is the unheated wall which serves as the heat sink. The aim of heating and cooling the two opposing vertical walls "3" and "7" is to induce thermal instability in the nanofluid medium and consequently natural circulation will ensue once the buoyancy force is sufficient to overcome the resistance due to viscous and gravitational force. The heater is connected to a HP6674A power supply which controls

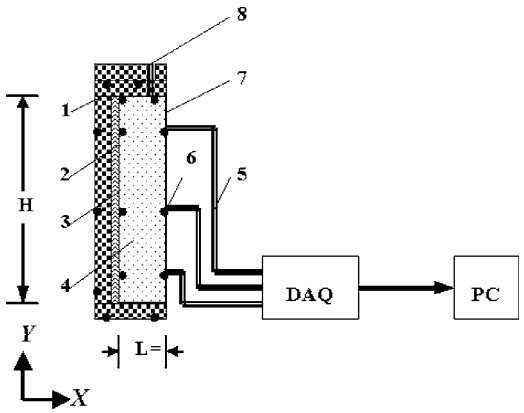

Fig. 1 Experimental setup. The numbers refer to: (1) insulation, (2) resistive electrical heater, (3) heated wall, (4) nanofluid medium, (5) thermocouple wire, (6) the black dots indicate the thermocouple locations, (7) unheated wall, and (8) spout; *L* =35 mm, *H*=215 mm.

the voltage and current output from the heater.

All the external surfaces of the test apparatus, with the exception of the vertical aluminum surfaces where the heat load and heat sink are applied, labeled "3 and 7" in Fig. 1, were insulated with a 21.3-mm-thick Polystyrene board in order to reduce heat losses from the sides to the surroundings. The exposed surface of the resistive heater was insulated to minimize heat loss to the ambient air. The thermal conductivity of Polystyrene board is $\sim$0.027 W/mK [21]. A 6.3-mm-diameter spout connected to the top horizontal wall (see Fig. 1) serves as an orifice through which nanofluid is poured into the test apparatus, and also as a means of reducing thermally induced internal pressure in the enclosure during the heating process. The spout is properly insulated to minimize heat losses to the surrounding.

The black circles shown in Fig. 1 indicate the locations of the thermocouples. Additional thermocouple locations not shown in Fig. 1 are used to verify uniform distribution of temperature, to estimate lateral heat loss through insulation, measure ambient temperature, and to use them as backup sensors in case of material failure. The selected thermocouples are copper constantan, 40-gage T-type. A total of 38 thermocouples are deployed to monitor temperature variations at selected sites in the experimental facility. Six thermocouples are attached on each of the aluminum walls to measure the temperature change across the enclosure; six thermocouples are used to measure temperature on the top and bottom surfaces. Twenty additional thermocouples are employed: two to measure the temperature of the surroundings, and six attached to each insulation board to measure temperature across the insulation. The error in the thermocouple readings is estimated to be $\pm 0.2\,^{\circ}$C and verified under constant temperature condition.

All the thermocouple wires were connected to three 20-channel Reed plug-in modules with a built-in temperature compensation for direct temperature measurement. Each module has 20 channels and communicates with the floating logic via the internal isolated digital bus of the data logger HP34970A. Temperature measurements from the data logger are automatically recorded in the personal computer for further data reduction.

The nanofluid used in this study is an aluminum oxide/deionized water suspension donated by Nanophase Technologies Inc. It has a volume fraction of 0.266. The average nanoparticle diameter is 27 nm. The nanoparticles remains suspended for a period of 1 week, after which settling begins to occur. Even when settling occurs, the particles can be redistributed by agitation of the nanofluid [9]. Fresh nanofluids tested within 2 days of preparation exhibited slightly higher conductivities than fluids that were

stored up to 2 months prior to measurement [11]. An ultrasonic processor (UP200S) manufactured by Dr. Hielscher GmbH is used for the de-agglomeration of the nanoparticles.

2.2 Experimental Procedure. Preparation of nanofluid samples begins with agitation of the nanofluid with volume fraction of 26.6% to redistribute the nanoparticles. A measured volume of the agitated nanofluid is titrated and added into a beaker containing measured volume of distilled water. The volume fraction is determined as the ratio of the volume of nanoparticles to the total volume, where the total volume is the sum of the volume of the carrier fluid and the volume of nanoparticles. The beaker is placed in a controlled chamber where it is stirred for 2 h using ultrasonic processor. The purposes of agitation are to breakdown or de-agglomerate clustered nanoparticles, facilitate even particle distribution, and minimize nanoparticle sediment that may settle after a length of time. During agitation, the temperature of the colloid increases slightly higher than room temperature. Upon completion, it is set to cool down to room temperature before use in any of the experiments. A total of five nanofluid samples with volume fractions: 0.002, 0.015, 0.027, 0.045, and 0.079 were prepared.

The sample is siphoned into the test cell using an in-house delivery system. To permit for volumetric expansion due to thermally induced internal pressure, the test cell is filled up to a level that is approximately 1 mm below the inner top surface of the test cell. This gap is sufficient to accommodate volumetric expansion of the nanofluid. Prior to onset of experiments, tests were carried out to ensure accurate readings of the thermal sensors and uniformity of initial temperature measurement at all thermocouple locations. The readings are benchmarked with measurements obtained from a mercury-in-glass thermometer to ascertain correctness. Additional tests were performed to verify the nonexistence of Marangoni convection due to the 1 mm gap. This was done by comparing temperature measurements from experiments with and without the 1 mm gap. No difference in temperature and heat transfer was noted; hence, the effect of Marangoni convection is neglected.

As a preamble to the experimental simulation, the DAQ system is activated and the data acquisition parameters such as the sampling rate, gain, etc., are programmed. The sampling rate is 10 s for each thermocouple location and the test duration is 30,000 s. The experiment begins by initializing the scan command and simultaneously switching on the power supply that regulates the heater. Power produced from the heater is transferred to the nanofluid medium via wall "3," as shown in Fig. 1. Throughout the test, the thermocouple readings are automatically monitored and recorded in a personal computer for further analysis.

For the five volume fractions considered in this study, three sets of experiments were performed. One set for each heat load, q =9.16 W, 14.3 W, and 20.91 W. A set of experiment consists of three tests performed at the same heat load and volume fraction to ensure reproducibility of the temperature data. For five volume fractions and three heat loads, a total of 45 tests were conducted.

The main source of uncertainties is error due to the measurement of temperature, heat transfer rate, and physical dimensions. The combined uncertainty of the data logger HP34970A and the thermocouple calibration in the measurement of temperature is ±0.4% or ±0.5 °C, whichever is greater. The error associated with heat transfer rate is due to voltage and current measurements and are, respectively (U_v=0.05% of setting +90 mV) and (U_I=0.1% of settling +35 mA) [24]. The combined uncertainty of the current and voltage in the heat transfer rate is expressed as

$$U_q = \sqrt{(U_I\,\partial q/\partial I)^2 + (U_V\,\partial q/\partial V)^2} \tag{1}$$

For voltages of 39.99 V, 49.99 V, and 59.99 V, and their corresponding current of 0.229 A, 0.286 A, and 0.325 A, heat transfer rate values are 9.16 W ± 1.41 W, 14.3 W ± 1.76 W, and 20.91 W ± 2.12 W. The uncertainty in the caliper (Mitutoyo) for the measurement of the physical dimension of the test apparatus is ±0.02 mm.

2.3 Thermophysical Properties of Al_2O_3/De-ionized Water Nanofluid. The effective thermophysical properties of nanofluid depend on the volume fraction, particle size, properties of nanoparticle and carrier fluid, etc. The effective density and specific heat capacity of nanofluid are, respectively, given in Nnanna et al. [25], and are expressed as: $\rho_{nf}=(1-\phi)\rho_f+\phi\rho_s$, and $(\rho c_p)_{nf}=(1-\phi)(\rho c_p)_f+\phi(\rho c_p)_s$. The subscripts nf, f, and s refers to the nanofluid, carrier fluid, and nanoparticle, respectively.

Several studies [2,3,9,11] have cited that the classical effective thermal conductivity model of Maxwell [26]

$$k_{\text{eff}} = k_f\left[1 + \frac{3(ks/k_f - 1)\phi}{(k_s/k_f + 2) - (k_s/k_f - 1)\phi}\right] \tag{2}$$

and Hamilton and Crosser [27]

$$k_{\text{eff}} = k_f\left\{\frac{k_s/k_f + (n-1)[1 + \phi(k_s/k_f - 1)]}{k_s/k_f + (n-1)[1 - \phi(k_s/k_f - 1)]}\right\} \tag{3}$$

for micron- or millimeter-sized particle suspensions are inadequate to predict the effective thermal conductivity of nanofluid. Also, little or no work has been cited in published literature on the thermal conductivity of Al_2O_3 nanoparticles. According to Wang et al. [3], the thermal conductivity of Al_2O_3 nanoparticles (particle diameter of 28 nm) can be taken as 2.5 W/mK, lower than its bulk value of 36 W/mK. Because of the limited information on experimentally verifiable mathematical models of thermal conductivity of nanofluid, and the lack of thermophysical properties of nanoparticles, the use of experimentally measured effective thermal conductivity of nanofluid appears to be the most plausible option. To this end, the experimentally measured effective thermal conductivity data of Al_2O_3/de-ionized water nanofluid reported in Refs. [2,3,14,28] has been compiled and analyzed. The average nanoparticle diameter is 27 nm, which is the same particle size for this study. Analysis shows that the effective thermal conductivity increases with volume fraction and augments the thermal conductivity of the carrier fluid by over 30% for a volume fraction of 5%. The curve-fit of data from Refs. [2,3,14,28] is used for estimation of the effective thermal conductivity in this work and it takes into account the effect of Brownian motion, clustering of nanoparticles, ballistic phonon transport, and solid/liquid layering on effective thermal conductivity.

The effect of volume fraction on effective dynamic viscosity is analyzed using experimental data obtained from Refs. [3,29,30] for nanofluid. The measured effective dynamic viscosity data for nanofluid is compared with data calculated based on the effective viscosity models of Brinkman [31] and Einstein [32] for micron/millimeter-sized suspensions. It reveals that the classical models significantly underpredicts the effective dynamic viscosity.

To the author's knowledge, experimental measurement of the volumetric expansion coefficient of nanoparticles has not been reported in the literature. In the absence of experimental data, thermal expansion coefficient of micron/millimeter- or even macrosized aluminum oxide material should provide a reasonable estimate since the overall volumetric thermal expansion of a body is a consequence of the change in the average separation between its constituent atoms or molecules, and amplitude and frequency of atom vibration. According to Ref. [33], the volumetric expansion coefficient of aluminum oxide is $8.46\times10^{-6}\,^{\circ}\text{C}^{-1}$ for $20\,^{\circ}\text{C}\leqslant T\leqslant 2000\,^{\circ}\text{C}$. For water, β_f varies from $4.004\times10^{-4}\,^{\circ}\text{C}^{-1}$ to $6.24\times10^{-4}\,^{\circ}\text{C}^{-1}$ over a temperature range of $30\,^{\circ}\text{C}\leqslant T\leqslant 75\,^{\circ}\text{C}$ [21], which is two orders of magnitude higher than β_{np}. The effective volumetric expansion coefficient is expressed as

$$\beta_{nf} \approx (1-\phi)\beta_f + \phi\beta_{np} \tag{4}$$

Because $\beta_f \gg \beta_{np}$ and $(1-\phi)\gg\phi$, one can infer that the contribution of the second term in Eq. (4) to β_{nf} is small. Even if β_{np} increased or decreased by one order of magnitude in comparison

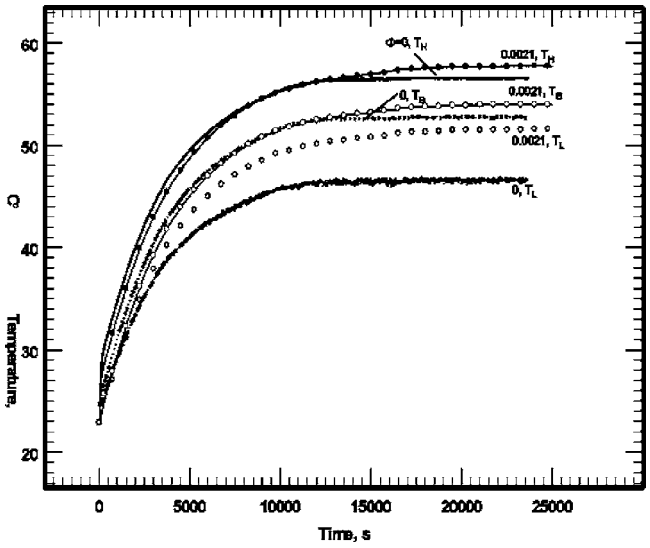

Fig. 2 Temperature as a function of time at Q=14.3 W for volume fraction, ϕ=0 and 0.0021

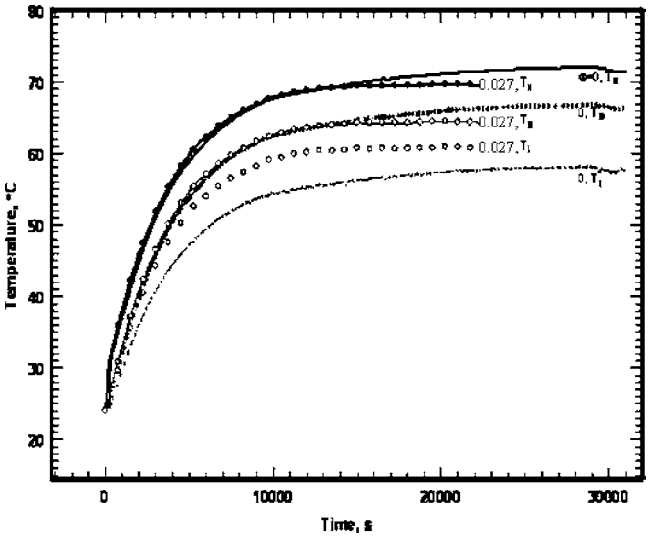

Fig. 4 Temperature as a function of time at Q=20.91 W for volume fraction, ϕ=0 and 0.027

to the bulk value, $8.46\times10^{-6}\,^{\circ}\mathrm{C}^{-1}$, its effect on β_{nf} will be negligible. Based on this assessment, the use of the bulk volumetric expansion coefficient of aluminum oxide to estimate the value of β_{nf} is reasonable.

In addition to thermophysical properties, the modified Rayleigh number is expressed as $\mathrm{Ra}_{\phi}=g\beta_{\mathrm{nf}}(T_H-T_L)L^3/\alpha_{\mathrm{nf}}\nu_{\mathrm{nf}}$, where $\alpha_{\mathrm{nf}}=k_{\mathrm{nf}}/(\rho c_p)_{\mathrm{nf}}$ is the thermal diffusivity, and $\nu_{\mathrm{nf}}=\mu_{\mathrm{nf}}/\rho_{\mathrm{nf}}$ is the kinematic viscosity. Ra_{ϕ} is a function of volume fraction, and when ϕ=0, Ra_{ϕ}=Ra.

3 Results and Discussion

3.1 Temperature Measurement. Figures 2–4 illustrate a sample of the temporal temperature profiles of the carrier fluid (ϕ=0) and nanofluid ($\phi\neq0$) caused by the imposed isothermal surface conditions, at x=0, for three data sets (ϕ=0, 0.002 and 0.027) at 14.3 W and 20.91 W. In these figures, the "lines" represent thermal response of the carrier fluid, and the "lines plus symbols" refer to the nanofluid. The legends, T_L, T_B, and T_H, signify the temperature distribution at the unheated, bulk, and heated surface, respectively. The bulk temperature is approximately the average of the heated and unheated surface temperature, and it represents the mean fluid temperature. Figures 2–4 compare the temperature profiles of the nanofluid (ϕ=0.002 and 0.027) with the carrier fluid (ϕ=0); accordingly, it shows that the temperature trend for both fluids are similar. This suggests that nanofluids behave like the carrier fluid not as a solid/fluid mixture. Data from Figs. 2–4 do not provide any information on the interaction between the nanoparticles and the carrier fluid; however, quantitatively it indicates that the nanofluid has a higher unheated surface temperature, T_L, and a lower temperature difference, $\Delta T=T_H-T_L$, than the carrier fluid. Heat transfer rate is enhanced as $T_L\rightarrow T_H$ or when $\Delta T\approx0$. This is attributed to the increase in thermal conductivity caused by the nanoparticles, particle-to-particle thermal interaction, and energy exchange between the particles and the surrounding fluid. A comparison of temperature profiles for various volume fractions: 0.002, 0.015, 0.027, 0.045, and 0.079 reveals no significant thermal enhancement with increase in volume fraction when $\phi>0.025$.

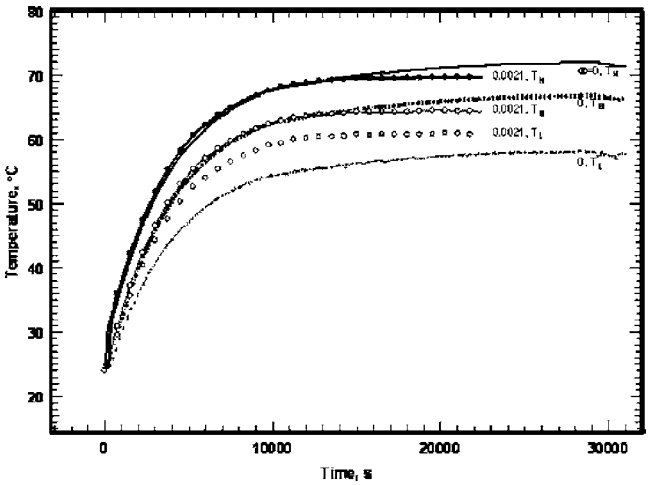

Fig. 3 Temperature as a function of time at Q=20.91 W for volume fraction, ϕ=0 and 0.0021

The spatial evolution of temperature in the X direction (see Fig. 1), which is the direction perpendicular to the plane of the heated wall of the enclosure, is presented in dimensionless form for various volume fractions in Figs. 5 and 6. The dimensionless parameters, θ and X, are expressed as $(T-T_L)/(T_H-T_L)$ and x/L, respectively. The measurement locations are: X=0, 0.174, 0.504, 0.863, and 1.0; where L=35.14 mm. For all values of ϕ, significant temperature gradient was registered in the vicinity of the heated surface, $0\leq X\leq0.2$, and near the unheated surface, $0.8\leq X\leq1.0$. However, experimental evidence shows thermal stratification and increase in temperature in the direction of heat flow in the core region, $0.2\leq X\leq0.8$. Physical reasoning dictates that the temperature should decrease in the direction of heat flow, but for natural convection in an enclosure, the rate of cooling is expected to be higher near the heated and unheated walls due to fluid motion and hydrodynamic effects. This phenomenon is attributed to buoyancy-induced cellular flows in the boundary layers adjoining the heated and unheated vertical walls; the fluid motion increases the heat transfer rate with maximum fluid motion in the vicinity of the heated wall and almost stagnant in the core. In the core, the cellular flow is almost nonexistent, hence heat transfer is generally by conduction. The temperature profiles reported in Figs. 5 and 6 are consistent with both theoretical and experimental observations in Ref. [18]. The temperature profile, θ, for the carrier fluid (ϕ=0) is compared with that of nanofluid for all the volume fractions. It confirms that the nanofluid behaves like the carrier fluid and that $\theta_{\mathrm{nf}}<\theta_f$.

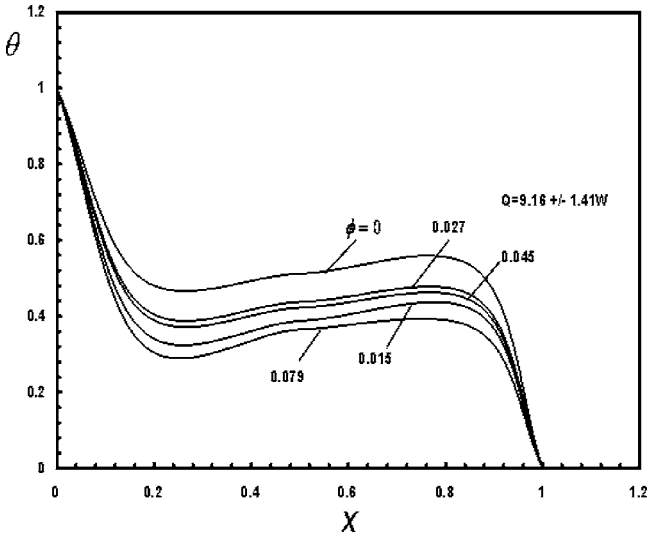

Fig. 5 Variation of dimensionless temperature with dimensionless distance across the cavity for Q=9.16 W

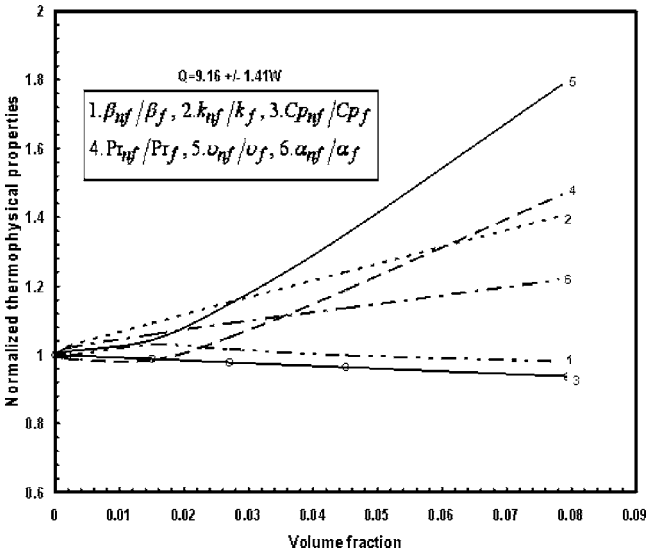

Fig. 7 Effect of volume fraction on thermophysical properties, Q=9.16 W

3.2 Effect of Volume Fraction on Thermophysical Properties and Rayleigh Number. It is generally accepted that the presence of nanoparticles affects the hydrodynamic and thermal characteristics of the carrier fluid and ultimately the rate of heat transfer. To clarify these points and to understand the degree with which the thermophysical properties that control natural convection are influenced by changes in volume fraction, Fig. 7 has been prepared for various properties of nanofluid: volumetric thermal expansion coefficient, thermal conductivity, specific heat capacity, kinematic viscosity, Prandtl number, and thermal diffusivity, and are, respectively, numbered from 1 to 6. The effective thermal conductivity and viscosity of nanofluids are obtained from experimental measurements reported in Refs. [2,3,14,28–30], respectively, and the formulas for computation of other effective properties are given in Sec. 2.3 of this paper. These properties are normalized using the corresponding thermophysical properties of the carrier fluid and are presented on the ordinate and the volume fraction on the abscissa of Fig. 7. It is observed that with the exception of the volumetric thermal expansion coefficient and specific heat capacity, all other properties increased with volume fraction; the kinematic viscosity has the highest enrichment. An increase in viscosity increases the required pumping power for heat transfer system and therefore is inimical to heat transfer. For natural convection heat transfer, the pumping power is self-induced by buoyancy force, a decline in volumetric expansion coefficient and increase in kinematic viscosity diminishes the Rayleigh number and consequently the rate of heat transfer. A close examination of Fig. 7 reveals that the kinematic viscosity and Prandtl number varies nonlinearly with volume fraction, particularly when $\phi \leqslant 0.03$. This nonlinearity is evident in the experimental measurements reported in Refs. [3,29,30].

For nanofluids, Ra should be modified to account for the effect of nanoparticles on the carrier fluid. This is done by applying the thermophysical properties discussed above for nanofluid on the Ra equation. For example, $\nu_{nf}=\mu_{nf}/\rho_{nf}$, where the effective dynamic viscosity is obtained from experimental measurements and the density is effective density. In this work, the modified Ra will be referred to as the "effective Rayleigh number" and is represented by Ra_ϕ. Figure 8 depicts the variation of effective Rayleigh number with volume fraction. Data from Fig. 8 reveal that the Ra_ϕ

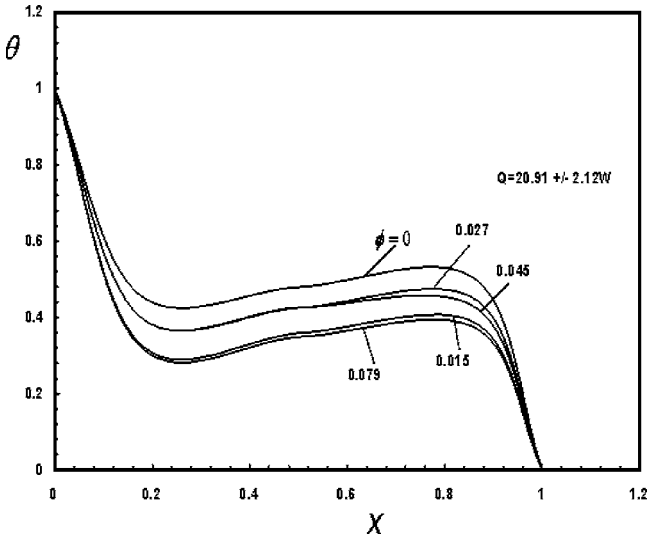

Fig. 6 Variation of dimensionless temperature with dimensionless distance across the cavity for Q=20.91 W

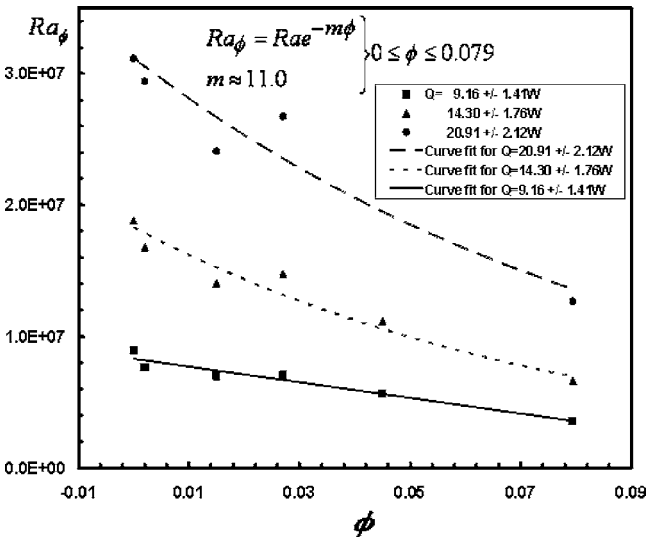

Fig. 8 Effect of volume fraction on Rayleigh number

Table 1 Nusselt number correlations for carrier fluid

Model	Nusselt number correlations for carrier fluid
Catton[a]	$\mathrm{Nu}_L=0.22[(\mathrm{Pr}/(0.2+\mathrm{Pr})]\mathrm{Ra}_L)^{0.28}(H/L)^{-0.25}$ $2\leqslant\frac{H}{L}\leqslant 10, \mathrm{Pr}\leqslant 10^5, 10^3\leqslant \mathrm{Ra}_L\leqslant 10^{10}$
Emery et al.[b]	$\mathrm{Nu}_x=0.0297\,\mathrm{Pr}^{7/15}[1+0.445(\mathrm{Pr})^{2/3}]^{-2/5}(\mathrm{Gr}_x)^{2/5}$ The Grashof number for this correlation is based on $\Delta T=T_H-T_\infty$, where $T_\infty=(T_H+T_L)/2$.
Kimura et al.[c]	$\mathrm{Nu}_H=0.364(L/H)(\mathrm{Ra}_H)^{1/4}$ where H and L are the height and length of the enclosure, respectively.
Present study	$\mathrm{Nu}=q''L/k(T_H-T_L)$ where q'' and (T_H-T_L) are obtained from experimental measurements.

[a]See Ref. [21].
[b]See Ref. [22].
[c]See Ref. [23].

decay exponentially with the increase in ϕ and are related in the form $\mathrm{Ra}_\phi\cong\mathrm{Ra}e^{-m\phi}$ for $0\leqslant\phi\leqslant 0.079$. The exponent "$m$" is a constant and has an approximate value of 11.0. When $\phi=0$, $\mathrm{Ra}_\phi=\mathrm{Ra}$. The decrease in Ra_ϕ is attributed to the rise in kinematic viscosity and decline in volumetric thermal expansion coefficient caused by the nanoparticles.

3.3 Heat Transfer Model. To ascertain the accuracy and reliability of the average Nusselt number evaluations for the nanofluid investigated in this study, temperature data collected from the carrier fluid, $\phi=0$, is used to calculate the Nusselt number as a function of Rayleigh number. The resulting Nusselt number is benchmarked with data predicted based on published Nusselt number correlations in the literature [21–23] for carrier fluids. A summary of the correlations is displayed in Table 1. The correlations shown in Table 1 are plotted in Fig. 9 and are compared with the Nusselt number calculations for this study. Figure 9 presents the variation of Nusselt number as a function of Rayleigh number. It shows that the Nusselt number increases with Rayleigh number and that the Nusselt number obtained from the present study agrees very well with all the other correlations. The average difference between the present study and other correlations is approximately 9.95%. This indicates that the experimental method employed in this study is satisfactory.

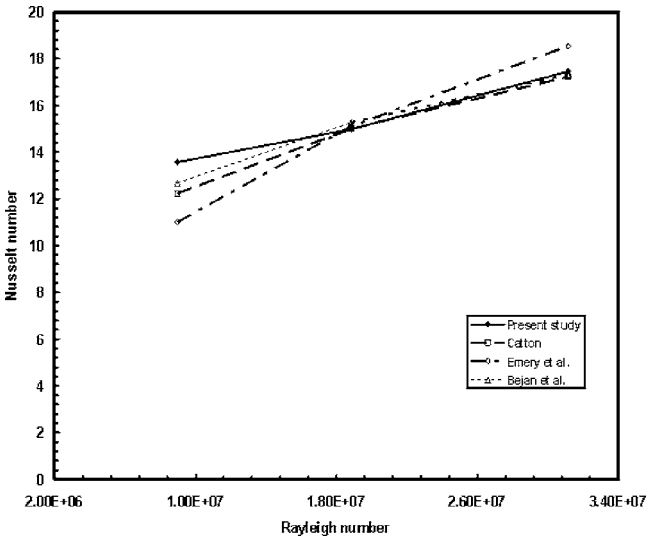

Fig. 9 Nusselt number as a function of Rayleigh number using de-ionized water. A comparison of the Nu obtained in this study with correlations for conventional fluid.

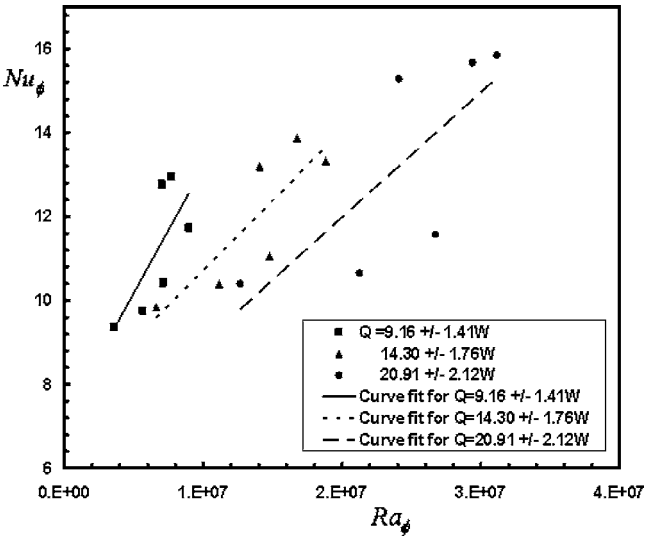

Fig. 10 Nusselt number as a function of modified Rayleigh number

The average Nusselt number, $\mathrm{Nu}=q''L/k_{\mathrm{nf}}(T_H-T_L)$, is computed based on the applied heat flux, $q''=q/A$, where q is the heat transfer rate measured electrically by recording the voltage across and current through the resistive electrical heater; and A is the heat transfer area, k_{nf} is the experimentally measured effective thermal conductivity of the nanofluid, (T_H-T_L) is the measured steady-state temperature difference between the heated and unheated vertical aluminum walls (see Fig. 1), and L is the horizontal distance perpendicular to the plane where heat load is applied. Prior to substitution of q into the Nusselt number definition, the heat loss from the apparatus during experiments is calculated. Heat loss to the surroundings is predominantly through the insulation material, Polystyrene board, on all three insulated surfaces. For each surface, the heat loss, q_i, is $(kAdT/dx)_i$, where the subscript i refers to the insulation material. Based on the measured temperature difference across the Polystyrene board, the total respective heat loss for the applied heat load of 9.16 W, 14.3 W, and 20.91 W is 0.37 W, 0.45 W, and 0.74 W, which represents about 4% of the total heat input. This shows that most of the power supplied to the nanofluid medium is transferred to the unheated wall. The uncertainty, U_{Nu}, in the Nusselt number is associated with the q, A, L, and T. This is expressed as

$$U_{\mathrm{Nu}_\phi}=\sqrt{\begin{matrix}(U_qL/k_{\mathrm{nf}}A\Delta T)^2+(qU_L/k_{\mathrm{nf}}A\Delta T)^2\\+(-qLU_A/k_{\mathrm{nf}}A^2\Delta T)^2+(-qLU_{\Delta T}/k_{\mathrm{nf}}\Delta T^2A)^2\end{matrix}} \quad (5)$$

Figure 10 depicts the average Nusselt number, Nu_ϕ, for the nanofluid as a function Ra_ϕ for various heat loads. The Nu_ϕ is calculated based on k_{nf}, and if the thermal conductivity of the carrier fluid is used, the value of Nu_ϕ will be higher than that presented in Fig. 10. It is seen that Nu_ϕ increases with Ra_ϕ, where a similar trend was observed in Fig. 9 for the carrier fluid.

The change in Nusselt number caused by volume fraction is examined in Fig. 11. Each data point signifies the average of three experiments performed at the specified volume fraction and heat load. The error bars placed on each data point refer to the uncertainty associated with the estimation of Nu_ϕ. Based on Eq. (5), the uncertainty varies from ±1.53 to ±3.61. According to Fig. 11, the Nu_ϕ strongly depends on ϕ even for a small change in effective Rayleigh number, $1E07\leqslant\mathrm{Ra}\leqslant 3E07$. Furthermore, it is noted that Nu_ϕ increased with small volume fraction, $0.2\leqslant\phi\leqslant 2\%$, and no

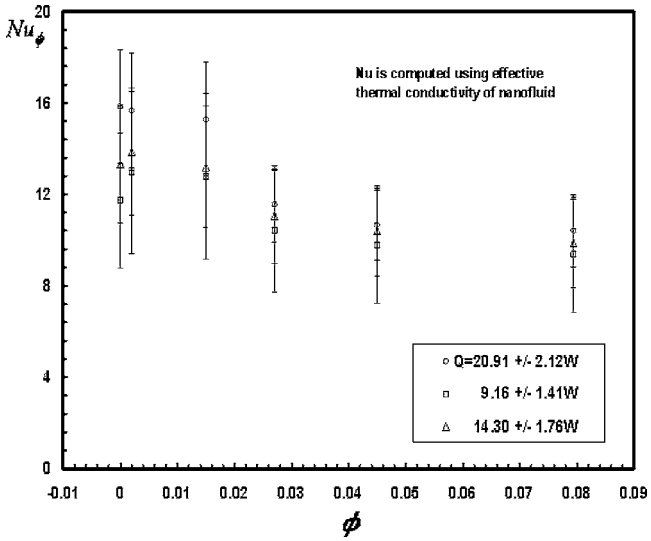

Fig. 11 Variation of Nusselt number with volume fraction

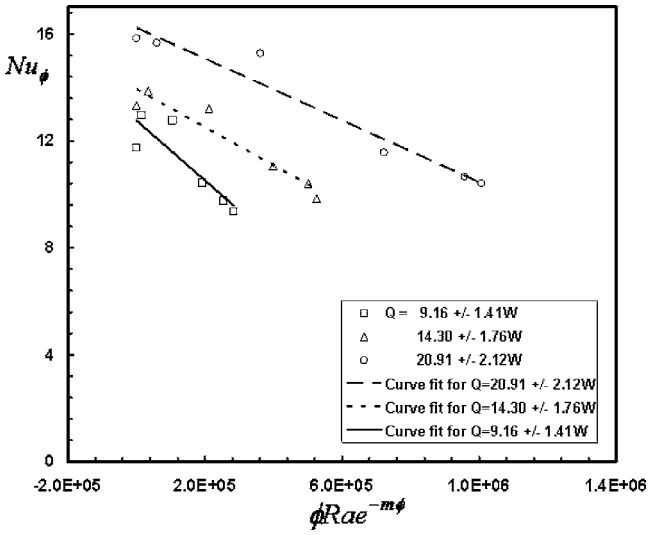

Fig. 12 Nu_ϕ as a function of parameter $\phi Ra e^{-m\phi}$

significant change in Nusselt number is observed in the range $2 \leqslant \phi \leqslant 7.9\%$. The maximum Nu_ϕ occurred at $\phi \approx 1.2\%$, which suggests that further increase in the volume fraction beyond $\phi \approx 1.2\%$ will not result in heat transfer enhancement. This raises interesting questions about the transport behavior of nanofluid at $\phi \approx 1.2\%$, the thermo-hydrodynamic forces driving such an increase in Nusselt number with a small volume fraction, the decrease in Nusselt number at $\phi \geqslant 2\%$, and the asymptotic behavior between $2 \leqslant \phi \leqslant 7.9\%$. This information is useful in the design of nanofluid systems for thermal augmentation and deserves further consideration. The report from this present study, which is that the Nusselt number increased with small volume fraction, $0.2 \leqslant \phi \leqslant 2\%$, concur with the findings reported in Koo and Kleinstreuer [34]. Koo and Kleinstreuer concluded from their work on the impact of nanoparticle motion mechanisms on the thermal conductivity of nanofluids that adding nanoparticles such as copper oxide having an average diameter of 20 nm at low volume fractions (which would be $1 \leqslant \phi \leqslant 4\%$) to liquids with high Prandtl numbers can significantly increase the heat transfer performance.

The mechanism(s) controlling the thermal enhancement when $0.2 \leqslant \phi \leqslant 2\%$ is examined. The Nusselt number, $\mathrm{Nu} = h_{\mathrm{nf}} L / k_{\mathrm{nf}}$, is regulated by two competing forces: thermal convection and conduction. The heat transfer coefficient, h_{nf}, associated with convection heat transfer is a function of $\mathrm{Ra}_\phi = g\beta_{\mathrm{nf}}(T_h - T_c)L^3/\alpha_{\mathrm{nf}}\upsilon_{\mathrm{nf}}$. When g and L are constant, which is the case in this study, change in Ra_ϕ occurs due to variation in β_{nf}, α_{nf}, ΔT, and υ_{nf}. In other words, $\delta(\mathrm{Ra}) = \delta(\beta_{\mathrm{nf}}) + \delta(\Delta T) - \delta(\upsilon_{\mathrm{nf}}) - \delta(\alpha_{\mathrm{nf}})$. The presence of nanoparticles in carrier fluid leads to the increase in υ_{nf} and decrease in β_{nf} as illustrated in Fig. 7, which ultimately lowers Ra_ϕ and h_{nf}, and increases the effective thermal conductivity k_{nf} since $k_{\mathrm{np}} \gg k_f$. An improvement in thermal conduction and decline in thermal convection consequently reduces the Nusselt number, $\mathrm{Nu} = h_{\mathrm{nf}} L / k_{\mathrm{nf}}$ and the required fluid pumping power. From Fig. 7, for small volume fraction, $0.2 \leqslant \phi \leqslant 2\%$, $\delta(\beta_{\mathrm{nf}})$ is negligible compared to $\delta(\upsilon_{\mathrm{nf}})$ and $\delta(\alpha_{\mathrm{nf}})$. It therefore seems that the thermal enhancement that occurred when $0.2 \leqslant \phi \leqslant 2\%$ can be attributed to the thermo-hydrodynamic effect caused by change in thermal conductivity and viscosity.

Earlier in this paper, it was shown that the nanoparticle impacts the Rayleigh number of the carrier fluid according to the relation, $\mathrm{Ra}_\phi \cong \mathrm{Ra} e^{-m\phi}$. To demonstrate the combined effect of ϕ and Ra_ϕ on the effective Nusselt number, Nu_ϕ is plotted as a function of parameter $\phi \mathrm{Ra} e^{-m\phi}$ for a wide range of Rayleigh number, heat load, and volume fraction in Fig. 12. Each symbol represents a unique set of conditions. The data points of each plot have been curve fitted and are depicted as "solid and dashed lines." The results associated with each heat load is represented by algebraic expression of the form

$$\mathrm{Nu}_\phi = \Gamma e^{-\mathrm{Ra}\lambda\phi(e^{-m\phi})} \tag{6}$$

and the R^2 value of the correlation shown in Eq. (6) is 95%. The values of Γ, λ, and m are not independent of the heat load and are obtained from experimental measurements. When $10^5 \leqslant \phi \mathrm{Ra} e^{-m\phi} \leqslant 10^6$, $\Gamma = 16.4$, $\lambda = 4E-07$, and $m = 11$.

4 Conclusions

An experimental investigation on the transport characteristics of buoyancy-driven nanofluids has been performed. The nanofluid is charged in a two-dimensional rectangular enclosure with adiabatic horizontal surface and isothermal vertical surface. The thermal response of the nanofluid caused by the imposed isothermal condition is measured and analyzed for various volume fractions. It is observed that the trend of the temporal and spatial evolution of temperature profile for the nanofluid mimics that of the carrier fluid. Hence, the behaviors of both fluids are similar.

The Nusselt number is determined based on experimentally measured effective thermal conductivity of nanofluid, and can be correlated to the volume fraction and Rayleigh number in the form $\mathrm{Nu}_\phi = \Gamma e^{-\mathrm{Ra}\lambda\phi(e^{-m\phi})}$. It reveals that Nu_ϕ strongly depends on volume fraction even for a small change in Rayleigh number, $1E07 \leqslant \mathrm{Ra} \leqslant 3E07$. Experimental evidence shows that heat transfer is enhanced at low volume fraction, $0.2 \leqslant \Phi \leqslant 2\%$, and that the presence of the nanoparticles ($0.2 \leqslant \Phi \leqslant 2\%$) does not impede the free convective heat transfer, rather it augment the rate of thermal diffusion. However, for large volume fraction, $\Phi > 2\%$, the free convective heat transfer is decreased due to reduction in the Rayleigh number caused by an increase in kinematic viscosity.

Acknowledgment

The author would like to thank the National Science Foundation, Grant No. 0427235-CTS, and the Purdue University Calumet Office of Undergraduate Research Grants Program for their financial support. Also, the support provided by Dr. Steve Choi of Argonne National Laboratory and Nanophase Technologies Inc. is greatly appreciated.

Nomenclature

$c_p = (1-\phi)(c_p)_f + \phi(c_p)_s$ (J/kg K)

g = gravitational force (m/s^2)
h = heat transfer coefficient ($W/m^2\,K$)
H = height of the enclosure (m)
k = thermal conductivity of nanofluid ($W/m\,K$)
L = length of the enclosure (m)
Nu = Nusselt number
Nu_ϕ = effective Nusselt number
Pr = Prandtl number
q'' = heat flux (W/m^2)
Ra = Rayleigh number
Ra_ϕ = effective Rayleigh number
T = temperature (K)
t = time (s)

Greek Symbols

α = thermal diffusivity (m^2/s)
β = volumetric thermal expansion coefficient ($1/K$)
ϕ = volume fraction
υ = kinematic viscosity (m^2/s)
μ = dynamic viscosity ($N\,s/m^2$)
ρ = $(1-\phi)\rho_f+\phi\rho_s$ (kg/m^3)

Subscripts

f = carrier fluid
H = heated
L = unheated
nf = nanofluid
s = nanoparticle

Appendix

Table 1 shows various Nu empirical correlations reported in literature for conventional fluids.

References

[1] Lee, S., and Choi, S. U. S., 1996, "Application of Metallic Nanoparticle Suspensions in Advanced Cooling Systems," *ASME Recent Advances in Solids/Structures and Application of Metallic materials*,PVP (Am. Soc. Mech. Eng.)-Vol. 342/MD-Vol. 72, pp. 227–234.
[2] Xue, Q.-Z, 2003, "Model for Effective Thermal Conductivity of Nanofluids," Phys. Lett. A, **307**, pp. 313–317.
[3] Wang, X., Xu, X., and Choi, U. S., 1999, "Thermal Conductivity of Nanoparticle-Fluid Mixture," J. Thermophys. Heat Transfer, **13**(4), pp. 474–480.
[4] Amiri, A., and Vafai, K., 1994, "Analysis of Dispersion Effects and Non-thermal Equilibrium, Non-Darcian, Variable Porosity Incompressible Flow through Porous Media," Int. J. Heat Mass Transfer, **37**, pp. 939–954.
[5] Amiri, A., and Vafai, K., 1998, "Transient Analysis of Incompressible Flow Through a Packed Bed," Int. J. Heat Mass Transfer, **41**, pp. 4259–4279.
[6] Bear, J., 1972, *Dynamics of Fluids in Porous Media*, Dover, New York.
[7] Kaviany, M., 1991, *Principles of Heat Transfer in Porous Media*, Springer, New York.
[8] Nield, D. A., and Bejan, A., 1992, *Convection in Porous Media*, Springer, New York.
[9] Eastman, J. A., Choi, S. U. S., Li, S., Soyez, G., Thompson, L. J., and Melfi, Di., 1999, "Novel Thermal Properties of NanoStructured Materials," Mater. Sci. Forum, **312–314**, pp. 629–634.
[10] Xuan, Y., and Roetzel, W., 2000, "Conceptions for Heat Transfer Correlation of Nanofluids," Int. J. Heat Mass Transfer, **43**, pp. 3701–3707.
[11] Eastman, J. A., Choi, S. U. S., Li, S., Yu, W., and Thompson, L. J., 2001, "Anomalously Increased Effective Thermal Conductivity of Ethylene Glycol-based Nanofluids Containing Copper Nanoparticles," Appl. Phys. Lett., **78**(6), pp. 718–720.
[12] Xuan, Y., Li, Q., and Hu, W., 2003, "Aggregation Structure and Thermal Conductivity of Nanofluids," AIChE J., **49**(4), pp. 1038–1043.
[13] Wang, Bu-X., Zhou, Le-P., and Peng, X.-F., 2003, "A Fractal Model for Predicting the Effective Thermal Conductivity of Liquid With Suspension of Nanoparticles," Int. J. Heat Mass Transfer, **46**, pp. 2665–2672.
[14] Masuda, H., Ebata, A., Teramae, K., and Hishinuma, N., 1993, "Alteration of Thermal Conductivity and Viscosity of Liquid by Dispersing Ultra-Fine Particles (Dispersion γ-Al_2O_3, SiO_2, and TiO_2 Ultra-Fine Particles)," Netsu Bussei (Japan), **7**(4), pp. 227–233.
[15] Keblinski, P., Phillpot, S. R., Choi, S. U. S., and Eastman, J. A., 2002, "Mechanisms of Heat Flow in Suspensions of Nano-sized Particles (Nanofluids)," Int. J. Heat Mass Transfer, **45**, pp. 855–863.
[16] Xuan, Y., and Li, Q., 2000, "Heat Transfer Enhancement of Nanofluids," Int. J. Heat Fluid Flow, **21**, pp. 58–64.
[17] Pak, B. C., and Cho, Y. I., 1998, "Hydrodynamic and Heat Transfer Study of Dispersed Fluids with Submicron Metallic Oxide Particles," Exp. Heat Transfer, **11**(2), pp. 151–170.
[18] Khanafer, K., Vafai, K., and Lightstone, M., 2003, "Buoyancy-Driven Heat Transfer Enhancement in a Two-Dimensional Enclosure Utilizing Nanofluids," Int. J. Heat Mass Transfer, **46**(19), pp. 3639–3653.
[19] Ostrach, S., "Natural Convection in Enclosures," 1972, Adv. Heat Transfer, **8**, pp. 61–227.
[20] Gebhart, B., Jaluria, Y., Mahajan, R. L., and Sammakia, B., 1988, *Buoyancy-Induced Flows and Transport*, 3rd ed., Hemisphere, Washington, DC, pp. 737–808.
[21] Incropera, F. P., and Dewitt, D. P., 1990, *Fundamentals of Heat and Mass Transfer*, 3rd ed., Wiley, New York, pp. 530–567.
[22] Emery, A., and Chu, N. C., 1965, "Heat Transfer Across Vertical Layers," J. Heat Transfer, **87**, pp. 110–116.
[23] Kimura, S., and Bejan, A., 1980, "Experimental Study of Natural Convection in a Horizontal Cylinder With Different End Temperatures," Int. J. Heat Mass Transfer, **23**, pp. 1117–1126.
[24] "Agilent 34970A Data Acquisition/Switch Unit User's Guide," 2003, http://www.agilent.com
[25] Nnanna, A. G. A., Fistrovich, T., Malinski, J., and Choi, S. U. S., 2004, "Thermal Transport Phenomena in Buoyancy-Driven Nanofluids, Part I," ASME Paper No. IMECE 2004-62059.
[26] Maxwell, J., 1994, *A Treatise on Electricity and Magnetism*, 2nd ed., Oxford University Press, Cambridge, UK.
[27] Hamilton, R. L., and Crosser, O. K., 1962, "Thermal Conductivity of Heterogeneous Two-Component Systems," I & EC Fundamentals, **I**, pp. 182–191.
[28] Xue, Q., and Xu, W.-M., 2005, "A Model of Thermal Conductivity of Nanofluids With Interfacial Shells," Mater. Chem. Phys., **90**, pp. 298–301.
[29] Roy, G., Nguyen, C. T., and Lajoie, P.-R., 2004, "Numerical Investigation of Laminar Flow and Heat Transfer in a Radial Flow Cooling System With the Use of Nanofluids," Superlattices Microstruct., **35**, pp. 497–511.
[30] Maiga, S., Nguyen, C. T., Galanis, N., and Roy, G., 2004, "Heat Transfer Behaviours of Nanofluids in a Uniformly Heated Tube," Superlattices Microstruct., **35**, pp. 543–557.
[31] Brinkman, H. C., 1952, "The Viscosity of Concentrated Suspensions and Solution," J. Chem. Phys., **20**, pp. 571–581.
[32] Ding, Y., and Wen, D., 2005, "Particle Migration in a Flow of Nanoparticle Suspensions," Powder Technol., **149**, pp. 84–92.
[33] http://www.accuratus.com/alumox.html, 2006.
[34] Koo, J., and Kleinstreuer, C., 2005, "Impact Analysis of Nanoparticle Motion Mechanism on the Thermal Conductivity of Nanofluids," Int. Commun. Heat Mass Transfer, in press.

Thermal Conductivity of Individual Single-Wall Carbon Nanotubes

Jennifer R. Lukes
e-mail: jrlukes@seas.upenn.edu

Hongliang Zhong

Department of Mechanical Engineering and Applied Mechanics,
University of Pennsylvania,
Philadelphia, PA 19104

Despite the significant amount of research on carbon nanotubes, the thermal conductivity of individual single-wall carbon nanotubes has not been well established. To date only a few groups have reported experimental data for these molecules. Existing molecular dynamics simulation results range from several hundred to 6600 W/m K and existing theoretical predictions range from several dozens to 9500 W/m K. To clarify the several-order-of-magnitude discrepancy in the literature, this paper utilizes molecular dynamics simulation to systematically examine the thermal conductivity of several individual (10, 10) single-wall carbon nanotubes as a function of length, temperature, boundary conditions and molecular dynamics simulation methodology. Nanotube lengths ranging from 5 nm to 40 nm are investigated. The results indicate that thermal conductivity increases with nanotube length, varying from about 10 W/m to 375 W/m K depending on the various simulation conditions. Phonon decay times on the order of hundreds of fs are computed. These times increase linearly with length, indicating ballistic transport in the nanotubes. A simple estimate of speed of sound, which does not require involved calculation of dispersion relations, is presented based on the heat current autocorrelation decay. Agreement with the majority of theoretical/computational literature thermal conductivity data is achieved for the nanotube lengths treated here. Discrepancies in thermal conductivity magnitude with experimental data are primarily attributed to length effects, although simulation methodology, stress, and intermolecular potential may also play a role. Quantum correction of the calculated results reveals thermal conductivity temperature dependence in qualitative agreement with experimental data.
[DOI: 10.1115/1.2717242]

Keywords: thermal conductivity, molecular dynamics simulation, phonon, single-wall carbon nanotube

Introduction

Recent advances in micro- and nanofabrication have enabled the continuing reduction in size of electronic devices. Smaller sizes have led to higher device densities at the expense of increased power demand and the resultant heat generation. New thermal management strategies are thus critically important to continued high performance, reliability, and lifetime. One such strategy is to develop novel high thermal conductivity materials based on carbon nanotubes. Carbon nanotubes, which come in single- and multiwall forms, are rolled up from graphene sheets into cylinders. Early work predicted superior thermal conductivity, exceeding even that of diamond, for carbon nanotubes [1]. Most measurements on nanotube materials indicate that thermal conductivity increases monotonically with increasing temperature even above ambient temperature. Two groups have observed experimental thermal conductivity values of more than 3000 W/m K at room temperature for individual multiwall nanotubes (MWNTs), although the tube diameters are slightly different: 14 nm from Kim et al. [2] and 16.1 nm from Fujii et al. [3]. Choi et al. found a much lower value of 300 W/m K for MWNTs with 20 nm outer diameter and 1.4 μm length at room temperature [4]. Hone et al. [1] found that the thermal conductivity of aligned single-wall nanotube (SWNT) crystalline ropes is about 250 W/m K at 300 K and estimated that the longitudinal thermal conductivity of a single SWNT ranges from 1750 W/m K to 5800 W/m K. The first thermal conductance measurement on an isolated SWNT revealed a higher room-temperature thermal conductivity than that of MWNT, ranging from 2000 W/m K to 10000 W/m K depending on the diameter assumed in the conversion from conductance to conductivity [5]. More recent measurements, carried out above room temperature on a 2.6 μm long single wall carbon nanotube, display a peak thermal conductivity value of about 3400 W/m K near 300 K, decreasing to about 1200 W/m K at 800 K [6]. Within the above results (Table 1), there is significant variation in the data for nanotubes of varying diameters and lengths.

Molecular Dynamics Simulation Techniques. Molecular dynamics (MD) simulation [7] provides another approach for determining the thermal conductivity of carbon nanotubes, and yields additional atomistic information useful for analyzing thermal energy transport in SWNT and other carbon nanotube based materials. Classical MD involves integration of Newton's equations of motion for atoms interacting with each other through an empirical interatomic potential. It does not explicitly model electrons and therefore cannot simulate electron–electron or electron–phonon interactions. The phonon contribution for thermal conductivity is dominant in both MWNTs and SWNTs at all temperatures [8–10], which justifies neglecting electronic effects in simulations of carbon nanotubes.

In general there are three ways to compute the thermal conductivity in a solid. Nonequilibrium molecular dynamics (NEMD) [11] is based on Fourier's law, which relates the heat current in the axial direction to the axial temperature gradient through thermal conductivity

Contributed by the Heat Transfer Division of ASME for publication in the JOURNAL OF HEAT TRANSFER. Manuscript received December 21, 2005; final manuscript received September 15, 2006. Review conducted by Ranga Pitchumani. Paper presented at the 2004 ASME International Mechanical Engineering Congress (IMECE2004), Anaheim, CA, USA, November 13–19, 2004.

Table 1 Thermal conductivity of isolated single-wall carbon nanotubes at T_{MD}=300 K

	k (W/m K)	Tube length (nm)	Cross-sectional area (m^2)	Chirality	Simulation technique
Molecular dynamics simulation					
Berber et al. [16]	6600	2.5	29×10^{-19}	(10, 10)	HNEMD
Osman et al. [17]	1700	30	14.6×10^{-19}	(10, 10)	NEMD
Che et al. [18]	2980	40	4.3×10^{-19}	(10, 10)	EMD
Yao et al. [19]	$1-4\times10^{23}$	6–60	14.6×10^{-19}	(10, 10)	EMD
Padgett and Brenner [20]	40–320	20–310	14.6×10^{-19}	(10, 10)	NEMD
Moreland et al. [21]	215–831	50–1000	14.6×10^{-19}	(10, 10)	NEMD
Maruyama [22]	260–400	10–400	14.6×10^{-19}	(10, 10)	NEMD
Boltzmann–Peierls phonon transport equation (316 K)					
Mingo and Broido [24]	80–9500	$10-10^9$		(10,0)	
Experimental measurement[a]					
	k (W/m K)	Tube length (nm)	Diameter (nm)		
Kim et al. [2] (MWNT)	3000	2500	14		
Fujii et al. [3] (MWNT)	500	3600	28.2		
	1800	1890	16.1		
	2800	3700	9.8		
Yu et al. [5]	2000	2600	1		
	10,000	2600	3		
Pop et al. [6]	3400	2600	1.7		
Choi et al. [4] (MWNT)	300	1400	20		

[a]Chirality unknown.

$$J_z = q_z V = -kV\frac{dT}{dz} \tag{1}$$

Equilibrium molecular dynamics (EMD) [12] is based on the Green–Kubo formula derived from linear response theory [13]. Simplifying for the case of axial conduction yields the thermal conductivity expression

$$k = \frac{1}{Vk_BT^2}\int_0^\infty \langle J_z(0)J_z(t)\rangle dt \tag{2}$$

where J_z is the axial component of the heat current $\vec{J}$ [14]

$$\vec{J}(t) = \sum_i \vec{v}_i\varepsilon_i + \frac{1}{2}\sum_{ij,i\neq j} \vec{r}_{ij}(\vec{f}_{ij}\cdot\vec{v}_i) \tag{3}$$

and the term inside the angle brackets in Eq. (2) represents the axial heat current autocorrelation function (HCACF). The temporal decay of the average HCACF represents the time scale of thermal transport.

The third method, homogeneous NEMD (HNEMD) [15], is a nonequilibrium approach in which an external field is applied to the system to represent the effects of heat flow without physically imposing a temperature gradient or flux. $\vec{F}_e$ is the external field that adds an extra force $\Delta\vec{F}_i$ to each individual atom by

$$\Delta\vec{F}_i = (\varepsilon_i - \langle\varepsilon\rangle)\vec{F}_e - \sum_{j(\neq i)} \vec{f}_{ij}(\vec{r}_{ij}\cdot\vec{F}_e) + \frac{1}{N}\sum_{jk(j\neq k)} \vec{f}_{jk}(\vec{r}_{jk}\cdot\vec{F}_e) \tag{4}$$

Extrapolating to zero external field [15] and applying $\vec{F}_e$ in the axial direction allows the thermal conductivity to be determined from

$$k = \lim_{F_e\to 0}\lim_{t\to\infty} \frac{\langle J_z(\vec{F}_e,t)\rangle}{F_eTV} \tag{5}$$

where the axial heat current is time averaged. This method is computationally efficient, but the extrapolation to zero $\vec{F}_e$ can be a challenge as is shown later.

Previous Modeling Work. Several classical MD simulations have been performed in order to pinpoint the thermal conductivity of isolated (10, 10) SWNT [16–22]. Table 1 lists these results. It is seen that the values vary from several hundred to 6600 W/m K, with one outlier point [19] estimated at 10^{23} W/m K! In general, most values are lower than experimental data [5,6]. As the structural details of the tubes measured in the experiments are not known, it is difficult to compare to simulations on specific tube chiralities. There is still significant uncertainty as to the correct value of SWNT thermal conductivity.

Berber et al. [16] found that thermal conductivity increases with increasing temperature, reaches a peak at around 100 K, and finally decreases to about 6600 W/m K at room temperature. Osman et al. [17] found a similar behavior with a peak of near 400 K and a conductivity of about 1700 W/m K at 300 K. Che et al. [18] claimed to find length convergent thermal conductivity of about 2980 W/m K for a 40 nm long tube at room temperature. Yao et al. [19] calculated thermal conductance of carbon nanotubes; a conversion to conductivity by dividing thermal conductance by cross-sectional area gives results 23 orders of magnitude higher than other literature values. Additionally their phonon spectra appear quite different from those of other MD simulations [17,22]. The reason for those extreme values might be the violation of the ballistic upper bound to thermal conductivity pointed out by Mingo and Broido [23]. Padgett and Brenner [20] predicted thermal conductivity about 160 W/m K at 300 K, and Moreland et al. [21] found that the thermal conductivity at 300 K increases

from 215 W/m K at 50 nm to 831 W/m K at 1000 nm tube length. Maruyama [22] showed that the thermal conductivity is around 400 W/m K for a 400 nm long tube and increases steadily with length with an exponent of 0.15. In the latter two results, length convergence is still not achieved even for the longest nanotubes simulated. Mingo and Broido [24] solved the linearized Boltzmann–Peierls phonon transport equation by considering three-phonon scattering processes to higher order and showed that at short lengths the thermal conductivity increases with length (ballistic regime) while at longer lengths (diffusive regime) a length convergent value is achieved. The thermal conductivity of individual 100 nm long (10, 0) SWNT at 316 K was about 100 W/m K, and the length convergent value is as high as about 9500 W/m K.

Possible Reasons for Literature Discrepancies. As discussed above, nanotube length is a significant reason for the discrepancies in the literature. Various groups have performed calculations and measurements at different lengths and thus at different locations in the ballistic-diffusive continuum, so the observed length dependence is not surprising in light of these observations. Temperature effects are also important, as indicated by the peaking behavior observed by several authors [5,16,17]. Another reason for these discrepancies arises from differing choices for the nanotube cross-sectional area. In Eqs. (1), (2), and (5) it is evident that thermal conductivity is inversely proportional to nanotube volume, which is equal to cross-sectional area multiplied by nanotube length. The choice of nanotube area thus influences the calculated thermal conductivity value, and to compare obtained thermal conductivities from different groups it is imperative to scale all values by the same area. Berber et al. [16] calculated the area based upon the fact that tubes have an interwall separation of about 3.4 Å in nanotube bundles. Che et al. [18] chose a ring of 1 Å thickness for the cross-sectional area as the geometric configuration, while Maruyama [22] used a ring of van der Waals thickness of 3.4 Å. The rest [17,19–21] calculated the area as a circle with circumference defined by the centers of the atoms around the nanotube. Scaling all tubes by the same area still does not eliminate the differences. All of the above studies except for one used the Tersoff–Brenner (TB) bond order potential [25] to model the carbon nanotubes. Padgett and Brenner [20] used the reactive bond order potential (REBO) [26], an improved second-generation version of the TB potential, in an NEMD simulation. They found a thermal conductivity of 160 W/m K at 61.5 nm nanotube length. Moreland et al. [21] and Maruyama [22], who also used NEMD, employed the TB potential and found somewhat higher values: 215 W/m K at 50 nm length and 321 W/m K at 20 nm length, respectively. These differences may be partially caused by the slightly different form of the potential used.

Stress in the nanotubes may also contribute to the discrepancies. Moreland et al. [21] determined the stress-free tube length by running simulations with free boundaries at the tube ends to allow for longitudinal expansion/contraction, and then applied periodic boundary conditions (PBCs) for the remainder of the simulations. They found much lower thermal conductivity than that from experiments and from some of the papers above. As no mention of efforts to mitigate stress by relaxing the structure is discussed in these other papers, it is possible that some of the high calculated values [16–19] may be caused by compression of the tubes. Stress/strain effects have already been demonstrated to be important in other nanostructures [27]. The stress state of the experimental measurements is unknown.

It is not clear whether EMD or NEMD is better for simulating SWNT [21]. Also, the choice of axial boundary condition influences the thermal transport. The phonon mean free path in SWNT is several microns [28], and for nanotubes shorter than this length phonon scattering from free boundaries will be important. Nanotubes modeled with periodic boundary conditions have no free boundary and thus boundary scattering is eliminated, leaving phonon–phonon interactions as the only scattering mechanism. For a finite-length tube in which the phonons are scattered at the ends, it is more physically meaningful to use free boundary conditions in the simulations.

To clarify the correct temperature and length dependence of individual (10, 10) SWNTs, this paper investigates the effects of boundary conditions and MD simulation methods under a consistent set of cross-sectional areas, potentials, and stress conditions. Phonon density of states and phonon relaxation times are also calculated to better understand phonon modes and phonon scattering. Although the study of thermal conductance rather than thermal conductivity may be more appropriate in systems like carbon nanotubes that experience ballistic transport, thermal conductivity is investigated here for ease of comparison to available literature data.

Computational Procedure

In order to study the temperature and length dependence of thermal conductivity, four different (10, 10) SWNTs are investigated using classical MD. They have 800, 1600, 3200, and 6400 atoms corresponding to nanotube lengths of about 5 nm, 10 nm, 20 nm, and 40 nm, respectively. The temperature ranges from 100 K to 500 K. The initial configuration of (10, 10) SWNT is constructed using a bond length of 1.42 Å. To study the effect of different boundary conditions, both free boundary and PBC are used. In PBC simulations, an extra simulation is run first with free boundaries to obtain the stress-free tube length. This length is typically very close to the original starting length.

To model the bonded carbon–carbon interactions, the REBO potential is used [26]. The nonbonded interactions between atoms are modeled using the Lennard-Jones potential. The total initial linear and angular momenta are removed once at the beginning of the simulation by subtracting the linear and angular velocity components [29]

$$\vec{v}_i|_{\text{new}} = \vec{v}_i|_{\text{old}} - \sum_j \frac{\vec{v}_j|_{\text{old}}}{N} - \vec{\omega} \times \vec{r}_i \tag{6}$$

This procedure ensures that the isolated carbon nanotube does not have translational or rotational movement, which simplifies the calculation of the heat current along the tube axis. In all simulations, a 3.4 Å thickness cylinder is chosen as the geometric configuration. Zero linear and angular momenta are well conserved at all time steps. Details on the calculation of the instantaneous angular velocity of the system can be found in Ref. [30]. The resulting velocities are scaled to match the initial temperature. The time step is 1 fs for all cases. For the first 40 ps a constant temperature simulation with the Nosé–Hoover thermostat [31] is used to equilibrate the system to the desired temperature. Then a 400 ps long simulation is performed in the microcanonical ensemble to compute the heat current along the tube axis. The HCACF is calculated up to 200 ps, after which time it has decayed to approximately zero.

To calculate thermal conductivity using EMD it is necessary to integrate the HCACF (Eq. (2)). If PBCs are used, phonons will reenter the simulation box and interfere with themselves at times longer than the time a phonon takes to ballistically traverse the nanotube, τ_b, resulting in spurious self-correlation effects in the HCACF [32]. This time is estimated conservatively as the nanotube length L divided by the speed of sound of the longitudinal acoustic mode c_{LA}, which, at 20 km/s [8], is the fastest traveling mode in the nanotube. To avoid these spurious effects, a best fit curve to the HCACF decay is found for $t < \tau_b$ ("early time").

As suggested by Che et al. [33], the decay is fitted by a double exponential function

$$\text{HCACF} = A_1 \exp(-t/\tau_1) + A_2 \exp(-t/\tau_2) \tag{7}$$

where τ_1 and τ_2 are time constants associated with fast and slow decays, respectively. Physically τ_1 and τ_2 are interpreted as half of

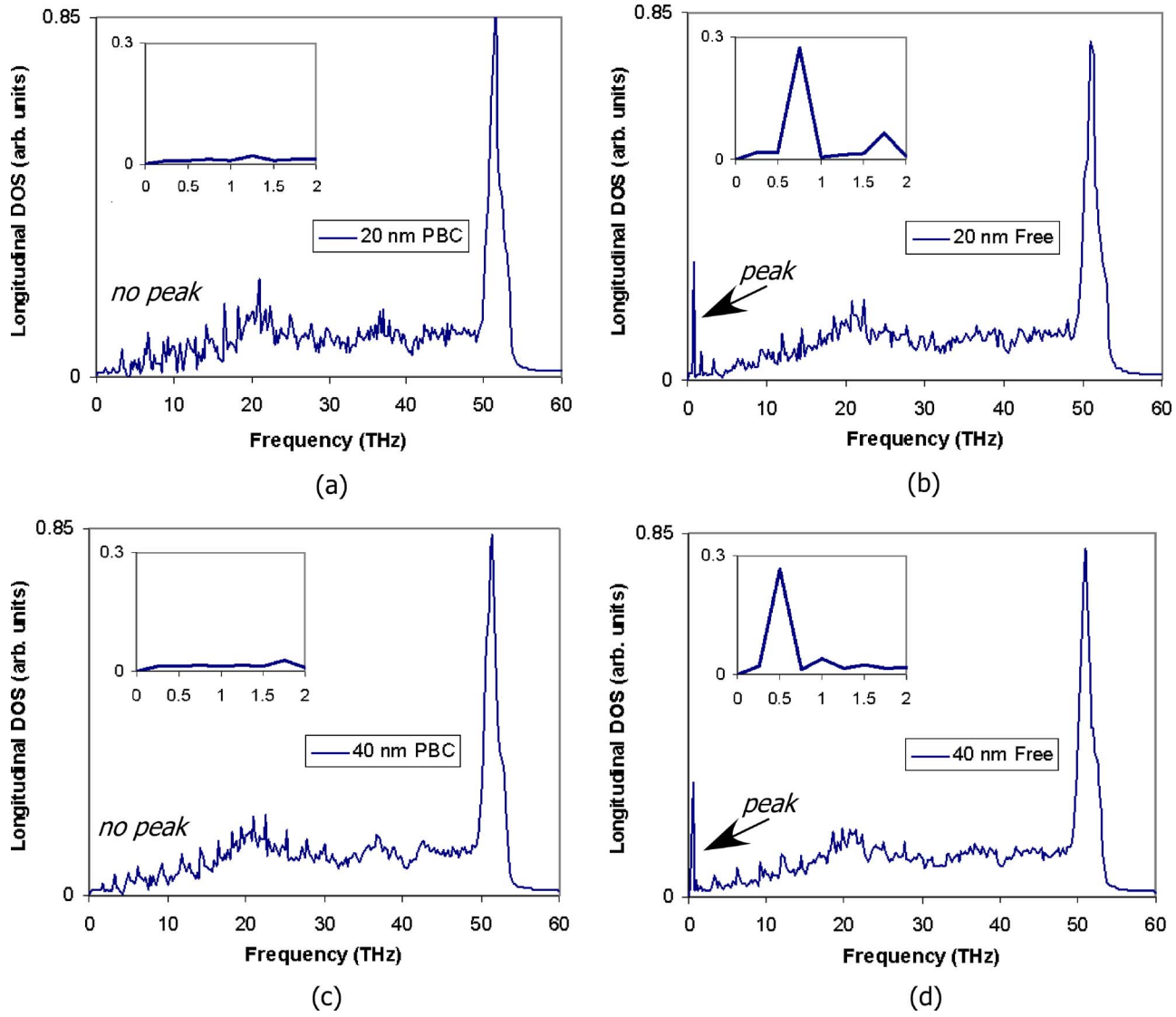

Fig. 1 Longitudinal phonon density of states at T_{MD}=300 K for (10, 10) SWNTs with different lengths and boundary conditions: (*a*) 20 nm periodic; (*b*) 20 nm free; (*c*) 40 nm periodic; and (*d*) 40 nm free

the period for energy transfer between two neighboring atoms or the "local" time decay, and as the average phonon–phonon scattering time, respectively [34]. Thermal conductivity is then computed analytically by integrating Eq. (7) from $t=0$ to ∞ using the best fit τ_1 and τ_2 values. In each simulation, the general expression for error propagation [35] is used to calculate the probable error of thermal conductivity

$$\sigma_k = \sqrt{\sigma_T^2\left(\frac{\partial k}{\partial T}\right)^2 + \sigma_{\langle J_z(t)J_z(0)\rangle}^2\left(\frac{\partial k}{\partial \langle J_z(t)J_z(0)\rangle}\right)^2} \tag{8}$$

Because thermal expansion of the tube is negligible [36], variation of the tube volume is not included in the error estimation. The standard error of the HCACF depends on the simulation run time t_{run} and the correlation time t_{corr} [37]

$$\sigma_{\langle J_z(t)J_z(0)\rangle} = \sqrt{\frac{2t_{corr}}{t_{run}}}\langle J_z^2\rangle \tag{9}$$

where the correlation time is defined by

$$t_{corr} = \frac{2\int_0^\infty dt\ \langle J_z(t)J_z(0)\rangle^2}{\langle J_z^2\rangle^2} \tag{10}$$

Results and Discussion

Phonon Density of States. Thermal properties strongly depend on the phonon density of states (DOS) which is the number of vibrational states per unit frequency. In MD simulations, the longitudinal DOS is calculated as

$$D_{long}(\omega) = S\int dt\ e^{-i\omega t}\langle v_z(t)v_z(0)\rangle = S\Delta t \cdot \mathrm{FFT}[\langle v_z(t)v_z(0)\rangle] \tag{11}$$

where the product of the scale factor $S=Nm/k_BT_{MD}$, the MD simulation timestep Δt, and the fast Fourier transform of the averaged axial velocity autocorrelation function is taken. Often in MD studies the DOS is plotted in arbitrary units rather than units of states per unit frequency; typically this is done by neglecting

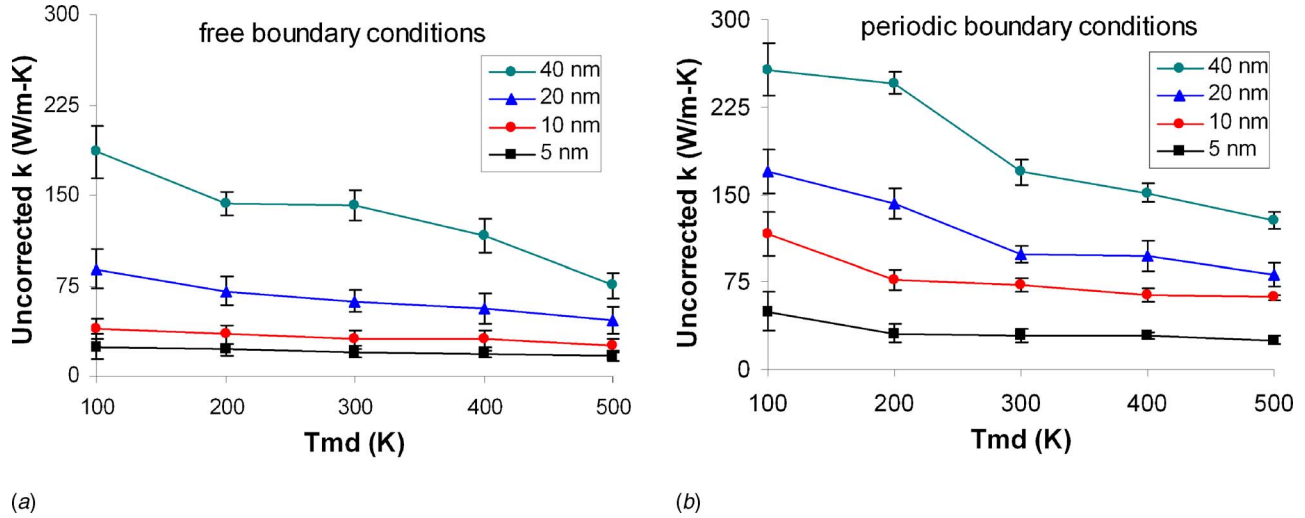

(*a*) (*b*)

Fig. 2 Uncorrected thermal conductivity versus temperature at different nanotube lengths for (10, 10) SWNTs with both: (*a*) free; and (*b*) periodic boundary conditions

the $S\Delta t$ product in Eq. (11). The effect of neglecting $S\Delta t$ is to remove the effects of total (classical) lattice energy and number of atoms, so that different domain sizes and temperatures can be compared using axes with the same scales. This convention is also followed here for all DOS plots. Figure 1 shows the longitudinal phonon DOS (arbitrary units) at 300 K for (10, 10) SWNTs with two different lengths and two different boundary conditions. Four thousand temporal points are used in calculating the density of states. Therefore the spectral resolution is 0.25 THz. All graphs have a strong peak around 52 THz, which is characteristic of the two-dimensional (2D) graphene sheet phonon spectrum [38]. In all plots with free boundaries, there is also a strong low-frequency peak. This peak is absent in PBC cases. The physical meaning of the peak is that there is an additional vibrational mode not present in the PBC tubes, which represents the periodic axial oscillation of the free tube ends. Dickey and Paskin [39] found a similar low frequency mode for small particles with free surfaces. The peak appears at 1.25 THz, 0.75 THz, 0.5 THz, and 0.25 THz at nanotube lengths 5 nm, 10 nm, 20 nm, and 40 nm, respectively. The reduction in peak position with tube length does not scale linearly; this is likely a result of the 0.25 THz resolution. The resolution can be increased by using significantly longer simulation times; however, such times are computationally intensive and beyond the scope of the present study.

The full DOS was also calculated. This was done by replacing the product of axial velocity components in Eq. (11) with the dot product of velocities

$$D_{\text{full}}(\omega) = S\int dt\, e^{-i\omega t}\langle \vec{v}(t)\cdot\vec{v}(0)\rangle = S\Delta t\cdot \text{FFT}[\langle \vec{v}(t)\cdot\vec{v}(0)\rangle] \tag{12}$$

Unlike the clear "peak" / "no peak" behavior of the longitudinal density of states, the full density of states shows a low-frequency peak for both PBC and free cases that is more pronounced with free boundary conditions. The inclusion of radial and tangential velocity components in the full DOS (Eq. (12)) contributes additional vibrational modes and it is likely that these partially obscure any "peak"/"no peak" effect occurring at low frequencies.

Temperature Dependence and Quantum Correction. For both free boundary and PBC cases, thermal conductivity monotonically decreases with increasing temperature as shown in Fig. 2. This temperature dependence disagrees with the available low-temperature (<500 K) experimental data. The reason for this disagreement is that quantum effects, which are important at temperatures below the Debye temperature, are completely neglected in the classical MD approach. Thus, quantum corrections to the MD calculations of temperature and thermal conductivity are necessary. Temperature in MD simulations (T_{MD}) is typically calculated based on the mean kinetic energy of the system. By assuming that the total system energy is twice the mean kinetic energy at T_{MD} (equipartition) and equal to the total phonon energy of the system at the quantum temperature T, correction is made through [40]

$$m\sum_{i=1}^{N}\vec{v}_i\cdot\vec{v}_i = 3Nk_BT_{\text{MD}} = \int_0^{\omega_{\max}} D_{\text{tot}}(\omega)\left[\frac{1}{(e^{\hbar\omega/k_BT}-1)}+\frac{1}{2}\right]\hbar\omega\, d\omega \tag{13}$$

where $D_{\text{tot}}(\omega)$ is the phonon density of states summed over all acoustic branches and the $\frac{1}{2}$ term represents the effect of zero point energy. Essentially, this procedure corrects for the low-temperature heat capacity variation with temperature that is not accounted for in the classical simulation. It provides a means for mapping results calculated classically onto their quantum analogs at the same energy level.

To implement the quantum correction here, the Debye density of states [41] is used. On a per atom basis and converting from angular frequency to frequency Eq. (13) becomes

$$T_{\text{MD}} = \frac{1}{3k_B}\int_0^{\nu_D} b_{\text{tot}}(\nu)\left[\frac{1}{(e^{h\nu/k_BT}-1)}+\frac{1}{2}\right]h\nu\, d\nu \tag{14}$$

The total DOS is the sum over the longitudinal, two degenerate transverse, and twist densities of states

$$b_{\text{tot}} = b_{\text{LA}} + 2b_{\text{TA}} + b_{\text{TW}} = \frac{4\pi\nu^2}{\left(\frac{N}{V}\right)}\left(\frac{1}{c_{\text{LA}}^3}+\frac{2}{c_{\text{TA}}^3}+\frac{1}{c_{\text{TW}}^3}\right) = 4\left[\frac{4\pi\nu^2}{c_{\text{av}}^3\left(\frac{N}{V}\right)}\right] \tag{15}$$

and $c_{\text{av}}=11.26$ km/s is the speed of sound averaged over the four branches according to their weights in the density of states. The velocities of the individual branches are given as $c_{\text{LA}}=20.35$ km/s, $c_{\text{TA}}=9.43$ km/s, and $c_{\text{TW}}=15$ km/s [8].

The upper limit of Eq. (14) is the Debye frequency, which scales with Debye temperature through the proportionality factor k_B/h. It is not entirely clear what the correct Debye temperature value is for carbon nanotubes, but it is expected to be similar to that of graphite [8]. Several studies quote or estimate high values

for graphite, e.g., >2000 K [8] and 2500 K [42]. A recent first-principles study of graphite [43] reveals a temperature dependent Debye temperature: ~400 K at 0 K rising dramatically to ~1900 at high temperature. It is important to note that dramatically different Debye temperatures are often quoted for different modes in the same material, for example 2100 K for longitudinal modes versus 614 K for transverse modes propagating in-plane in graphite [44]. In other cases a single value, determined from fitting experimental heat capacity data or from DOS calculations that average among the various vibrational modes, is reported. The latter approach is used here (Eq. (15)). The Debye frequency is found from the number of modes in a single acoustic branch, which is equal to the number of primitive cells in the domain [41] and also to the number of atoms divided by the number of basis atoms per primitive cell p

$$M = \frac{N}{p} = \int_0^{\nu_D} D_{\mathrm{av}}(\nu)d\nu = \int_0^{\nu_D} \frac{Nb_{\mathrm{tot}}(\nu)}{4}d\nu = \int_0^{\nu_D} \frac{4N\pi\nu^2}{c_{\mathrm{av}}^3\left(\frac{N}{V}\right)}d\nu \tag{16}$$

with the Debye frequency evaluated from the integral as

$$\nu_D = c_{\mathrm{av}}\left[\frac{3\left(\frac{N}{V}\right)}{4\pi p}\right]^{1/3} = \frac{k_B T_D}{h} \tag{17}$$

The Debye frequency, using the average branch speed c_{av} and assuming the cross-sectional area of the nanotube is a ring of van der Waals thickness 3.4 Å, is 9.86 THz. The corresponding Debye temperature, 473 K, is comparable to reported values of 475 K [45] and 580 K [46]. It should be noted that our value is lower than other reported values for nanotubes such as 960 K [9], 1000 K [47], and the ~2000 K values reported for graphite. These differences may arise from the different treatments of the density of states used (e.g., Refs. [9,47]) or possibly from the use of longitudinal instead of averaged phonon velocity. Regardless, the use of a "low" Debye temperature will give a conservative estimate of the quantum correction, which is why it has been used here.

The relation between T_{MD} and T obtained from Eq. (14) is shown in Fig. 3(*a*). T_{MD} and quantum temperature T differ at low temperature but approach one another at high temperature. This is more clearly illustrated in Fig. 3(*b*), which shows the temperature dependence of dT_{MD}/dT. In this figure the slope approaches 1 as temperature increases. Inclusion of the zero point energy in Eq. (14) results in a corresponding "zero point temperature": an MD temperature below which there is no classical analog to any quantum temperature.

The quantum correction is incorporated in the thermal conductivity expression by multiplying the thermal conductivity in Fourier's law by a factor dT_{MD}/dT [48]

$$k_{\mathrm{qc}} = -\frac{q_z}{dT/dz} = -\frac{q_z}{(dT/dT_{\mathrm{MD}})(dT_{\mathrm{MD}}/dz)} = \left(\frac{dT_{\mathrm{MD}}}{dT}\right)k \tag{18}$$

This calculation reflects that the thermal conductivity directly calculated from MD (k) differs from the quantum corrected thermal conductivity (k_{qc}) due to the differing classical and quantum definitions of temperature. It is evident from Eq. (18) and Fig. 3(*b*) that the quantum correction is largest at low temperature and is negligible at high temperature.

The corrected thermal conductivities are shown in Fig. 4. They should be viewed as qualitative in nature due to the assumptions of Debye density of states, definition of nanotube cross-sectional area, and averaged velocity that have been used. Corrections have not been applied to the $T_{\mathrm{MD}}=100$ K values since they are below the zero point temperature. In general, the corrected thermal conductivities are lower than the uncorrected (classical) thermal conductivities. The difference between quantum corrected and classical thermal conductivities decreases with increasing temperature, as is expected from Fig. 3. Unlike the uncorrected results, which monotonically decrease with temperature, the corrected results display a slight increase with temperature to a maximum value at ~400 K, then a slight decrease. This trend is consistent with thermal conductivity measurements for single-wall carbon nanotubes [5] and multiwall carbon nanotubes [2,3] and is also consistent with the Debye temperature calculated above. The use of a higher Debye temperature/frequency yields a stronger correction due to inclusion of higher frequency modes; these modes are more quantum in nature [33]. This results in a sharper peak and lower values than in Fig. 4 but qualitatively the results are similar, as ascertained from another set of simulations run at a higher Debye temperature. It is questionable that some other studies [16,17] using classical MD simulations can also attain this peaking behavior without a quantum correction, as $k \sim 1/T$ temperature dependence is expected in the purely classical regime. We agree with Maruyama [22] that these studies are likely suffering from artifacts of small simulation cell size, which cuts off long wavelengths at lower temperatures and thus artificially reduces the low-temperature thermal conductivity.

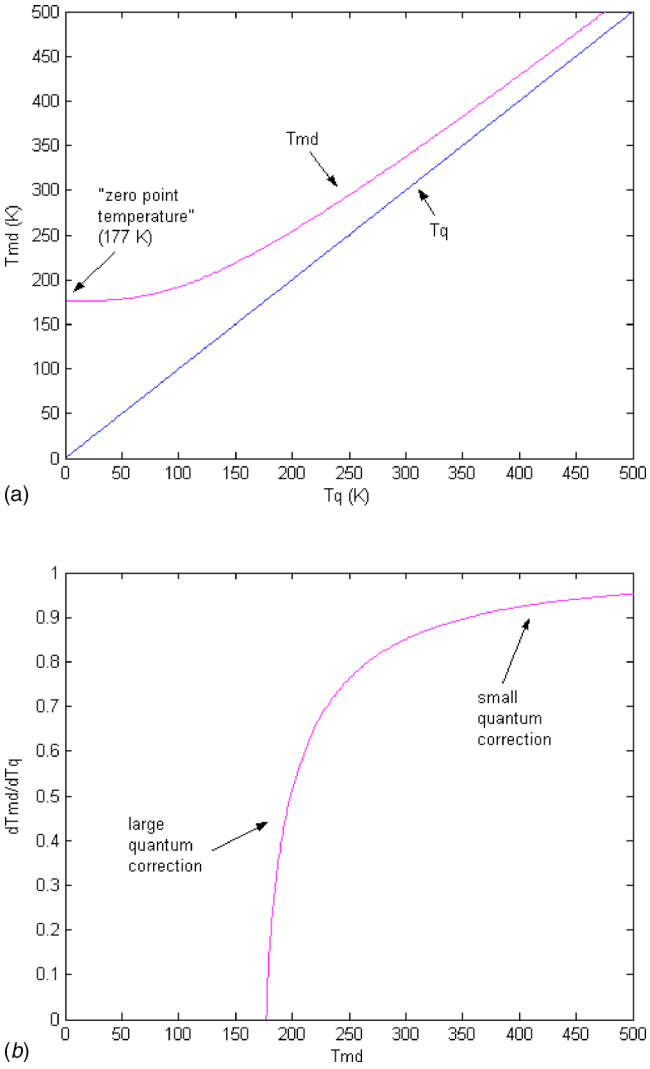

Fig. 3 (*a*) **MD temperature versus quantum temperature for (10, 10) SWNTs; and (*b*) ratio of MD to quantum temperature versus MD temperature**

Effect of Boundary Conditions. Figures 2 and 4 illustrate that thermal conductivity in nanotubes with free boundaries is lower

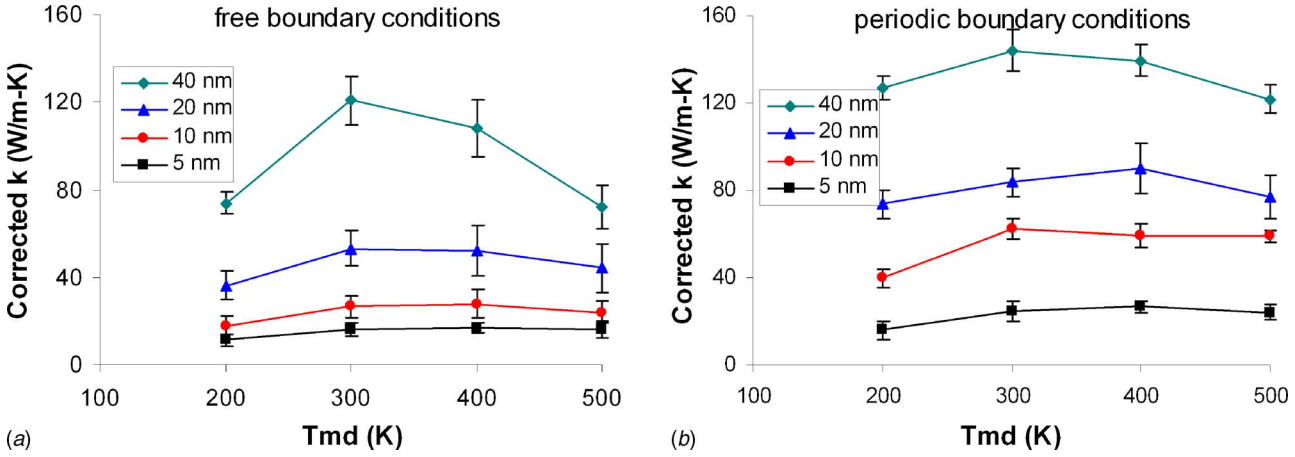

Fig. 4 Estimated values of quantum corrected thermal conductivity versus temperature at different nanotube lengths for (10, 10) SWNTs with both: (*a*) free; and (*b*) periodic boundary conditions

than that with periodic boundary conditions. The effect of the free boundary is to reduce the phonon lifetime due to additional scattering at the tube ends, which reduces the correlation of heat flux vector at time t with the initial heat flux vector. This reduction is very strong in the 5 nm tubes. In Fig. 5(*a*) it is seen that the HCACF decays to zero very quickly and then fluctuates about this value, which leads to much lower thermal conductivity compared to that of the PBC case (Eq. (2)). With increasing tube length the effect of boundary scattering is less severe, as indicated in Fig. 5(*b*) for the 40 nm free boundary case. The HCACF curve starts to have a long decaying tail and becomes similar to that of the PBC. For all PBC simulations and for free simulations of 20 nm or longer, the HCACF has a fast decay followed by a longer decay. In general, HCACF in PBC nanotubes decays more slowly than those with free boundary conditions, which leads to higher thermal conductivity. For both cases, HCACF decays more slowly with increasing length, leading to a length dependent thermal conductivity.

It is also evident in Fig. 5 that there are pronounced high-frequency oscillations for the free boundary condition cases as compared to the PBC cases. This is believed to arise from the dangling carbons at the free ends, whose vibrations contribute strongly to the periodic reversals of the heat current.

Phonon Decay Times. For the thermal conductivity calculations described above, the phonon decay times τ_1 and τ_2 were calculated based on double exponential fits to the free and PBC nanotube HCACF before the ballistic transport time τ_b. Although this "early time" fitting was a requirement for the PBC nanotubes, it was only done for the free nanotubes to provide a consistent basis for comparison to the free case. Free nanotubes require no such time truncation, so HCACF fits were also performed for much longer times, up to 100 ps, to see the effects of fitting time. The overall time constants were not observed to change significantly for the fitting times investigated, although as expected the 100 ps fits resulted in the lowest fitting errors.

Results for τ_2 from the 100 ps HCACF fitting are shown in Fig. 6 for nanotubes with free boundary conditions, and the corresponding results for τ_1 are found in Table 2. For PBC nanotubes it was not possible to perform reasonable 100 ps fits for τ_1 and τ_2 directly due to the spurious self correlation effects that appeared much earlier than this time. From Fig. 6 it is clear that τ_2 for nanotubes with free boundaries increases linearly with nanotube length and increases as temperature decreases. These phenomena can be understood from Matthiessen's rule

$$\frac{1}{\tau_{2,\text{free}}} = \frac{1}{\tau_{p-p}} + \frac{2}{\tau_b} = \frac{1}{\tau_{p-p}} + \frac{2c}{L} \tag{19}$$

Here the overall scattering rate for the free nanotube $1/\tau_{2,\text{free}}$ is determined by the characteristic times for phonon–phonon scattering, τ_{p-p}, and boundary scattering, τ_b. Note that τ_b is the same as

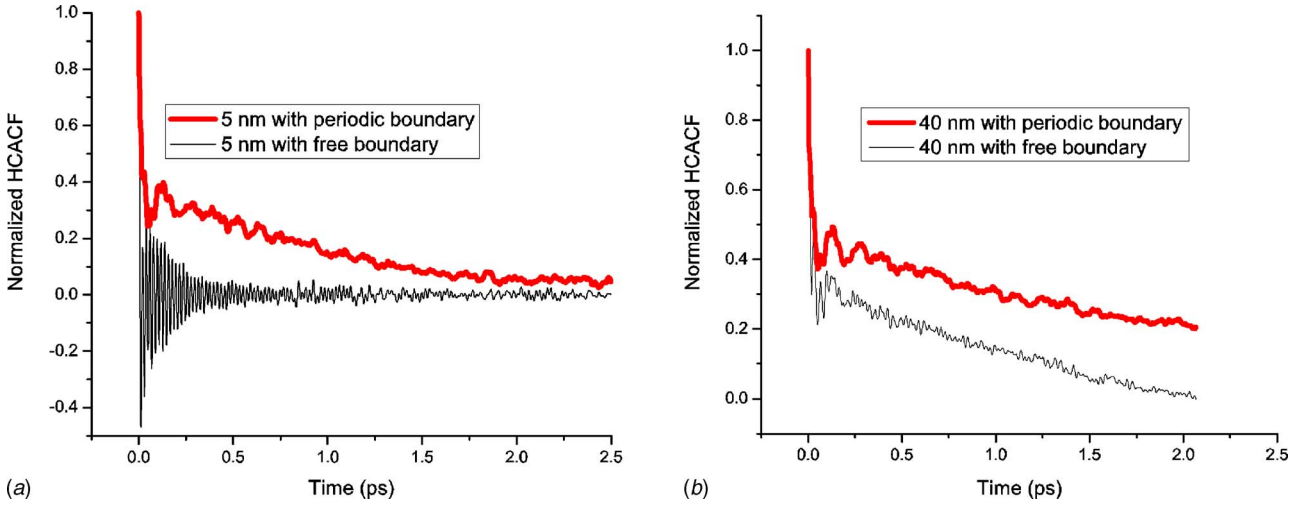

Fig. 5 Normalized HCACF for (*a*) 5 nm, and (*b*) 40 nm (10, 10) SWNTs at T_{MD}=300 K

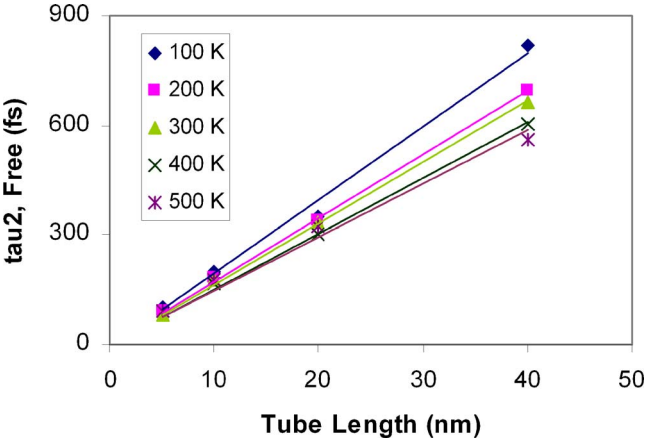

Fig. 6 Time constant τ_2 versus length at different temperatures (T_{MD}) for (10, 10) SWNTs with free boundary conditions

the ballistic transport time. Similar approaches have been used to account for finite size effects on phonon mean free path in MD simulations [49,50]. The $\tau_b/2$ represents the average time a phonon has traveled (one-dimensional geometry) since last scattering from either end of the nanotube

$$\tau_{av} = \frac{l}{c} = \frac{\int_0^L z\,dz}{c\int_0^L dz} = \frac{L}{2c} = \frac{\tau_b}{2} \tag{20}$$

Equation (19) shows that as length increases, $\tau_{2,free}$ also increases. This increase is linear when $\tau_{av} \gg \tau_{p-p}$, leading to

$$\tau_{2,free} \approx \tau_{av} = \frac{L}{2c} \quad \text{(ballistic regime)} \tag{21}$$

The linear increase in Fig. 6 thus indicates that the observed nanotubes are in the ballistic transport regime: nanotube lengths are much shorter than the phonon mean free path l in this regime. The decrease in $\tau_{2,free}$ as temperature increases indicates that the transport, although still largely ballistic, is moving toward the diffusive end of the ballistic–diffusive continuum. This is supported by Eq. (19) and by the well known $\tau_{p-p} \sim 1/T$ temperature dependence in the classical regime. Assuming that the kinetic theory proportionality of thermal conductivity and phonon scattering time

$$k = \rho C c l = \rho C c^2 \tau_{p-p} \tag{22}$$

holds, this behavior is also consistent with the linear dependence of thermal conductivity on length found in Ref. [24]. From Eq. (19) it is evident that as temperature increases, τ_{p-p} decreases and the diffusive phonon–phonon scattering term $1/\tau_{p-p}$ in the denominator becomes larger. At high enough temperatures it will become dominant, leading to fully diffusive transport, which is characterized by no length dependence (i.e., convergence).

In the fully ballistic limit the speed of sound may be estimated from

Table 2 Fast decay time constant τ_1 (in fs) for nanotubes with free boundaries at different lengths and temperatures (T_{MD})

	100 K	200 K	300 K	400 K	500 K
5 nm	4.02	4.098	4.116	4.182	4.249
10 nm	3.834	3.506	4.16	4.377	4.41
20 nm	3.936	4.225	4.566	4.59	5.585
40 nm	4.507	5.205	5.733	6.123	7.08

Table 3 Apparent (10,10) carbon nanotube speed of sound (m/s) estimated from Fig. 6 and Eq. (23) at different temperatures (T_{MD})

100 K	200 K	300 K	400 K	500 K
25,100	28,800	30,041	32,900	34,100

$$c \approx \frac{L}{2\tau_{2,free}} \quad \text{(ballistic regime)} \tag{23}$$

Applying this to the reciprocals of the slopes in Fig. 6 yields the results in Table 3. The apparent speed of sound magnitudes range from 25 to 34 km/s as temperature increases from 100 to 500 K. These values are comparable to the 20 km/s L_{LA} value in Ref. [8], but the increase with temperature requires some discussion. Equation (23) is only truly valid when $\tau_{p-p} \to \infty$, which occurs as $T \to 0$. The apparent speed of sound calculated at higher temperatures is too large since $\tau_{2,free}$ is reduced from the ballistic value by the increasing effects of diffusive phonon–phonon scattering. Thus, Eq. (23), taken in the low-temperature limit, provides a simple estimate of the speed of sound that is much easier to use than conventional calculations based on the dispersion relation.

In general, the free nanotube fast decay times τ_1 in Table 2 increase slightly with temperature and nanotube length, ranging between 4 fs and 7 fs for the various cases considered. These local decay times are typically associated with half the vibration period of the carbon–carbon bond, which is in general a length and temperature independent quantity. Using the 52 THz C–C vibration found in Fig. 1 yields a τ_1 value of 9.6 fs, which is a factor of ~2 higher than the τ_1 values in Table 2. The slight length and temperature dependences observed in the table are likely due to minor fitting errors. The reason for the low τ_1 values for free nanotubes is not fully understood but may be an artifact of the pronounced high-frequency oscillations in the HCACF decay in the free boundary cases. It is likely that the double exponential fit samples only the initial, overly steep high frequency decay for τ_1 rather than the time averaged decay over several oscillations. This is supported by the fact that PBC "early time" autocorrelation data, which did not exhibit pronounced high-frequency oscillations, were fitted by a double exponential to yield τ_1 values in the range 8.4–11.7 fs that match the C–C vibration value well. From visual analysis of Fig. 5, it is evident that fitting an envelope to the peaks and valleys of the autocorrelation decay for free boundary cases yields a slower decay approximately equal to both the C–C and PBC "early time" τ_1 values.

Length Dependence of Thermal Conductivity. With increased system size, thermal conductivity is increased for both free and PBC cases shown in Fig. 7. This is consistent with the length dependence found by others [18,20–22,24]. Since the longest tube length modeled here is 40 nm, the thermal conductivity is still far from its ultimate bulk value. The thermal conductivity value is 158 W/m K for a 40 nm tube at 300 K. This is similar to the ~160 W/m K at 61.5 nm length value reported in Ref. [20] and somewhat lower than the 215 W/m K at 50 nm length value reported in Ref. [21]. A significant question that arises is: why does thermal conductivity of the PBC cases increase with length, since there are no free ends and thus no boundary scattering should occur?

The length dependence of thermal conductivity is not a simulation artifact but rather is a real physical effect arising both from the boundary scattering effects discussed above (Eq. (19)) and from the vibrational modes in the nanotube. Longer nanotubes allow additional vibrational modes, and each mode created by increasing the nanotube length provides a new channel for heat transport. Thus, the *heat capacity* increases with length. However, thermal conductivity is proportional to heat capacity per unit vol-

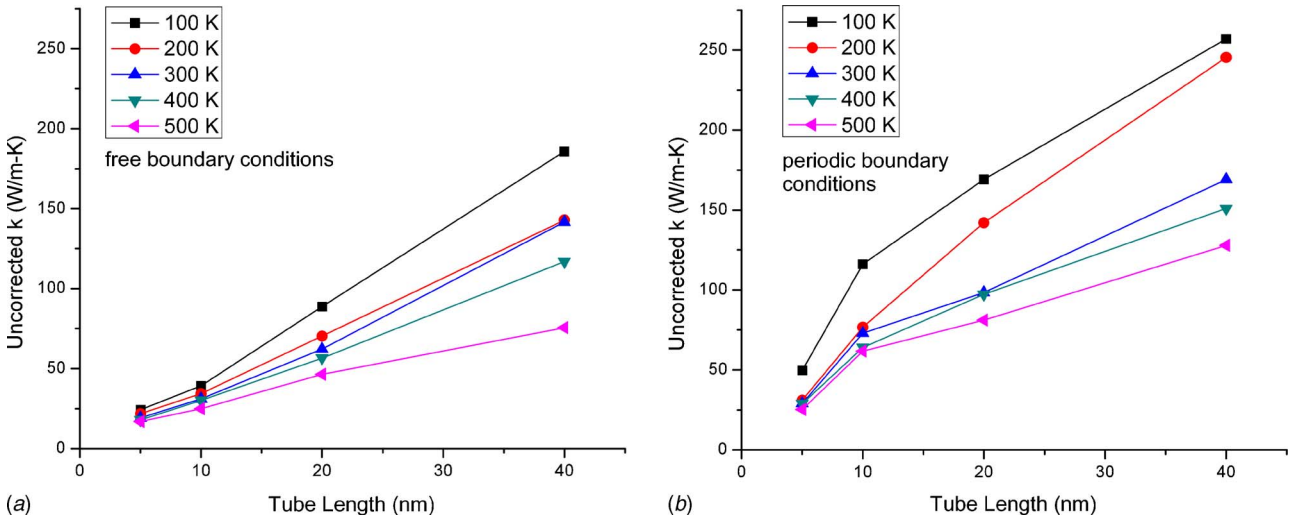

Fig. 7 Uncorrected thermal conductivity versus length at different temperatures (T_{MD}) for (10, 10) SWNTs with both: (*a*) free; and (*b*) periodic boundary conditions

ume ρC, which does not increase with length. So, something else must be responsible for the length dependence of thermal conductivity in PBC nanotubes. Two explanations come to mind. First, the additional modes allowed by the longer nanotubes have smaller wave vectors. Modes with low wave vector have a lower probability of Umklapp scattering, and thus are more long lived than the already existing higher frequency modes. When included with these modes, the net effect is to increase the overall relaxation time and thermal conductivity. Additionally, the results of a recent study [51] indicate that normalized phonon density of states of (10,10) nanotubes does display some length dependence. Briefly, the frequency distribution does not remain constant with increases in length, but instead a redistribution toward lower frequencies occurs. Generally the lower frequencies have higher group velocities which, along with Eq. (22), might explain the observed increase in PBC thermal conductivity with length. It is possible that the length dependence arises as an artifact of the artificial self-correlation that occurs as the phonon circles the simulation cell multiple times. Such correlation effects would be likely to decrease with length as the simulation cell dimension approaches and then exceeds the phonon correlation length, so are not likely to contribute to the observed increase in thermal conductivity with length.

Homogeneous Nonequilibrium Molecular Dynamics. To determine the effect of MD simulation method on calculated thermal conductivity, the homogeneous NEMD method was applied to 5 nm and 10 nm SWNTs with PBC at 300 K. A perturbing force $\vec{F}_e$ was applied in the axial direction with magnitudes ranging from 0.05 to 0.4, the resultant heat current components $J_z(\vec{F}_e,t)$ were calculated, and $k(\vec{F}_e)$ was found using Eq. (5). A plot of perturbed thermal conductivity versus magnitude of perturbing force is shown in Fig. 8. Also shown in Fig. 8 for comparison are thermal conductivity values and data points read from a similar plot from Berber et al. [16]. Note that these data are for a 2.5 nm nanotube at 100 K; Ref. [16] does not provide perturbed thermal conductivity versus magnitude of perturbing force plots at other temperatures or nanotube lengths.

A fit to these data points is required in order to estimate the macroscopic (unperturbed) thermal conductivity $k(\vec{F}_e=0)$. As there is no unambiguous choice for the fitting function in the literature, two types of fits have been chosen: a $1/x$ type fit, which appears to be the type employed by Berber et al., and an exponential fit. The functional forms of the fits are $k(\mathrm{Fe})=a/(\mathrm{Fe}-b)$ and $k(\mathrm{Fe})=A_1\exp(-\mathrm{Fe}/t_1)$, each with two fitting parameters (Table 4). The $1/x$ fit is shifted along the abscissa by the amount b in order to allow extrapolation to a finite macroscopic conductivity. A simple power law fit $y=a/x$ is not used because extrapolation to zero $\vec{F}_e$ gives an unphysical infinite thermal conductivity.

Extrapolation to zero $\vec{F}_e$ by the exponential fit gives thermal conductivities 233 W/m K for 5 nm and 240 W/m K for 10 nm SWNT at 300 K, and using the $1/x$ fit gives 345 W/m K for 5 nm and 375 W/m K for 10 nm (Fig. 4). These values are significantly higher than the corresponding values calculated in this paper by the EMD method (73 W/m K for EMD with PBC for 10 nm SWNT at 300 K), but still much lower than the 300 K value of 6600 W/m K reported in Ref. [16]. To explain the discrepancy with Berber et al.'s value, we have fit their available (100 K,2.5 nm) data points using both exponential and $1/x$ type fits. We were unable to reproduce their 100 K value of 37,000 W/m K. Our exponential fit to their data yielded a value of about 235 W/m K, which is similar to our exponential fitting

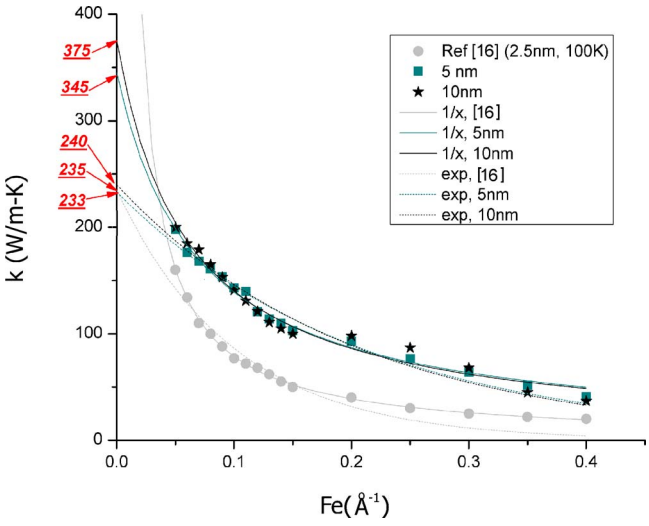

Fig. 8 Perturbed thermal conductivity versus perturbation (Fe) calculated by homogeneous molecular dynamics simulation at T_{MD}=300 K. Macroscopic thermal conductivity values for the various cases are underlined.

Table 4 Fitting parameters and macroscopic thermal conductivities from homogeneous nonequilibrium molecular dynamics

	$1/x$ fit			Exponential fit		
	Macroscopic thermal conductivity (W/m K)	a (W/m K Å^{-1})	b (Å^{-1})	Macroscopic thermal conductivity (W/m K)	A_1 (W/m K)	t_1 (Å^{-1})
5 nm	**345**	23.3	−0.0675	**233**	233	0.210
10 nm	**375**	22.3	−0.0595	**240**	240	0.202
Ref. 16 (2.5 nm, 100 K)	**undefined**	7.72996	0.00171	**235**	235	0.0999

values for 5 nm and 10 nm nanotubes at 300 K, while the $1/x$ type fit did not yield any value as the fitted curve never intercepted the y axis. The influence of error in reading data from the plot was investigated by incorporating small changes in the obtained data points and observing the resultant change in fitting parameters and conductivity. No significant changes were observed; the exponential fit macroscopic thermal conductivity changed by $<5\%$ and the $1/x$ fit conductivity was still undefined. So, it is unlikely that the discrepancies between the present results and those in Ref. [16] are due to misreading of the published data.

The overall error in the exponential fit values for 5 nm and 10 nm nanotubes is about 4%, while that of the $1/x$ fit is about 13%. The macroscopic thermal conductivity values for 5 nm and 10 nm nanotubes differ by less than this error, so no clear length effect can be determined from the HNEMD data points. The $1/x$ and exponential fits differ by about 35%, with the $1/x$ fit consistently higher than the exponential fit. This difference may be taken as a rough estimate of the uncertainty in the values obtained by HNEMD.

Comparison to Literature Values. Although extrapolation using different fitting functions will result in different thermal conductivity values from homogeneous NEMD, it is not clear how the presented k versus Fe data in Berber's paper could be extrapolated to yield a 100 K thermal conductivity value of 37,000 W/m K. This also brings into question the value of 6600 W/m K reported at 300 K. Moreland et al. [21], Maruyama [22], and recently Padgett and Brenner [20] all used direct NEMD and found similar conductivity values, despite using different potentials and boundary conditions. Results in the present paper for both EMD and homogeneous NEMD cases are similar to those in the above three papers but are much smaller than that from Che et al. [18] who used EMD and the same boundary conditions. The only difference is the potential, REBO versus Tersoff–Brenner, which did not appear to play a significant role in the three direct NEMD simulations above. The reason for the difference between Che's and the present data are thus still not clear, although scaling by the same cross-sectional area reduces the discrepancy to a factor of ~5. It is possible that the precise procedure used in the autocorrelation decay calculation and fitting process in Ref. [18] may also play some role, but these details are not provided so no definitive statement can be made. Osman et al. [17] used the same NEMD and heat flux control technique as Padgett and Brenner [20] but got much higher values. At present, these discrepancies are also not understood, unless they are a result of stress or some other unknown factor.

The earlier thermal conductivity results in Table 1 show considerable scatter and have not been replicated by other groups. The more recent results, including those of the present paper, are all on the order of a few hundred W/m K for the tube lengths considered. Due to the consistency found in these later results, it is believed that these are more likely to be correct than the earlier values. This is confirmed by Mingo and Broido [24] who found about 100 W/m K for a 100 nm (10, 0) SWNT at 316 K. Although the temperature and chirality are different, the order of magnitude is the same. The ultimate test of correctness is, however, similarity to experimental data. The "correct" simulations in Table 1 are an order of magnitude lower than available experimental data, but are also performed on tubes that are short (most are less than a few hundred nm) relative to the expected experimental lengths of a few microns in order to enable comparison of a variety of papers. Simulations on longer tubes (400 nm [22] and 1000 nm [21]) indicate that thermal conductivity has still not converged and will continue to increase with tube length. This behavior is expected due to the long phonon mean free path and is a likely reason for the low "correct" values. This indicates that calculated values approaching experimental values may be attainable for simulations performed on sufficiently long tubes. Additionally, HNEMD yields values a factor of 3–12 higher than EMD PBC results calculated for the same tube length. Detailed discussion of the differences among the various simulation methods is the subject of another publication [51]. It remains to be seen whether differences in intermolecular potential will have a significant effect at longer tube lengths.

Conclusions

Using molecular dynamics simulations we have calculated the thermal conductivity for (10, 10) single-wall carbon nanotubes as a function of temperature, length, and simulation method for both free boundary and periodic boundary conditions. To qualitatively account for the quantum effect, a correction is made to the thermal conductivity. The corrected values increase with increasing temperature and fall off at high temperature, showing a trend that is consistent with experimental observations. The free boundaries reduce phonon lifetime due to additional phonon scattering at tube ends and therefore give lower thermal conductivity than that of periodic boundary conditions. Thermal conductivity increases with length at all temperature and boundary conditions. Linear increases in τ_2 and monotonic increases in thermal conductivity indicate ballistic transport in these simulations, and provide a simple means to estimate phonon speed of sound. An uncorrected value of about 160 W/m K is found at 300 K for a 40 nm tube length using equilibrium molecular dynamics. Homogeneous nonequilibrium molecular dynamics simulation indicates a factor of 3–12 increase as compared to equilibrium molecular dynamics with periodic boundary conditions for nanotubes at 300 K. The present results agree well with recent theoretical results for carbon nanotube thermal conductivity, which are consistent with each other at comparable nanotube lengths. Discrepancies between simulated and experimental values are attributed to length effects, and may also arise due to the effects of simulation method, stress, and intermolecular potential.

Acknowledgment

This work was supported by the Office of Naval Research (Grant No. N00014-03-1-0890).

Nomenclature

b = density of states per atom
C = heat capacity (per unit mass)
c = speed of sound
D = density of states (states/frequency)
ε = atomic energy including both potential and kinetic
EMD = equilibrium molecular dynamics
$\vec{f}_{ij}$ = force on atom i due to atom j
$\vec{F}_e$ = external force field in homogeneous NEMD
$\vec{F}_i$ = total force on atom i
HCACF = heat current autocorrelation function
HNEMD = homogeneous nonequilibrium molecular dynamics
h, $\hbar$ = Planck's constant, Planck's constant divided by 2π
J = heat current
k = thermal conductivity (axial direction)
k_B = Boltzmann's constant
L = nanotube length
l = phonon mean free path
m = atomic mass
M = number of primitive cells in simulation domain
MD = molecular dynamics
MWNT = multi-wall carbon nanotube
N = number of atoms
NEMD = nonequilibrium molecular dynamics
p = number of basis atoms per primitive cell
PBC = periodic boundary conditions
r_{ij} = distance between atom i and j
$\vec{r}$ = atomic position vector
REBO = reactive bond order potential
SWNT = single-wall carbon nanotube
S = scale factor in density of states
q = heat flux
T, T_q = (quantum) temperature
T_{MD} = MD temperature
Δt = MD simulation timestep
t_{corr} = correlation time
t_{run} = simulation run time
TB = Tersoff–Brenner potential
$\vec{v}$ = atomic velocity vector
V = volume of nanotube

Greek

ν = frequency
ν_D = Debye frequency
ρ = mass density
τ_1, τ_2 = time constant in double exponential fit for HCACF
τ_b = boundary scattering time
$\tau_{p\text{-}p}$ = phonon–phonon scattering time
ω = angular frequency
$\vec{\omega}$ = angular velocity of simulation system
σ_k = probable error of thermal conductivity
σ_T = probable error of temperature
$\sigma_{\langle J(t)J(0)\rangle}$ = probable error of HCACF
$\langle\rangle$ = average

Subscripts

acoustic = acoustic modes
av = averaged over all four acoustic modes
D = Debye
i, j, k = summation index, atom index
free = free boundary condition
full = full
LA = longitudinal acoustic mode
long = longitudinal
max = maximum angular frequency in density of states
PBC = periodic boundary condition
qc = quantum corrected
TA = transverse acoustic mode
tot = total density of states
TW = twist acoustic mode
z = axial direction

References

[1] Hone, J., Whitney, M., Piskotti, C., and Zettl, A., 1999, "Thermal Conductivity of Single-Walled Carbon Nanotubes," Phys. Rev. B, **59**(4), pp. R2514–R2516.
[2] Kim, P., Shi, L., Majumdar, A., and McEuen, P. L., 2001, "Thermal Transport Measurements of Individual Multiwalled Nanotubes," Phys. Rev. Lett., **87**(21), p. 215502.
[3] Fujii, M., Zhang, X., Xie, H., Ago, H., Takahashi, K., and Ikuta, T., 2005, "Measuring the Thermal Conductivity of a Single Carbon Nanotube," Phys. Rev. Lett., **95**, p. 065502.
[4] Choi, T.-Y., Poulikakos, D., Tharian, J., and Sennhauser, U., 2006, "Measurement of the Thermal Conductivity of Individual Carbon Nanotubes by the Four-Point Three-ω Method," Nano Lett., **6**(8), pp. 1589–1593.
[5] Yu, C. H., Shi, L., Yao, Z., Li, D. Y., and Majumdar, A., 2005, "Thermal Conductance and Thermopower of an Individual Single-Wall Carbon Nanotube," Nano Lett., **5**(9), pp. 1842–1846.
[6] Pop, E., Mann, D., Wang, Q., Goodson, K., and Dai, H., 2006, "Thermal Conductance of an Individual Single-Wall Carbon Nanotube Above Room Temperature," Nano Lett., **6**(1), pp. 96–100.
[7] Haile, J. M., 1992, *Molecular Dynamics Simulation: Elementary Methods*, Wiley, New York.
[8] Dresselhaus, M. S., and Eklund, P. C., 2000, "Phonons in Carbon Nanotubes," Adv. Phys., **49**(6), pp. 705–814.
[9] Hone, J., 2001, "Phonons and Thermal Properties of Carbon Nanotubes," *Carbon Nanotubes, Topics in Applied Physics*, M. S. Dresselhaus, G. Dresselhaus, and P. Avouris, eds., Springer, Berlin, Germany, **80**, pp. 273–286.
[10] Yi, W., Lu, L., Zhang, D.-L., Pan, Z. W., and Xie, S. S., 1999, "Linear Specific Heat of Carbon Nanotubes," Phys. Rev. B, **59**(14), pp. R9015–R9018.
[11] Hoover, W. G., and Ashurst, W. T., 1975, "Nonequilibrium Molecular Dynamics," in *Theoretical Chemistry: Advances and Perspectives*, H. Eyring and D. Henderson, eds., Academic, New York, **1**, pp. 1–51.
[12] Frenkel, D., and Smit, B., 2002, *Understanding Molecular Simulation: From Algorithms to Applications*, 2nd ed., Academic, San Diego, Chap. 3.
[13] Hansen, J.-P., and McDonald, I. R., 1986, *Theory of Simple Liquids*, 2nd ed., Academic, London, Chap. 5.
[14] Irving, J. H., and Kirkwood, J. G., 1950, "The Statistical Mechanical Theory of Transport Processes. IV. The Equations of Hydrodynamics," J. Chem. Phys., **18**(6), pp. 817–829.
[15] Evans, D. J., 1982, "Homogeneous NEMD Algorithm for Thermal Conductivity—Application of Non-Canonical Linear Response Theory," Phys. Lett., **91A**(9), pp. 457–460.
[16] Berber, S., Kwon, Y. K., and Tomanek, D., 2000, "Unusually High Thermal Conductivity of Carbon Nanotubes," Phys. Rev. Lett., **84**, pp. 4613–4616.
[17] Osman, M. A., and Srivastava, D., 2001, "Temperature Dependence of the Thermal Conductivity of Single-Wall Carbon Nanotubes," Nanotechnology, **12**, pp. 21–24.
[18] Che, J., Çagin, T., and Goddard, W. A., III, 2000, "Thermal Conductivity of Carbon Nanotubes," Nanotechnology, **11**, pp. 65–69.
[19] Yao, Z., Wang, J., Li, B., and Liu, G., 2005, "Thermal Conduction of Carbon Nanotubes Using Molecular Dynamics," Phys. Rev. B, **71**, p. 085417.
[20] Padgett, C. W., and Brenner, D. W., 2004, "Influence of Chemisorption on the Thermal Conductivity of Single-Wall Carbon Nanotubes," Nano Lett., **4**(6), pp. 1051–1053.
[21] Moreland, J. F., Freund, J. B., and Chen, G., 2004, "The Disparate Thermal Conductivity of Carbon Nanotubes and Diamond Nanowires Studied by Atomistic Simulation," Microscale Thermophys. Eng., **8**(1), pp. 61–69.
[22] Maruyama, S., 2003, "A Molecular Dynamics Simulation of Heat Conduction of a Finite Length Single-Walled Carbon Nanotube," Microscale Thermophys. Eng., **7**, pp. 41–50.
[23] Mingo, N., and Broido, D. A., 2005, "Carbon Nanotube Ballistic Thermal Conductance and Its Limits," Phys. Rev. Lett., **95**, p. 096105.
[24] Mingo, N., and Broido, D. A., 2005, "Length Dependence of Carbon Nanotube Thermal Conductivity and the "Problem of Long Waves"," Nano Lett., **5**(7), pp. 1221–1225.
[25] Brenner, D. W., 1990, "Empirical Potential for Hydrocarbons for use in Simulating the Chemical Vapor Deposition of Diamond Films," Phys. Rev. B, **42**(15), pp. 9458–9471.
[26] Brenner, D. W., Shenderova, O. A., Harrison, J. A., Stuart, S. J., Ni, B., and Sinnott, S. B., 2002, "A Second-Generation Reactive Empirical Bond Order (REBO) Potential Energy Expression for Hydrocarbons," J. Phys.: Condens. Matter, **14**, pp. 783–802.
[27] Abramson, A. R., Tien, C.-L., and Majumdar, A., 2002, "Interface and Strain Effects on the Thermal Conductivity of Heterostructures: A Molecular Dynamics Study," J. Heat Transfer, **124**(5), pp. 963–970.

[28] Shi, L., 2001, "Mesoscopic Thermophysical Measurements of Microstructures and Carbon Nanotubes," Ph.D. thesis, University of California, Berkeley, CA.
[29] Zhou, Y., Cook, M., and Karplus, M., 2000, "Protein Motions at Zero-Total Angular Momentum: The Importance of Long-Range Correlations," Biophys. J., **79**, pp. 2902–2908.
[30] Goldstein, H., 1980, *Classical Mechanics*, Addison-Wesley, Reading, MA, Chap. 3.
[31] Hoover, W. G., 1985, "Canonical Dynamics: Equilibrium Phase-Space Distribution," Phys. Rev. A, **31**(3), pp. 1695–1697.
[32] Volz, S. G., and Chen, G., 2000, "Molecular-Dynamics Simulation of Thermal Conductivity of Silicon Crystals," Phys. Rev. B, **61**(4), pp. 2651–2656.
[33] Che, J., Çagin, T., Deng, W., and Goddard, W. A., III, 2000, "Thermal Conductivity of Diamond and Related Materials from Molecular Dynamics Simulations," J. Chem. Phys., **113**(6), pp. 6888–6900.
[34] McGaughey, A. J. H., and Kaviany, M., 2004, "Thermal Conductivity Decomposition and Analysis Using Molecular Dynamics Simulations. Part I. Lennard-Jones Argon," Int. J. Heat Mass Transfer, **47**, pp. 1783–1798.
[35] Press, W. H., Teukolsky, S. A., Vetterling, W. T., and Flannery, B. P., 1992, *Numerical Recipes in FORTRAN: The Art of Scientific Computing*, 2nd ed., Cambridge University Press, Cambridge, UK, Chap. 2.
[36] Schelling, P. K., and Keblinski, P., 2003, "Thermal Expansion of Carbon Structures," Phys. Rev. B, **68**, p. 035425.
[37] Allen, M. P., and Tildesley, D. J., 1987, *Computer Simulation of Liquids*, Clarendon, Oxford, UK, Chap. 2.
[38] Sokhan, V. P., Nicholson, D., and Quirke, N., 2000, "Phonon Spectra in Model Carbon Nanotubes," J. Chem. Phys., **113**(5), pp. 2007–2015.
[39] Dickey, J. M., and Paskin, A., 1970, "Size and Surface Effects on the Phonon Properties of Small Particles," Phys. Rev. B , **1**(2), pp. 851–857.
[40] Maiti, A., Mahan, G. D., and Pantelides, S. T., 1997, "Dynamical Simulations of Nonequilibrium Processes-Heat Flow and the Kapitza Resistance Across Grain Boundaries," Solid State Commun., **102**(7), pp. 517–521.
[41] Kittel, C., 1996, *Introduction to Solid State Physics*, 7th ed., Wiley, New York.
[42] Chiu, H.-Y., Deshpande, V. V., Postma, H. W. C., Lau, C. N., Mikó, C., Forró, L., and Bockrath, M., 2005, "Ballistic Phonon Thermal Transport in Multiwalled Carbon Nanotubes," Phys. Rev. Lett., **95**, p. 226101.
[43] Tohei, T., Kuwabara, A., Oba, F., and Tanaka, I., 2006, "Debye Temperature and Stiffness of Carbon and Boron Nitride Polymorphs from First Principles Calculations," Phys. Rev. B, **73**, p. 064304.
[44] Gurney, R. W., 1952, "Lattice Vibrations in Graphite," Phys. Rev., **88**(3), pp. 465–466.
[45] Charlier, A., and McRae, E., 1998, "Lattice Dynamics Study of Zigzag and Armchair Carbon Nanotubes," Phys. Rev. B, **57**(11), pp. 6689–6696.
[46] Benoit, J. M., Corraze, B., and Chauvet, O., 2002, "Localization, Coulomb Interactions, and Electrical Heating in Single-Wall Carbon Nanotubes/Polymer Composites," Phys. Rev. B, **65**, p. 241405(R).
[47] Benedict, L. X., Louie, S. G., and Cohen, M. L., 1996, "Heat Capacity of Carbon Nanotubes," Solid State Commun., **100**(3), pp. 177–180.
[48] Lee, Y. H., Biswas, R., Soukoulis, C. M., Wang, C. Z., Chan, C. T., and Ho, K. M., 1991, "Molecular-Dynamics Simulation of Thermal Conductivity in Amorphous Silicon," Phys. Rev. B, **43**(8), pp. 6573–6580.
[49] Schelling, P. K., Phillpot, S. R., and Keblinski, P., 2002, "Comparison of Atomic-Level Simulation Methods for Computing Thermal Conductivity," Phys. Rev. B, **65**, p. 144306.
[50] Chen, Y., Li, D., Lukes, J. R., Ni, Z., and Chen, M., 2005, "Minimum Superlattice Thermal Conductivity from Molecular Dynamics," Phys. Rev. B, **72**, p. 174302.
[51] Lukes, J. R., and Zhong, H., 2006, "Thermal Conductivity of Single Wall Carbon Nanotubes: A Comparison of Molecular Dynamics Simulation Approaches," *Proceedings of the Thirteenth International Heat Transfer Conference*, Sydney, Australia, August 8–13, NAN-29.

Natural Convection in a Partitioned Vertical Enclosure Heated With a Uniform Heat Flux

Kamil Kahveci
Faculty of Engineering and Architecture,
Trakya University,
22030 Edirne, Turkey
e-mail: kamilk@trakya.edu.tr

This numerical study looks at laminar natural convection in an enclosure divided by a partition with a finite thickness and conductivity. The enclosure is assumed to be heated using a uniform heat flux on a vertical wall, and cooled to a constant temperature on the opposite wall. The governing equations in the vorticity-stream function formulation are solved by employing a polynomial-based differential quadrature method. The results show that the presence of a vertical partition has a considerable effect on the circulation intensity, and therefore, the heat transfer characteristics across the enclosure. The average Nusselt number decreases with an increase of the distance between the hot wall and the partition. With a decrease in the thermal resistance of the partition, the average Nusselt number shows an increasing trend and a peak point is detected. If the thermal resistance of the partition further declines, the average Nusselt number begins to decrease asymptotically to a constant value. The partition thickness has little effect on the average Nusselt number. [DOI: 10.1115/1.2717241]

Keywords: natural convection, PDQ, enclosure, partition, vorticity, stream function

1 Introduction

Natural convection in an enclosure has been receiving considerable attention due to its importance in various engineering applications, such as double-pane windows, solar energy collectors, double-wall insulation, and the cooling of electronic equipments. The primary focus of previous studies has been that of a simple enclosure with no partitions, and a comprehensive overview of the published results on this subject has been provided by Ostrach [1]. However, real systems can differ significantly from the simple enclosure model. For example, in some building applications the model must include the association of two enclosures which communicate laterally through a doorway, window, or corridor. Natural convection in the air layer of a double-pane window or double-wall insulation is coupled with the internal natural convection in the room and external convection. The case is similar for the solar collector, where the internal and external convection are coupled at the glazing. In addition, enclosures with partitions are frequently used to modify heat transfer in practice.

Ho and Yih [2] performed a numerical study of natural convection in an air-filled vertically partitioned enclosure, and concluded that the heat transfer rate is considerably attenuated in a partitioned enclosure in comparison with that for a nonpartitioned enclosure. Dzodzo et al. [3] studied natural convection in an enclosure with a centrally located vertical partition. Their results indicate that partitioning the enclosure vertically can reduce the convective heat transfer by up to 64%. Tong and Gerner [4] investigated the effect of partition location on natural convection in an air-filled enclosure, and found that placing a partition exactly midway between the vertical walls of an enclosure produces the greatest reduction in heat transfer. Elsherbiny et al. [5] found that the thermal boundary conditions at the end walls influence the effect of partitions on reducing heat transfer rates across the enclosure. Acharya and Tsang [6] studied inclined enclosures with a centrally located partition. It was found that for an inclined enclosure, the maximum local Nusselt number occurs at the partition center only at low Rayleigh numbers. At high Rayleigh numbers, the maximum is shifted toward the two corners of the partition. Ciofalo and Karayiannis [7] investigated the effect of using a fixed-width barrier that protrudes centrally from the end walls of an enclosure on natural convection. The efficacy of such a partitioning was found to depend upon the aspect ratio and to strengthen as the value of that ratio increases. Nishimura et al. [8] studied natural convection in an enclosure divided by multiple vertical thin partitions. It was found that the average Nusselt number is inversely proportional to $(1+N)$ where N is the partition number. Jones [9] reported numerical results for the case of an enclosure with five vertical partitions. It was concluded that the effect of dividing the enclosure into six cells reduces the convective heat transfer by a factor of six.

Most previous studies of natural convection in the partitioned enclosures have been concerned with cases where the hot and cold walls are isothermal. There is rather insufficient knowledge regarding more complex boundary conditions, such as a case where the hot wall has a uniform heat flux and where the cold wall is isothermal, although this may be a better model for many real situations. The case where there is a uniform heat flux at both the hot and cold walls received some consideration, e.g., see Vasseur et al. [10]. However, there are few real situations in which there is, even approximately, a uniform heat flux at the cold wall. In addition, the low-order methods such as finite difference, finite element, and finite volume were more commonly used in the studies dealing with natural convection in enclosures, and in general, the low-order methods need a large number of grid points to ensure a reliable level of accuracy.

This paper focuses on a numerical study of steady-state laminar natural convection in a partitioned enclosure heated by a uniform heat flux on a vertical wall and cooled to a constant temperature on the opposite wall, using a polynomial-based differential quadrature method.

2 Differential Quadrature Method

The differential quadrature (DQ) method [11,12] is a new and efficient discretization technique to obtain accurate numerical solutions using a considerably small number of grid points. In the DQ method, the derivative of a function is approximated by a

Contributed by the Heat Transfer Division of ASME for publication in the JOURNAL OF HEAT TRANSFER. Manuscript received December 2, 2005; final manuscript received June 19, 2006. Review conducted by Suresh V. Garimella.

weighted linear sum of the function values at given grid points. The weighting coefficients are not related to any particular problem and only depend on the grid spacing. Thus, any differential equation can be reduced to a set of algebraic equations using these coefficients. One essential issue pertaining to the method is how to compute the weighting coefficients. In the DQ method, the first- and second-order derivatives of $f(x)$ at a point x_i are approximated by

$$f_x(x_i) = \sum_{j=0}^{n} a_{ij} f(x_j) \quad \text{for } i = 0,1,2,\ldots,n$$
$$f_{xx}(x_i) = \sum_{j=0}^{n} b_{ij} f(x_j) \quad \text{for } i = 0,1,2,\ldots,n \tag{1}$$

where n is the number of the grid points, and a_{ij} and b_{ij} are the first- and second-order weighting coefficients, respectively. Two different techniques have been proposed to determine the weighting coefficients for the first-order derivatives. While the first method is implemented by solving a system of algebraic equations, the second method is realized by a simple algebraic formulation. Since the grid points can be chosen arbitrarily, the first method is more popular. Its matrix becomes ill conditioned when the number of grid points is large. Therefore, it is very difficult to obtain weighting coefficients with this method. To overcome this difficulty, Shu and Richards [12] proposed a polynomial-based differential quadrature (PDQ) method for the calculation of the weighting coefficients.

2.1 Polynomial-Based Differential Quadrature Method. In the PDQ method, it is assumed that the function $f(x)$ is approximated by an nth degree polynomial in the form

$$f(x) = \sum_{k=0}^{n} c_k x^k \tag{2}$$

Shu and Richards [12] derived the following explicit formulations to calculate the weighting coefficients

$$a_{ij} = \frac{M^{(1)(x_i)}}{(x_i - x_j) M^{(1)}(x_j)}, \quad \text{when } j \neq I, \quad a_{ii} = -\sum_{k=1,k\neq i}^{n} a_{ik} \tag{3}$$

$$b_{ij} = 2a_{ij}\left[a_{ii} - \frac{1}{(x_i - x_j)}\right], \quad \text{when } j \neq I, \quad b_{ii} = -\sum_{k=1,k\neq i}^{n} b_{ik} \tag{4}$$

where

$$M^{(1)}(x_i) = \prod_{k=1,k\neq i}^{n} (x_i - x_k) \tag{5}$$

When the coordinates of grid points are known, the weighting coefficients for the discretization of derivatives can easily be calculated from Eqs. (3)–(5).

3 Analysis

The schematic of the system with the coordinates is shown in Fig. 1. The square enclosure contains a vertical partition which separates the enclosure into two regions. The partition has a variable thickness w and conductivity k_p. It is assumed that a uniform heat flux is applied to the heated vertical wall, the other vertical wall is kept at a uniform temperature, and that the horizontal walls are adiabatic. The conjugate heat transfer boundary conditions on both sides of the partition wall are taken into consideration.

The dimensionless variables are defined as follows

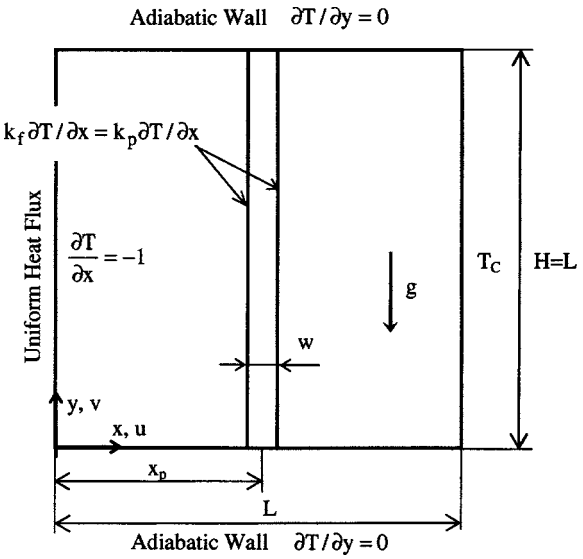

Fig. 1 The geometry and the coordinate system

$$x = \frac{x^*}{L}, \quad y = \frac{y^*}{L}, \quad x_p = \frac{x_p^*}{L}, \quad r_w = \frac{w}{L}, \quad r_k = \frac{k_f}{k_p}$$
$$\psi = \frac{\psi^*}{\alpha}, \quad \omega = \frac{\omega^*}{\alpha/L^2}, \quad T = \frac{T^* - T_C^*}{T_R^* - T_C^*} \tag{6}$$

where L is the width of the enclosure; k_f and k_p are the thermal conductivities of the fluid and partition, respectively; r_k and r_w are the thermal conductivity ratio and dimensionless partition thickness, respectively; α is the thermal diffusivity of the fluid; and T^* is the dimensional temperature. The reference temperature T_R^* may be selected without a loss of generality to scale the dimensionless heat flux to unity as $T_R^* = T_C^* + Lq/k_f$, with q being the uniform heat flux applied to the heated wall.

The dimensionless governing equations for the laminar steady-state natural convection after invoking the Bousinesq approximation and neglecting viscous dissipation and thermal radiation can be written as follows in the vorticity-stream function formulation

$$\frac{\partial^2 \psi}{\partial x^2} + \frac{\partial^2 \psi}{\partial y^2} = -\omega \tag{7}$$

$$\frac{\partial \psi}{\partial y}\frac{\partial \omega}{\partial x} - \frac{\partial \psi}{\partial x}\frac{\partial \omega}{\partial y} = \Pr\left(\frac{\partial^2 \omega}{\partial x^2} + \frac{\partial^2 \omega}{\partial y^2}\right) + \mathrm{Ra}\,\Pr\frac{\partial T}{\partial x} \tag{8}$$

$$\frac{\partial \psi}{\partial y}\frac{\partial T}{\partial x} - \frac{\partial \psi}{\partial x}\frac{\partial T}{\partial y} = \frac{\partial^2 T}{\partial x^2} + \frac{\partial^2 T}{\partial y^2} \quad \text{(for the fluid)}$$
$$\frac{\partial^2 T}{\partial x^2} + \frac{\partial^2 T}{\partial y^2} = 0 \quad \text{(for the partition)} \tag{9}$$

Here the Prandtl and Rayleigh numbers are defined as

$$\Pr = \frac{\nu}{\alpha}, \quad \mathrm{Ra} = \frac{g\beta L^3 \Delta T^*}{\nu\alpha} \tag{10}$$

where ν is the kinematic viscosity of the fluid; g is the gravitational acceleration; and β is the coefficient of thermal expansion.

The dimensionless stream function and vorticity are defined as follows

$$u = \frac{\partial \psi}{\partial y}, \quad v = -\frac{\partial \psi}{\partial x}, \quad \omega = \frac{\partial v}{\partial x} - \frac{\partial u}{\partial y} \tag{11}$$

where u and v are the dimensionless velocity components.

The boundary conditions for the problem are

$$\psi(x,0)=0, \quad \left.\frac{\partial T}{\partial y}\right|_{x,0}=0, \quad \psi(x,1)=0, \quad \left.\frac{\partial T}{\partial y}\right|_{x,1}=0 \tag{12}$$

$$\psi(0,y)=0, \quad \left.\frac{\partial T}{\partial x}\right|_{0,y}=-1, \quad \psi(1,y)=0, \quad T(1,y)=0 \tag{13}$$

$$\psi(x_p-0.5r_w,y)=0, \quad \left.\frac{\partial T_p}{\partial x}\right|_{x_p-0.5r_w,y}=r_k\left.\frac{\partial T}{\partial x}\right|_{x_p-0.5r_w,y} \tag{14}$$

$$\psi(x_p+0.5r_w,y)=0, \quad \left.\frac{\partial T_p}{\partial x}\right|_{x_p-0.5r_w,y}=r_k\left.\frac{\partial T}{\partial x}\right|_{x_p+0.5r_w,y} \tag{15}$$

There is no physical boundary condition for the vorticity. However, an expression can be derived from Taylor series expansion of the stream function equation as $\omega_{\text{wall}}=-\partial^2\psi/\partial\eta^2$ [13]. Here η is the outward direction normal to the surface. The equation given above is therefore used in this study as the boundary condition for the vorticity on the partition walls, as well as for the enclosure walls.

The average Nusselt number can be defined as

$$\text{Nu}_a=\frac{T_R^*-T_C^*}{T_a^*-T_C^*}=\frac{1}{T_a} \tag{16}$$

Here T_a is the average temperature of the hot wall, i.e., $T_a=\int_0^1 T\,dy$.

This definition of the average Nusselt number follows from the fact that with the present thermal boundary conditions, the effect of convection is not to increase the heat flux across the enclosure but rather to decrease the intensity of the temperature field within the enclosure. With this definition, the average Nusselt number represents the usual enhancement of natural convection heat transfer compared to that by pure conduction.

4 Results and Discussion

The governing equations discretized by employing the PDQ method become as follows

$$\sum_{k=0}^{N_x} b_{i,k}\psi_{k,j}+\sum_{k=0}^{N_y}\bar{b}_{j,k}\psi_{i,k}=-\omega_{i,j} \tag{17}$$

$$\sum_{k=0}^{N_y}\bar{a}_{j,k}\psi_{i,k}\sum_{k=0}^{N_x}a_{i,k}\omega_{k,j}-\sum_{k=0}^{N_x}a_{i,k}\psi_{k,j}\sum_{k=0}^{N_y}\bar{a}_{j,k}\omega_{i,k}=\text{Ra}\,\text{Pr}\left(\sum_{k=0}^{N_x}a_{i,k}T_{k,j}\right)+\text{Pr}\left(\sum_{k=0}^{N_x}b_{i,k}\omega_{k,j}+\sum_{k=0}^{N_y}\bar{b}_{j,k}\omega_{i,k}\right) \tag{18}$$

Table 1 The grid dependency for Ra=10^6, x_p=0.5, r_w=0.1, r_k=10^{-2}

	Partition wall	Cold wall	
Grid size	$\text{Nu}_{\max}$	$\text{Nu}_{\max}$	$\lvert\psi\rvert_{\max}$
21×21	1.57	1.86	8.71
26×26	1.61	1.92	8.59
31×31	1.62	1.93	8.57
36×36	1.63	1.94	8.57
41×41	1.63	1.94	8.57

$$\sum_{k=0}^{N_y}\bar{a}_{j,k}\psi_{i,k}\sum_{k=0}^{N_x}a_{i,k}T_{k,j}-\sum_{k=0}^{N_x}a_{i,k}\psi_{k,j}\sum_{k=0}^{N_y}\bar{a}_{j,k}T_{i,k}=\left(\sum_{k=0}^{N_x}b_{i,k}T_{k,j}+\sum_{k=0}^{N_y}\bar{b}_{j,k}T_{i,k}\right) \tag{19}$$

$$\sum_{k=0}^{N_x}b_{i,k}T_{k,j}+\sum_{k=0}^{N_y}\bar{b}_{j,k}T_{i,k}=0 \tag{20}$$

where the indices i and j indicate a grid point, and N_x and N_y represent the total number of grid points in directions x and y, respectively. This study uses a nonuniform grid point distribution defined as

$$x_i=\frac{1}{2}\left[1-\cos\left(\frac{i}{n_x}\pi\right)\right], \quad i=0,1,2,\ldots,n_x$$
$$y_j=\frac{1}{2}\left[1-\cos\left(\frac{j}{n_y}\pi\right)\right], \quad j=0,1,2,..,n_y \tag{21}$$

The points in this grid system are more closely spaced in regions near the walls where the higher velocity and temperature gradients are expected to develop.

A series of grid systems of up to 41*41 points are performed to obtain a grid-independent mesh size. This suggests that when the mesh size is above 36×36, $\text{Nu}_{\max}$ along the hot wall and $\lvert\psi\rvert_{\max}$ remain the same. The results in the case of Ra=10^6, x_p=0.5, r_w=0.1, and r_k=10^{-2} are shown in Table 1.

The solutions of the governing equations are obtained by the successive over-relaxation (SOR) iteration method for an air-filled (Pr=0.7) square cavity, with the Rayleigh number varying from 10^4 to 10^6 for the partition location ranging from 0 to 0.5, for partition thickness of up to 0.3 and for thermal conductivity ratios between 10^0 and 10^{-3}. The convergence criteria are chosen as $\lvert R\rvert_{\max}\leqslant 10^{-6}$, where $\lvert R\rvert_{\max}$ is the maximum absolute residual value for the vorticity, stream function, and temperature equations.

In order to validate the numerical code, the solutions for the nonpartitioned square enclosure with differentially heated sidewalls and adiabatic top and bottom walls are also obtained and

Table 2 The validation of the numerical code

	Ra=10^4		Ra=10^5		Ra=10^6	
	Vahl Davis	Present	Vahl Davis	Present	Vahl Davis	Present
$\lvert\psi\rvert_{\max}$	—	5.07	9.61	9.57	16.75	16.76
Nu_a	2.24	2.24	4.52	4.52	8.80	8.82
$\text{Nu}_{\max}$	3.53	3.53	7.72	7.71	17.93	17.53
$\text{Nu}_{\min}$	0.59	0.59	0.73	0.73	0.99	0.98

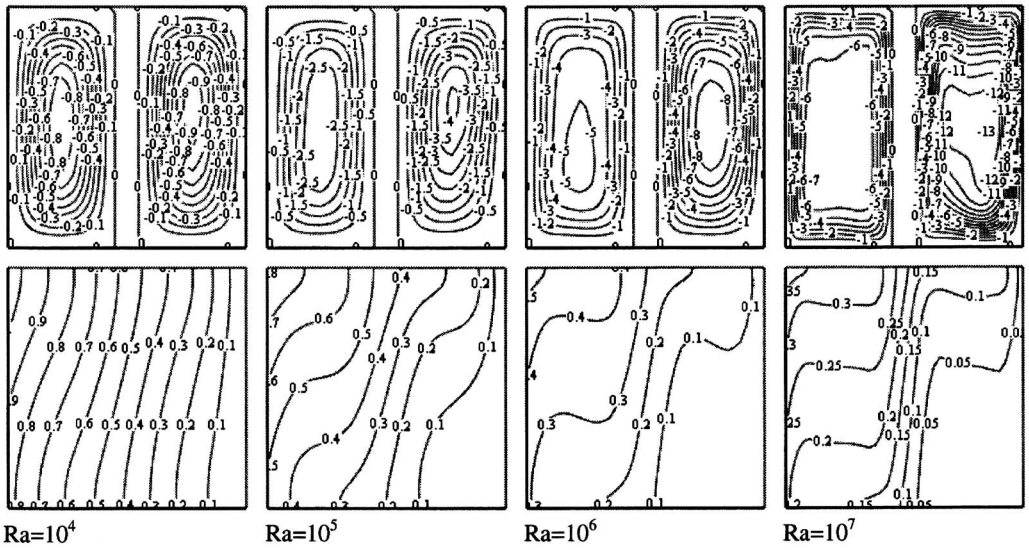

Fig. 2 The streamline and isotherm patterns for x_p=0.5, r_w=0.1, r_k=1

compared with the benchmark results obtained by de Vahl Davis [14] through a standard finite-difference method. The results presented in Table 2 show that there is excellent agreement between the results of the PDQ method for the grid 41*41 and the benchmark results of de Vahl Davis [14] based on low-order methods for the grids up to 81×81.

The main characteristics of natural convection flow and energy transport in the enclosure for the case x_p=0.5, r_w=0.1 are shown in Figs. 2–4 by the streamlines and isotherms for various values of the thermal conductivity ratio. It can be observed that the flow on both sides of the enclosure is unicellular. For Ra=10^4, the circulation is so weak that the viscous forces are dominant over the buoyancy force. The isotherms deviate slightly from the parallel structure to the vertical walls, which is the conduction solution (Ra=0). This causes the conduction to be the dominant heat transfer mechanism inside the enclosure. At higher Rayleigh numbers, the evolution of the flow structure, toward the boundary layer regime, can be observed in the figures. The development of the boundary layer regime with an increasing Rayleigh number is clearly illustrated by increasing steepness of the velocity and temperature profiles near the walls, as well as the formation of a plateau in the core region of the two fluid layers. When the circulation intensity increases, the temperature at the bottom part of the heated wall decreases significantly due to the necessity of preserving the uniform heat flux condition. This situation has a negative effect on the circulation intensity of the left zone. As the core temperature on both sides of the partition does not increase at the same rate as the partition temperature, it can be concluded that the partition cannot be under a uniform heat flux condition. On the contrary, as can be observed in Figs. 2–4, the partition is closer to isothermal. Therefore, the negative effect of the uniform heat flux on the circulation intensity is not seen inside the right zone, and the higher circulation intensity can be observed inside the right zone when it is compared to the left zone. The hot fluid from the hot wall impinges on the upper half of the partition while the cold fluid from the cold wall impinges on the bottom half. Thus, the partition tends to be hotter at the top than at the bottom. Because of this temperature difference along the partition, heat flows from the top to the bottom of the partition by conduction. As the thermal conductivity ratio decreases, the thermal resistance of the partition decreases. This situation causes either an increase in the thermal interaction between the zones, or facilitation of the heat

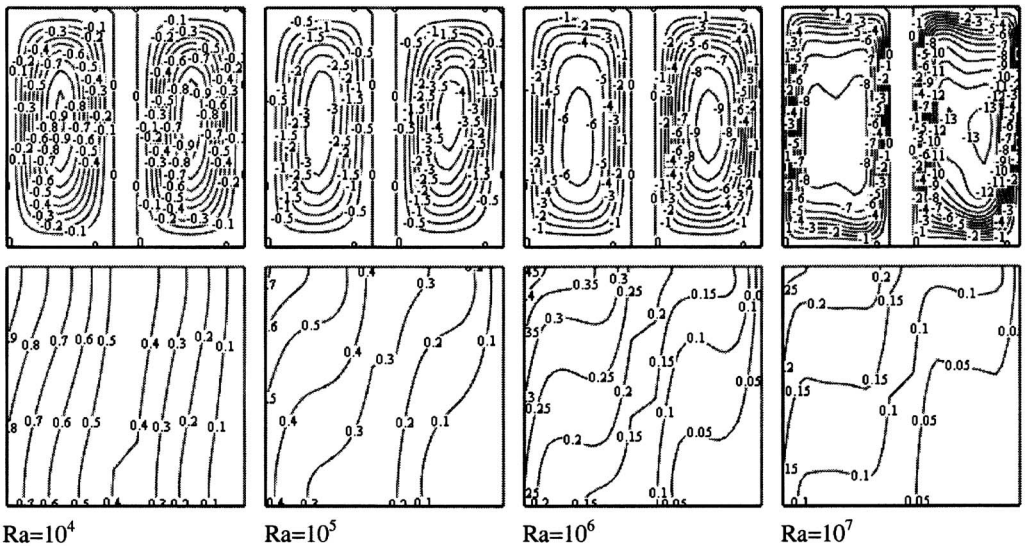

Fig. 3 The streamline and isotherm patterns for x_p=0.5, r_w=0.1, r_k=0.1

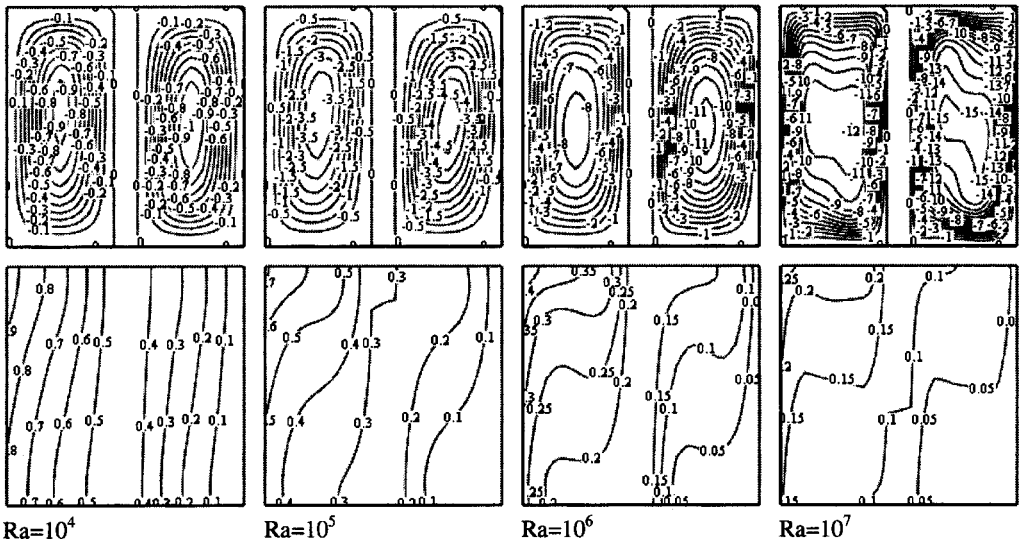

Fig. 4 The streamline and isotherm patterns for x_p=0.5, r_w=0.1, r_k=0.01

transfer by conduction from the top to bottom parts of the partition. Because of these two reasons, a decrease of the temperature of the top part and an increase of the temperature of the bottom part of the partition can be seen. Thus, the circulation intensity in both zones increases.

The streamlines and isotherms for x_p=0.5, r_k=0.01, and r_w =0.1, 0.3 are presented in Figs. 4 and 5. As the partition thickness is increased, the convective circulation on both sides of the enclosure weakens and therefore the undulation in the isotherms decreases.

Figures 4, 6, and 7 show the streamlines and isotherms for r_w =0.1, r_k=0.01, and for various values of the partition location. When the partition is moved to the heated wall, the circulation intensity decreases in the smaller zone and increases in the larger zone. Thus, heat transfer by conduction in the left zone increases and convection in the right zone strengthens. The effect of decreasing the distance between the heated wall and the partition on natural convection can also be seen by inspecting the isotherms on both zones. While the distortion of the isotherms decreases in the smaller zone, it increases in the large zone.

The effect of the horizontal and vertical heat conduction along the partition on the natural convection can be seen by inspecting the streamlines and isotherms in Figs. 2 and 5, which is a thin poorly conducting and a thick highly conducting partition. Because heat is easily transferred horizontally, the temperature of the top part of the thicker partition has lower values than the thinner one. For the thinner partition, heat flow from the top to the bottom experiences greater difficulty. Thus, the temperature of the bottom part of the partition is lower at the thin partition than at the thicker one. This situation has a negative effect on the circulation intensity by causing lower temperature values to be attained near the bottom end of the enclosure. Therefore, there is a stronger circulation for the thicker partition, although increasing the partition thickness has a negative effect on the circulation intensity.

The dependence of the temperature along the hot wall and the center of the partition on the Rayleigh number is shown in Fig. 8. The lower half of the surfaces is washed by fluid that comes from the cold surfaces, while the upper half of them receives heated fluid from the hot surfaces. Therefore, the temperature along the uniformly heated wall and along the center of the partition in-

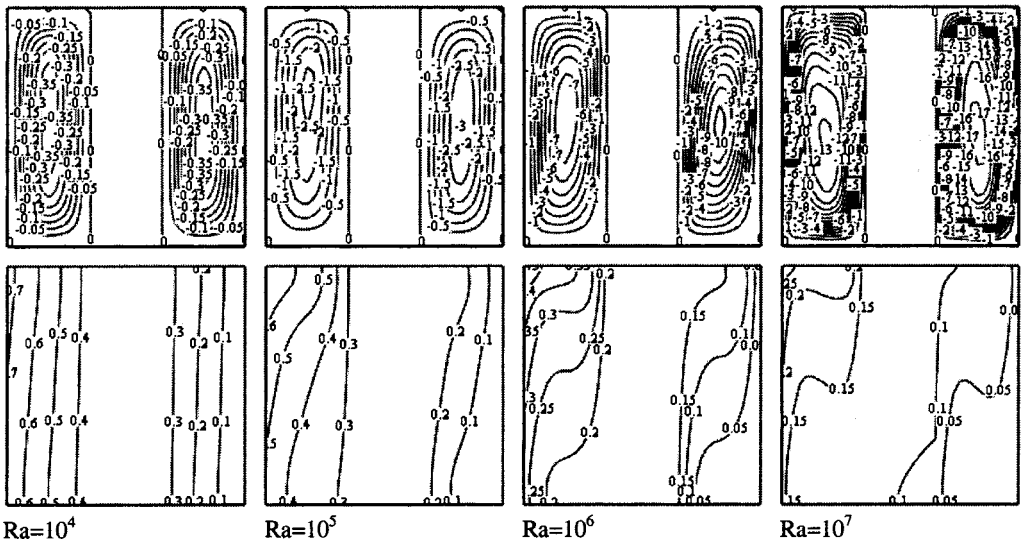

Fig. 5 The streamline and isotherm patterns for x_p=0.5, r_w=0.3, r_k=0.01

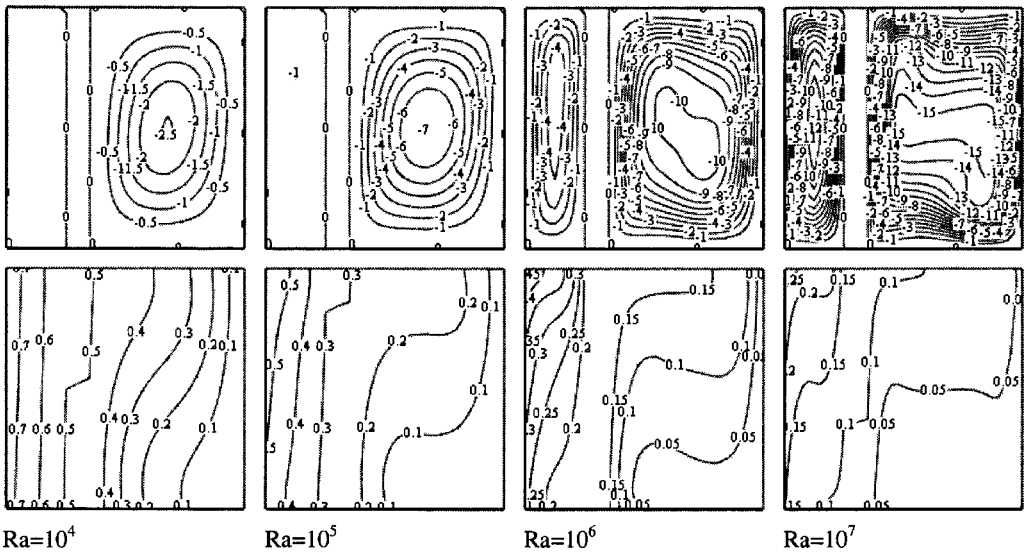

Fig. 6 The streamline and isotherm patterns for x_p=0.3, r_w=0.1, r_k=0.01

creases from y=0 to y=1. As the Rayleigh number is increased, the convective circulation becomes stronger and the temperatures take lower values.

The effect of the thermal conductivity ratio on the temperature of the heated wall and the center of the partition is shown in Fig. 9. For the case when the thermal resistance is small enough, an almost isothermal temperature profile is attained along the partition. When the thermal resistance of the partition is increased, the temperature in the lower part of the partition takes lower values. This situation results in a decrease of the temperature of the lower

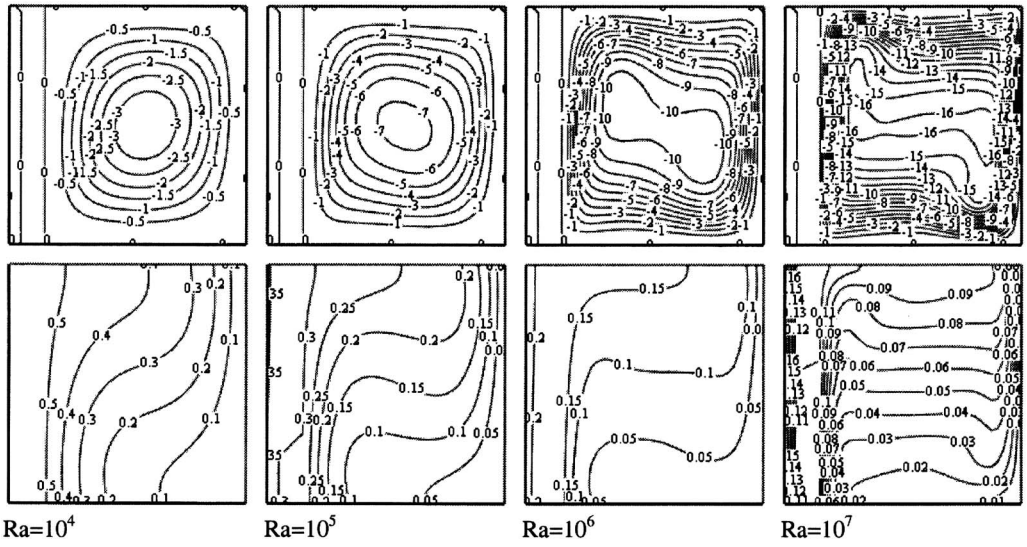

Fig. 7 The streamline and isotherm patterns for x_p=0.1, r_w=0.1, r_k=0.01

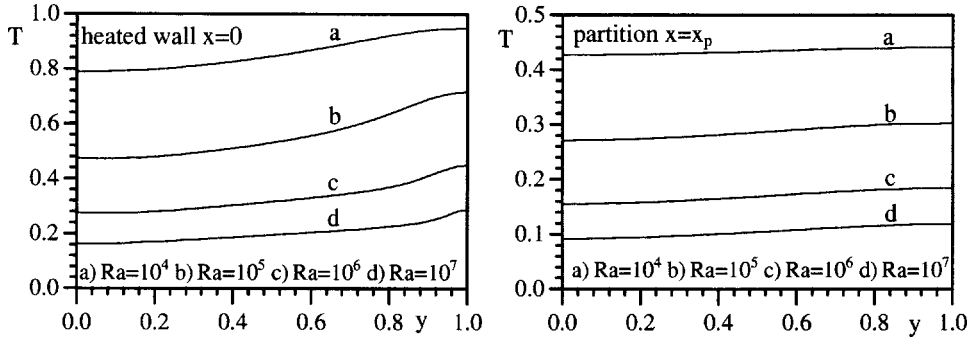

Fig. 8 The variation of the temperature for x_p=0.5, r_w=0.1, r_k=0.01

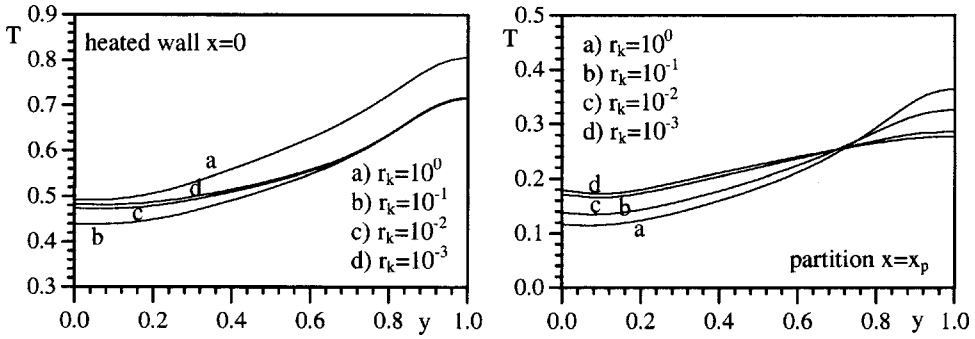

Fig. 9 The variation of the temperature for x_p=0.5, r_w=0.1, Ra=10^5

part of the heated wall as the heat transfer rate must remain fixed. If an increase in the thermal resistance of the partition is continued, it causes an increase of the temperature of the hot wall since the partition begins to act as an insulator and the thermal interaction between the two zones decreases.

The effect of the partition thickness on the temperature of the heated wall and the center of the partition is shown in Fig. 10. As the partition thickness increases, the temperatures of the heated wall and of the partition increase to a certain extent due to its weakening effect on the convective circulation.

The variations in the temperature of the heated wall and the center of the partition with the partition location are shown in Fig. 11. Placing a partition between the vertical walls of the enclosure has a negative effect on convection and therefore the temperature of the heated wall takes higher values compared with that for the nonpartitioned enclosure. Since heat transfer is governed almost exclusively by conduction on the left zone for the low values of x_p, the temperature is nearly uniform along the heated wall and along the center of the partition. As x_p increases, convection gradually becomes the dominant heat transfer mechanism inside the left zone by causing a nonuniform temperature profile along the heated wall and the center of the partition. Because of a decrease in the intensity of convective circulation inside the right zone, the temperature along the heated wall takes higher values as x_p increases. As expected, the temperature along the partition decreases as the distance of the partition from the heated wall increases.

The local Nusselt numbers along the right surface of the partition and the surface of the cold wall are presented in Fig. 12 for various values of the Rayleigh number. The local Nusselt number is strongly dependent on the Rayleigh number and becomes nonuniform as a result of stronger convection as the Rayleigh number increases. It can be observed in Fig. 13 that the heat transfer rate along the partition surface is almost constant for the higher values of the thermal conductivity ratio. This is expected because the partition corresponds to an insulating layer for these values of the thermal conductivity ratio and the energy within the system is transported from the left to the right zone by conduction only ($Nu \approx 1$). As stated previously, with a decrease in the thermal conductivity ratio, the temperature of the lower half increases while a decrease is seen at the upper half of the partition. There-

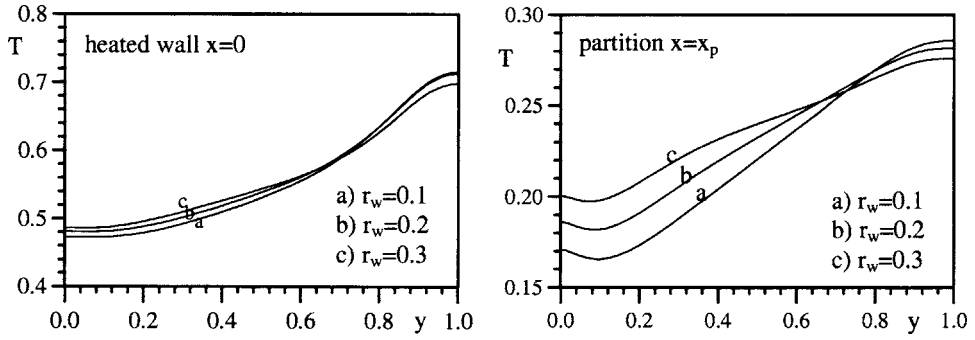

Fig. 10 The variation of the temperature for x_p=0.5, r_k=0.01, Ra=10^5

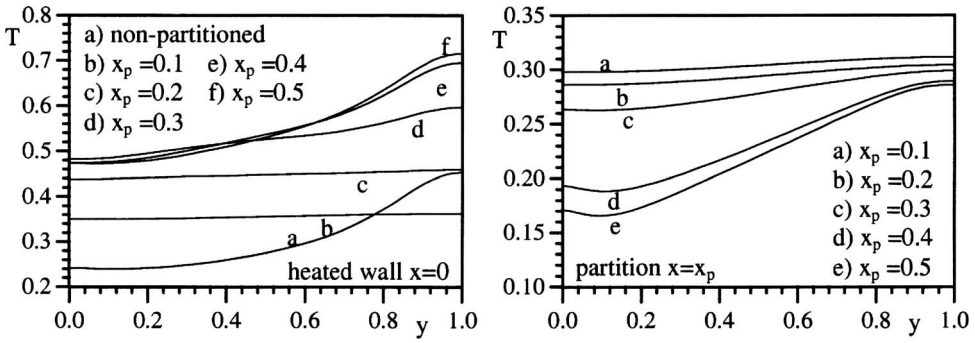

Fig. 11 The variation of the temperature for r_w=0.1, r_k=0.01, Ra=10^5

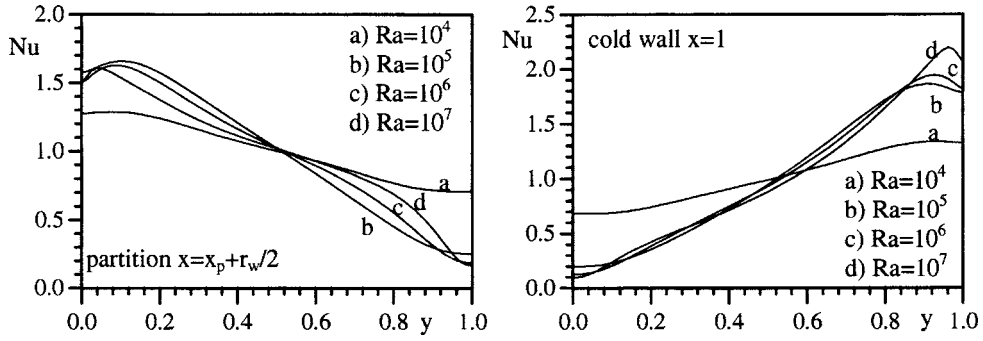

Fig. 12 The variation of the local Nusselt number for x_p=0.5, r_w=0.1, r_k=0.01

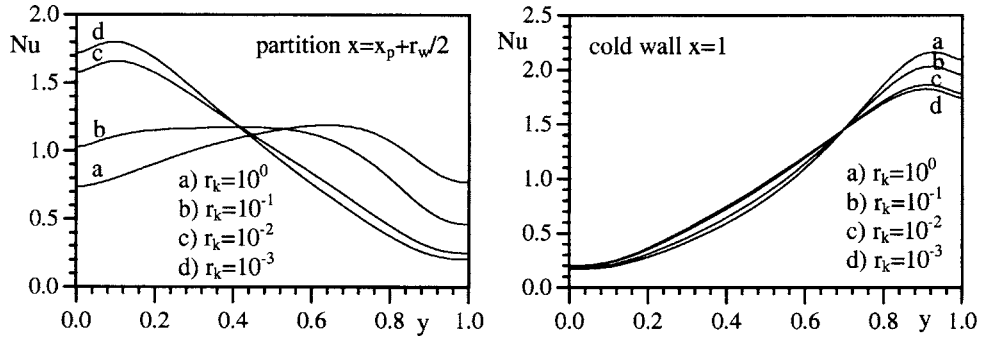

Fig. 13 The variation of the local Nusselt number for x_p=0.5, r_w=0.1, Ra=10^5

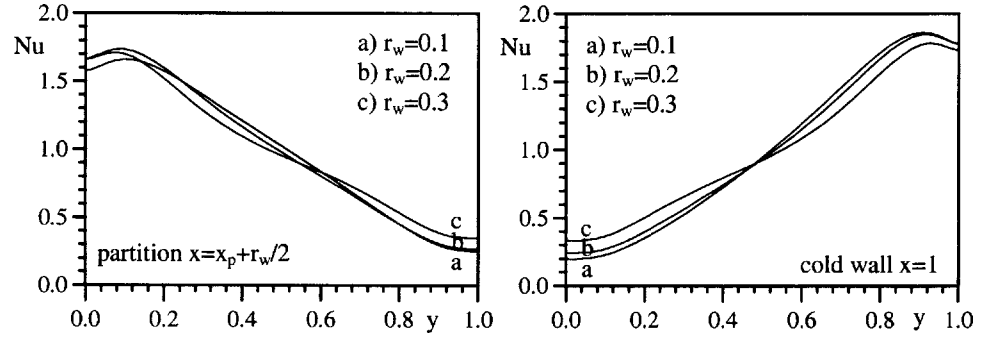

Fig. 14 The variation of the local Nusselt number for x_p=0.5, r_k=0.01, Ra=10^5

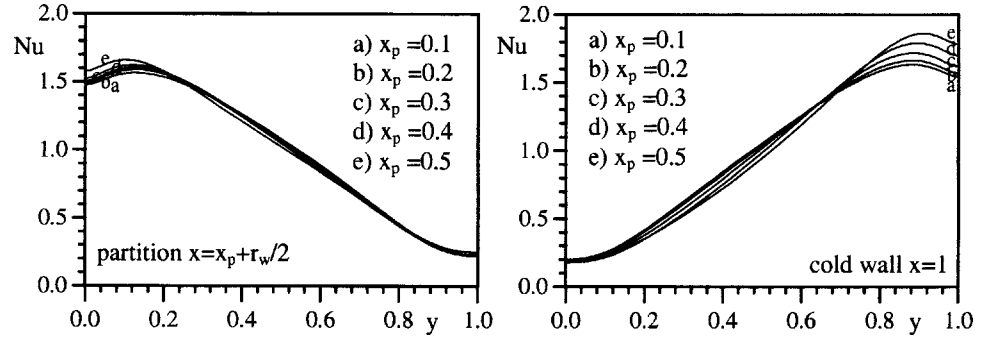

Fig. 15 The variation of the local Nusselt number for r_w=0.1, r_k=0.01, Ra=10^5

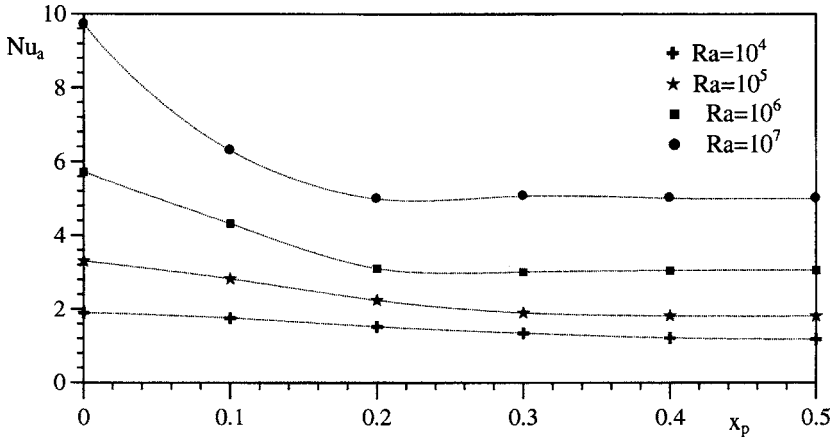

Fig. 16 The variation of the average Nusselt number for r_w=0.1, r_k=0.01

fore, the heat transfer rate takes higher values in the lower part and lower values in the upper part of the partition. It can be observed in Figs. 14 and 15 that the partition thickness and location have little effect on the local Nusselt number along the right surface of the partition and along the surface of the cold wall.

The variation of the average Nusselt number with the partition location is shown in Fig. 16. The average Nusselt number decreases as the partition moves toward the right since the thickness of the fluid layer in the right cell, which governs the natural convection flow, decreases. Although the decrease in the average Nusselt number diminishes as the partition gets closer to the center of the enclosure since a gradually strengthening circulation begins in the left zone, the greatest reduction in heat transfer occurs for the centrally located partition. This trend is similar to that reported by Tong and Gerner [4] for a system having isothermal vertical walls and Vasseur et al. [10] for a system having a uniform heat flux at both the hot and cold walls.

The variation of the average Nusselt number with the thermal conductivity ratio in the case of x_p=0.5 and r_w=0.1, i.e., a centrally located partition, is shown in Fig. 17 for various values of the Rayleigh number. As r_k is decreased, the average Nusselt number increases first, passes through a maximum and then begins to decrease. A similar trend for the average Nusselt number was observed by Vasseur et al. [10]. For lower values of the thermal conductivity ratio, the results indicate that the average Nusselt number tends to a constant value.

As it can be observed in Fig. 18, for the higher values of the Rayleigh number, the average Nussselt number remains nearly constant with an increase in the partition thickness. At Ra=10^4, a slight increase of the average Nusselt number occurs with an increase in the partition thickness. As stated before, heat is transferred almost exclusively by conduction for Ra=10^4. Furthermore, the thermal resistance of the partition is higher than that of the air in the case considered in Fig. 18. Therefore, the heat transfer across the enclosure slightly increases with an increase in the partition thickness for Ra=10^4.

The problem considered in this paper was also studied by Oothuzien [15] for the nonpartitioned enclosure case. The comparison of the values of the average Nusselt number for the nonpartitioned enclosure case, which was obtained in the work of Oosthuzien [15] and in this work, was given in Table 3. When Table 3 is examined, it can be concluded that there is an acceptable agreement between the results.

5 Conclusion

A numerical study based on the PDQ method was carried out on the natural convection in a partitioned enclosure with a uniform heat flux on the hot wall and with a constant temperature on the cold wall. The results show that the presence of a vertical partition inside the enclosure has a considerable influence on the circulation intensity, and therefore the characteristics of heat transfer across the enclosure. The intensity of the circulation in the right zone is higher than in the left zone even if the partition is in the middle of the enclosure. The average Nusselt number decreases toward a constant value with an increase in the distance between the hot wall and the partition. When the thermal conductivity ratio is relatively higher, the average Nusselt number is an

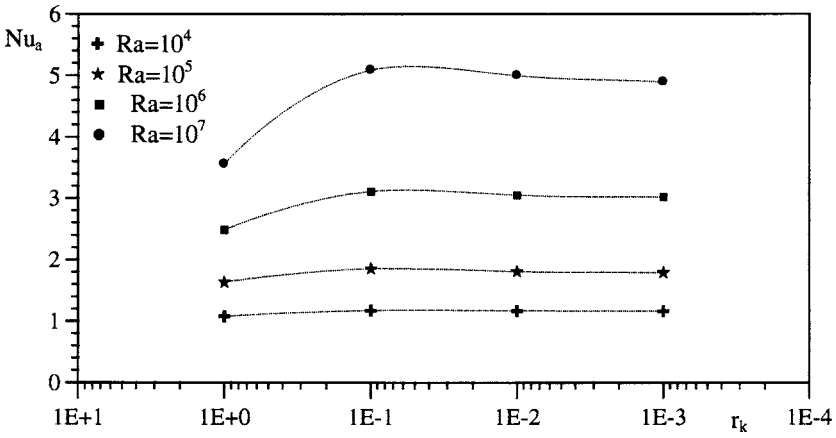

Fig. 17 The variation of the average Nusselt number for x_p=0.5, r_w=0.1

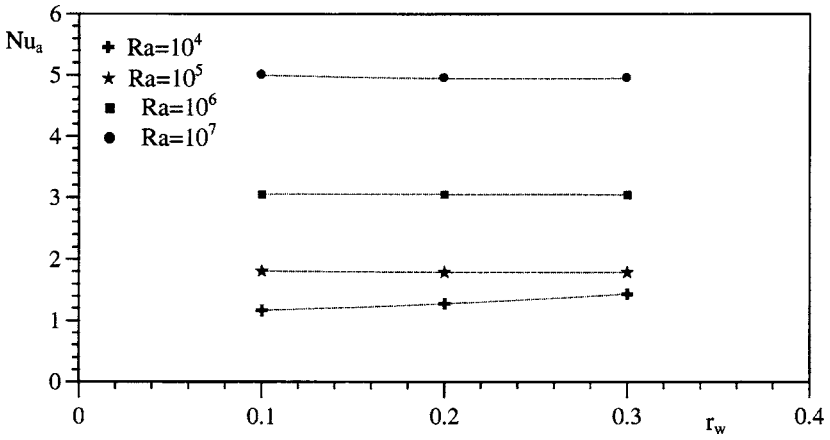

Fig. 18 The variation of the average Nusselt number for x_p=0.5, r_k=0.01

Table 3 A comparison for the average Nusselt number (nonpartitioned case)

	Ra=10^4		Ra=10^5		Ra=10^6	
	Oosthuizen	Present	Oosthuizen	Present	Oosthuizen	Present
Nu_a	1.83	1.88	3.32	3.31	5.94	5.72

increasing function of the thermal conductivity ratio. However, as the thermal conductivity ratio shrinks, the average Nusselt number begins to decrease asymptotically toward a constant value after attaining a maximum. The partition thickness has little effect on the average Nusselt number.

Nomenclature

a = first-order weighting coefficient
b = second-order weighting coefficient
g = gravitational acceleration, m^2/s
H = height of the enclosure, m
k = thermal conductivity, W/(mK)
L = width of the enclosure, m
Nu = Nusselt number, $=-(\partial T/\partial \eta)|_{\eta=0}$
Pr = Prandtl number, $=\nu/\alpha$
q = heat flux, W
R = residue
Ra = Rayleigh number, $=g\beta L^3\Delta T^*/(\nu\alpha)$
r_k = the ratio of thermal conductivities, $=k_f/k_p$
r_w = dimensionless thickness of the partition, $=w/L$
T = dimensionless temperature, $=(T^*-T_C)/(T_R-T_C)$
u = dimensionless horizontal velocity
v = dimensionless vertical velocity
w = thickness of the partition, m
x = dimensionless horizontal coordinate, $=x^*/L$
y = dimensionless vertical coordinate, $=y^*/L$
α = thermal diffusivity, m^2/s
β = thermal coefficient of volume expansion, L/K
ν = kinematic viscosity, m^2/s
η = outward direction normal to the surface
ω = dimensionless vorticity, $=\omega^* L^2/\alpha$
ψ = dimensionless stream function, $=\psi^*/\alpha$

Subscripts

a = average
C = cold
f = fluid
k = thermal conductivity
p = partition
R = reference
w = width

Superscripts

$*$ = dimensional quantities
$-$ = for y direction

References

[1] Ostrach, S., 1988, "Natural Convection in Enclosures," J. Heat Transfer, **110**, pp. 1175–1190.
[2] Ho, C. J., and Yih, Y. L., 1987, "Conjugate Natural Heat Transfer in a Air-Filled Rectangular Cavity," Int. Commun. Heat Mass Transfer, **14**, pp. 91–100.
[3] Dzodzo, D. M. C., Dzodzo, M. B., and Pavlovic, M. D., 1999, "Laminar Natural Convection in a Fully Partitioned Enclosure Containing Fluid With Nonlinear Thermophysical Properties," Int. J. Heat Mass Transfer, **20**, pp. 614–623.
[4] Tong, T. W., and Gerner, F. M., 1986, "Natural Convection in Partitioned Air-Filled Rectangular Enclosures," Int. Commun. Heat Mass Transfer, **10**, pp. 99–108.
[5] Elsherbiny, S. M., Holland, K. G. T., and Raithby, G. T., 1981, "Effect of the Thermal Boundary Condition on Natural Convection in Vertical and Inclined Air Layers," *Proceedings 20th ASME-AICHE National Heat Transfer Conference*, Milwaukee, WI, August 2-5, HT 16, pp. 127–133.
[6] Acharya, S., and Tsang, C. H., 1985, "Natural Convection in a Fully Partitioned Inclined Enclosure," Numer. Heat Transfer, **8**, pp. 407–428.
[7] Ciofalo, M., and Karayiannis, T. G., 1991, "Natural Convection Heat Transfer in a Partially- or Completely-Partitioned Vertical Rectangular Enclosure," Int. J. Heat Mass Transfer, **34**, pp. 167–179.
[8] Nishimura, T., Shiraishi, M., Nagasawa, F., and Kawamura, Y., 1998, "Natural Convection Heat Transfer in Enclosures With Multiple Vertical Partitions," Int. J. Heat Mass Transfer, **31**, pp. 1679–1998.
[9] Jones, I. P., 1982, "Numerical Predictions from the IOTA2 Code for Natural Convection in Vertical Cavities," ASME Paper No. 82-HAT-70.
[10] Vasseur, P., Hasnaoui, M., and Bilgen, E., 1994, "Analytical and Numerical Study of Natural Convection Heat Transfer in an Inclined Composite Enclosure," Appl. Sci. Res., **52**, pp. 187–207.
[11] Shu, C., 2000, *Differential Quadrature and its Application in Engineering*, Springer, New York.
[12] Shu, C., and Richards, B. E., 1992, "Application of Generalized Differential Quadrature to Solve Two-Dimension Incompressible Navier Stokes Eequations," Int. J. Numer. Methods Fluids, **15**, pp. 791–798.
[13] Elkaim, D., Reggio, M., and Camarero, R., 1992, "Simulating Two-Dimensional Turbulent Flow by Using k-ε Model and the Vorticity-Stream Function Formulation," Int. J. Numer. Methods Fluids, **14**, pp. 961–980.
[14] de Vahl Davis, G., 1983, "Natural Convection in a Square Cavity," Int. J. Numer. Methods Fluids, **3**, pp. 249–264.
[15] Oosthuzien, P. H., 2000, "Natural Convective Flow in a High Aspect Ratio Rectangular Enclosure With a Uniforn Heat Flux on the Heated Wall," *Proceedings of the 3rd European Thermal Sciences Conference*, Vol. 1, Heidelberg, September 10-13, pp. 159–164.

Buoyancy Driven Flow in Saturated Porous Media

H. Sakamoto[1]
Member ASME
e-mail: sakamoto@ce.jp.nec.com

F. A. Kulacki
Fellow ASME
e-mail: kulacki@me.umn.edu

Thermodynamics and Heat Transfer Laboratory,
Department of Mechanical Engineering,
University of Minnesota,
Minneapolis, MN 55455

*Measurements are reported of heat transfer coefficients in steady natural convection on a vertical constant flux plate embedded in a saturated porous medium. Results show that heat transfer coefficients can be adequately determined via a Darcy-based model, and our results confirm a correlation proposed by Bejan [Int. J. Heat Mass Transfer. **26**(9), 1339–1346 (1983)]. It is speculated that the reason that the Darcy model works well in the present case is that the porous medium has a lower effective Prandtl number near the wall than in the bulk medium. The factors that contribute to this effect include the thinning of the boundary layer near the wall and an increase of effective thermal conductivity.* [DOI: 10.1115/1.2717937]

Keywords: porous media, natural convection

Introduction

In free convection from an external surface in a fluid, the Nusselt number can be expressed as a power law function of the Rayleigh (or Grashof) number. Similar correlations have been attempted for surfaces bounding a saturated porous medium, and the literature shows that such attempts have not been entirely successful, especially for large Rayleigh numbers. Part of the difficulty in obtaining such correlations lies with determining effective thermophysical properties, dispersion effects, and near wall nonuniformity in the solid phase morphology.

Figure 1 summarizes the results of several experimental investigations of the Rayleigh-Bénard problem for saturated flat porous layers [1–6]. Nusselt numbers based on the stagnant thermal conductivity, k_m, and layer thickness, L, are plotted against the Rayleigh-Darcy number, $\mathrm{Ra}_m\mathrm{Da}$, also scaled with layer thickness. Note that the Rayleigh-Darcy number correctly predicts the onset of convection at $\mathrm{Ra}_m\mathrm{Da} \approx 40$. Measured Nusselt numbers then diverge with increasing $\mathrm{Ra}_m\mathrm{Da}$, implying that no general power-law correlation exists between the two parameters. It has been speculated that the motion of the fluid through the tortuous paths in the porous solid phase is responsible for such divergence and thus makes $\mathrm{Ra}_m\mathrm{Da}$ a poor predictor of heat transfer coefficients.

Measurements of convective heat transfer from a vertical wall in free convection are reported in only a few published experimental studies [7,8]. The first attempt at this problem is apparently the analytical study of Cheng and Minkowycz [9], which employs the similarity method. For a constant wall heat flux and the assumptions of a uniform permeability and Darcy flow,

$$\mathrm{Nu}_x = 0.772(\mathrm{Ra}_m^*\mathrm{Da})_x^{1/3}, \tag{1}$$

where the modified Rayleigh-Darcy number is based on heat flux and stagnant thermal conductivity, and the Nusselt number is based as well on the stagnant conductivity. Note that Eq. (1) is obtained without the need to determine the effective thermophysical properties. However, its application in the laboratory and in thermal design runs up against this requirement directly. Additionally, in all experiments, the effects of fluid motion near the heated boundary must be addressed.

The governing equations used by Cheng and Minkowycz [9] and Wooding [10] are,

$$\frac{\partial u}{\partial x} + \frac{\partial v}{\partial y} = 0, \tag{2}$$

$$u = -\frac{K}{\mu}\left(\frac{\partial p}{\partial x} + \rho g\right), \tag{3}$$

$$v = -\frac{K}{\mu}\frac{\partial p}{\partial y}, \tag{4}$$

$$u\frac{\partial T}{\partial x} + v\frac{\partial T}{\partial y} = \alpha_m\left(\frac{\partial^2 T}{\partial x^2} + \frac{\partial^2 T}{\partial y^2}\right). \tag{5}$$

In Eq. (3), the Oberbeck-Boussinesq [11,12] approximation is used, which allows density variation only in the body force term so as to feed the longitudinal component of momentum and advection. Two key assumptions are the existence of local thermal equilibrium and the validity of volume-averaged quantities. Most importantly, it is assumed that the effective thermal conductivity of the medium is known a priori, which is necessary to calculate the Rayleigh number. Other assumptions include steady two-dimensional transport, a power-law wall temperature profile, no work, no chemical reaction or phase change, negligible viscous dissipation, negligible wall effect (i.e., no Brinkman effect), negligible inertial effect (i.e., no Forchheimer effect), and the validity of Darcy's law [13].

The energy equation parallels that of a pure fluid, except for the thermal diffusivity of the porous medium. Further, Eq. (5) is a volume-averaged equation and is written for quantities that are representative values averaged over a small volume element containing both the solid and fluid phases. Averaging methods and related theorems are discussed by Whitaker [14]. The implication of Eq. (5) therefore is that the thermal diffusivity contains all of the effects of the averaging process. Further, the volume averaging theorems do not directly determine how the convective terms in Eq. (5) average themselves. An analysis of the averaging process suggests that the by-products of the averaging process contain second derivatives of local temperature and that these terms are essential components of the averaged thermal diffusivity [15]. Formally, Eqs. (2)–(5) do not contain the Brinkman terms in the momentum equation, and thus velocity slip is allowed at the boundary between the solid wall and the porous medium. Vafai and Tien [16] suggest the inclusion of the Brinkman and Forchheimer terms in their study of external forced convection, and they note that the effects of the momentum boundary layer are important only when its thickness is larger than that of the thermal boundary layer, which is not the case in free convection on vertical surfaces. Nevertheless, the Brinkman effect is to reduce the

[1]Current address: NEC Corporation, Tokyo, Japan.

Contributed by the Heat Transfer Division of ASME for publication in the JOURNAL OF HEAT TRANSFER. Manuscript received October 26, 2005; final manuscript received September 24, 2006. Review conducted by Jay M. Khodadadi. Paper presented at the 2005 ASME Heat Transfer Summer Conference (HT2006), July 15–22, 2005, San Francisco, CA.

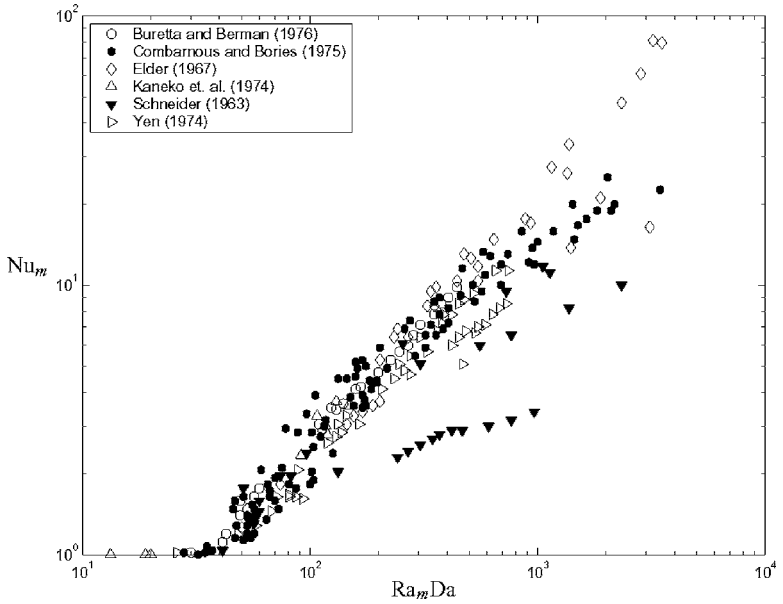

Fig. 1 Experimental results for free convection between horizontal plates in a saturated porous medium [1–6]. Here Nu, Ra$_m$, and Da are scaled to the layer thickness, *L*.

heat transfer rates from that predicted by the Darcy model because of zero velocity slip at the solid wall. This conclusion would also hold for external free convection. How pronounced this effect would be in laboratory measurements remains to be seen, and quantifying it is often avoided in the determination of heat transfer coefficients at rigid impermeable surfaces.

Beginning with Eqs. (2)–(5), Bejan [17] analyzes two-dimensional free convection from a vertical wall that is one side of the two-dimensional cavity (Fig. 2). Based on his scale analysis, the local Nusselt number is,

$$\mathrm{Nu}_x = \frac{1}{2}\left(\frac{H}{2L}\right)^{1/5} (\mathrm{Ra}_m^* \mathrm{Da})_x^{2/5}. \tag{6}$$

While the dependence of the Nusselt number on the Rayleigh-Darcy number of Cheng and Minkowycz [9] (Eq. (1)) is understandably different from Bejan's result, it is surprising how well they both represent existing heat transfer data, as will be shown later.

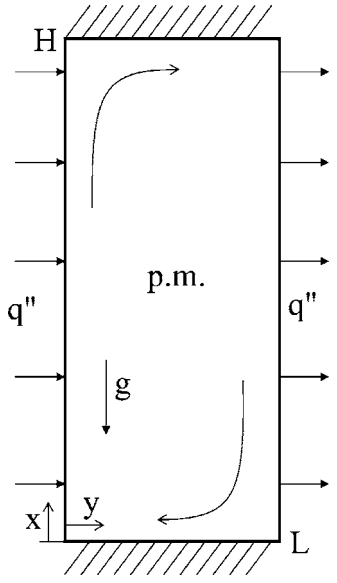

Fig. 2 Geometry used in the scale analysis of Bejan [17]

Experiments and analysis by Masuoka et al. [7] are reported for a vertical annulus. Their annulus has a height of 250 mm and an outer diameter of 328 mm. Heated inner cylinders of 180 and 280 mm are used, and the gap is filled with glass beads of 2.88 mm DIA. Water is the interstitial fluid. Steady state Nusselt numbers are based on the stagnant thermal conductivity of the saturated porous media, and the Rayleigh-Darcy number is based on the gap width and height of the annulus. Their analysis predicts that Nusselt numbers would be reduced for a large conductivity ratio in the porous medium, i.e., $\kappa \gg 1$, because of the higher fraction of heat transfer that would be conducted through the solid phase at the expense of convective transport. They associate this effect with the porosity variation near the wall, as shown by Ofuchi and Kunii [18]. When the solid phase comprises spherical beads, local spanwise porosity varies asymptotically from a high value at the wall to the lower bulk porosity away from the wall. Thus if the conductivity ratio is large, the stagnant conductivity will be lower than the bulk value near the wall. Masuoka et al. make no mention of the Brinkman effect, but it would reduce heat transfer rates as well.

Imadojemu and Johnson [8] report an experimental investigation of heat transfer from a vertical wall using glass beads in water for the porous medium. The particle diameter is 14.6 mm, which gives $\phi=0.43$ and $K=4.5\times10^{-7}$ m^2. The stagnant thermal conductivity of the medium is reported to be 3.9 W/m-K. Their heated wall is 50.8 cm high and 25.4 cm wide. Experiments are conducted with two different heat inputs, 558 and 1178 W/m^2, and temperature is measured along the wall at 20 locations at 2.54 cm intervals. Steady state heat transfer results are reported in terms of a Nusselt number versus a temperature-based Rayleigh number and suggest a power law correlation with a smaller value of the exponent than that of Cheng and Minkowycz [9]. Examination of their data shows that relatively low Nusselt numbers at high Rayleigh number accounts for the lower exponent.

Given the paucity of experimental studies on the vertical wall embedded in a saturated porous medium, the present study seeks to develop the Nusselt number correlation for the case of constant wall heat flux. We report measurements of steady heat transfer from a plate bounding porous medium comprising water and a

variety of spherical particles as the solid phase. A range of conductivity ratios is therefore included in the present database.

Apparatus

Steady state measurements of wall temperatures, the reference temperature away from the wall, and heat flux provide data for calculation of the Nusselt number,

$$\mathrm{Nu}_x = \frac{q''_w x}{k_m[T_w(x) - T_\infty]}. \tag{7}$$

The stagnant thermal conductivity is evaluated from the combined results of past studies [19,20].

Figure 3 shows the experimental apparatus comprising a thick, nearly adiabatic plastic cylinder with the constant heat flux plate mounded inside near the centerline. The cylinder is 350 $\times$200 mm^2 inner DIA. The heated plate is symmetric laminate (230 mm high$\times$175 mm wide) with alloy 260 brass surface plates each (3.175 mm thick) and two identical central thin foil heaters on the center plane. The plates and heaters are glued together and sealed on their edges. The location at the center cross section of the cylinder produces minimal effects on the two-dimensionality of the boundary layer as it develops along the plate surface. With pure water as the working fluid, the boundary layer thickness is $\approx$1 mm, and there is enough room in the cylinder for a boundary layer thickness to be larger by an order of magnitude in the saturated porous medium.

The conductivity and diffusivity of the plate material (111 W/m-K and 3.412×10^4 m^2/s at 293 K [21]) are advantageous with respect to assessing and minimizing conduction errors. A conduction analysis of the plate-heater assembly shows that the longitudinal heat transfer reduces heat flux to the plate surface by 2.5% with an uncertainty of 2%. This analysis pertains to operating conditions that produce an upper bound for the distortion of the heat flux at the surface of the plate.

Wall temperatures are measured along the longitudinal centerline of the plate at nine equidistant locations beginning near the leading edge, which is located 50 mm above the bottom of the cylinder. Wall thermocouples are potted with high conductivity cement in 1.6 mm DIA holes that are drilled to within approximately 100 μm of the surface of the plate. The number of thermocouple locations is chosen to optimize spatial resolution, address machining requirements, and allow for accurate tracking of the time variation of wall temperature, which is designed for a transient study of the present apparatus [22]. Steady state data are collected once the temperature difference between the wall and the far field reaches a value that would be achieved after five times the time constant of the system apparent from the temperature profile. The geometry of the plate-cylinder system near the leading edge is similar to that in the experiments of Imadojemu and Johnson [8].

In the work of Imadojemu and Johnson [8], temperatures near the top of their heated plate and in the porous medium are higher than that for a power-law temperature distribution typical of free convection. It is not clear whether such behavior is either fundamental to the heat transfer problem or a result of warm stagnant fluid that rises to the top of the container. The latter cannot be dismissed in their experiments because the gap between the top of their vertical plate and the top of the container is approximately 30 mm, and they record data when their system has reached steady state. In the present experiments, the heated plate is designed to have approximately 76 mm between its trailing edge and top of the porous medium up to the top of the cylinder, the goal being to eliminate (or minimize) effects of the such stratification.

The heated plate is designed to permit a comparison of heat transfer in free convection in a pure fluid at up to $\mathrm{Ra}_m \sim 10^{12}$ based on the maximum length of the plate. For laminar free convection, Nusselt numbers are given by,

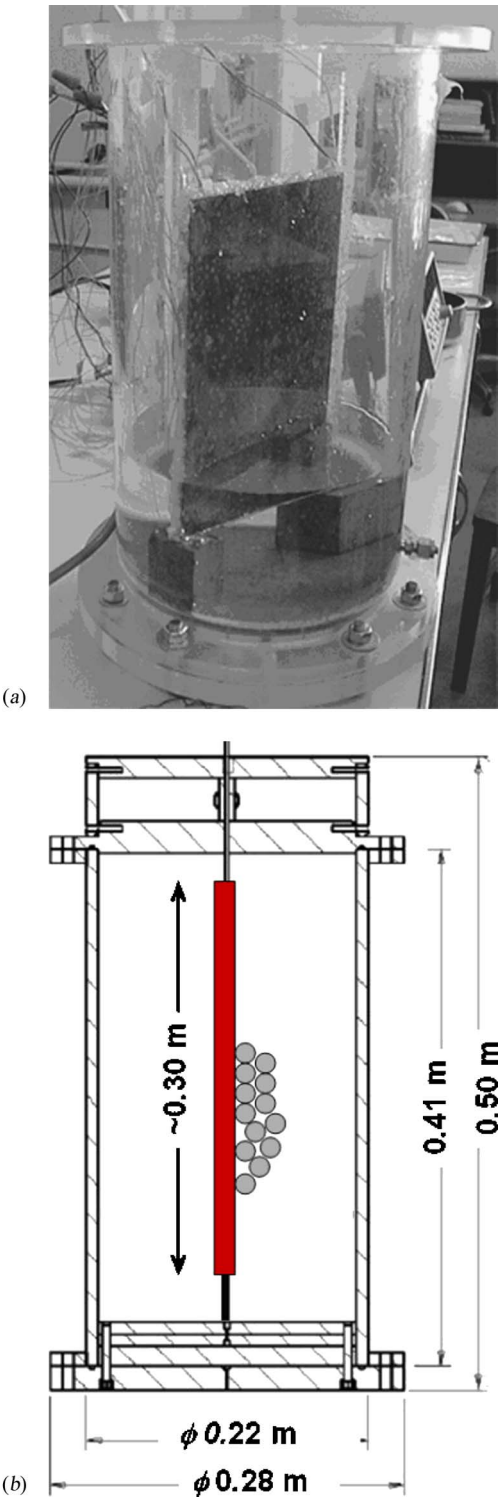

Fig. 3 Container with heater and plate assembly (*a*) side view and (*b*) top view

$$\mathrm{Nu}_x = 0.60(\mathrm{Ra}_x^*)^{1/5}, \tag{8}$$

where $\mathrm{Ra}_x^* > 10^5$ [[23], Chap. 7]. As a qualification of the heater design and reliability of the wall temperature measurements, experiments for steady convection in water produce excellent agreement with Eq. (8), and the results are shown in Fig. 4.

Randomly stacked spheres of glass, steel, and polyethylene comprise the solid phase of the porous media, and water is the interstitial fluid. Tables 1 and 2 summarize key properties with

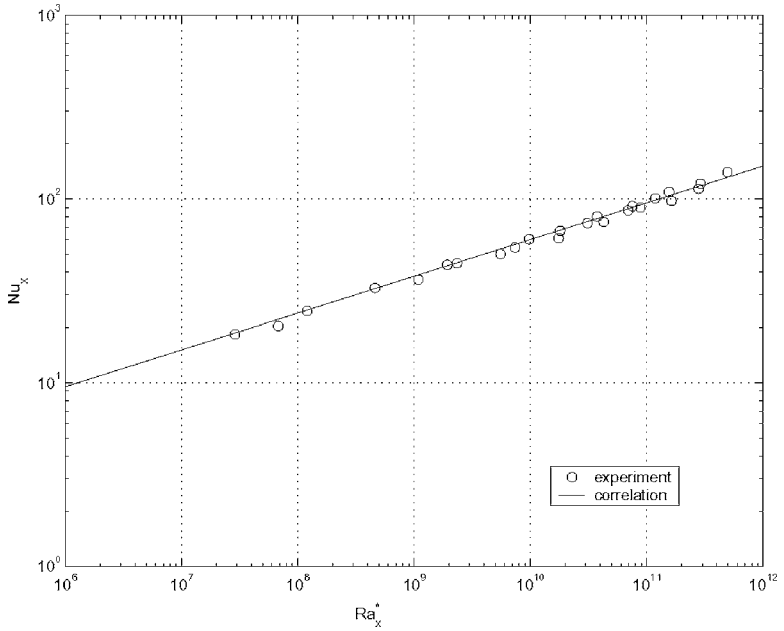

Fig. 4 Steady state heat transfer data in water with regression equation, Eq. (8)

sources for completeness. The combination of these fluids and solids produce saturated porous media with $\kappa=1$ (glass-water), 25 (glass-air), 100 (steel-water), and 2400 (steel-air). The macroscopic volume fraction of the fluid phase is determined by measuring the volume of water that can be contained in the fully packed cylinder. An uncertainty is expected due to the effects of the impermeable surfaces present in the assembly. Along the container wall, the vertical plate and the supports for the plate create a surface along which the spheres are aligned with local values of porosity reaching 1.0. Generally, the high porosity region near a solid surface in a situation like this extends more than a few particle diameters away from the surface [[24] Sec. 2.12]. At about one-half a bead diameter from the wall, the porosity falls to <0.20, which is much lower than the bulk value of 0.36 to 0.38 far away from the wall.

Thermocouples throughout the apparatus are 36 AWG type E because of the sensitivity of 80 μV/K offered by the Chromega-constantan combination (Chromega® is a commercially available chromium-nickel alloy). The calibration standard is a mercury-in-glass thermometer with a resolution of ±0.1 K and with a traceable calibration supplied by the manufacturer. Calibration curves were developed for each thermocouple used in the present study between 298 and 328 K. The two-dimensionality of the heater assembly is verified via measurement during experimental trials, as well as through a numerical model developed in conjunction with the design of the plate-heater assembly [15].

Table 1 Characterization of the solid phase comprising randomly stacked spherical particles. Permeability is determined from the Kozeny relation, $K=d^2\phi^3/180(1-\phi^2)$.

Material (Average ϕ)	Average diameter (mm)	Standard deviation of diameter (mm)	Sample size	Permeability (m^2)
Steel	6.00	0.0	10	3.6×10^{-8}
(0.40)	14.00	0.0	10	1.9×10^{-7}
Glass	1.47	0.11	14	1.7×10^{-9}
(0.38)	6.01	0.06	10	2.9×10^{-8}
Polyethylene	25.4	0.00	10	6.4×10^{-7}
(0.40)				

Results

Figure 5 summarizes steady state data obtained with a medium comprising 6 mm DIA glass particles and water with the results of Cheng and Minkowycz [9] and Bejan [17]. The three data points lying above the theoretical predictions and the bulk of the data correspond to very low heat flux and temperature differences of ~1 K. Bejan's prediction is plotted in Fig. 5 with upper and lower bounds based on the geometry of the present apparatus. A minimum aspect ratio, H/L, is obtained by comparing the height of the heated plate to the radius of the cylindrical container, which gives $H/L=2.1$. The maximum aspect ratio possible is $H/L=7.6$, where the height of the cylindrical container and the normal distances from the plate to the container wall are used.

It is clear that Bejan's correlation works better than that of Cheng and Minkowycz [9] with the present database, and the

Table 2 Thermophysical properties of materials of the porous medium

Material	Property	Source
AISI 52100 Chrome steel (1.34 percent Cr)	$\rho_s=7865$ kg/m^3 $c_s=460$ J/kg-K $k_s=61$ W/m-K $\alpha_s=1.69\times10^{-5}$ m^2/s	[21]
Soda silicate glass	$\rho_s=2500$ kg/m^3 $c_s=918.2$ J/kg-K $k_s=0.64$ W/m-K $\alpha_s=2.79\times10^{-7}$ m^2/s	[25]
High density polyethylene	$\rho_s=958$ kg/m^3 $c_s=2100$ J/kg-K $k_s=0.329$ W/m-K $\alpha_s=1.57\times10^{-7}$ m^2/s	[26]
Water (300 K, 1 atm)	$\rho_s=996.6$ kg/m^3 $c_s=4180.6$ J/kg-K $k_s=0.6103$ W/m-K $\alpha_s=1.46\times10^{-7}$ m^2/s	[27]

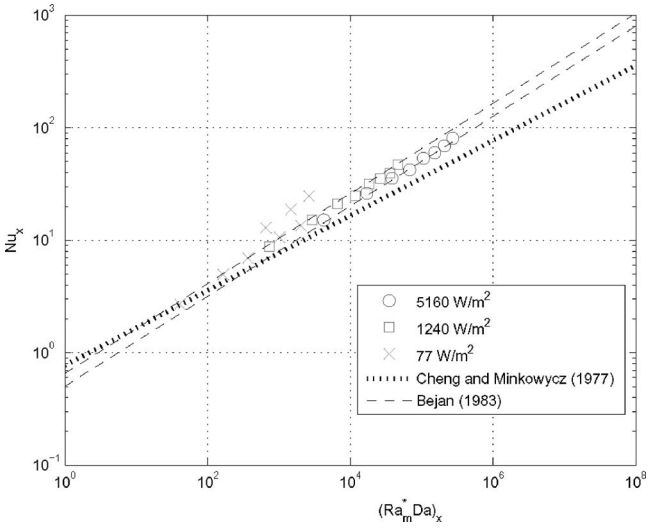

Fig. 5 Nusselt numbers of 6-mm DIA glass particles in water compared with results of Bejan [17] and Cheng and Minkowycz [9]. The two lines for Bejan's prediction are extreme values based on the aspect ratio pertaining to the present study.

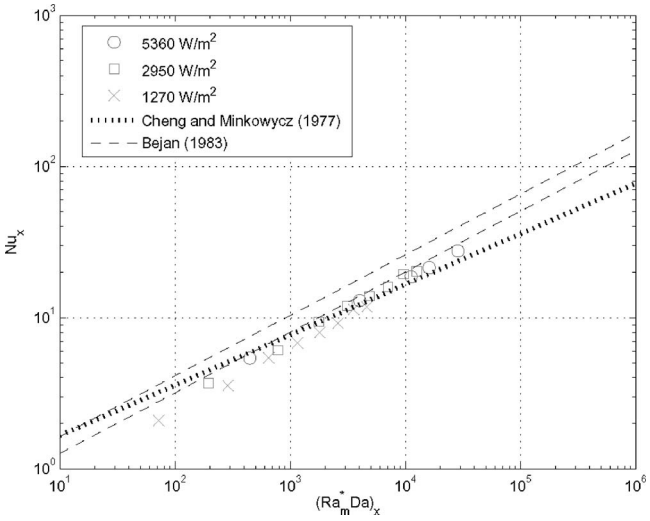

Fig. 7 Nusselt number for 1.5 mm DIA glass particles in water with predictions [17,9]

interpretation is that the plate and container should be treated as an enclosure. For the true enclosure problem, fluid circulates, and there is a vertical temperature gradient both along the heated wall and in the porous medium under the constant heat flux boundary condition. Thus, the far field temperature is not constant as it would be if the plate bounded a semi-infinite porous medium. Bejan finds that the wall temperature is linear with distance along plate, and the boundary layer thickness is constant. The present experiment does not have any cooling mechanism on the container wall, and the medium has a free surface exposed to the ambient temperature at the top. The far field temperature is thus not strictly constant. It is measured at 5 cm in the longitudinal position and at 7 cm in the transverse position within the porous medium. It turns out that measured temperatures are stable and remain at their initial values during the experimental trials, with no observable increase at the resolution of our instruments. This finding confirms the analytical results that in the enclosure the core region is motionless [17].

Figure 6 shows the steady state temperature profiles along the plate for several values of applied heat flux. Steady temperatures are calculated as averages over ten or more readings of each thermocouple, assuming that the system has reached steady state. The temperature difference in Fig. 6 is the difference between the initial system temperature and the plate temperature once heating has begun. The experimental profiles for two heat flux settings are fit to an $x^{1/3}$ power law as suggested by Cheng and Minkowycz [9], but, owing to edge effects and end losses, a linear fit suggested by Bejan [17] could be used.

Figure 7 summarizes the experiment with 1.5 mm DIA glass particles and water. Good agreement is seen with the Bejan result. However, there is a slight shift from the region predicted by the Bejan result. All experimental data are lower than the prediction, and the shift is larger for the lowest heat flux. This shift is not observed for the 6 mm DIA case, and a plausible explanation for this difference is that the boundary layer in the 1.5 mm DIA case involves fluid-particle interaction more than in the 6 mm DIA case. For the heat fluxes used in the present study, the boundary layer is estimated to be $\leqslant 1$ mm.

Figure 8 shows the data for the case of 14 mm DIA steel beads in water. Again, the slope of the Nusselt-versus-Rayleigh number

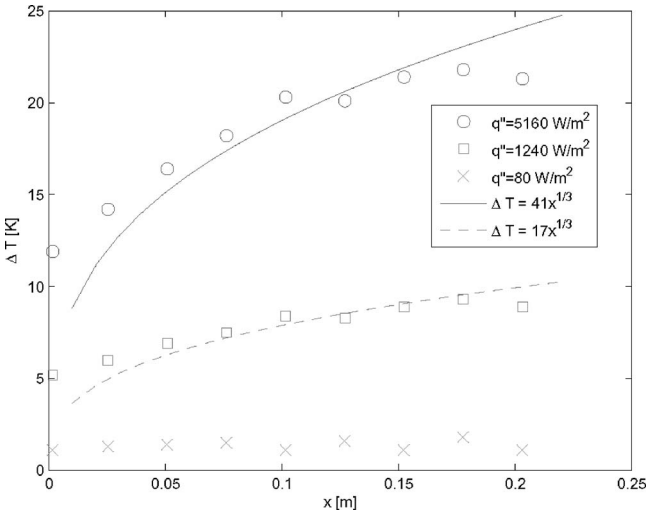

Fig. 6 Steady state temperature profiles as function of longitudinal position with power-law profiles suggested by Cheng and Minkowycz [9] superposed

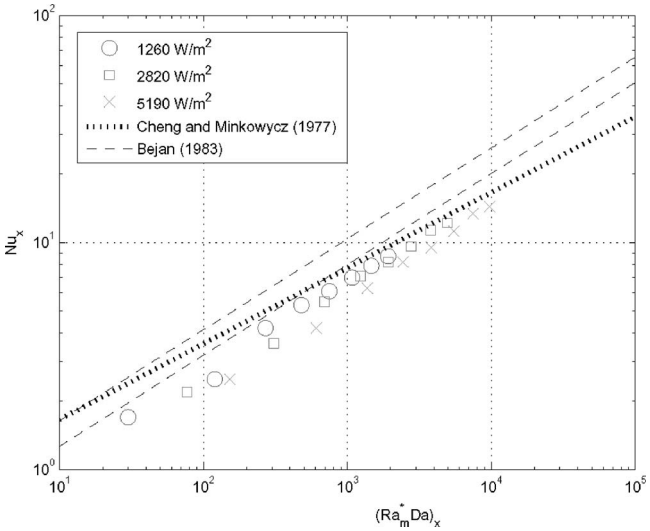

Fig. 8 Nusselt number of 14 mm DIA steel particles in water compared to predictions [17,9].

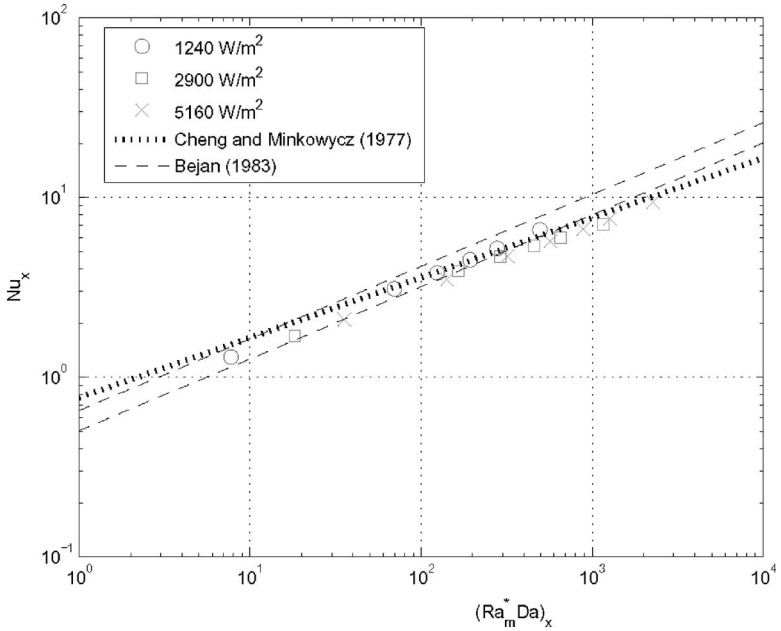

Fig. 9 Nusselt number of 6 mm DIA steel particles in water compared to predictions [17,9]

relation appears to agree with the Bejan result, but there is a more pronounced shift in the data below the prediction. In this case, the near-wall particle morphology, the boundary layer thickness, and the conductivity ratio play roles in the reduction of the Nusselt number. Figure 9 shows the results for three heat fluxes for 6 mm DIA steel beads in water. In this case, the agreement with Bejan's result is very good, but the slope of the data when correlated is slightly different and somewhat in agreement with the slope suggested by Cheng and Minkowycz. It should be noted that the 6 mm DIA data lie in the Rayleigh-region where the Cheng and Minkowycz and the Bejan results meet, and the small deviation in the Rayleigh exponent from 0.4 is not statistically significant. In other words, the present study suggests an exponential relation of 0.4.

Figure 10 combines all steady state data, along with the two analytical studies. Data grouped by solid phase material appear to follow the Bejan slope of 0.4. In terms of solid phase materials, glass cases lie closest to Bejan's correlation. Because data for the 6 mm DIA steel particles lie close to the glass data, the shifts in the 14 m DIA steel and 25.4 mm DIA polyethylene particle cases suggest the effects of large diameter.

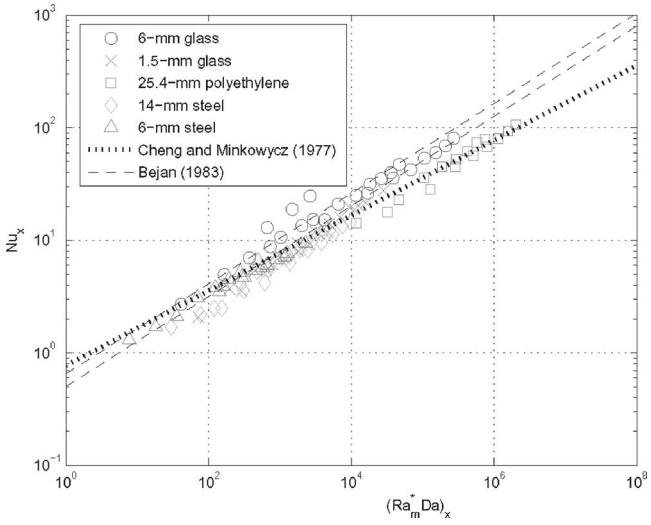

Fig. 10 Nusselt numbers for all steady state data by particle type compared to predictions [17,9]

Table 3 lists resulting regression coefficients by bead type based on the data presented in Fig. 10, using the functional form,

$$\mathrm{Nu}_x = C(\mathrm{Ra}_m^* \mathrm{Da})_x^n. \quad (9)$$

The average exponent of 0.39 is in excellent agreement with 0.40 exponent of Eq. (7). The average coefficient of 0.45 is outside the range for the Bejan correlation, which is assumed for the present apparatus to be between 0.51 and 0.66 based on the aspect ratio of the apparatus. This small difference is within experimental uncertainty, which is discussed in the next section, and is speculated to be due to the effects of near wall morphology.

Figure 11 presents all the data in a Nusselt-Rayleigh space, where both of the parameters are based on water. The figure allows examination of possible agreement with the pure water correlation of Eq. (8). The data sets that are closest to the correlation are the large diameter sets, i.e., 14 mm DIA steel and 25.4 mm DIA polyethylene. Other sets not only shift away from the correlation but also diverge within each set. It appears that the diverging behavior within each set of the same material is an indication of a significant Darcy effect. A set of data that is aligned with the correlation is for the same heat flux setting. Sets with different fluxes are shifted in the horizontal direction by the difference in Darcy numbers. If there is no appearance of divergence, no Darcy

Table 3 Correlation constants of the heat transfer data in the form of Eq. (9) for each solid-fluid phase combination

Medium (d)	C	n
Glass (6 mm)	0.66	0.38
Glass (1.5 mm)	0.35	0.43
Steel (14 mm)	0.34	0.40
Steel (6 mm)	0.65	0.35
Polyethylene (25.4 mm)	0.24	0.41
Average	0.45	0.39

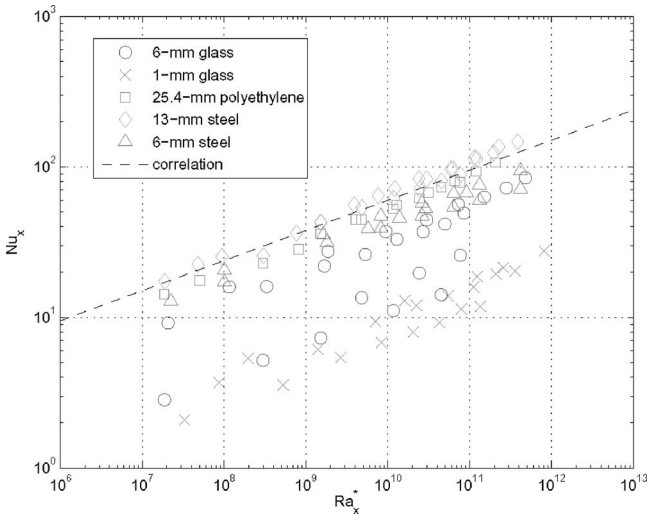

Fig. 11 Nusselt number passed on Rayleigh number for the interstitial fluid (water) with the measured correlation for water, Eq. (8)

effect is implied. In that case, heat transfer from the wall does not experience significant effects due to the presence of the solid phase material.

Experimental Uncertainty

The uncertainty in longitudinal location is mainly due to locating the true leading edge, which gives $\Delta x = \pm 4$ mm. The uncertainty in thermal conductivity is estimated to be 5%, but a large variation in earlier experimental results give an uncertainty of ±40% for the medium made of steel beads with water. The uncertainty in temperature measurement using thermocouples is estimated to be 0.5 K. Overall average uncertainties for Nusselt and Rayleigh-Darcy numbers are 18% and 58%, respectively. A comprehensive uncertainty analysis is presented elsewhere [15].

Conclusions

The present experiments have been designed to achieve two objectives. The most important objective is to construct a Nusselt number correlation for free convection from a vertical impermeable wall embedded in a fluid-saturated porous medium. Correlations for this geometry are rarely reported in the literature with a quantified uncertainty analysis. Our second objective is to compare the measurements with predictions of prior analytical studies. Existing analytical studies assume that the porous medium is homogeneous up to the rigid heated wall and thus do not take into account the near wall region of high porosity and permeability. This, however, is the region that is the most important in free convection.

The heat transfer correlation proposed by Bejan [17] is verified. Based on the present results, and for $0.54 < \kappa < 100$, and $10 < \mathrm{Ra}_m \mathrm{Da}_x < 10^6$, it is recommended that

$$\mathrm{Nu}_x = 0.5(\mathrm{Ra}_m^* \mathrm{Da})_x^{0.4}. \quad (10)$$

Further, it should be noted that the nonlinear behavior of the Nusselt number with the Rayleigh-Darcy product seen in the data of Imadojemu and Johnson [7] is not observed, and the present data sets are well represented by relations of linear logarithmic regressions. Experimental results suggest possible effects of near-wall particle morphology on Nusselt number and that these effects may be as much as or more pronounced than those of the aspect ratio of the container containing the porous medium. Owing to the random stacking of particles in all studies, it is not possible to speculate on how specific aspects of the wall region morphology influence the heat transfer coefficient. Cases with large particle diameter, e.g., 25.4 mm DIA polyethylene and 14 mm DIA steel, have resulted in correlations that are close to the pure-fluid correlation, Eq. (8), suggesting relatively minor effects of shear at the particle, or pore, level and slight disturbance of the boundary layer by the few particles in contact with the wall.

Nomenclature

c = heat capacity, J/kg-K
Da = Darcy number, K/x^2
d = particle diameter, m
g = gravitational acceleration, m/s^2
H = height of porous medium (Fig. 2), m
K = permeability, m^2
k_m = stagnant conductivity, W/m-K
L = depth of porous medium (Fig. 2), m
Nu = Nusselt number, hx/k_m
p = pressure, Pa
q''_w = wall heat flux, W/m^2
Ra = Rayleigh number, $g\rho_o\beta\Delta T x^3/\mu\alpha_m$
Ra* = modified Rayleigh number, $g\beta q''_w x^4/\nu\alpha_m k_m$
T = temperature, K
u = x velocity, m/s
v = y velocity, m/s
x = longitudinal location, m
y = transverse location, m

Greek Symbols

α = thermal diffusivity, m^2/s
β = volumetric expansion coefficient, K^{-1}
κ = ratio of thermal conductivities, k_s/k_f
μ = dynamic viscosity, N/m-s
ν = kinematic viscosity, m^2/s
ρ = density, kg/m^3
ϕ = porosity

Subscripts

0 = reference
∞ = far field
f = fluid
m = porous medium with stagnant fluid
s = solid
w = wall

References

[1] Buretta, R. J., and Berman, A. S., 1976, "Convective Heat Transfer in a Liquid Saturated Porous Layer," ASME J. Appl. Mech., **98**(2), pp. 249–253.
[2] Combarnous, M. A., and Bories, S., 1974, "Modelisation De La Convection Naturelle Au Sein D'une Couche Poreuse Horizontale a L'Laide D'Un Coefficient De Transfert Solide- Fluide," Int. J. Heat Mass Transfer, **17**(4), pp. 505–515.
[3] Elder, J. W., 1967, "Steady Free Convection in a Porous Medium Heated From Below," J. Fluid Mech., **27**(1), pp. 29–48.
[4] Kaneko, T., Mohtadi, M. F., and Aziz, K., 1974, "An Experimental Study of Natural Convection in Inclined Porous Media," Int. J. Heat Mass Transfer, **17**(4), pp. 485–496.
[5] Schneider, K.-J., 1963, "Investigation of the Influence of Free Thermal Convection on Heat Transfer Through Granular Material," *Proceedings, 11th International Congress of Refrigeration*, August 27–September 4, Munich, Vol. II-4, pp. 247–254.
[6] Yen, Y.-C., 1974, "Effects of Density Inversion on Free Convective Heat Transfer in Porous Layer Heated From Below," Int. J. Heat Mass Transfer, **17**(11), pp. 1349–1356.
[7] Masuoka, T., Yokote, Y., and Katsuhara, T., 1981, "Heat Transfer by Natural Convection in a Vertical Porous Layer," Bull. JSME, **24**(192), pp. 995–1001.
[8] Imadojemu, H., and Johnson, R., 1991, "Convective Heat Transfer From a Heated Vertical Plate Surrounded by a Saturated Porous Medium," *Proceedings, ASME/JSME Thermal Engineering Joint Conference*, March 17–22, Reno, NV, ASME, New York, pp. 203–212.
[9] Cheng, P., and Minkowycz, W. J., 1977, "Free Convection About a Vertical Flat Plate Embedded in a Porous Medium With Application to Heat Transfer From a Dike," J. Geophys. Res., **82**(14), pp. 2040–2044.
[10] Wooding, R. A., 1963, "Convection in a Saturated Porous Medium at Large Rayleigh Number or Peclet Number," J. Fluid Mech., **15**(4), pp. 527–544.
[11] Oberbeck, A., 1879, "Ueber Die Warmeleitung Der Flussigkeiten Bei Beruck-

sichtigung Der Stromungen Infolge Von Temperaturdifferenzen," Ann. Phys. Chem., **7**, pp. 271–292.
[12] Boussinesq, J., 1901, *Theorie analytique de la chaleur:mise en harmonie avec la thermodynamique et avec la theoriemecanique de la lumiere*, Gauthier-Villars, Paris.
[13] Cheng, P., 1985, "Natural Convection in a Porous Medium: External Flows," in *Natural Convection: Fundamentals and Applications*, S. Kakac, W. Aung, and R. Viskanta, eds., Hemisphere, Washington, pp. 475–513.
[14] Whitaker, S., 1999, *The Method of Volume Averaging*, Kluwer Academic, Dordrecht, The Netherlands.
[15] Sakamoto, H., 2005, "Buoyancy-Driven Flow in Fluid-Saturated Porous Media Near a Bounding Surface," Ph.D. thesis, University of Minnesota, Minneapolis.
[16] Vafai, K., and Tien, C. L., 1981, "Boundary and Inertia Effects on Convective Mass Transfer in Porous Media," Int. J. Heat Mass Transfer, **25**(8), pp. 1183–1190.
[17] Bejan, A., 1983, "The Boundary Layer Regime in Porous Layer With Uniform Heat Flux From the Side," Int. J. Heat Mass Transfer, **26**(9), pp. 1339–1346.
[18] Ofuchi, K., and Kunii, D., 1965, "Heat-Transfer Characteristics of Packed Beds With Stagnant Fluids," Int. J. Heat Mass Transfer, **8**(5), 749–757.
[19] Aichlmayr, H. T., 1999, "The Effective Thermal Conductivity of Saturated Porous Media," Master's thesis, University of Minnesota, Minneapolis.
[20] Kristoffersen, M., 2001, "Metastable Convection in a Porous Medium Heated From Below," Master's thesis, University of Minnesota, Minneapolis.
[21] Eckert, E. R. G., and Drake, R. M., 1971, *Analysis of Heat and Mass Transfer*, McGraw-Hill, New York.
[22] Sakamoto, H., and Kulacki, F. A., 2005, "Effective Thermal Diffusivity of Porous Media in the Wall Vicinity," ASME Paper No. IMECE2005–81623.
[23] Bejan, A., 1993, *Heat Transfer*, Wiley, New York.
[24] Kaviany, M., 1995, *Principles of Heat Transfer in Porous Media*, 2nd ed., Springer-Verlag, New York.
[25] Bansal, N. P., and Doremus, R. H., 1986, *Handbook of Glass Properties*, Academic, Orlando, FL.
[26] Lindfors, J., 1999, "Boundary Layer Effects on the Stagnant Effective Thermal Conductivity of a Saturated Porous Medium," Honor's thesis, University of Minnesota (unpublished), Minneapolis.
[27] Lemmon, E., McLinden, M., and Friend, D., 2003, "Thermophysical Properties of Fluid Systems: Water," *NIST Chemistry WebBook, NIST Standard Reference Database Number 69*, P. J. Linstrom and W. G. Mallard, Eds., National Institute of Standards and Technology, Gaithersburg (http://webbook.nist.gov).

Enhanced Heat Transfer Using Porous Carbon Foam in Cross Flow—Part I: Forced Convection

Yorwearth L. Jamin

Abdulmajeed A. Mohamad[1]
e-mail: mohamad@ucalgary.ca

Department of Mechanical and Manufacturing Engineering,
University of Calgary,
2500 University Drive NW,
Calgary, Alberta T2N 1N4, Canada

Cogeneration of heat and power has become standard practice for many industrial processes. Research to reduce the thermal resistance in heat exchangers at the gas/solid interface can lead to greater energy efficiency and resource conservation. The main objective of this experimental study is to quantify and compare the heat transfer enhancement of carbon foam and aluminum fins. The study measures the heat transfer rate and pressure drop from a heated vertical pipe, with and without porous medium, in forced convection. The largest increase in Nusselt number was achieved by aluminum fins, which was about three times greater than the best carbon foam case.
[DOI: 10.1115/1.2717240]

Keywords: heat transfer, forced convection, porous medium, carbon foam, cogeneration, experimental

1 Introduction

In most heat exchangers the thermal resistance is highest at the fluid/solid interface, especially if the fluid has a Prandtl number order of one (i.e., exhaust gas). This makes heat recovery from waste exhaust gas a difficult and often costly process requiring large surface areas. Porous mediums have been identified as a means to reduce the thermal resistance at the gas/solid interface and enhance heat transfer rates. Vafai and Kim [1] investigated a thin porous layer attached to a flat plate in a forced convection environment. They noted that enhanced heat transfer could be achieved when the effective conductivity of the porous layer was higher than that of the fluid. Angirasa [2] conducted an experimental investigation of forced air convection enhancement with metallic fibrous materials with porosities of 0.93 and 0.97. When a porous layer was attached to a flat plate he observed an increase in Nusselt number up to four times relative to a bare plate. The work also noted that Nusselt number increased with decreasing porosity up to a critical point where flow resistance adversely affected heat transfer. Pavel and Mohamad [3] also found heat transfer could be enhanced using porous inserts in a pipe under forced convection conditions. Further improvements to their system could be made with lower porosity and higher effective conductivity. Gallego and Klett [4] presented the case for using carbon foam as a thermal management material. They found carbon foam heat transfer coefficients were approximately ten times greater than those for aluminum foam. However, this increase in heat transfer coefficient was often achieved at the expense of high-pressure drops.

The objective of the present experimental study is to quantify the heat transfer enhancement of carbon foam and its suitability for industrial applications. The study investigates steady state heat transfer and pressure drop from a heated vertical pipe, with and without porous medium, in a forced convection environment. Heat transfer performance for carbon foam is compared to a bare copper pipe and an aluminum finned pipe. The aluminum finned pipe is included in order to gauge the merit of carbon foam performance for industrial applications.

2 Porous Carbon Foam

The porous medium under investigation is high thermal conductivity (HTC) carbon foam which is commercially produced by Poco Graphics Inc. Production of HTC foam is based on a process developed at the Oak Ridge National Laboratory which turns mesophase pitch into carbon foam. The end product is composed of uniformly shaped bubbles with even distribution set within carbon ligaments. The z direction has different thermal conductivity than the x-y direction which results in nonisotropic material. That is, there is less resistance to heat transfer and therefore a higher thermal conductivity in the z direction [4]. It should also be noted that thermal conductivities decrease with increasing temperature.

Material properties published by Poco Graphics Inc. are presented in Table 1. Thermal conductivity, porosity, and permeability of the HTC foam sample used in this investigation were experimentally determined and also included in Table 1. The experimental uncertainty associated with the experimental conductivity data is approximately ±15%. Experimental methodology for determining effective thermal conductivity and permeability are presented in Appendices A and B, respectively.

3 Experimental Setup and Procedure

The wind tunnel and data acquisition system are illustrated in Fig. 1. Air at ambient temperature (1) is drawn through a honeycomb straightener (2) and then into the converging section of the wind tunnel (3). Air flow is induced by an inline airfoil centrifugal fan (8). Steady flow with linear velocity profile blows across the pipe assembly and its velocity is measured by a pitot-static tube (4) and pressure transducer (10). Uncertainty due to the pressure transducer (Omega PX278 05D5V) used for velocity measurement is ±12.6 Pa. A range of Reynolds numbers is achieved by choking the flow downstream of the diffuser with a damper (7). Static pressure drop across the pipe assembly is measured by a differential pressure transducer (Omega PX277 01D5V) (10) with ports upstream (9) and downstream of the pipe assembly. Uncertainty associated with static pressure drop measurement is ±3.2 Pa. The pipe assembly is mounted within the wind tunnel on two Teflon rods (5) as illustrated in Fig. 2. Teflon is used to mount the pipe in order to minimize heat losses. A heating cartridge with uniform rated wattage of 50 W (Omega CIR-3051/120V) is inserted into the pipe and connected to a variable current power supply (11). Power supplied to the heating cartridge (41.14 Ω) is measured with a rectifier (12) and is calculated using the formula,

[1]Corresponding author.

Contributed by the Heat Transfer Division of ASME for publication in the JOURNAL OF HEAT TRANSFER. Manuscript received September 22, 2005; final manuscript received August 15, 2006. Review conducted by Jose L. Lage.

Table 1 Material properties for HTC foam

	Manufacturer specifications	Experimental results
Effective thermal conductivity		
z direction (20°C):	245 W/mK	Not available
z direction (100°C):	165 W/mK	80 W/mK
xy direction (20°C):	70 W/mK	Not available
xy direction (100°C):	Not available	39 W/mK
Porosity (%)	61	57
Open porosity (%)	95	Not available
Pore diameter (μm)	350	Not available
Emissivity	0.62	Not available
Permeability	Not available	7.5×10^{-13} m^2

$P=Vs^2/R$, where Vs is the measured voltage and R is the heater resistance. Propagated uncertainty associated with power measurement is ±0.2 W. Six type-K thermocouples (Omega TT-K-36) were soldered into the pipe wall to provide temperature measurements (14). Maximum uncertainty associated with mean surface temperature is ±2.1°C. A single type-K thermocouple wire, inserted into the wind tunnel upstream of the heated pipe at a central elevation, measures ambient air temperature inside the test section. HTC foam is press fit onto the pipe with Dow 340 thermal grease applied to the interface between the pipe and HTC foam to reduce thermal contact resistance. Thermocouple and power wires are routed through the hollow bottom Teflon rod to a FieldPoint data acquisition system (13).

A National Instruments, FieldPoint, PC-based, distributed input–output (I/O) data acquisition system is used for this investigation. The FieldPoint (FP) system is connected to a laptop and LabVIEW 6.1 via a serial port. dc signals generated by the sensors are transmitted to the FieldPointI/O modules. The I/O modules filter, digitize, calibrate, and scale raw sensor signals to engineering units. The LabVIEW application queries the FieldPoint network interface at a sampling rate equal to the slowest I/O module sampling rate (i.e., 0.88 Hz). The parameters measured with corresponding sensors, I/O modules, sampling rate and uncertainty are summarized in Table 2.

Tests were completed over a range of air velocities (8–45 m/s) and for the same power input 20 W. For each case investigated, the power supply to the heating cartridge was switched on and the wind tunnel damper fully closed (Re≈7000). The apparatus was left running for approximately 2 h and allowed to reach thermal steady state (achieved when the mean surface temperature did not

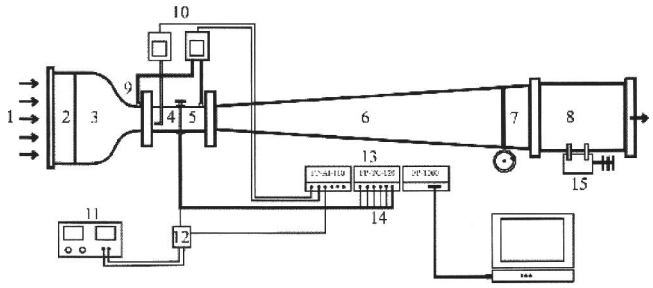

1. Ambient air
2. Straightener
3. Contraction cone
4. Pitot-static tube
5. Heated vertical pipe
6. Diffuser
7. Flow damper
8. Fan chamber
9. Static pressure port
10. Differential pressure transducers
11. AC power supply
12. Signal rectifier
13. Signal conditioning hardware
14. Thermocouples
15. Fan motor

Fig. 1 Schematic layout of wind tunnel and DAQ

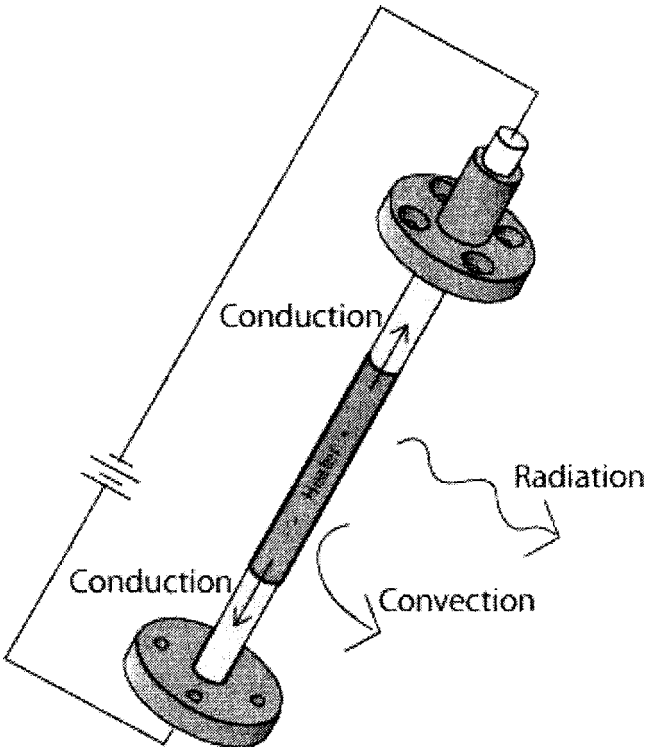

Fig. 2 Experimental apparatus and heat loss mechanisms

fluctuate more than ±0.1°C over a 5 min period). The data acquisition system was turned on and sampled temperature, pressure and power signals at 0.88 Hz. A routine in the LabVIEW buffered the data (106 unique points), performed appropriate data reductions and statistics before logging results in an excel spreadsheet. The wind tunnel damper was opened, increasing Reynolds number by about 3000, and the next set of data was logged when steady state conditions prevailed. This procedure was repeated until a Reynolds number of about 40,000 was reached.

4 Heat Loss Estimation

Heat loss from the vertical pipe due to conduction through the Teflon mounts was estimated as follows. During no flow conditions an energy balance on the vertical pipe in Fig. 2 indicates that the heat input to the polished copper pipe is lost by three mechanisms (i.e., conduction, natural convection, and radiation). Since this study is focused on quantifying heat transferred by convection and radiation it is necessary to isolate the conduction term (i.e., heat loss). Therefore, small amounts of heat were supplied to the bare pipe and surface temperatures were measured. Natural convection was estimated using the empirical relation from Ref. [5] for a flat plate

$$\bar{\mathrm{Nu}}_L = 0.68 + \frac{0.670\mathrm{Ra}_L^{1/4}}{\left[1+\left(\frac{0.492}{\mathrm{Pr}}\right)^{9/16}\right]^{4/9}} \tag{1}$$

Heat transfer enhancement due to the pipe curvature was accounted for by applying the results from an investigation of laminar-free convection from the outer surface of a slender vertical cylinder [6]. The works provides a convenient expression to account for the transverse curvature influence of the pipe on heat transfer. Radiation from the pipe was determined from Ref. [7] using

$$Q_{\mathrm{rad}} = \sigma\varepsilon A(T_s^4 - T_\infty^4) \tag{2}$$

where copper emissivity is equal to 0.03. The difference between the heat supplied and heat lost by natural convection plus radia-

Table 2 Data acquisition system

Measurement	Sensor	I/O module	Sample rate (Hz)	Uncertainty
Mean surface temperature	(6) Type *K* thermocouples (Omega TT-K-36-25)	FP-TC-120 (National Instruments)	0.88	±2.1 °C (max) ±1.1 °C (min)
Ambient temperature	(1) Type *K* thermocouple (Omega TT-K-20-25)	FP-TC-120 (National Instruments)	0.88	±0.5 °C
Air velocity	(1) Pitot-static tube & pressure transducer (Omega PX278 05D5V)	FP-AI-110 (National Instruments)	1.9	±0.55 m/s (max) ±0.36 m/s (min)
Pressure drop	(2) Static pressure ports & pressure transducer (Omega PX277 01D5V)	FP-AI-110 (National Instruments)	1.9	±3.2 Pa
Power	(1) dc signal rectifier	FP-AI-110 (National Instruments)	1.9	±0.2 W

tion is the heat lost by conduction. Conduction heat losses from the bare copper pipe were plotted as a function of mean surface temperature and a least-square fit was obtained. The heat losses were then subtracted from the heat input during forced convection experiments at corresponding values of surface temperature.

Several different geometric arrangements were investigated in this experiment. Figure 3(*a*) presents the bare copper pipe. Figure 3(*c*) illustrates the dimensions of the large and small diameter HTC sleeves with the z direction of HTC foam indicated. Dimensions of the large and small diameter HTC Fins are presented in Fig. 3(*d*) with z direction indicated. An aluminum finned copper pipe was also investigated and its dimensions are presented in Fig. 3(*b*).

The copper pipe dimensions remained constant for all cases studied (i.e., o.d. 15.875 mm, length 152.2 mm). For each of these cases the nondimensional parameter, Nusselt number, is calculated in relation to Reynolds number. The mean Nusselt number is defined as

$$\bar{\mathrm{Nu}} = \frac{\bar{h}D}{k} \tag{3}$$

where D is the outside diameter of the copper pipe and k is the thermal conductivity of air at the film temperature. For the sake of comparison between different cases, the variable D remains constant regardless of the material attached to the pipe surface. Mean heat transfer coefficient is based on Newton's law of cooling.

$$\bar{h} = \frac{Q}{\pi DL(\overline{T_s} - T_\infty)} \tag{4}$$

This calculation assumes isothermal surface temperature. Ambient air temperature is measured inside the wind tunnel, upstream of the heated pipe. Conduction losses are accounted for in the heat input value, Q. In order to evaluate the influence of external surface area on Nusselt number a surface area coefficient, λ, was defined

$$\lambda = \frac{\text{Surface Area}_{\text{porouslayer}}}{\text{Surface Area}_{\text{barepipe}}} \tag{5}$$

$\text{SurfaceArea}_{\text{porouslayer}}$ is defined as the external surface of porous material and pipe exposed to air. The Reynolds number was calculated as

$$\mathrm{Re} = \frac{u_\infty D}{\nu} \tag{6}$$

where kinematic viscosity is evaluated at the film temperature. The range of Reynolds numbers encountered in this study was 7000–40,000. All primary variables (i.e., T_s, T_∞, Q, and u_∞) are time averaged over a 2 min interval.

In order to verify results obtained with the methodology and apparatus described above, experimental results for Nusselt number from a bare pipe were compared with empirical predictions [5,8]. Experimental results illustrated in Fig. 4 show excellent agreement with empirical predictions over the studied range of Reynolds numbers tested.

5 Results and Discussion

In order to test the repeatability of measurements, surface temperature readings were taken on different days for the small diameter HTC fins. Results are plotted versus Reynolds number in Fig. 5. These results indicate that the maximum deviation between two sets of data is less than 3%.

The length-averaged surface temperature of the pipe, mean Nusselt number, and pressure drop versus Reynolds number are presented in Figs. 6(*a*)–6(*c*) respectively, for all cases studied. The length-averaged surface temperature is based on the normalized integration of temperature along the pipe length. Figure 6(*a*) illustrates that the pipe surface temperature decreases with increasing Reynolds number as well as the addition of porous material or aluminum fins to the pipe surface. The aluminum fins achieved the largest temperature drop relative to the bare pipe. These results also indicate that increasing the diameter of the porous layers reduces the pipe surface temperature, which consequently increases the Nusselt number and heat transfer rate.

Results presented in Fig. 6(*b*) indicate that Nusselt number increases with Reynolds number for all cases studied. The aluminum fins achieved a Nusselt number of about nine times greater than the bare pipe which is three times greater than the large diameter HTC fins. The heat transfer enhancement of the aluminum fins is less than the increase in its surface area (13.7 times).

The low values of Nu observed for the HTC foam cases suggest that fluid flow is restricted to the external surface of the porous layer and is not penetrating the HTC foam. The low permeability value presented in Table 1 also indicates that resistance to flow within the porous medium is very high. This reduces or even eliminates convective heat transfer at the pipe surface, meaning that convective heat transfer is restricted to the external surface of

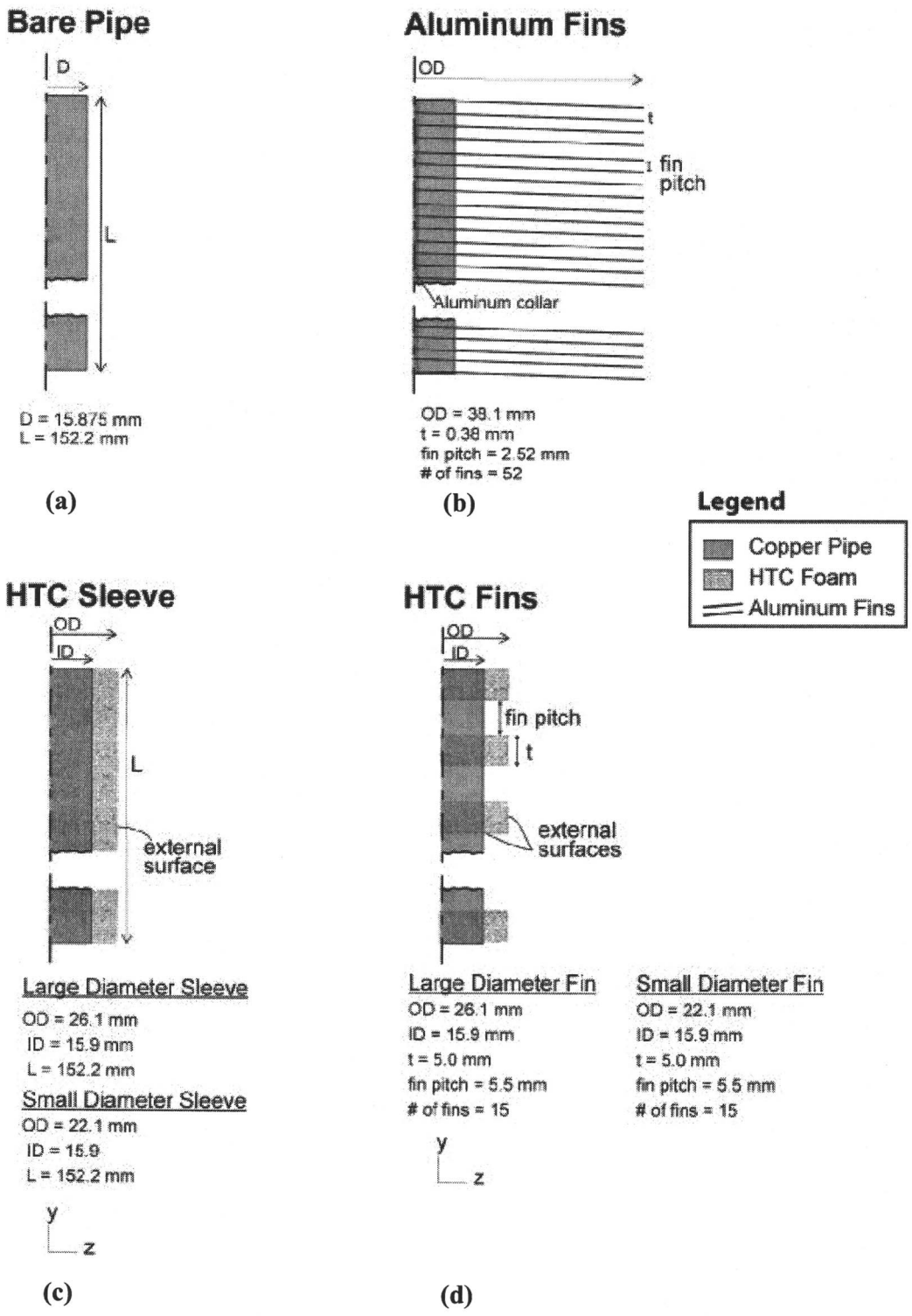

Fig. 3 (*a*)–(*d*) **Geometric details of a bare copper pipe, aluminum fins, HTC sleeves, and HTC fins, respectively**

the porous layer. The small increases in heat transfer rate achieved by the HTC foam are primarily due to the increase in fin surface area. Thus the HTC fins have higher Nusselt numbers than the HTC sleeves.

Radiation has only a minor influence on Nusselt number accounting for 4%, 2%, and 1% of the total heat transfer for HTC sleeves, HTC fins, and aluminum fins, respectively. Therefore, heat transfer enhancement is primarily due to larger surface areas exposed to forced convection. The contribution of radiation relative to overall heat transfer for the HTC sleeves was estimated using Eq. (1), while a more elaborate analysis utilizing the net radiation method [9] was employed to estimate radiation from the two finned cases.

Forced convection heat transfer enhancement, defined as the

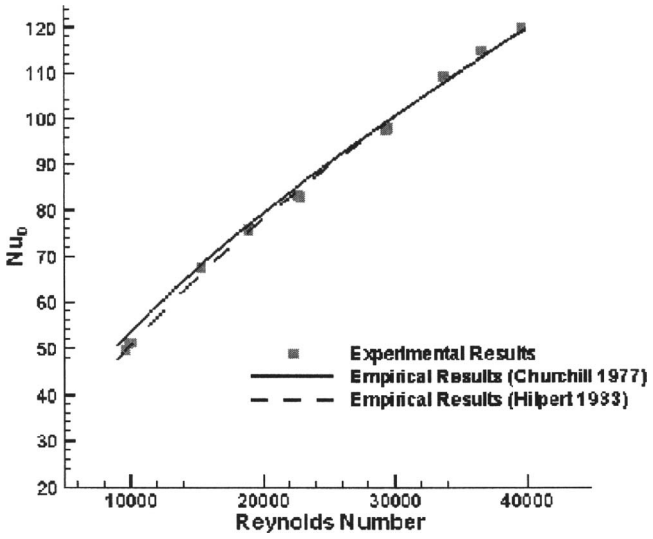

Fig. 4 Comparison of experimental and empirical forced convection results for a bare pipe in cross flow

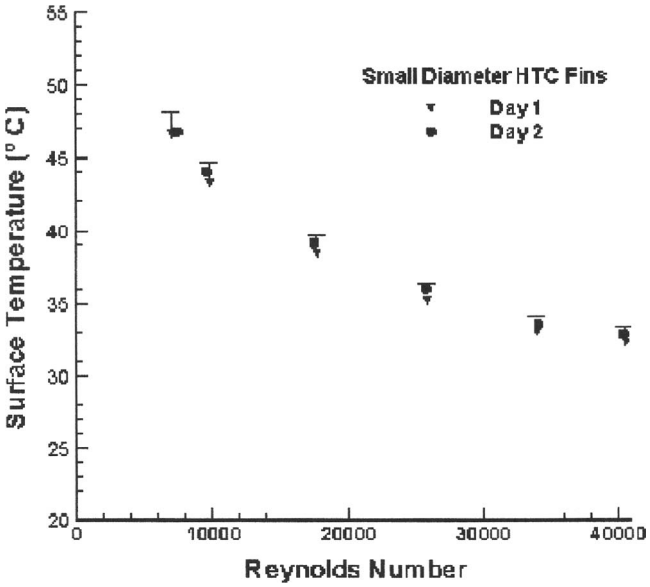

Fig. 5 Repeated measurement of surface temperature to confirm consistency of temperature measurements

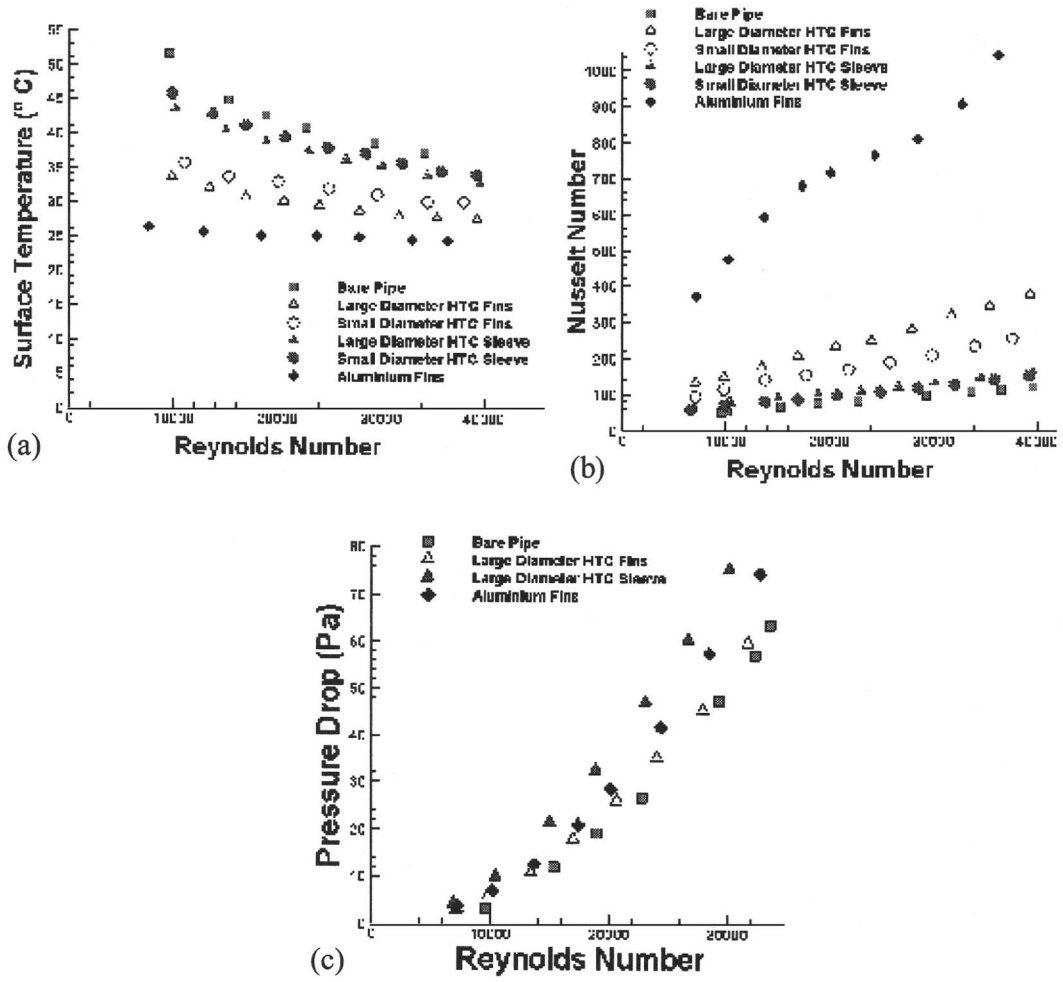

Fig. 6 (*a*)–(*c*) Variation of mean surface temperature (°C), mean Nusselt number, and pressure drop with Re, respectively

Table 3 Forced convection heat transfer enhancement and surface area ratios

	Heat transfer enhancement ratio (relative to the bare pipe)	λ (surface area coefficient)
Bare pipe	1	1
Large HTC fins (15)	3.05	2.65
Small HTC fins (15)	2.2	1.93
Large HTC sleeve	1.4	1.64
Small HTC sleeve	1.3	1.40
Aluminium fins (52)	9.1	13.69

ratio of mean Nusselt number to bare pipe Nusselt number, for each case studied is presented in Table 3. The only scenarios in which heat transfer enhancement exceeds the corresponding increase in surface area happen for HTC fins. This observation suggests that it may be possible for HTC fins to achieve the same performance as aluminum fins if a greater surface area ratio was designed for the HTC fins.

Figure 6(*c*) indicates that the largest pressure drop observed, from vertical pipe assemblies in an otherwise unobstructed wind tunnel, was produced by the large diameter HTC sleeve. This observation suggests that very little air flows through the carbon foam and that it acts like a "solid" blunt body. The aluminum fins produced less pressure drop than the large diameter HTC sleeve even though it has a much greater surface area. The HTC fins produce less pressure drop than both the HTC sleeve and the aluminum fins.

6 Uncertainty

The uncertainty associated with Nusselt numbers and pressure drop are presented in Table 4. These values are based on the measurement uncertainty methodology published in Ref. [10]. Uncertainty values are given for both high and low Reynolds numbers and represent maximum and minimum errors. The uncertainty associated with Reynolds number are 4.1% at low Re and 1.4% at high Re. The range of uncertainties produced by the equipment, methodology, and data reduction is reasonable for an experimental investigation. The maximum errors encountered for forced convection do not exceed 21% (with 95% confidence) of the measured values.

7 Conclusions

Test results for a bare pipe validated the methodology and assumptions employed during apparatus design and construction. Subsequent testing of HTC foam cases yielded results for variations in length-averaged surface temperature, mean Nusselt number, and pressure drop for forced flow conditions. HTC foam results were compared to corresponding results for aluminum fins and the merits of each were discussed.

Several conclusions can be made regarding the application of HTC foam layers in forced convection:

1. Nusselt number increased as HTC foam surface area increased;
2. The influence of radiation on overall heat transfer rate was very small;
3. HTC sleeves produced the highest pressure drop across the test section and behave like a "solid" blunt body. Low permeability of the porous layer presents a large resistance to fluid flow inside the porous medium and especially near the pipe wall, thus reducing or even eliminating convective heat transfer at the wall; and
4. Therefore, high-velocity air flow is restricted to the external surface of the porous layer. It is likely that a no-slip boundary condition exists at the external surface with boundary layer development and convective heat transfer similar to that occurring on a solid blunt body.

The performance of HTC foam was compared to that of aluminum fins:

1. The aluminum finned pipe achieved the highest Nusselt number of the cases studied; about three times greater than the best HTC foam case;
2. However, the aluminum fins provide less heat transfer enhancement than their surface area would indicate; and
3. The pressure drop due to aluminum fins is larger than HTC fins but less than HTC sleeves.

Given the forced convection experimental results obtained in this study, aluminum fins are the most suitable medium for use in cross-flow heat exchangers.

Nomenclature

A_s = surface area
D = outside diameter
$\bar{h}$ = mean convective heat transfer coefficient
k = thermal conductivity
L = pipe length
$\overline{\mathrm{Nu}}_D$ = mean Nusselt number for forced convection
Pr = Prandtl number
p = power
Q = heat transfer rate
R = electrical resistance
Re = Reynolds number
T_f = film temperature (average between $\bar{T}_s$ and T_∞)
$\bar{T}_s$ = length-averaged surface temperature
T_∞ = ambient temperature
u_∞ = free stream velocity
V_s = supplied power voltage

Greek Symbols

ε = surface emissivity coefficient
λ = surface area ratio
ν = kinematic viscosity (m^2/s)

Table 4 Uncertainty associated with forced convection Nusselt numbers

	Nusselt uncertainty at low Re (%)	Nusselt uncertainty at high Re (%)	Pressure drop uncertainty at low Re (%)	Pressure drop uncertainty at high Re (%)
Large diameter HTC sleeve	9.1	14.9	12.8	1.5
Small diameter HTC sleeve	8.5	14.7	14.4	1.5
Large diameter HTC fins	10.1	16.5	16.0	1.5
Small diameter HTC fins	9.1	15.0	15.5	1.5
Aluminium fins	15.8	20.9	15.6	1.5
Bare pipe	8.1	14.7	20.0	1.5

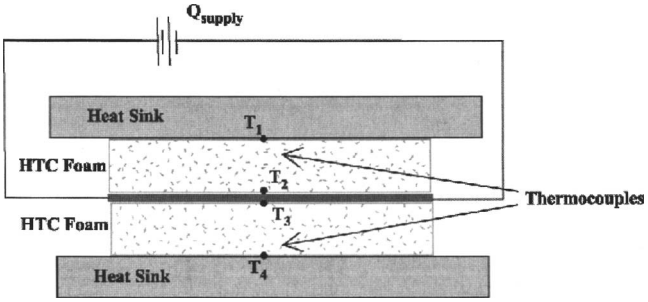

Fig. 7 Experimental apparatus for HTC foam conductivity analysis

Appendix A: Effective Thermal Conductivity of HTC Foam

The experimental apparatus used to determine effective conductivity of HTC foam, fully saturated with air, is based on the steady state, one-dimensional energy equation

$$\frac{d}{dx}\left(k_{\text{eff}}\frac{dT}{dx}\right)=0 \tag{A1}$$

The boundary conditions for this equation are achieved by heating one HTC foam surface and cooling the other in the plane of interest with insulation on all other sides. Thus we have constant heat flux on one surface and isothermal conditions on the other surface

$$\text{at } x=0; \quad -k_{\text{eff}}A_s\frac{dT}{dx}=q_{\text{supply}} \tag{A2}$$

$$\text{at } x=L; \quad T=T_s \tag{A3}$$

Solving the energy equation with boundary conditions (A2) and (A3) yields a relationship for temperature as a function of position within the porous medium

$$T(x)=\frac{q_{\text{supply}}}{2A_sk_{\text{eff}}}(L-x)+T_s \tag{A4}$$

This equation, using experimental data for temperature at $x=0$, can be rearranged to provide an expression for power input and effective conductivity, k_{eff}

$$q_{\text{supply}}=\frac{k_{\text{eff}}A_s(T_0-T_s)}{L} \tag{A5}$$

$$k_{\text{eff}}=\frac{q_{\text{supply}}L}{A_s(T_0-T_s)} \tag{A6}$$

To minimize heat loss and ensure one-dimensional 1D conduction, the heat source was "sandwiched" between two samples of HTC foam as illustrated in Fig. 7. Metal blocks were placed on the external surfaces (top and bottom) to provide uniform heat sinks. The heat supplied to the system is divided between top and bottom HTC sample and Eqs. (A5) and (A6) are modified accordingly

$$q_{\text{supply}}=q_{\text{up}}+q_{\text{down}}=\frac{K_{\text{eff}}A_s(T_2-T_1)}{L}+\frac{K_{\text{eff}}A_s(T_3-T_4)}{L} \tag{A7}$$

$$k_{\text{eff}}=\frac{q_{\text{supply}}L}{A_s(T_2-T_1)+A_s(T_3-T_4)} \tag{A8}$$

Equation (A8) is used with experimental values for temperature and heat input in Labview to calculate effective thermal conductivity. Because the material is not isotropic, conductivity is determined for both the z plane and the x-y plane.

An important phenomenon to understand when measuring heat transfer in a composite system is thermal contact resistance at the material interfaces. Air pockets and larger porosity exists at the HTC foam–solid interface. Because air conductivity is much less than HTC foam conductivity, there is greater resistance to heat transfer at these interfaces. To minimize this phenomenon, "thermal grease" (i.e., Dow 340) is used to fill void spaces and ensure good contact.

In addition, the apparatus was designed to measure conductivity of the plane orientated in the vertical direction. The vertical direction was chosen because it minimizes natural convection within the porous medium.

A.1 Procedures

Procedures for a typical experimental run are as follows. The appropriate HTC foam plane was chosen and installed as illustrated in Fig. 7 with insulation applied to all surfaces except those in the plane of 1D conduction. A constant power supply (50 W) to the heating cartridge was switched on. The apparatus was left running for approximately 4 h to reach thermal steady state (achieved when the surface temperatures did not fluctuate more than ±0.05°C over a 10 m period). The data acquisition system was turned on and sampled the temperature, and power signals at 2 Hz. One hundred sample values were acquired. LabVIEW calculated effective conductivity using mean values for power input and temperature.

A.2 Results

Results for effective conductivity of the anisotropic porous medium, HTC foam, are presented in Table 5. These results were measured when the HTC foam was heated to 90–100°C. Error is based solely on bias uncertainties.

Table 5 Effective thermal conductivity for HTC foam

Plane	Effective conductivity (W/mK)	Error (W/mK)
Z	79.7	±11.9
X-Y	39.1	±3.1

Appendix B: Permeability of HTC Foam

B.1 Theoretical Background

Calculation of permeability follows the methodology proposed by Antoche et al. [11] and the Forchheimer-extended Darcy equation presented by Joseph et al. [12]. That is, the steady-state unidirectional pressure drop across a porous medium, fully saturated with a Newtonian incompressible fluid, can be obtained from

$$\frac{\Delta p}{L}=\frac{\mu}{K}v_D+\rho\frac{C_F}{\sqrt{K}}v_D^2 \tag{B1}$$

Equation (B1) can be re-written as

$$\frac{\Delta p}{L}=\alpha v_D+\beta v_D^2 \tag{B2}$$

where C_F=Forchheimer coefficient; K=permeability (m^2); L=length of the sample (m); Δp=pressure drop across porous medium (Pa); v_D^{nu}=Darcy velocity (m/s); ρ=fluid density (kg/m^3); μ=fluid dynamic viscosity (m^2/s); $\alpha=\mu/K$; and $\beta=\rho C_F/\sqrt{K}$.

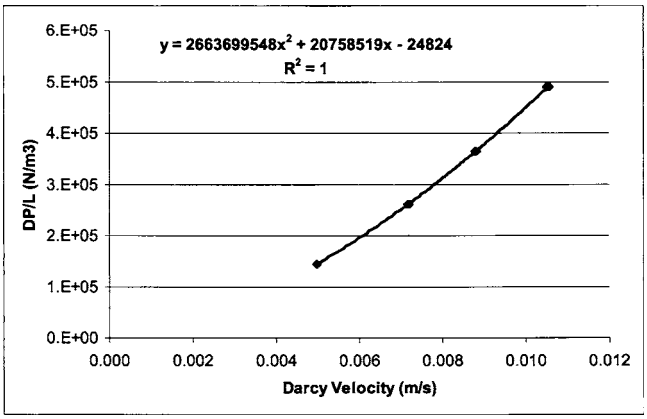

Fig. 8 Pressure drop versus Dacry velocity in HTC foam sample

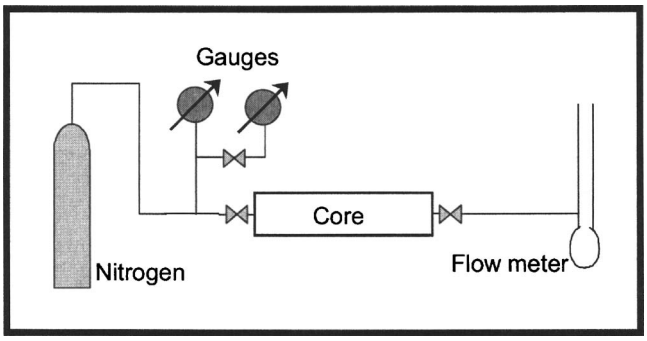

Fig. 9 Schematic of apparatus for gas permeability measurement

Coefficients α and β can be determined from experimental data for pressure drop and flow rate. Delta P normalized along the sample length is plotted against Darcy velocity in Fig. 8. Darcy velocity is defined as the volumetric flow rate divided by the HTC foam cross-sectional area. Volumetric flow is determined at the experimental inlet pressure (i.e., 33.85 kPa). From Fig. 8, a second-order polynomial function is generated using the least squares curve fitting technique. α and β are simply the coefficients of the first-order and second-order velocity terms. Permeability and Forchheimer term can then be calculated.

B.2 Procedures

Permeability was measured on a cylindrical core plug cut from the HTC foam. The plug of known dimensions is fully saturated with nitrogen, confined axially by a rubber sleeve and inserted into a core holder. Inlet and outlet ports are attached and the flow rate and pressure drop are measured. The apparatus used for this experiment is illustrated in Fig. 9.

B.3 Results

The permeability of the HTC foam sample was found to be 7.5×10^{-13} m^2, while the Forchheimer term was found to be 604.

References

[1] Vafai, K., and Kim, S., 1990, "Analysis of Surface Enhancement by Porous Substrate," ASME J. Heat Transfer, **112**, pp. 700–706.

[2] Angirasa, D., 2002 "Experimental Investigation of Forced Convection Heat Transfer Augmentation with Metallic Fibrous Materials," Int. J. Heat Mass Transfer, **45**, pp. 912–922.

[3] Pavel, B., and Mohamad, A. A., 2004, "An Experimental and Numerical Study on Heat Transfer Enhancement for Gas Heat Exchangers Fitted with Porous Media," Int. J. Heat Mass Transfer, **47**, 4939–4952.

[4] Gallego, N., and Klett, J., 2003, "Carbon Foams for Thermal Management," Carbon, **41**(7), pp. 1461–1466.

[5] Churchill, S., and Chu, H., 1975, "Correlating Equations for Laminar and Turbulent Free Convection from a Vertical Plate," Int. J. Heat Mass Transfer, **18**, pp. 1323–1329.

[6] Sparrow, E. M., and Gregg, J. L., 1956, "Laminar Free Convection from a Vertical Plate with Uniform Surface Heat Flux," Trans. ASME, **78**, pp. 435–440.

[7] Incropera, F., and DeWitt, D., 2002, *Introduction to Heat Transfer*, 4th ed., Wiley, New York, pp. 748–768.

[8] Hilpert, R., 1933, Forsch. Geb. Ingenieurwes., **4**, p. 215.

[9] Siegel, R., and Howell, J. R., 1971, "Thermal Radiation Heat Transfer," *Radiation Transfer with Absorbing, Emitting, and Scattering Media*, NASA SP 164, Vol. 3, New York.

[10] Abernethy, R., Benedict, R., and Dowdell, R., 1985, "ASME Measurement Uncertainty," J. Fluids Eng., **107**, pp. 161–164.

[11] Antohe, B., Lage, J., Price, D., and Weber, R., 1997, "Experimental Determination of Permeability and Inertia Coefficients of Mechanically Compressed Porous Matrices," ASME J. Fluids Eng., **119**, pp. 404–412.

[12] Joseph, D., Nield, D., and Papanicoulaou, G., 1982, "Nonlinear Equation Governing Flow in a Saturated Medium," Water Resour. Res., **18**(4), pp. 1049–1052.

Treatment of Wall Emission in the Narrow-Band Based Multiscale Full-Spectrum *k*-Distribution Method

Liangyu Wang

Michael F. Modest[1]
Fellow ASME
e-mail: MFModest@psu.edu

Department of Mechanical and Nuclear Engineering,
The Pennsylvania State University,
University Park, PA 16802

The multiscale full-spectrum k-distribution (MSFSK) method has become a promising method for radiative heat transfer in inhomogeneous media. In this paper a new scheme is proposed to extend the MSFSK's ability in dealing with boundary wall emission by distributing this emission across the different gas scales. This scheme pursues the overlap concept of the MSFSK method and requires no changes in the original MSFSK formulation. A boundary emission distribution function is introduced and two approaches of evaluating the function are outlined. The first approach involves line-by-line integration of the spectral absorption coefficients and is, therefore, impractical. The second approach employs a narrow-band k-distribution database to calculate all parameters as in the original narrow-banded based MSFSK formulation and is, therefore, efficient. This distribution scheme of wall emission is evaluated and the two approaches are compared by conducting sample calculations for radiative heat transfer in strongly inhomogeneous media using both the MSFSK method and the line-by-line method.
[DOI: 10.1115/1.2717936]

Keywords: k-distribution method, inhomogeneous gas mixture, multiscale approach, wall emission

Introduction

Because of the strongly irregular spectral variations of gas absorption coefficients, high spectral resolution calculations (often referred to as line-by-line, LBL, approach) have to be generally invoked to accurately predict radiative heat transfer in participating media. LBL calculations require millions of evaluations of the radiative transfer equation (RTE) and, therefore, consume an enormous computational effort. On the other hand, the *k*-distribution method [1,2] reorders the absorption coefficients into monotonic *k*-distributions and, thus, greatly reduces the computational cost by using only ten or fewer quadrature evaluations of the RTE. The development of the full-spectrum *k*-distribution method (FSK) [3] further facilitates the application of the method to practical problems.

Challenges remain, however, in applying the FSK method to inhomogeneous emitting and absorbing mixtures. Inhomogeneities in total pressure, temperature, and component gas mole fraction (partial pressure) change the spectral distribution of the absorption coefficient, which is critical to the FSK reordering process. The effect of varying total pressure on the FSK reordering process is relatively small, as evidenced by the success of applying the correlated-*k* method in the field of meteorology, where strong total pressure variations occur while temperatures stay relatively uniform [1,4,5]. The effects of varying temperature and varying gas concentrations can be substantial, as recognized by Rivière et al. [6–8] and by Modest and Zhang [3]. They are the focus of further FSK developments.

The multigroup FSK (MGFSK) [9] and multiscale FSK (MSFSK) [10] have been developed to deal with the temperature and partial pressure inhomogeneities. The MGFSK method arranges spectral positions into M separate groups according to their temperature and partial pressure dependencies. There is no overlap among different groups and, therefore, the method requires only $M \times N$ (N being the number of quadrature points) RTE evaluations without any further approximation. Although the MGFSK method can achieve great accuracy for individual gases, groups from different gases are incompatible and it appears impossible to apply the MGFSK method to problems involving inhomogeneous mixtures.

The MSFSK method, on the other hand, groups individual spectral lines comprising the absorption coefficient into M separate scales according to their temperature dependence: The overlap in spectrum between different scales is treated in an approximate way so that $M \times N$ RTE evaluations are required. The MSFSK method can also treat the absorption coefficient of an individual species in a mixture as one of its scales. It has been found that in addition to eliminating the error caused by partial pressure (gas concentration) inhomogeneities, breaking up a gas mixture into gas scales reduces the error caused by temperature inhomogeneities [11]. The multiscale approach is therefore preferred in the treatment of mixture inhomogeneities with the FSK method.

One of the essential features of the MSFSK method is the overlap coefficient λ, and this coefficient is determined such that the radiative transfer in a homogeneous medium is predicted exactly using the MSFSK scheme. At the present state of development, however, the MSFSK method, unlike the single scale FSK method [3], and the spectral-line-based weighted-sum-gray-gases method [12,13], is limited to media surrounded by cold, nonemitting walls. It is desirable to include wall emission in the general MSFSK formulation, so that the method can also handle situations in which wall emission plays an important role in the radiative heat transfer.

It is the purpose of this paper to introduce an effective scheme to account for gray wall emission in the MSFSK method. The scheme pursues the concept of the overlap coefficient and keeps

[1]Corresponding author.
Contributed by the Heat Transfer Division of ASME for publication in the JOURNAL OF HEAT TRANSFER. Manuscript received October 18, 2005; final manuscript received September 27, 2006. Review conducted by Bakhtier Farouk.

the original MSFSK formulation unchanged. A boundary emission distribution function is introduced. To keep the method as practical as the original narrow-band based MSFSK method, a formula is derived that employs the same database of narrow-band k-distributions to calculate the distribution function. The mathematical development for the boundary scheme is described, followed by validation of the approach. Sample calculations are performed for a mixture with extreme inhomogeneities in gas concentration and temperature, and the results are compared with LBL calculations.

Theoretical Development

MSFSK Formulation With Boundary Emission. Although the following development can easily be extended to include gray absorbing and scattering particles, for clarity a medium consisting of a mixture of molecular gases is considered, and the RTE is then written as [14]

$$\frac{dI_\eta}{ds} = \kappa_\eta(\boldsymbol{\phi})(I_{b\eta} - I_\eta) \tag{1}$$

subject to the boundary condition

$$\text{at } s=0: \quad I_\eta = \epsilon I_{b\eta w} + \frac{1-\epsilon}{\pi}\int_{2\pi} I_\eta |\hat{n}\cdot\hat{s}| d\Omega \tag{2}$$

Here, I_η is the spectral radiative intensity, κ_η the absorption coefficient, $I_{b\eta}$ the spectral blackbody intensity (or Planck function), and wave number η is the spectral variable. The vector $\boldsymbol{\phi}$ contains state variables that affect κ_η, which include temperature T, total pressure P, and gas mole fractions $\boldsymbol{x}$: $\boldsymbol{\phi}=(T,P,\boldsymbol{x})$. The boundary wall has been assumed to be gray with ϵ being the emittance, $\hat{n}$ the surface normal, $\hat{s}$ the unit direction vector of incoming ray radiation, and Ω the solid angle. If one separates the contributions to κ_η from the M component gases and breaks up the radiative intensity I_η accordingly, i.e.,

$$\kappa_\eta = \sum_{m=1}^{M} \kappa_{m\eta} \quad I_\eta = \sum_{m=1}^{M} I_{m\eta} \tag{3}$$

then the RTE (1) is transformed into M component RTEs, one for each gas or scale. In this paper, we will deal only with the treatment of concentration inhomogeneities, i.e., each gas species will be treated as a single scale. Temperature inhomogeneities will be addressed in a follow-up paper. Then the RTE for each gas scale is

$$\frac{dI_{m\eta}}{ds} = \kappa_{m\eta}(\boldsymbol{\phi})I_{b\eta} - \kappa_\eta(\boldsymbol{\phi})I_{m\eta} \quad \text{for } m=1,\ldots,M \tag{4}$$

It is observed that, physically, the intensity $I_{m\eta}$ for the mth scale is due to emission from the mth gas species but subject to absorption from all gases.

It is important to note that in Eq. (4), if there is no wall emission, the spectral locations where κ_η contributes to the absorption of $I_{m\eta}$ (i.e., absorption by all the scales) are only those wave numbers for which $\kappa_{m\eta}$ is nonzero. Therefore, the overlap region is only a subset of those wave numbers with $\kappa_{m\eta}\neq 0$, across which absorption from other gases occurs as well. The original MSFSK formulation takes advantage of the fact that the overlap regions for each scale are relatively small compared to the total emission/absorption spectrum of each scale, and the fact that the absorption coefficients in the overlap regions are mostly small. If there is wall emission, however, absorption by other than the emitting scale will take place not just over the small overlap regions but across the entire spectrum. Therefore, the underlying justification of the MSFSK scheme to treat the absorption by other scales in the overlap region in an approximate fashion is no longer valid, and large errors may occur.

There are several strategies to deal with wall emission. For example, an additional scale could be used, but this would require N additional RTE evaluations, and would complicate the accurate evaluation of an appropriate overlap coefficient. Here we propose a strategy consistent with the logic of the MSFSK method and requiring no additional computational cost: Wall emission is distributed across all scales according to the absorption coefficient of each scale, that is,

$$\text{at } s=0: \quad I_{m\eta} = \frac{\kappa_{m\eta}(\boldsymbol{\phi}_0)}{\kappa_\eta(\boldsymbol{\phi}_0)}\epsilon I_{b\eta w} + \frac{1-\epsilon}{\pi}\int_{2\pi} I_{m\eta}|\hat{n}\cdot\hat{s}|d\Omega \tag{5}$$

where $\boldsymbol{\phi}_0$ denotes the reference state of the mixture. Note that the sum of Eq. (5) over all the scales reduces to Eq. (2). With such distribution, wall emission exists within each scale only at the spectral locations where medium emission takes place, and, therefore, the overlap approximation of the MSFSK method remains valid.

The overlap coefficient in the MSFSK formulation is determined by considering a homogeneous medium without wall emission. Additional considerations are required to include wall emission. We now apply the FSK scheme [15] to the RTE of each scale: First, Eq. (4) is multiplied by Dirac's delta function $\delta(k_m - \kappa_{m\eta}(\boldsymbol{\phi}_0))$, followed by division with the k-distribution of the mth scale, or

$$f_m(T_0,\boldsymbol{\phi}_0,k_m) = \frac{1}{I_b(T_0)}\int_0^\infty I_{b\eta}(T_0)\,\delta(k_m - \kappa_{m\eta}(\boldsymbol{\phi}_0))d\eta \tag{6}$$

where, $\boldsymbol{\phi}_0$ and T_0 refer to a reference state. The resulting equation is then integrated over the whole spectrum, leading to

$$\frac{dI_{mg}}{ds} = k_m(T_0,\boldsymbol{\phi},g_m)a_m I_b - \lambda_m I_{mg} \quad \text{for } m=1,\ldots,M \tag{7}$$

where

$$I_{mg} = \int_0^\infty I_{m\eta}\delta(k_m - \kappa_{m\eta}(\boldsymbol{\phi}_0))d\eta \Big/ f_m(T_0,\boldsymbol{\phi}_0,k_m) \tag{8}$$

$$g_m = \int_0^{k_m} f_m(T_0,\boldsymbol{\phi}_0,k)dk \tag{9}$$

$$a_m = \frac{f_m(T,\boldsymbol{\phi}_0,k_m)}{f_m(T_0,\boldsymbol{\phi}_0,k_m)} \tag{10}$$

$$\lambda_m I_{mg} = k_m(T_0,\boldsymbol{\phi},g_m)I_{mg} + \int_0^\infty \left(\sum_{n\neq m}\kappa_{n\eta}(\boldsymbol{\phi})\right) I_{m\eta} \times \delta(k_m - \kappa_{m\eta}(\boldsymbol{\phi}_0))d\eta \Big/ f_m(T_0,\boldsymbol{\phi}_0,k_m) \tag{11}$$

Here the correlated-k (FSCK) approach has been taken and $k_m(T_0,\boldsymbol{\phi},g_m)$ is the k-distribution of the absorption coefficient for the mth scale at state $\boldsymbol{\phi}$ using T_0 as the Planck function temperature [15]. Equation (11) defines the overlap coefficient, λ_m, which represents the overlap of the absorption coefficient of the mth scale, $\kappa_{m\eta}$, with those of all other scales. Overlap occurs only over a small part of the spectrum, and the overlap coefficients λ_m are in effect reordered absorption coefficients of the mth scale taking into account the overlap with all other scales. In the MSFSK approach, the λ_m are determined approximately, based on the argument that overlap effects between scales (individual gas species in this work) are relatively small.

Applying the same reordering procedure to the boundary condition (Eq. (5)), one obtains the reordered condition corresponding to Eq. (7):

$$\text{at } s=0: \quad I_{mg} = \mu_m \epsilon I_{bw} + \frac{1-\epsilon}{\pi}\int_{2\pi} I_{mg}|\hat{n}\cdot\hat{s}|d\Omega \tag{12}$$

where

$$\mu_m = \frac{1}{I_{bw}} \int_0^\infty \frac{\kappa_{m\eta}(\boldsymbol{\phi}_0)}{\kappa_\eta(\boldsymbol{\phi}_0)} I_{b\eta w} \delta(k_m - \kappa_{m\eta}(\boldsymbol{\phi}_0)) d\eta / f_m(T_0, \boldsymbol{\phi}_0, k_m) \tag{13}$$

Here μ_m is the boundary emission distribution function and can be evaluated from Eq. (13) without approximation.

Following the approach in the MSFSK method to determine the overlap coefficient, we consider the radiative intensity within a semi-infinite homogeneous gas mixture. To be consistent with the evaluation of λ_m for medium emission, the medium is assumed bounded by a black wall at a different temperature than that of the medium. The analytical solution to Eq. (7) for a homogeneous mixture bounded by a black wall may be written as

$$I_m = \int_0^1 I_{mg} dg = \int_0^\infty \mu_m I_{bw} \exp(-\lambda_m s) f_m(T, \boldsymbol{\phi}, k_m) dk_m + \int_0^\infty \frac{k_m}{\lambda_m} I_b [1 - \exp(-\lambda_m s)] f_m(T, \boldsymbol{\phi}, k_m) dk_m = I_{m1} + I_{m2} \tag{14}$$

where I_{m1} is short-hand for the first term (wall emission) in the second step, and I_{m2} for the second term (medium emission); the mixture temperature is T and the wall temperature is T_w.

The reordering of Eq. (4) can also be performed in terms of κ_η, which, for a homogeneous layer at temperature T, leads to

$$\frac{dI^*_{mg}}{ds} = \frac{k^*_m(T) I_b}{f(T, \boldsymbol{\phi}, k)} - k I^*_{mg} \quad \text{for } m = 1, \ldots, M \tag{15}$$

and the corresponding boundary condition,

$$\text{at } s = 0: \quad I^*_{mg} = \frac{k^*_m(T_w)}{k} I_{bw} / f(T, \boldsymbol{\phi}, k) + \frac{1 - \epsilon}{\pi} \int_{2\pi} I^*_{mg} |\hat{n} \cdot \hat{s}| d\Omega \tag{16}$$

where

$$f(T, \boldsymbol{\phi}, k) = \frac{1}{I_b(T)} \int_0^\infty I_{b\eta}(T) \delta(k - \kappa_\eta(\boldsymbol{\phi})) d\eta \tag{17}$$

$$I^*_{mg} = \int_0^\infty I_{m\eta} \delta(k - \kappa_\eta(\boldsymbol{\phi})) d\eta / f(T, \boldsymbol{\phi}, k) \tag{18}$$

$$k^*_m(T) = \frac{1}{I_b(T)} \int_0^\infty I_{b\eta}(T) \kappa_{m\eta} \delta(k - \kappa_\eta(\boldsymbol{\phi})) d\eta \tag{19}$$

The analytical solution to Eq. (15) for a homogeneous mixture bounded by a black wall is then written as

$$I^*_m = \int_0^1 I^*_{mg} dg = \int_0^\infty \frac{k^*_m(T_w)}{k} I_{bw} \exp(-ks) dk + \int_0^\infty \frac{k^*_m}{k} I_b [1 - \exp(-ks)] dk = I^*_{m1} + I^*_{m2} \tag{20}$$

where again I^*_{m1} abbreviates the first term (wall emission) in the second step, and I^*_{m2} the second term (medium emission).

The spectrally integrated intensity, I_m, must be equal to I^*_m. In the original MSFSK formulation there is no wall emission, and equating I_{m2} and I^*_{m2} leads to the determination of the overlap coefficient as [10,11]

$$\lambda_m = k \quad k_m f_m(T, \boldsymbol{\phi}, k_m) dk_m = k^*_m(k) dk \tag{21}$$

The overlap coefficient is then found implicitly from [10,11]

$$\int_0^{k_m} k'_m f_m(T, \boldsymbol{\phi}, k'_m) dk'_m = \int_0^{k' = \lambda_m} k^*_m(k') dk' \tag{22}$$

In the presence of wall emission, I_{m1} may, in general, not be equal to I^*_{m1} if λ_m is determined from Eq. (22), since the equation is derived from considering medium emission only. In addition, the evaluation of μ_m from Eq. (13) appears to be inconvenient. We can, however, modify the definition for μ_m, Eq. (13), such that I_{m1} equals I^*_{m1} and, therefore, total intensity I_m equals I^*_m for the homogeneous case with a wall temperature different from the medium temperature. Furthermore, the modified expression for μ_m can be evaluated easily, as shown in the following.

To equate I_{m1} and I^*_{m1}, the expression for I^*_{m1} is rearranged employing the approximation of λ_m, Eq. (21):

$$I^*_{m1} = \int_0^\infty \frac{k^*_m(T_w, k)}{k^*_m(T, k)} \frac{k^*_m(T, k)}{k} I_{bw} \exp(-ks) dk = \int_0^\infty \frac{k^*_m(T_w, \lambda_m)}{k^*_m(T, \lambda_m)} \frac{k_m}{\lambda_m(k_m)} f_m(T, \boldsymbol{\phi}, k_m) I_{bw} \exp(-\lambda_m s) dk_m \tag{23}$$

By comparison with the expression for I_{m1} in Eq. (14), it is clear that if

$$\mu_m = \frac{k^*_m(T_w, \lambda_m)}{k^*_m(T, \lambda_m)} \frac{k_m}{\lambda_m(k_m)} \tag{24}$$

then I_{m1} equals I^*_{m1}. Note that in the limit of $s = 0$,

$$\sum_m \int_0^\infty \mu_m f_m dk_m = \sum_m \int_0^\infty \frac{k^*_m}{k} dk = 1 \tag{25}$$

i.e., the modified definition of μ_m satisfies Eq. (13) in an integral sense.

In Eq. (24), the overlap coefficient λ_m must be calculated in any case with or without wall emission and it is determined implicitly from Eq. (22). A convenient way of calculating the left- and right-hand side of Eq. (22) using a database of narrow-band k-distributions has been developed [11]. For a mixture of two gases, Eq. (22) reduces to the following equation to determine, for example, the λ_1–k_1 relation for gas 1 [11]:

$$\sum_{i=1}^{N_{\text{nb}}} \frac{I_{bi}}{I_b} \int_0^{g_{1,i}(k_1)} k_{1,i} dg_{1,i} = \sum_{i=1}^{N_{\text{nb}}} \frac{I_{bi}}{I_b} \int_{g_{1,i}=0}^1 k_{1,i} g_{2,i}(\lambda_1 - k_{1,i}) dg_{1,i} \tag{26}$$

where $k_{1,i}$–$g_{1,i}$ is the k–g distribution for the ith narrow band, N_{nb} is the number of narrow bands comprising the entire spectrum, and the NB Planck function I_{bi} is defined as

$$I_{bi} = \int_{\Delta\eta i} I_{b\eta i} d\eta \tag{27}$$

A similar equation can be obtained for gas 2. In the narrow-band k–g database published by Wang and Modest [16], the data are organized in such a way that the narrow-band k–g pairs obtained from the database for a certain condition correspond to the quadrature points of a Gaussian quadrature scheme. Therefore, the integrals in Eq. (26) can be evaluated efficiently based on the narrow-band database.

For the ratio of k^*_m in Eq. (24), a formula that is similar to the evaluation of the right-hand side (RHS) of Eq. (26) can be derived to calculate k^*_m using the same narrow-band database. Alternatively, k^*_m can be determined by differentiating the RHS of Eq. (22), which must be calculated for the determination of λ_m. The alternative approach was found to be accurate and robust and was implemented as follows: The RHS is calculated from Eq. (26) for

a set of λ_m values using the narrow-band database; since it is a monotonically increasing function of λ_m, a monotonic cubic spline can be constructed readily; then the polynomial coefficients for the first-order term are the k_m^* for the corresponding λ_m values. Thus, with the above-noted considerations all terms in Eq. (24) can be evaluated efficiently from a narrow-band $k-g$ database. Note that k_m^* needs to be evaluated twice, at both T_w and T.

In summary, the wall emission distribution scheme, Eq. (5), introduces the boundary emission distribution function μ_m in the MSFSK formulation. The coefficient μ_m can be evaluated by two approaches: from the direct definition, Eq. (13), and from the modified definition, Eq. (24). MSFSK calculations using the directly calculated μ_m may not recover the LBL result for a homogeneous medium bounded by a gray wall at a different temperature from that of the medium, due to the approximation made for λ_m. In addition, the direct approach involves line-by-line integration of the absorption coefficient and is, therefore, impractical for engineering applications. On the other hand, MSFSK calculations using the modified μ_m from Eq. (24) recover the LBL result for homogeneous media with arbitrary boundary wall temperatures, since it is formulated to incorporate the approximation made for λ_m. In addition, the modified approach can utilize a database of narrow-band k-distributions and is, therefore, efficient for practical problems. While the direct μ_m does not depend on gas temperature, the modified μ_m does since it incorporates the temperature-dependent overlap coefficient, in order to ensure that the radiative heat transfer in a homogenous medium is predicted correctly. If the gas is nonisothermal, then the modified μ_m is evaluated at the reference temperature.

Validation of Approach. In order to verify the accuracy of the two methods to calculate the boundary emission distribution function μ_m, the radiative heat flux emerging from a homogeneous layer (by volume 20% CO_2, 20% H_2O, and 60% N_2) bounded by a gray, diffuse emitting wall is calculated by both the MSFSK and and the LBL method. LBL calculations provide the benchmark for the validation of the MSFSK method. In LBL calculations, the HITEMP [17] and CDSD [18] spectral databases are used for the absorption coefficients of H_2O and CO_2, respectively. In the MSFSK calculations, the $k-g$ distributions and the nongray stretching functions a_m are constructed directly from the spectral absorption coefficients; the reference states are determined according to the formulas in Modest and Zhang [3]. For the purpose of validation, the distribution function μ_m, from both the direct formula, Eq. (13), and the modified formula, Eq. (24), are calculated directly from the absorption coefficient of the medium. The same is true for the evaluation of the overlap coefficient λ_m. The layer has a thickness of 50 cm and the wall temperature varies from 300 K to 2000 K. The calculated nondimensional exiting heat fluxes and the percentage errors of the MSFSK calculations compared to the LBL results are plotted in Fig. 1 for a medium temperature of 1000 K. The error is defined as

$$\text{Error} = \frac{\text{MSFSK} - \text{LBL}}{\text{LBL}} \times 100\% \tag{28}$$

It is shown that the modified-μ_m MSFSK calculations (green dash-dot lines) show small (less than 0.5%) errors, indicating that the modified μ_m are correctly formulated. The MSFSK calculations using the direct μ_m function show slightly larger errors. Within the wall temperature range considered, however, the error of using the directly calculated μ_m is still reasonably small.

Sample Calculations

To evaluate the distribution strategy of treating wall emission in the MSFSK method, and to illustrate the performance of the two approaches of computing the boundary emission distribution function μ_m, a few sample calculations were performed. In all cases, a mixture of CO_2-H_2O-N_2 confined between a hot gray wall and a cold black wall was considered. The mixture was at a total pressure of 1 bar and consists of two different homogeneous layers (denoted as left and right layer/column). Both layers had a fixed width of 50 cm. The hot gray wall was on the left and its temperature varies from 300 K to 2000 K while the right wall was kept cold and black. The left layer contained 20% CO_2 and 2% H_2O, and the right layer contained 2% CO_2 and 20% H_2O (i.e., the compositions are switched). The radiative heat flux leaving from the right layer and the radiative heat source within the medium were calculated using the LBL method, the MSFSK method with the direct and modified μ_m, and the (single scale) full-spectrum correlated-k (FSCK) method. The FSCK method was included in the calculations to demonstrate the improvement made by the MSFSK method.

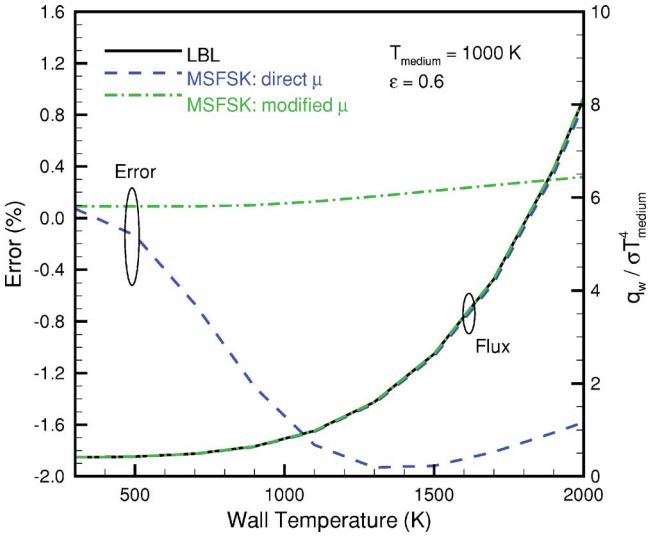

Fig. 1 Nondimensional heat flux leaving a homogeneous layer containing 20% CO_2 and 20% H_2O at 1000 K

In the MSFSK calculations, the direct μ_m were constructed from the medium absorption coefficient, while the modified μ_m were computed using the database of narrow-band $k-g$ distributions by Wang and Modest [16], as outlined in the previous section. When the direct μ_m were used in the calculation, all other parameters, such as the $k-g$ distribution, the stretching function a_m, and the overlap coefficient λ_m, were also constructed directly from the medium absorption coefficient. When the modified μ_m were used, they and all the other parameters were computed using the W&M narrow-band database [16]. In both FSCK and MSFSK calculations, the spectral integrations over g-space were performed using the trapezoidal rule together with all available data points in order to limit the error caused by numerical integration. Here 2000 data points were used in the FSCK and direct-μ_m MSFSK calculations, while only 128 points were available for the modified-μ_m MSFSK calculations, since the modified μ_m were constructed from the narrow-band database that contains at most 128 quadrature points for each of the narrow bands [16]. For practical applications of the MSFSK methods, an efficient quadrature scheme is desired, and therefore, a Gaussian quadrature scheme with 10 quadrature points was also employed for the modified-μ_m MSFSK calculations using the narrow-band database. The computational cost of FSK calculations include CPU time for both RTE solution and assembly of $k-g$ distributions from the narrow-band database. The MSFSK CPU time for RTE solutions will be M-fold (number of scales) larger than the FSCK CPU time, but remains only a tiny fraction of the LBL cost. Besides the assembly of $k-g$ distributions, the MSFSK method also needs to compute the medium and wall emission overlap coefficients. It was found in the following sample calculations that the

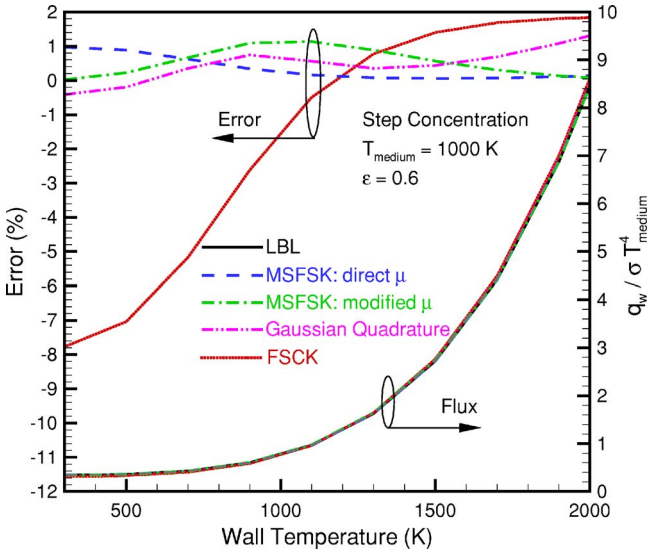

Fig. 2 Nondimensional heat flux leaving an inhomogeneous layer at 1000 K with step changes in mole fraction: 20% CO_2 and 2% H_2O in the left layer, with the composition switched in the right layer

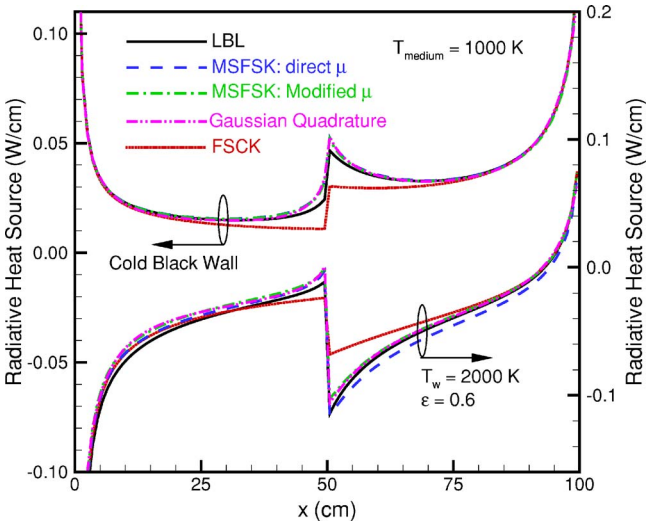

Fig. 3 Radiative heat source distribution for an inhomogeneous layer at 1000 K with step changes in mole fraction: 20% CO_2 and 2% H_2O in the left layer, with the composition switched in the right layer

computation of the medium and wall emission overlap coefficients each needs about the same CPU time as the assembly of $k-g$ distributions, which is also M-fold larger than that required by FSCK.

Figure 2 shows the calculated nondimensional radiative heat fluxes for the case of severe step changes in gas concentration. The temperature of both layers was at a uniform 1000 K. Also shown in the figure are the percentage errors of the MSFSK and FSCK calculations compared to LBL results. In the MSFSK calculations, both the direct- and modified-μ approaches give small errors of less than 2%, and the direct-μ approach performs slightly better than the modified-μ approach for higher wall temperatures. In comparison, the FSCK method incurs much larger errors for low wall temperature, although the error decreases as wall emission becomes dominant. The better performance of the MSFSK method over the FSK method shows that the multiscale scheme resolves the inhomogeneous problem due to partial pressure variations and the scheme is robust even under conditions of severe step changes. Figure 2 also demonstrates that the distribution scheme for wall emission and the formulation for the wall emission distribution function are successful.

The Gaussian quadrature evaluation with ten quadrature points, as also shown in Fig. 2, has the same order of accuracy as the direct integration. The choice of quadrature points, however, required some attention. In general, in a FSK calculation the quadrature points are chosen such that more points are distributed toward larger g-values (corresponding to large k-values), since the larger k-values usually determine radiative heat transfer rates if the optical thickness of the medium is small to moderate. In the cases when wall emission becomes dominant, the part of the spectrum corresponding to smaller k-values is nearly transparent to wall emission. This requires the quadrature points to be distributed toward the smaller g-values as well. In the sample calculation, a Gauss-Chebyshev quadrature scheme was used that places more points symmetrically toward both ends of the g-range, 0 and 1. This quadrature scheme gives errors of less than 2% compared to the LBL results for a large range of wall temperatures (300 K to 2000 K).

Figure 3 shows the distribution of radiation heat loss for the same inhomogeneous medium as used in the previous calculations. Two different boundary conditions, cold black and hot gray at 2000 K, for the left wall bounding the medium were considered. The distributions calculated again by LBL, MSFSK, and FSCK methods are compared in Fig. 3. Because of the step change in medium concentration, there is a discontinuity in the middle of the medium since H_2O is a stronger emitter and absorber than CO_2: without wall emission (upper jump) H_2O emits more energy than CO_2; with wall emission, H_2O absorbs more wall-emitted energy than CO_2. The FSCK method responds poorly to the step change in concentration and fails to capture the trend predicted by the LBL approach. The MSFSK methods, on the other hand, perform well in this severe case and follow closely the discontinuity caused by the step change in medium concentration. Note that, when radiative heat loss is calculated using Gaussian quadrature, the quadrature scheme need not put emphasis on the lower end of the g-values, since those spectral regions have small k-values and, therefore, negligible emission and absorption inside the medium. However, when radiation heat flux and heat source are calculated all at once, the quadrature scheme with emphasis on both ends of the g-values would be preferred.

Figure 4 shows the results for an even more severe case, in which a step change in temperature was added to the mixture's inhomogeneity together with step changes in gas concentration. The current MSFSK formulation does not deal with temperature inhomogeneities, which will be addressed in a follow-up paper. The error of the MSFSK method for media with temperature inhomogeneities has been discussed in the previous MSFSK development [11]. Here the focus is the treatment of boundary wall emission within the MSFSK method. It is seen from the figure that, even in the presence of a temperature inhomogeneity, the MSFSK method performs about five times better than the FSCK method, although, as expected, the advantage of the MSFSK method diminishes again as the wall temperature becomes large and wall emission dominates over medium emission. In the MSFSK calculations, the modified-μ approach performs equally well as the direct-μ approach, but it holds the advantage of efficiency derived from using a narrow-band $k-g$ distribution database.

Summary and Conclusions

In this paper a distribution scheme for the treatment of boundary wall emission within the MSFSK method has been proposed. This scheme is consistent with the overlap concept of the MSFSK method and requires no changes in the original MSFSK formulation. A boundary emission distribution function has been introduced and two approaches to evaluate the function have been

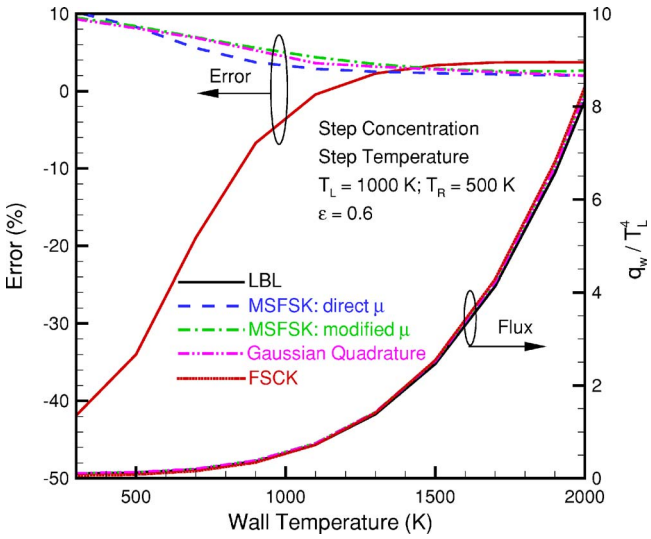

Fig. 4 Nondimensional heat flux leaving an inhomogeneous layer with step change in mole fraction and temperature: 20% CO_2 and 2% H_2O at 1000 K in the left layer and 2% CO_2 and 20% H_2O at 500 K in the right layer

derived: a direct approach and a modified approach. The wall emission distribution scheme and the two approaches were evaluated by performing sample calculations for radiative transfer in strongly inhomogeneous media. It was found that the distribution scheme successfully handled boundary wall emission of arbitrary temperature. The direct approach for the calculation of the boundary distribution function is somewhat cumbersome and does not recover LBL results for homogeneous media. The modified approach, on the other hand, is readily evaluated at no additional computational cost from the database of narrow-band k–g distributions used in the MSFSK scheme and does recover LBL results for homogeneous media. For inhomogeneous media, the modified approach performs equally well as the direct approach.

Acknowledgment

This research has been sponsored by National Science Foundation under Grant Nos. CTS-0112423 and CTS-0121573.

Nomenclature

a = stretching factor for FSK method
f = k-distribution function (cm)
g = cumulative k-distribution
I = radiative intensity (W/m^2sr)
k = absorption coefficient variable (cm^{-1})
k^* = overlap parameter defined in Eq. (19)
L = geometric length (cm)
M = total number of scales
$\hat{n}$ = surface normal
P = pressure, bar
q = radiative heat flux (W/m^2)
s = distance along path (cm)
$\hat{s}$ = unit direction vector
T = temperature (K)
x,$\boldsymbol{x}$ = mole fraction (vector)

Greek Symbols

η = wave number (cm^{-1})
$\boldsymbol{\phi}$ = composition variable vector
δ = Dirac's delta function
λ = overlap coefficient defined in Eq. (11), cm^{-1}
μ = boundary emission distribution function defined in Eq. (13)
κ = absorption coefficient (cm^{-1})
ϵ = wall emittance
Ω = solid angle (sr)
σ = Stefan–Boltzmann constant

Subscripts

0 = reference condition
b = blackbody emission
g = spectral in g-space
i = ith narrow band
L = left layer
m = mth scale
R = right layer
w = wall
η = spectral in wave-number space

References

[1] Lacis, A. A., and Oinas, V., 1991, "A Description of the Correlated-k Distribution Method for Modeling Nongray Gaseous Absorption, Thermal Emission, and Multiple Scattering in Vertically Inhomogeneous Atmospheres," J. Geophys. Res., **96**(D5), pp. 9027–9063.
[2] Goody, R. M., and Yung, Y. L., 1989, *Atmospheric Radiation—Theoretical Basis*, 2nd ed., Oxford University Press, New York.
[3] Modest, M. F., and Zhang, H., 2002, "The Full-Spectrum Correlated-k Distribution for Thermal Radiation From Molecular Gas-Particulate Mixtures," ASME J. Heat Transfer, **124**(1), pp. 30–38.
[4] Goody, R. M., West, R., Chen, L., and Crisp, D., 1989, "The Correlated k Method for Radiation Calculations in Nonhomogeneous Atmospheres," J. Quant. Spectrosc. Radiat. Transf., **42**, pp. 539–550.
[5] Fu, Q., and Liou, K. N., 1992, "On the Correlated k-Distribution Method for Radiative Transfer in Nonhomogeneous Atmospheres," J. Atmos. Sci., **49**(22), pp. 2139–2156.
[6] Rivière, P., Soufiani, A., and Taine, J., 1992, "Correlated-k and Fictitious Gas Methods for H_2O near 2.7 μm," J. Quant. Spectrosc. Radiat. Transf., **48**, pp. 187–203.
[7] Rivière, P., Scutaru, D., Soufiani, A., and Taine, J., 1994, "*A New c−k Data Base Suitable from 300 to* 2500 K *for Spectrally Correlated Radiative Transfer in* CO_2-H_2O *Transparent Gas Mixtures*," in Tenth International Heat Transfer Conference, Taylor & Francis, London, pp. 129–134.
[8] Rivière, P., Soufiani, A., and Taine, J., 1995, "Correlated-k and Fictitious Gas Model for H_2O Infrared Radiation in the Voigt Regime," J. Quant. Spectrosc. Radiat. Transf., **53**, pp. 335–346.
[9] Zhang, H., and Modest, M. F., 2003, "Scalable Multi-Group Full-Spectrum Correlated-k Distributions for Radiative Heat Transfer," ASME J. Heat Transfer, **125**(3), pp. 454–461.
[10] Zhang, H., and Modest, M. F., 2002, "A Multi-Scale Full-Spectrum Correlated-k Distribution for Radiative Heat Transfer in Inhomogeneous Gas Mixtures," J. Quant. Spectrosc. Radiat. Transf., **73**(2-5), pp. 349–360.
[11] Wang, L., and Modest, M. F., 2005, "Narrow-Band Based Multi-Scale Full-Spectrum k-Distribution Method for Radiative Transfer in Inhomogeneous Gas Mixtures," ASME J. Heat Transfer, **127**, pp. 740–748.
[12] Denison, M. K., and Webb, B. W., 1993, "A Spectral Line Based Weighted-Sum-of-Gray-Gases Model for Arbitrary RTE Solver," ASME J. Heat Transfer, **115**, pp. 1004–1012.
[13] Denison, M. K., and Webb, B. W., 1994, "*k-Distributions and Weighted-Sum-of-Gray Gases: A Hybrid Model*," In Tenth International Heat Transfer Conference, Taylor & Francis, London, pp. 19–24.
[14] Modest, M. F., 2003, *Radiative Heat Transfer*, 2nd ed., Academic, New York.
[15] Modest, M. F., 2003, "Narrow-band and Full-Spectrum k-Distributions for Radiative Heat Transfer—Correlated-k vs. Scaling Approximation," J. Quant. Spectrosc. Radiat. Transf., **76**(1), pp. 69–83.
[16] Wang, A., and Modest, M. F., 2005, "High-Accuracy, Compact Database of Narrow-Band k-Distributions for Water Vapor and Carbon Dioxide," J. Quant. Spectrosc. Radiat. Transf., **93**, pp. 245–261.
[17] Rothman, L. S., Camy-Peyret, C., Flaud, J.-M., Gamache, R. R., Goldman, A., Goorvitch, D., Hawkins, R. L., Schroeder, J., Selby, J. E. A., and Wattson, R. B., 2000, "HITEMP, the High-Temperature Molecular Spectroscopic Database," available through http://www.hitran.com.
[18] Tashkun, S. A., Perevalov, V. I., Bykov, A. D., Lavrentieva, N. N., and Teffo, J.-L., 2002, "Carbon Dioxide Spectroscopic databank (CDSD)," available from ftp://ftp.iao.ru/pub/CDSD-1000.

Enhancing Thermoelectric Energy Recovery via Modulations of Source Temperature for Cyclical Heat Loadings

R. McCarty
e-mail: robin.mccarty@wpafb.af.mil

K. P. Hallinan
e-mail: kevin.hallinan@notes.udayton.edu

Department of Mechanical and Aerospace Engineering,
University of Dayton,
300 College Park,
Dayton, OH 45469-0210

B. Sanders
Air Force Research Laboratories,
VAS,
2210 Eight Street,
Wright-Patterson, AFB, OH 45433-7542
e-mail: brian.sanders@wpafb.af.mil

T. Somphone
Department of Mechanical Engineering,
Tuskegee University,
333 Engineering Building,
Tuskegee, AL 36088

Recent improvements in thermoelectric (TE) materials have expanded the potential to use this technology to generate electricity from waste heat in a variety of applications. The performance of a TE generator improves when the temperature difference across the generator is as large as possible given the constraints associated with its application. This paper considers the use of a "thermal switch," located physically between the heat source and the TE device, to modulate the heat flow through the TE device. A control schema is envisioned which permits heat to flow from the source to the TE device only when the source temperature is near maximum, yielding a higher time-averaged temperature drop across the TE and therefore a higher efficiency. A numerical model is used to evaluate the benefits of an active thermal switch in series with a TE generator relative to a baseline case defined by the absence of a thermal switch for both time-varying and constant heat inputs. The results demonstrate that modulating the heat flow through the TE device and maintaining the source temperature at a near constant maximal value is capable of improving the time-averaged TE device energy recovery efficiency. For some conditions, improved efficiencies of more than five times are realized. The requisite physical conditions necessary for achieving these improvements are also identified.
[DOI: 10.1115/1.2717238]

Keywords: thermoelectric generator, thermal switch, energy harvesting

Introduction

Recently, breakthrough developments have been reported in thermoelectric devices. For, example, Dresselhaus et al. have demonstrated improvement in the *ZT* figure of merit as dimensionality is reduced from bulk to two-dimensional quantum wells to one-dimensional quantum wires to zero-dimensional nanowire superlattices [1]. In 2001, Venkatasubramanian used nanoscale superlattice materials based on the concept of phonon blocking electron transmission to demonstrate *ZT* values of 2.4 at ambient temperature, exceptionally high power densities, and 1/40,000th of the active material mass as compared to bulk thermoelectric technology [2]. Finally, Martin described progress in the scale-up of thermoelectric quantum well thermoelectrics. *ZT* values approaching 5 were reported [3].

Thus in a mere half-decade, *ZT* values have increased from 1 to 5. Such advances have practical importance. Bell illustrated that surpassing the threshold *ZT* of 2 in a cost effective manner can enable significant use of thermoelectric (TE) energy harvesting in the automotive industry [4]. Recently, Fairbanks of the U.S. Department of Energy noted that further improvements in *ZT* to approximately 10 could make TE power conversion competitive with the internal combustion engine [5]. Finally, Elder et al. stated recently that for automotive applications, TE utilization is possible if the module cost is brought down to approximately \$0.10/W and a *ZT* value above 3 can be achieved over a broad temperature range [6].

Relative to aircraft energy harvesting from power electronics, Hallinan et al. [7] showed that TE technology is already at a state where positive system level impact can be realized. The application they considered was energy harvesting from a concept radar aircraft.

It is clear that TE technology is at least on the cusp of practical feasibility. Within this context, we seek to explore the potential for using these new thermoelectric technologies in applications where either the heat loading is cyclic or constant but the source temperature is below its maximum allowable value. Such systems must necessarily be designed to accommodate peak heat loading by maintaining the source temperature at or below the maximum permissible temperatures under these conditions. Consequently, when the heat loading is off-peak, the source temperature decreases, thereby diminishing the recovery efficiency of the TE generator.

The baseline waste heat recovery system considered in this analysis is shown schematically in Fig. 1(*a*), where constant or time-varying heat dissipated from a source passes directly into a TE generator, where some of the heat is converted to electrical energy. The remainder is rejected to the sink. In practice, this system must be designed for worst case heat input scenarios which must account for variations in source heat output, sink temperature or thermal resistance, and manufacturing. Thus, for a worst-case design, the system may operate, at least at times, well below the maximum allowable temperature of the source, therefore reducing the temperature drop across the TE device relative to the maximum possible and lowering the efficiency of energy recovery. Such a case is illustrated by the source temperature and TE power output time histories shown illustratively in Fig. 1(*a*).

In an effort to maximize TE energy recovery, it is proposed to employ a thermal switch having controllable thermal resistance between the heat source and TE generator, as is shown schematically in Fig. 1(*b*). This thermal switch would ideally provide a negligible thermal resistance in its closed state and a dominant thermal resistance in its open state. Moreover, it would ideally

Contributed by the Heat Transfer Division of ASME for publication in the JOURNAL OF HEAT TRANSFER. Manuscript received August 26, 2005; final manuscript received September 19, 2006. Review conducted by Phillip M. Ligrani. Paper presented at the 2005 International Electronic Packaging Technical Conference and Exhibition (IPACK2005), San Francisco, CA, USA, July 15–22, 2005.

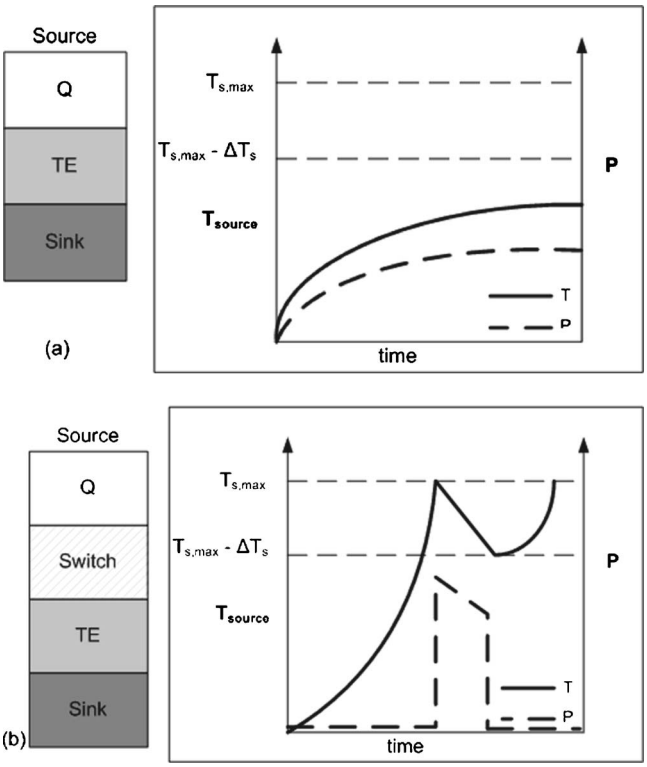

Fig. 1 Physical model considered

have a negligible thermal capacitance relative to the other elements in the system. As such, its response would be nearly instantaneous. Under these conditions, the thermal switch operation would then be as follows. If the source temperature was below its allowable maximum, $T_{s,\max}$, the switch is open. When the source reaches a temperature at or near its maximum, the switch closes, thereby connecting the hot side of the TE device to the source and enabling heat transport into the TE device. The switch remains closed only while the source remains at or near its maximum temperature. Finally, when the source temperature falls below its maximum value by a prescribed amount (ΔT_s), the switch would then be reopened. The temperature and TE power output histories associated with this process are shown schematically in Fig. 1(*b*). This control then would guarantee that heat is transferred to the TE device and electrical energy harvested only when the temperature drop across the TE is maximal. As a result, such control results ideally in greater time-averaged energy recovery by the TE device. Still such improvements could mean nothing if such a device could not be manufactured. As discussed later, we are confident that MEMs approaches could be used to produce this switch.

Model

The baseline no-control system and the actively controlled thermal switch system shown, respectively, in Figs. 1(*a*) and 1(*b*) are modeled analytically. In the model, all material constants are considered constant. Contact thermal resistances between the source, thermal switch, TE, and sink are not considered. Most important, is how the model treats the transient behavior of the TE generator. Such behavior has been a well studied topic [8–12]. As a cooler, the TE device instantly absorbs electric energy at the *p-n* junctions when current is applied. Simultaneously, Joule heating results, but this thermal energy diffuses towards the *p-n* junction at a much slower rate than the electron flow. As a result, the TE device performance is temporarily enhanced until the Joule heating effects reach steady state. When the TE device operates as a generator, Joule heating diffusion begins at the *p-n* junction when a temperature difference is applied across the device. Almost instantaneously, electrical energy adsorption commences, thus temporarily degrading the TE device performance until Joule heating reaches steady state. One previous study of a TE refrigerator showed that microsecond current pulses could enhance the Seebeck effect and therefore cooler performance [13] Most relevant for this study is that the switching cycle exceeds several seconds. Thus, for a typical bismuth telluride TE device, the transient effects occur for very small time durations relative to the switching time. The characteristic timescale for the dynamic response of a typical bismuth telluride TE device can be calculated using Eq. (1), and is seen to be just a fraction of a second [12]. For emerging and next generation TE technologies with substantially reduced mass, much lower time scales are realized

$$\tau_{\mathrm{TE}} = \frac{cml}{kA} = \frac{c\rho l^2}{k} = \frac{(16\ \mathrm{J/kg\ K})(7730\ \mathrm{kg/m^3})(0.002\ \mathrm{m})^2}{3\ \mathrm{W/m\ K}} = 0.16\ \mathrm{s} \tag{1}$$

In contrast, the nominal time scale for the rest of the system, as shown in Eq. (2), can be estimated from the controlling system thermal resistance and capacitance due, respectively, to the TE device and the source, equal to 100 K/W and 1 J/K. Thus, the time constant for the TE generator is less by at least three orders of magnitude than that associated with the remainder of the system considered. As a consequence, the relatively slow changes in source and sink temperature are quickly accommodated by the TE device. The TE generator can then be appropriately analyzed as if operating in quasi-steady state

$$\tau_{\mathrm{system}} \approx R_{\mathrm{TE}} C_s = (100\ \mathrm{W/K})(1\ \mathrm{J/kg}) = 100\ \mathrm{s} \tag{2}$$

All resistances and capacitances in the numerical model are consistent with the Cauer network representation for power electronics assuming one heat source, several different materials with corresponding resistances and capacitances, one heat sink, and adiabatic lateral walls [14–17].

Under these assumptions, the following system of equations results. Conservation of energy is applied to each of the subelements.

Conservation of Energy

1. Source

$$\frac{dT_s}{dt} = \frac{1}{C_s}[Q_{\mathrm{in}}(t) - Q_{\mathrm{out}}] \tag{3a}$$

   Here, Q_{in} and Q_{out} are, respectively, the heat dissipation by the source and the heat leaving the source and passing either into the TE device (for the baseline case) and into the thermal switch otherwise.
2. Thermal switch

$$\frac{dT_p}{dt} = \frac{1}{C_p}\left(k_p \frac{\partial^2 T_p}{\partial x^2}\right) \tag{3b}$$

3. Sink heat exchanger

$$\frac{dT_{\mathrm{SINK}}}{dt} = \frac{1}{C_{\mathrm{SINK}}}\left(k_{\mathrm{SINK}} \frac{\partial^2 T_{\mathrm{SINK}}}{\partial x^2}\right) \tag{3c}$$

Finally, for the TE device, the quasi-steady assumption permits determination of the TE energy recovery efficiency from the hot side and cold side TE temperatures from Eq. (4) [18]

$$\eta = \frac{P_{\mathrm{out}}}{Q_{\mathrm{out}}} = \frac{T_{\mathrm{TE},H} - T_{\mathrm{TE},L}}{T_{\mathrm{TE},H}}\left(\frac{\sqrt{1+ZT}-1}{\sqrt{1+ZT}+\dfrac{T_{\mathrm{TE},L}}{T_{\mathrm{TE},H}}}\right) \tag{3d}$$

Table 1 Physical and spatial variables that remain fixed for all numerical cases studied

Variable	Value
C_S	1 J/K
R_{TE}	100 K/W
$\hat{R}_{P,\text{LOW}}$	0.001
$\hat{C}_{\text{TE}}$	0
$\hat{C}_P$	0
T_{SINK}	−20°C
ZT	3

The boundary conditions employed for these elements are continuity of heat flow and temperature at each interface. For convenience all temperatures are initially set equal to the sink temperature, T_{sink}.

The physical model given by Eq. (3) and the specified boundary and initial conditions are evaluated using a finite difference formulation. The ultimate aim of this formulation is to evaluate the time-averaged TE energy recovery efficiency shown in Eq. (4)

$$\bar{\eta} = \frac{\bar{P}_{\text{out}}}{\bar{P}_{\text{in}}} = \frac{\int_0^T P_{\text{out}}(t)dt}{\int_0^T Q_{\text{in}}(t)dt} \tag{4}$$

Results

The systems of equations given by Eq. (3) for both the baseline system without thermal switching and the thermal switching system are solved via a finite difference technique in a MatLab Simulink environment. The benefit of using the Simulink environment for solving this dynamic system is that an active feedback schema can be easily employed. This active approach considered for the thermal switch model is the use of the simplest feedback schema; namely a "relay" or "on/off" control. More complicated control schemes did not improve the results significantly. When the temperature of the source reaches the maximum allowable or upper set-point temperature, the thermal resistance of the switch is set to its minimum value. Subsequently, as heat is drawn from the source, the source temperature diminishes. When this temperature falls below a lower set-point value, the thermal resistance is then set to its maximum value. For the purpose of the numerical experiments conducted here, the upper set-point temperature was set to 150°C, consistent with the maximum temperature allowance for electronic cooling, and the lower set-point temperature was varied from 148°C to 100°C. Spatial and temporal grid insensitivity of all results was assured.

The specific application considered is associated with energy harvesting from integrated radar arrays in aircraft wings proposed for a new type of sensorcraft. A heating rate of above 1 W/cm^2 and both transient (sinusoidal) and steady-state heat rates are analyzed. Consistent with this application, the source thermal capacitance, C_s, TE thermal resistance, R_{TE}, dimensionless thermal switch low state thermal resistance, $\hat{R}_{P,\text{LOW}}$, TE thermal resistance, $\hat{C}_{\text{TE}}$, thermal switch thermal capacitance, $\hat{C}_P$, sink temperature, T_{sink}, and TE ZT value given in Table 1 are specified for all cases. The carat in the table for the thermal resistance terms means that the actual thermal resistance is normalized with respect to the controlling thermal resistance associated with the TE generator, whereas the carat thermal capacitance terms are normalized relative to the controlling thermal capacitance associated with the source.

In order to maximize the output power from the thermoelectric device, the thermal resistance of the TE device was set as the controlling thermal resistance for the system (exclusive of the thermal switch in its high thermal resistance state), since in order for the TE to be effective, a majority of the system temperature drop should occur across the TE device.

Two sets of numerical experiments were conducted. The first set was conducted to evaluate the time-averaged efficiency of the TE with thermal switching relative to the baseline case for no switching subject to a sinusoidal heat input. The latter set of numerical experiments was conducted to evaluate the benefits of thermal switching for a constant heat load when operating below maximal heat loading conditions.

Table 2 describes the test cases considered for the sinusoidal heat input numerical experiments. In this table, the specific cases are characterized by: the control condition; heat input amplitude; frequency; thermal switch to TE thermal resistance; sink thermal resistance and capacitance; and low set-point temperature. The "no-control" condition refers to the baseline case with no thermal switch. The heat input amplitude was selected to yield a maximum source temperature nearly equal to the maximum allowable temperature 150°C for the thermal switching cases. In all, the test

Table 2 Numerical cases for variable heat flow input, $Q_{\text{IN}} = \beta + \beta \sin(\hat{\omega}\hat{t})$

Case No.	Control (C) or No-control (NC)	β (W)	$\hat{\omega}$	$\hat{R}_{P,\text{HIGH}}$	$\hat{R}_{\text{SINK}}$	$\hat{C}_{\text{SINK}}$	T_{OFF} (°C)	Evaluating effect of changes in:
1	NC	0.85	0.5	1	0.01	0.1	N/A	Lower set-point temperature
1	C	0.85	0.5	1	0.01	0.1	148	
2a	C	0.85	0.5	1	0.01	0.1	140	
2b	C	0.85	0.5	1	0.01	0.1	125	
2c	C	0.85	0.5	1	0.01	0.1	100	
3a	NC	0.85	0.5	10	0.01	0.1	N/A	Thermal switch high to low resistance
3b	NC	0.85	0.5	0.1	0.01	0.1	N/A	
3a	C	0.85	0.5	10	0.01	0.1	140	
3b	C	0.85	0.5	0.1	0.01	0.1	140	
4a	NC	0.85	0.5	10	0.1	1	N/A	Sink thermal capacitance & resistance
4b	NC	0.85	0.5	10	0.001	0.01	N/A	
4a	C	0.85	0.5	10	0.1	1	140	
4b	C	0.85	0.5	10	0.001	0.01	140	
5a	NC	0.83	0.05	10	0.001	0.01	N/A	Frequency of heat input
5b	NC	1.5	5	10	0.001	0.01	N/A	
5c	NC	1.51	50	10	0.001	0.01	N/A	
5a	C	0.83	0.05	10	0.001	0.01	140	
5b	C	1.5	5	10	0.001	0.01	140	
5c	C	1.51	50	10	0.001	0.01	140	

Table 3 Numerical cases for constant heat flow input

Case No.	Control (C) or no control (NC)	Case No.	Q_{IN} (W)	$\hat{R}_{P,HIGH}$	$\hat{R}_{SINK}$	$\hat{C}_{SINK}$	T_{OFF} (°C)	Evaluating effect of changes in:
6a	NC	6a	1.68	1	0.01	0.1	N/A	Steady heat input rate
6b	NC	6b	0.84	1	0.01	0.1	N/A	
6c	NC	6c	0.42	1	0.01	0.1	N/A	
6d	NC	6d	0.21	1	0.01	0.1	N/A	
6a	C	6a	1.68	1	0.01	0.1	140	
6b	C	6b	0.84	1	0.01	0.1	140	
6c	C	6c	0.42	1	0.01	0.1	140	

cases assessed were chosen to evaluate changes in lower set-point temperature, the ratio of high to low thermal resistance for the thermal switch, sink thermal resistance and capacitance, and heat input frequency.

Table 3 presents similar information for the constant heat input numerical experiments. The specific cases considered were chosen to yield source temperatures below the allowable maximum for the baseline system. Thus, the no-control baseline cases represent off-peak design conditions. These cases are posed primarily to evaluate the effect of changes in the steady heat input at constant control conditions.

Figure 2 shows the time history of the ratio of the overall recovery efficiency, $\bar{\eta}$, for Case 1 with and without active control. Comparing the case of active control to no control, it is apparent that the active control case yields a substantially higher steady-state energy recovery efficiency (15.9% compared to 7.2%) which is a remarkable enhancement. The reason for this improvement is apparent from examination of the source temperature time history in Fig. 3. It is clear from this figure that, in the absence of thermal switching, the maximum source temperature is well below that achievable with control. Thus, thermal switching yields a greater temperature drop across the TE device when heat is permitted to flow through it when the thermal switch is closed. Consequently the TE energy recovery efficiency is improved relative to the no-control baseline case.

Figures 4(a) and 4(b), which show a finer presentation of the Case 1 time histories for the source as well as hot and cold side TE temperatures, for control and no control conditions, respectively, further illustrate this difference. With active control, the source temperature is maintained near 150°C at all times, whereas the hot side TE temperature cycles between the source temperature and just above the sink temperature as the switch thermal resistance state is changed. The thermal switch resistance is in its low state (high conduction heat transfer from source to TE device) only when the TE hot side temperature is high, whereas the thermal switch is in its high state (poor conduction heat transfer from source to TE device) when the TE hot side temperature is low. Thus a majority of heat leaves the source when the source is near its maximum temperature. In contrast, for the baseline system, the source and TE hot side temperatures are nearly the same at all times, cycling between a low of 40°C to the maximum of 100°C.

The significance of these temperature histories is apparent from examination of Fig. 5, which shows the heat flow transient for Case 1 with active control. Both the heat input to the source and TE heat are shown. It is clear from Fig. 5 that at peak heat loading, no switching of the thermal switch is required, since the temperature (shown in Fig. 4(a)) is at its maximum. At minimum heat loading, the thermal switch is at its high thermal resistance state. At intermediate heat loading, the thermal switch is observed to cycle between its high and low thermal resistances. Most interesting is that the frequency of the switching increases as the source heat input decreases. It is noted that only when the switching frequency becomes large the assumption of quasi-steady TE operation breaks down. Case 6c represents the lowest heat input that could be appropriately considered with the quasi-steady TE model.

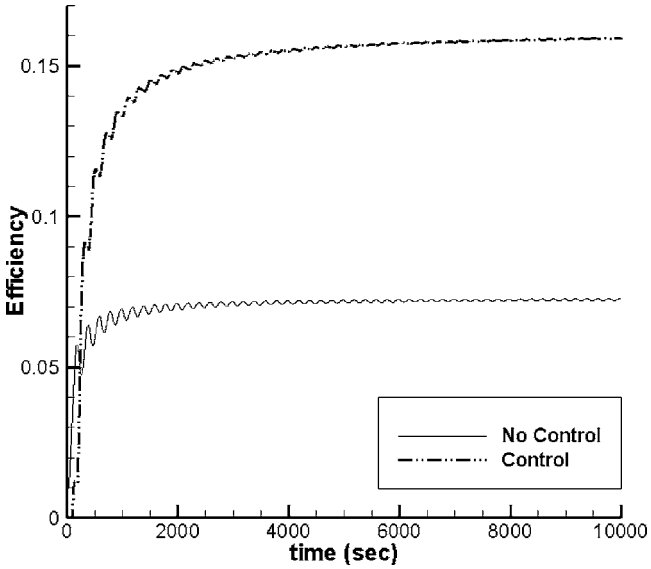

Fig. 2 Overall TE generator efficiency, $\bar{\eta}$, for Case 1 with and without source temperature control, β=0.85, $\hat{\omega}$=0.5, $\hat{R}_{P,HIGH}$=1, $\hat{R}_{SINK}$=0.01, $\hat{C}_{SINK}$=0.1, and T_{OFF}=148°C

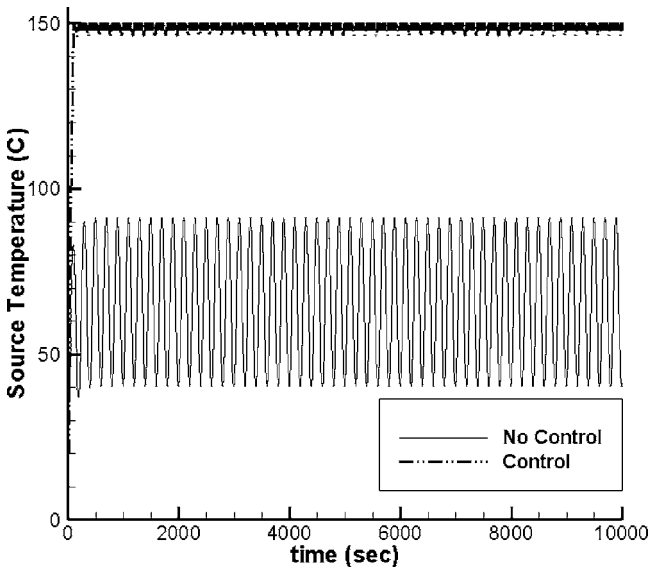

Fig. 3 Source temperature for Case 1 with and without source temperature control, β=0.85, $\hat{\omega}$=0.5, $\hat{R}_{P,HIGH}$=1, $\hat{R}_{SINK}$=0.01, $\hat{C}_{SINK}$=0.1, and T_{OFF}=148°C

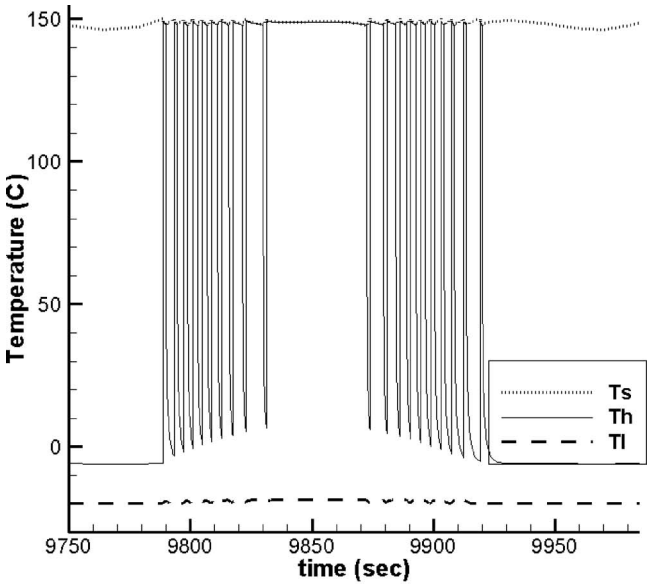

(*a*)

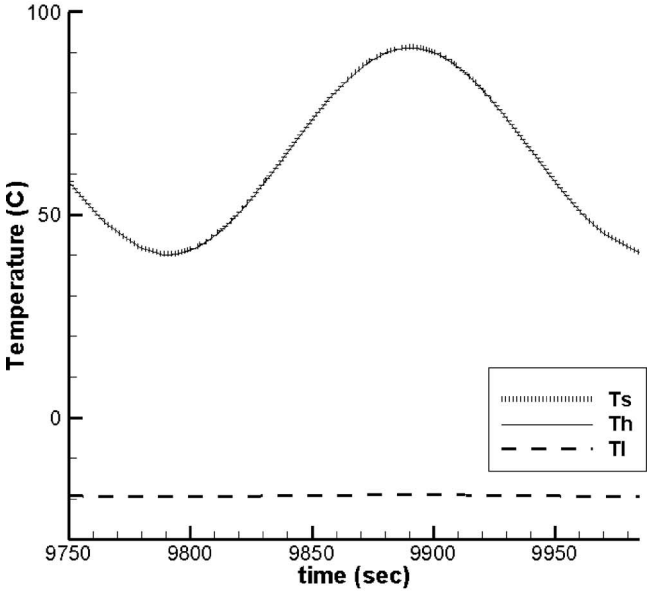

(*b*)

Fig. 4 (*a*) Source and hot/cold side of TE temperature histories for Case 1 with active control once system reached steady state, β=0.85, $\hat{\omega}$=0.5, $\hat{R}_{P,\mathrm{HIGH}}$=1, $\hat{R}_{\mathrm{SINK}}$=0.01, $\hat{C}_{\mathrm{SINK}}$=0.1, T_{OFF}=148°C; and (*b*) source and hot/cold side of TE temperature histories for Case 1 without active control once system reached steady state, β=0.85, $\hat{\omega}$=0.5, $\hat{R}_{P,\mathrm{HIGH}}$=1, $\hat{R}_{\mathrm{SINK}}$=0.01, $\hat{C}_{\mathrm{SINK}}$=0.1, and T_{OFF}=148°C

Table 4 summarizes the time averaged overall TE energy recovery efficiency for Case 1–5 simulations relative to changes in the lower set-point temperature, thermal switch high state resistance, sink thermal resistance and capacitance, and source heat frequency. Most apparent from this table is that thermal switching produces an improved energy recovery efficiency for all cases considered. The improvement is seen to be somewhat insensitive to changes in the lower set-point temperature, as long as the lower set-point temperature is not too low. The improvement is also seen to be strongly dependent upon the high thermal resistance state for the thermal switch. A thermal switch high resistance value approximately 10 times the TE thermal resistance is seen to be

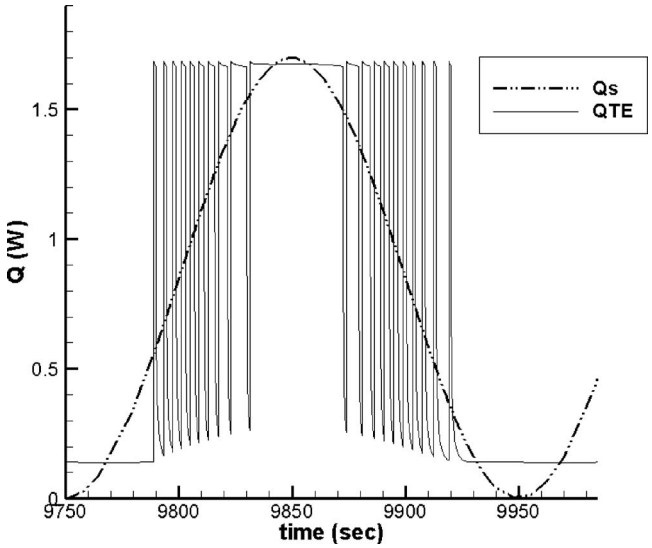

Fig. 5 Source and TE heat flow transients for Case 1 with active control once system reached steady state, β=0.85, $\hat{\omega}$=0.5, $\hat{R}_{P,\mathrm{HIGH}}$=1, $\hat{R}_{\mathrm{SINK}}$=0.01, $\hat{C}_{\mathrm{SINK}}$=0.1, and T_{OFF}=148°C.

highly desirable. The sink thermal resistance and capacitance, which in all cases considered is at most 1/10th that of the TE device, is seen to have only a slight impact on the improvement. Of course, a larger sink thermal resistance and capacitance is seen to be detrimental to the recovery efficiency. Finally, the results demonstrate thermal switching improvement is most prominent at moderate source heat input frequency. When this frequency is very large, thermal switching offers no improvement in energy recovery since the source temperature varies only slightly with time due to the filtering effect of the source thermal capacitance. At very low frequencies, the recovery efficiency for the control case is still relatively high, however, the baseline no-control recovery efficiency is greater than for higher source heat input frequencies since the source temperature is permitted to cycle hotter when the heat input is high. Thus, the source rejects heat to the TE primarily when the source temperature is high, and therefore when the temperature drop across the TE device is high.

Table 5 summarizes the overall recovery efficiencies for the constant heat input numerical experiments. As seen in the table, the most substantial improvement in energy recovery efficiency occurs when the steady heat input rate is well below the rated maximum, which results in a source temperature also well below the maximum permissible. Case 6c shows a remarkable improvement over the no-control case of 554%. These results demonstrate that for multi-state heat generation systems, e.g., where the heat dissipation is steady state, but can be at two or more levels, the active thermal switch concept has the most benefit, since the switch continues to maintain the source temperature at near maximum whenever heat is permitted to flow from the source to the TE device.

Finally, to investigate the feasibility of using a thermal switch in current and future applications, an additional numerical test set was considered where the TE *ZT* value was varied from 1 to 5. Both constant heat input and a variable heat input cases were evaluated. The test conditions for this set shown in Table 6, other than the *ZT* value, were identical to those employed in Case 2a, where thermal switching was demonstrated to provide sizeable benefit relative to no control. The constant heat input case assumed a heat input of 0.84 W, and the nondimensional cyclic heat input was considered to be $0.85+0.85\sin(0.5)$ W.

The energy recovery efficiency for the constant and cyclic heat input cases is summarized in Tables 7 and 8 for *ZT* values of 1, 2, 3, 4, and 5, respectively, for variable and constant heat input.

Table 4 Summary of overall energy recovery efficiency with and without control for variable heat flow input

Case no.	Parameter changing for control case	Change direction	$\bar{\eta}$ (%) No control	$\bar{\eta}$ (%) Control
1			7.2	15.9
2a	Lower set-point temperature	↓	7.2	16.3
2b			7.2	16.1
2c			7.2	15.7
3a	Thermal switch resistance	↓	7.2	17.5
3b			7.2	9.1
4a	Sink thermal resist. & capac.	↓	6.9	15.7
4b			7.3	17.8
5a	Source heat input frequency	↑	12.6	17.9
5b			8.7	18.0
5c			18.9	18.9

These results show that source temperature modulation for both constant and cyclic heat input has substantial benefit over the entire *ZT* range considered. From these results it can generally be stated that source temperature modulation via a thermal switch is equally beneficial for currently available TE devices and for future state-of-the-art high *ZT* devices.

Conclusions and Implications for Future Research

The analysis presented here reveals the significance of active thermal switching for TE thermal energy harvesting in applications when the heat generation may have several states, when the heat flow or the overall thermal resistance is variable with time. Generally, thermal management systems are designed for the worst case heat load, and even here, always with a safety factor to guarantee that the maximum source temperature is not reached. The presence of an active thermal switch in series with the TE generator in such applications would permit maximizing the source temperature at all times, thereby allowing greater extraction of electrical energy. This scenario would be acceptable as long as the failure mode of the active thermal switch was its low thermal resistance state. Given that thermoelectric technology is on the cusp of practicality for automotive, aerospace, and other applications, the coupling of TE devices with an active thermal switch seems to offer potential for pushing TE technology into the realm of commercial application in a multitude of applications.

Table 5 Summary of overall energy recovery efficiency with and without control for constant heat flow input

Case no.	Parameter changing	Change direction	$\bar{\eta}$ (%) No control	$\bar{\eta}$ (%) Control
6a	Source heat input	↓	18.6	18.8
6b			6.6	15.7
6c			2.1	13.73

The question is "How can one make a thermal switch?" For certain, a practical solution would necessarily be one that is compact and easily integrable into a TE heat recovery system. Micro electromechanical systems (MEMS)-based approaches likely offer the most promise. Christensen et al. have recently reported on the fabrication and characterization of a liquid-metal microdroplet array for use as a thermal switch [19]. Based upon experimental data, they infer that such a thermal switch has the potential for a 100-fold swing in thermal resistance. For satellite thermal control, Beasley et al. have reported on a MEMS thermal switch, relying upon electromechanical actuation to move a radiator surface into contact with a heat source [20].

We envision an approach similar to that shown in Fig. 6. We propose to coat the source—TE interfaces with a dense patterning of carbon nanofibers. These carbon nanofibers have thermal conductivities on the order of diamond. A piezoelectric or thermal bimorph actuator would be used to open and close a "vacuum" gap. In the absence of contact with the nanofibers, the heat transfer across the gap would be only by thermal radiation. Actuation would press the nanofibers into contact with the heat source, and the thermal resistance is anticipated to be very small.

The requisite features of the thermal switch/TE system are as follows:

1. In its low thermal resistance state, the thermal switch MUST have negligible thermal resistance compared to the downstream thermal resistances;
2. In its high thermal resistance state, the thermal switch thermal resistance should be at least as great as the downstream thermal resistances and ideally substantially greater; and
3. The TE thermal resistance should be the limiting thermal resistance in the system when the thermal switch is "closed" in order to maximize the temperature drop across the thermal resistance device.

Substantial research is still needed to determine when such requirements can be achieved.

Table 6 Physical and spatial variable for *ZT* sensitivity study for constant and cyclic heat input

Variable	C_S	R_{TE}	$\hat{R}_{P,LOW}$	$\hat{C}_{TE}$	$\hat{C}_P$	T_{SINK}	$\hat{R}_{P,HIGH}$	$\hat{R}_{SINK}$	$\hat{C}_{SINK}$	T_{OFF}
Value	1 J/K	100 K/W	0.001	0	0	−20°C	1	0.01	0.1	140°C

Table 7 Summary of overall energy recovery efficiency with and without control for variable heat input and varying *ZT* values

	$\bar{\eta}$ (%)	
ZT	No control	Control
1	3.4	8.6
2	5.6	13.8
3	7.2	17.5
4	8.5	20.2
5	9.6	22.5

Acknowledgment

We would like to thank the Dayton Area Graduate Studies Institute and AFOSR for their continued funding and support.

Nomenclature

C = heat capacity (J/K)
$\hat{C}$ = normalized heat capacity, $\hat{C}=C/C_s$
Q = heat dissipation (W)
P = power (W)
R = thermal resistance (K/W)
$\hat{R}$ = normalized thermal resistance, $\hat{R}=R/R_{\mathrm{TE}}$
T = temperature (°C)
T = period (s)
ZT = thermoelectric device figure of merit
β = magnitude of heat input (W)
η = thermoelectric device efficiency (%)
$\bar{\eta}$ = time-averaged overall TE energy recovery efficiency (%)

Table 8 Summary of overall energy recovery efficiency with and without control for constant heat input and varying *ZT* values

	$\bar{\eta}$ (%)	
ZT	No control	Control
1	3.1	7.8
2	5.1	12.4
3	6.6	15.7
4	7.7	18.2
5	8.7	20.2

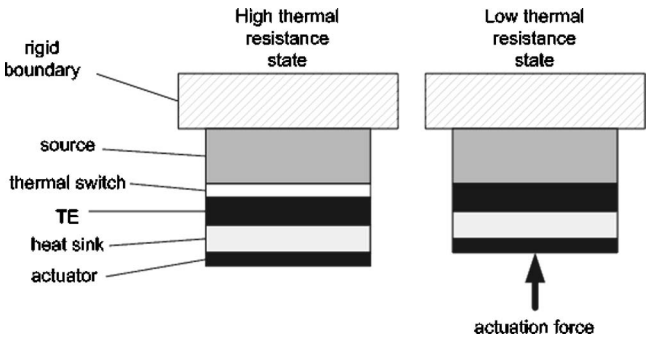

Fig. 6 Conceptual thermal switch design considered

ω = frequency of heat input (Hz)
$\hat{\omega}$ = normalized heat input frequency, $\hat{\omega}=\omega R_{\mathrm{TE}}C_s$
t = time (sec)
$\hat{t}$ = normalized time, $\hat{t}=t/(R_{\mathrm{TE}}C_s)$
x = distance (m)

Subscripts

HIGH = high resistance setting of thermal potentiometer
in = referring to dissipation by the source
LOW = low resistance setting of thermal potentiometer
out = Output leaving source
TE = thermoelectric device
$\mathrm{TE_H}$ = hot side of thermoelectric device
TE_L = cold side of thermoelectric device
p = thermal switch
s = heat source
sink = heat sink

References

[1] Dresselhaus, M. S., Lin, Y. M., Black, M. R., Rabin, O., and Dresselhaus, G., 2003, "New Directions for Low Dimensional Thermoelectricity," Mater. Res. Soc. Symp. Proc., **793**, pp. 419–430.
[2] Venkatasubramanian, R., Viivola, E., Calpitts, T., and O'Quinn, B., 2001, "Thin Film Thermoelectric Devices with High Room Temperature Figures of Merit," Nature (London), **413**(6856), pp. 597–602.
[3] Martin, P. M., and Olsen, L. C., 2004, "Recent Progress in Scale Up of Multilayer Thermoelectric Films," Proceedings 2004 DOE/EPRI High Efficiency Thermoelectrics Workshop, San Diego, CA, February 17–20.
[4] Bell, L., 2004, "Thermoelectric Technology Readiness for Large Scale Commercialization," Proceedings 2004 DOE/EPRI High Efficiency Thermoelectrics Workshop, San Diego, CA, February 17–20.
[5] Fairbanks, J., 2004, "Chair's Overview of High Efficiency Thermoelectrics and Potential," Proceedings DOE/EPRI High Efficiency Thermoelectrics Workshop, San Diego, CA, February 17–20.
[6] Elder, A., Bertram, M., and Liebl, J., 2004, "Visions of Possible Thermoelectrics for Vehicle Applications," Proceedings DOE/EPRI High Efficiency Thermoelectrics Workshop, San Diego, CA, February 17–20.
[7] Hallinan, K. P., and Sanders, B., 2005, "Entropy Generation Metric for Evaluating and Forecasting Aircraft Energy Management Systems," Int. J. Exergy, **2**(2), pp. 120–145.
[8] Hoyos, G. E., Rao, K. R., and Jerger, D., 1977, "Fast Transient Response of Novel Peltier Junction," Energy Convers., **17**(1), pp. 45–54.
[9] Stilbans, L. S., and Fedorovich, N. A., 1958, "The Operation of Thermoelectric Elements in Non-stationary Conditions," Sov. Phys. Tech. Phys., **3**, pp. 460–462.
[10] Landecker, K., and Findlay, A. W., 1961, "Study of the Fast Transient behavior of Peltier Junctions," Solid-State Electron., **3**, pp. 239–260.
[11] Idnurm, M., and Landecker, K., 1963, "Experiments With Peltier Junctions Pulsed With High Transient Currents," J. Appl. Phys., **34**(6), pp. 1806–1810.
[12] Gray, P. E., 1963, "Approximate Dynamics Response Calculations for Thermoelectric Peltier-Effect Devices," Solid-State Electron., **6**, pp. 339–348.
[13] Miner, A., Majumdar, A., Ghoshal, U., 1999, "Thermo-Electro-Mechanical Refrigeration Using Transient Thermoelectric Effects," Appl. Phys. Lett., **75**, pp. 1176–1178.
[14] Bagnoli, P. E., 1998, "Thermal Resistance Analysis by Induced Transient (TRAIT) Method for Power Electronic Devices Thermal Characterization—Part I: Fundamentals and Theory," IEEE Trans. Power Electron., **13**(6), pp. 1208–1219.
[15] Bagnoli, P. E., 1998, "Thermal Resistance Analysis by Induced Transient (TRAIT) Method for Power Electronic Devices Thermal Characterization—Part II: Practice and Experiments," IEEE Trans. Power Electron., **13**(6), pp. 1220–1228.
[16] Ozisik, M. N., 1993, *Heat Conduction*, Wiley, New York.
[17] Szekely, V., 1997, "A New Evaluation Method of Thermal Transient Measurement Results," Microelectron. J., **28**, pp. 277–292.
[18] Goldsmid, H. J., 1994, "Conversion Efficiency and Figure-of-Merit," *CRC Handbook of Thermoelectrics*, CRC, Boca Raton, FL.
[19] Christensen, A. O., Jacob, J. P., Richards, C. D., Bahr, D. F., and Richards, R. F., 2003, "Fabrication and Characterization of a Liquid-Metal Micro-Droplet Array for Use as a Thermal Switch," HT2003-47317, Proceedings ASME Summer Heat Transfer Conference, Las Vegas, NV, July 21–23, pp. 97–100.
[20] Beasley, M. A., Firebaugh, S. L., Edwards, R. L., Keeney, A. C., and Osiander, R., 2004, "MEMS Thermal Switch for Spacecraft Thermal Control." MEMS/MOEMS Components and Their Applications, **5344**, pp. 98–105.

Journal of Heat Transfer

Technical Briefs

Thermal Diffusivity Estimation in a Picosecond Photoreflectance Experiment

Jean-Luc Battaglia
e-mail: jean-luc.battaglia@ensam.bordeaux.fr

Andrzej Kusiak

Jean-Christophe Batsale

Laboratoire inter Établissement 'TRansferts Ecoulements Fluides Energétique',
UMR 8508,
Ecole Nationale Supérieure d'Arts et Métiers,
Esplanade des Arts et Métiers,
33405 Talence Cedex, France

The aim of this work is to provide an analytical expression for the thermal diffusivity of a material in the configuration of the picosecond photoreflectance experiment. It is shown that the thermal diffusivity can be estimated from the absorption depth of the pump beam together with the probe beam as well as the time when the two asymptotic behaviors of the impulse response cross. Thereby, it is not required to measure absolute values of incident heat flux and average temperature on the aiming area.
[DOI: 10.1115/1.2717252]

Keywords: picosecond photoreflectance, thermal diffusivity, optical absorption, impulse response, asymptotic behaviors

1 Introduction

The thermal characterization of thin deposits or thin films, whose thickness varies from some nanometers to some micrometers, is now classically realized by using the picosecond photoreflectance technique in a time range that goes from the picosecond to the nanosecond (see for example Refs. [1–5]). As represented in Fig. 1, this technique consists of heating the surface of the sample by using a heating laser beam of radius r_0 at the surface. The duration of the pulse is some picoseconds. A probe beam, of radius r_m at the surface, is focused at the location of the heated area. The reflected part of the probe beam depends on the average temperature of the heated area. The measured quantity is the reflectivity change of the probe beam that is connected to the average temperature on the aiming area (disk of radius r_m). Thereby, the average temperature can only be deduced from a calibration stage. In practice, this stage requires much care. An objective of the present study is to show that, under the assumption of linearity, the thermal diffusivity of the material can be estimated accurately without the need to measure absolute values of heat flux and temperature.

In this work, heat transfer in the medium is mathematically described by the Fourier law that relates the heat flux to the temperature gradient according to the thermal conductivity of the material. This means that the measurements can only be exploited from a certain time after the pulse. This time, typically some tenth of picoseconds, depends on the mean free path of the carriers (electrons and/or phonons) in the medium. Specific literature is devoted to the molecular dynamic behavior, as for example the paper of Cahill et al. [6].

2 Mathematical Governing Equations

The heating laser beam provides an incident heat flux density at the surface of the material

$$\varphi_i(r,t) = F(r)\varphi_0(t) \tag{1}$$

with

$$F(r) = \begin{cases} e^{-\left(\frac{r}{r_0}\right)^2}, & \text{Gaussian profile} \\ \Pi_{r_0} = \begin{cases} 1, & \text{if } r \le r_0 \\ 0, & \text{elsewhere} \end{cases}, & \text{uniform profile} \end{cases} \tag{2}$$

The absorption depth of the incident heat flux depends on the extinction coefficient κ_λ of the medium. This parameter is the imaginary part of the refraction index of the medium which can be measured using the classical ellipsometry method. It depends on the wavelength λ of the laser. This heat source is expressed from the electromagnetic theory as

$$Q(r,z,t) = \tau_\lambda \varphi_i(r,t)\beta_h e^{-\beta_h z} \tag{3}$$

In this relation $1/\beta_h$ characterizes the absorption depth with $\beta_h = 4\pi\kappa_\lambda/\lambda$ and τ_λ is the transmittance of the medium that also depends on the wavelength λ.

The temperature $T(r,z,t)$ in the medium is given by the one-dimensional linear heat diffusion equation

$$\frac{1}{a}\frac{\partial T}{\partial t} = \frac{\partial^2 T}{\partial z^2} + \frac{1}{k}Q(r,z,t), \quad 0 < z < \infty,\ 0 < r < \infty,\ t > 0 \tag{4}$$

where a and k are the thermal diffusivity and the thermal conductivity of the medium, respectively.

With respect to the duration of an experiment, possible heat exchange between the medium and the ambient can be neglected

$$\frac{\partial T}{\partial z} = 0, \quad z = 0, \quad 0 < r < \infty, \quad t > 0 \tag{5}$$

Finally, the initial condition is

Contributed by the Heat Transfer Division of ASME for publication in the JOURNAL OF HEAT TRANSFER. Manuscript received March 1, 2006; final manuscript received August 29, 2006. Review conducted by Minking Chyu.

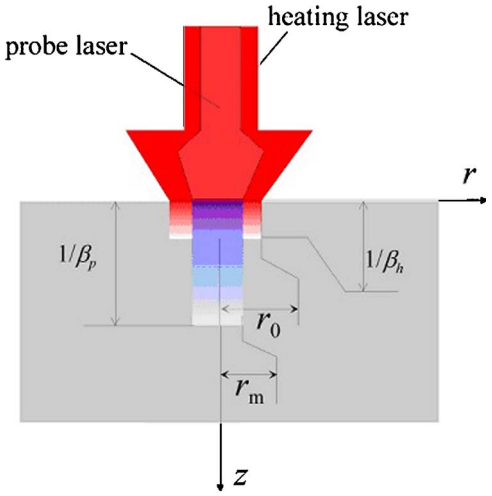

Fig. 1 Schematic description of the photoreflectance experiment

$$T=0, \quad 0\le r<\infty, \quad 0\le z<\infty, \quad t=0 \tag{6}$$

Laplace transform on the temperature with respect to time is

$$\theta(r,z,p)=\int_0^\infty T(r,z,t)e^{-pt}\,dt \tag{7}$$

Therefore, relations (4)–(6) become

$$\frac{p}{a}\theta=\frac{\partial^2\theta}{\partial z^2}+\frac{1}{k}\Delta(r,z,p), \quad 0<z<\infty,\ 0<r<\infty,\ t>0 \tag{8}$$

$$\frac{\partial\theta}{\partial z}=0, \quad z=0 \tag{9}$$

According to relations (1)–(3), the transformed heat source term is

$$\Delta(r,z,p)=\tau_\lambda F(r)\psi_0(p)\beta_h e^{-\beta_h z} \tag{10}$$

where $\psi_0(p)$ denotes the Laplace transform of $\varphi_0(t)$. By integrating relation (8) and using Eq. (9) leads to express the solution in the following form

$$\theta(r,z,p)=H(z,p)F(r)\psi_0(p) \tag{11}$$

After some calculus, it is found that

$$H(z,p)=\frac{\tau_\lambda\beta_h}{k(\beta_h^2-\gamma^2)}\left(\frac{\beta_h}{\gamma}e^{-\gamma z}-e^{-\beta_h z}\right), \quad \text{with } \gamma=\sqrt{\frac{p}{a}} \tag{12}$$

Obviously, the absorption depth of the probe beam must be taken into account. This depth is approximately $1/\beta_p$ where index p refers to the probe laser. In this case the measured temperature is given by

$$\theta_\nu(r,p)=\int_0^\infty \theta(r,z,p)\beta_p e^{-\beta_p z}\,dz=H_\nu(p)F(r)\psi_0(p) \tag{13}$$

According to relation (12), it is found that

$$H_\nu(p)=\frac{\tau_\lambda\beta_h}{k(\beta_h^2-\gamma^2)}\int_0^\infty\left(\frac{\beta_h}{\gamma}e^{-\gamma z}-e^{-\beta_h z}\right)e^{-\beta_p z}\,dz \tag{14}$$

that is equal to

$$H_\nu(p)=\frac{\tau_\lambda\beta_h\beta_p}{k(\beta_h^2-\gamma^2)}\left[\frac{\beta_h}{\gamma(\gamma+\beta_p)}-\frac{1}{(\beta_h+\beta_p)}\right] \tag{15}$$

Finally, it is then possible to calculate the average temperature on the measurement area (disk of radius r_m) as

$$\langle\theta_\nu(p)\rangle=\frac{2}{r_m^2}\int_0^{r_m}\theta_\nu(r,p)r\,dr=H_\nu(p)\psi_0(p)\frac{2}{r_m^2}\int_0^{r_m}F(r)r\,dr \tag{16}$$

According to relation (2), it is found the expression of the average temperature

$$\langle\theta_\nu(p)\rangle=H_\nu(p)\eta_{r_0,r_m}\psi_0(p) \tag{17}$$

with

$$\eta_{r_0,r_m}=\begin{cases}\dfrac{r_0^2}{r_m^2}\left(1-e^{-\left(\frac{r_0}{r_m}\right)^2}\right), & \text{Gaussian profile}\\ 1, & \text{uniform profile}\end{cases} \tag{18}$$

The inverse Laplace transform is performed by application of the Stehfest algorithm [7]

$$\langle T_\nu(t)\rangle=\frac{\ln 2}{t}\sum_{j=1}^{N}V_j\left\langle\theta_\nu\left(\frac{j\ln 2}{t}\right)\right\rangle \tag{19}$$

with

$$V_j=(-1)^{j+N/2}\sum_{i=\mathrm{Int}[(j+1)/2]}^{\mathrm{Min}(N/2,j)}\frac{i^{N/2}(2i)!}{(N/2-i)!\,i!\,(i-1)!\,(j-i)!\,(2i-j)!} \tag{20}$$

3 Expression of the Thermal Diffusivity

The impulse response is given from relation (17) with $\psi_0(p)=1$. From relation (15) it is found that the asymptotic behaviors at the small times are

$$\langle\theta_\nu(p)\rangle\to\eta_{r_0,r_m}\frac{\tau_\lambda\beta_h\beta_p}{k(\beta_h+\beta_p)\gamma^2}=\eta_{r_0,r_m}\frac{\tau_\lambda\beta_h\beta_p}{(\beta_h+\beta_p)(\rho C_p)_d}\frac{1}{p}, \quad \text{when } p\to\infty \tag{21}$$

On the other hand, the asymptotic behavior at the long times is

$$\langle\theta_\nu(p)\rangle\to\eta_{r_0,r_m}\frac{1}{k\gamma}=\eta_{r_0,r_m}\frac{\tau_\lambda}{\sqrt{k(\rho C_p)_d}}\frac{1}{\sqrt{p}}, \quad \text{when } p\to 0 \tag{22}$$

While equalizing these two last relations, a simple expression of the thermal diffusivity is obtained

$$a=\frac{(\beta_h+\beta_p)^2}{t_c\beta_p^2\beta_h^2\pi} \tag{23}$$

In this relation t_c is the time when the two asymptotic behaviors cross. It is worth noting that this estimation of the thermal diffusivity is independent from the beam profile.

4 Sensitivity Analysis

For this analysis the thermal properties of the deposit are $k=0.4$ W m^{-1} K^{-1} and $a=10^{-7}$ m^2 s^{-1}. The wavelength of the heating laser is $\lambda=400$ nm.

For the first time, it is considered that the absorption depth of the probe laser beam is equal to that of the heating laser. The impulse response is calculated by considering first a surface absorption (κ or $\beta\to\infty$) and second a volumic absorption with four different values of the extinction coefficient. The results are represented in Fig. 2. As mentioned in the Sec. 1, data in the time domain $[10^{-12}, \sim 10^{-11}]$ s have no physical meaning with respect to the Fourier law. For an ideal, but unrealistic, surface absorption (κ or $\beta\to\infty$) the slope of the curve is equal to $-1/2$ in a log–log scale, which corresponds to the typical semi-infinite behavior. The influence of the heat penetration depth on the slope of the curve appears clearly in the figure. The larger the absorption depth the

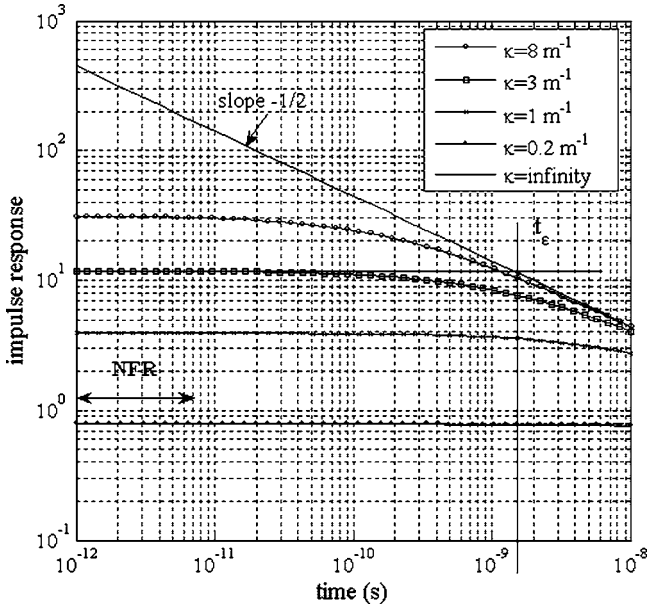

Fig. 2 Influence of heating laser penetration depth on the impulse response (with $\beta_p=\beta_h$) (NFR denotes the non-Fourier regime)

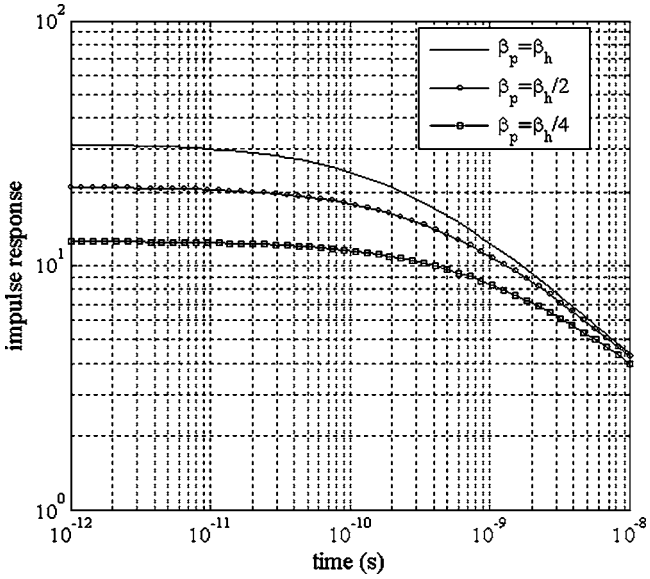

Fig. 3 Influence of the penetration depth of the probe laser on the impulse response

more the slope tends toward zero on an increasing time domain which agrees with relation (21). Considering the impulse response with $\kappa=3\ m^{-1}$ in Fig. 2, the two asymptotic behaviors cross at $t_c=1.4\ 10^{-9}$ s. Relation (23), with $\beta_h=\beta_p$, leads to the thermal diffusivity of the material: $\tilde{a}=1.024\ 10^{-7}\ m^2\ s^{-1}$, which is very close to the real value.

Figure 3 shows that the absorption depth of the probe beam significantly changes the form of the impulse response. This well known result shows that the higher the penetration depth of the probe laser beam in the medium the lower the accuracy on the thermal diffusivity estimation from relation (23). Indeed, it is necessary to have sufficient points for the slope at the long times in order to calculate t_c accurately.

5 Conclusion

This study deals with the thermal diffusivity estimation from a picosecond photoreflectance experiment. With respect to the duration of the pulse, the material is viewed as a semi-infinite medium. The optical absorption depth of the pump beam and probe beam plays a crucial role and must be known with high accuracy prior to the diffusivity estimation. A very simple relation that expresses the thermal diffusivity according to the penetration depth of the pump laser and the probe laser in the medium and to the time t_c when the two asymptotic behaviors cross has been found. Generally, the extinction coefficient of the material can be measured with a high accuracy on a large wavelength range. Thus, the estimation of the thermal diffusivity of the material essentially depends on the measurement of t_c.

References

[1] Clemens, B. M., et al., 1988, "Time-Resolved Thermal Transport in Compositionally Metal Films," Phys. Rev. B, **37**(3), pp. 1085–1096.

[2] Cahill, D. G., 2004, "Analysis of Heat Flow in Layered Structures for Time-Domain Reflectance," Rev. Sci. Instrum., **75**(12), pp. 5119–5122.

[3] Taketoshi, N., et al., 2002, "Thermal Diffusivity Measurement of a Thin Metal Film With a Picosecond Photoreflectance Technique," High Temp. - High Press., **34**, pp. 19–28.

[4] Li, B., et al., 1999, "Thermal Characterization of Thin Superconducting Films by Modulated Photoreflectance Microscopy," Thin Solid Films, **352**, pp. 91–96.

[5] Qiu, T. Q., et al., 1994, "Femtosecond Laser Heating of Multi-Layer Metals-II. Experiments," Int. J. Heat Mass Transfer, **37**(17), pp. 2799–2808.

[6] Cahill, D. G., et al., 2003, "Nanoscale Thermal Transport," J. Appl. Phys., **93**(2), pp. 793–818.

[7] Stehfest, H., 1970, "Algorithm 368. Numerical Inversion on the Laplace Transforms," Commun. ACM, **13**, pp. 47–49.

Numerical Investigation of the Thermally Developing Flow in a Curved Elliptic Duct With Internal Fins

P. K. Papadopoulos
e-mail: p.papadopoulos@des.upatras.gr

P. M. Hatzikonstantinou

Department of Engineering Science,
University of Patras,
GR 26500 Patras, Greece

The hydrodynamically fully developed and thermally developing flow inside a curved elliptic duct with internal longitudinal fins is studied numerically. The duct is subjected to the uniform temperature boundary condition on its wall and fins. The local and mean Nusselt numbers are examined for various values of the Dean and Prandtl numbers, the cross-sectional aspect ratio, and the fin height. The characteristics of the optimum duct, which achieves enhanced heat transfer rates combined with low friction losses, are determined in terms of the aspect ratio and the fin height. [DOI: 10.1115/1.2717254]

Keywords: curved elliptic duct, thermally developing flow

1 Introduction

Curved pipes of circular cross section are commonly used in engineering design due to their ability to satisfy space and geometric requirements. Studies investigating the thermal flow in curved pipes have been published by Akiyama et al. [1] who examined the laminar forced convection heat transfer in a duct with uniform wall temperature and Kalb and Seader who considered the same problem with boundary conditions of constant temperature [2] and axially constant heat flux and uniform temperature peripherally [3]. Dong and Ebadian [4] studied the case of a curved duct with elliptical cross section for constant heat flux in the longitudinal direction and uniform temperature peripherally. Their investigation included the effects of buoyancy forces which, as they showed, may alter the flow and heat transfer conditions, especially for low Dean numbers. The case of the isothermal flow was studied by Silva et al. [5] for elliptical ducts of aspect ratios both lower and higher than unity.

Prakash et al. [6] studied the properties of developing flow in straight pipes with multiple internal longitudinal fins placed in the radial direction. Dong et al. [7] extended the research to straight elliptical ducts with four symmetrical fins and determined an optimum fin height for the maximization of the heat transfer coefficient.

The present work deals with the study of the hydrodynamically fully developed and thermally developing flow in a curved elliptic duct with four internal longitudinal fins. The flow is studied numerically with the improved continuity vorticity pressure (CVP) variational method [8] applied on a vertex cell type grid. The thermal boundary condition concerned in this work is uniform temperature both axially and peripherally. Due to the increased practical importance of internal duct flows, the determination of an optimum fin height that will combine increased heat transfer rate with low friction losses is attempted. The effect of the curvature and the Prandtl number on the optimum fin height is also studied, leading to useful conclusions regarding the effectiveness of heat transfer through curved circular and elliptic ducts with internal fins.

Contributed by the Heat Transfer Division of ASME for publication in the JOURNAL OF HEAT TRANSFER. Manuscript received July 23, 2005; final manuscript received October 17, 2006. Review conducted by Bengt Sunden.

2 Analysis

The fully developed velocity profiles used here are based on the full continuity and Navier–Stokes equations for viscous flow of a constant property fluid in a toroidal geometry with generalized, boundary fitted (ξ, η) coordinates (Fig. 1). These equations were solved numerically using the improved CVP method developed by Papadopoulos and Hatzikonstantinou [8].

The energy equation in the toroidal, generalized coordinate system, when neglecting viscous dissipation and axial conduction, is

$$\bar{U}\frac{\partial\theta}{\partial\xi}+\bar{V}\frac{\partial\theta}{\partial\eta}+CJw\frac{\partial\theta}{\partial z}=\frac{1}{\mathrm{Pr}}\left[\frac{1}{J}\left(\alpha\frac{\partial^2\theta}{\partial\xi^2}-2\beta\frac{\partial^2\theta}{\partial\xi\,\partial\eta}+\gamma\frac{\partial^2\theta}{\partial\eta^2}\right)+\kappa C\left(\frac{\partial\theta}{\partial\xi}y_n-\frac{\partial\theta}{\partial\eta}y_\xi\right)\right] \tag{1}$$

where

$$\alpha=\left(\frac{\partial x}{\partial\eta}\right)^2+\left(\frac{\partial y}{\partial\eta}\right)^2,\quad \beta=\frac{\partial x}{\partial\xi}\frac{\partial x}{\partial\eta}+\frac{\partial y}{\partial\xi}\frac{\partial y}{\partial\eta},\quad \gamma=\left(\frac{\partial x}{\partial\xi}\right)^2+\left(\frac{\partial y}{\partial\xi}\right)^2$$

and $C=1/(\kappa x+1)$, $\bar{U}$, $\bar{V}$ are the contravariant velocities; and J is the Jacobian of transformation defined in the Nomenclature.

The duct is subjected to the thermal boundary condition of constant wall temperature axially and peripherally. The thermal boundary condition is $\theta=1$ at the walls and the fins. The mean axial velocity, which in the present nondimensional form, coincides with the Reynolds number Re, and the Dean number De are defined by

$$\bar{w}=\frac{\int_A w\,dA}{\int_A dA},\quad \mathrm{Re}=\bar{w},\quad \mathrm{De}=\bar{w}\sqrt{\kappa} \tag{2}$$

where A is the area of the cross section.

The Nusselt number, which is used to measure the heat transfer rate, is obtained by considering the axial overall energy balance

$$\mathrm{Nu}=\frac{1}{4(1-\theta_b)}\overline{w^*\mathrm{Pe}\frac{\partial\theta}{\partial z}} \tag{3}$$

The dimensionless bulk temperature θ_b is defined by the relation

$$\theta_b=\frac{\int_A w\theta\,dA}{\int_A w\,dA} \tag{4}$$

3 Numerical Implementation

The computations were conducted on a 48×48 mesh which was chosen after numerical experiments with test grids of sizes 30×30 and 60×60. The outcome of the comparison was that the results of the selected mesh presented a maximum difference of 2% with the first test grid and less than 1% with the second, while in some cases for large axial pressure gradients dp_a/dz the coarser grid was inadequate and a solution could not be reached. Thus it was concluded that the 48×48 mesh was capable of producing results for high Dean numbers with acceptable accuracy and considerable computational economy.

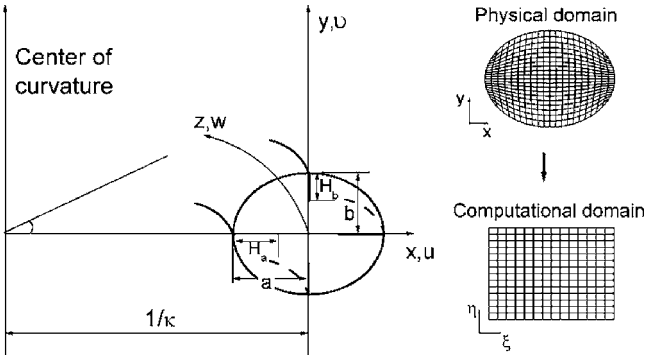

Fig. 1 Geometry and coordinate system

In order to assure the accuracy of the thermal results for the curved circular finless duct the predictions of the present work were tested against those of Akiyama et al. [1], who solved the energy equation using a flow field obtained with the boundary vorticity method. The comparison is shown in Fig. 2 where the local Nusselt number is plotted against the axial length z normalized with the Peclet number Pe, for various Dean and Prandtl numbers. It is observed that for Pr=0.1 and Pr=0.7 the results show very good agreement in both the developing Nu and its asymptotic value. The only difference of the compared results is in the Nusselt number for case Pr=10 which, according to the present prediction, is found to develop and reach its asymptotic value further downstream compared to the predictions of Akiyama et al. [1]. It is noted that the fluctuations that appear in the case for Pr=10 in the present results, are absent from the reference study since they were considered numerical instabilities and were eliminated from the corresponding diagrams. However, this wavy behavior of Nu has been observed in numerous experimental and numerical studies. It was found from our computations that, in agreement with the observations of Dravid et al. [9], these fluctuations are the result of the interaction between the thermal boundary layer and the secondary flow.

The present results for the fully developed Nusselt number were compared to the computations of Kalb and Seader [2]. The computations were for a range of Dean numbers from 17.5 to 567

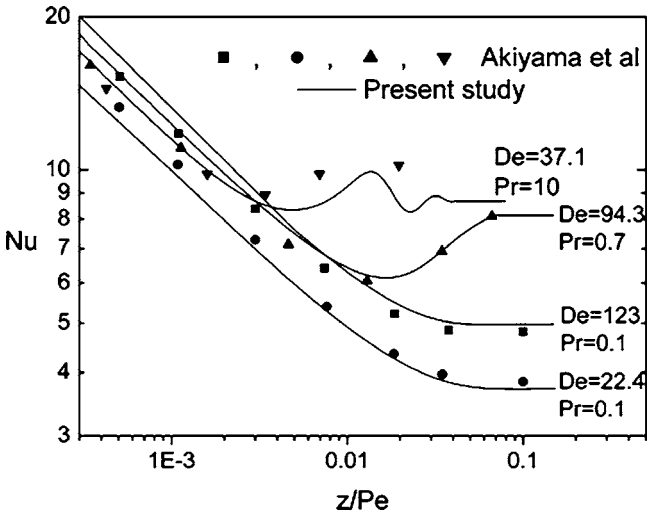

Fig. 2 Comparison of results for the local Nusselt number between the present work and Akiyama et al. [1] for the case of a curved circular finless duct

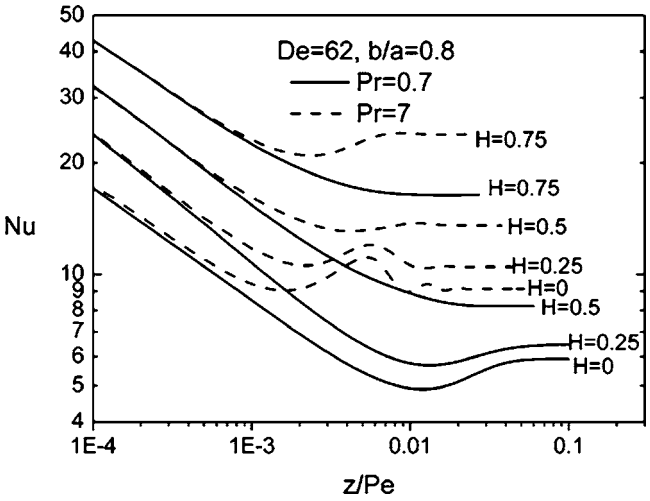

Fig. 3 Variation of the local Nu with z/Pe for De=62, b/a=0.8, Pr=0.7, 7, and various fin heights

and for Prandtl numbers from 0.05 to 100. In 16 test cases that were computed, the mean difference was 3.36% and the maximum was 7.12% for the case of De=35.2, Pr=100.

4 Results and Discussion

In Fig. 3, the local Nusselt number is plotted against the axial length normalized by the Peclet number z/Pe for b/a=0.8 and De=62, where the various curves correspond to different fin heights, beginning from the finless duct with H=0 and reaching a fin height of H=0.75. The solid lines represent Prandtl number Pr=0.7 and the dashed lines represent Pr=7. A first conclusion that can be deduced from Fig. 3 is that increase of either Pr or the fin height H results in a decrease of the entrance length and increase of the Nusselt number. Concerning the case of Pr=0.7 in particular, it is seen that the difference in the entrance length between ducts of H=0 and H=0.25 is rather insignificant. However for fins of H=0.5 and H=0.75 there is a considerable reduction of the entrance length, with respect to the finless duct, of 50% and 81% accordingly. Concerning the asymptotic value of the Nusselt number, it is seen that the difference between the finless duct and the duct with fins of H=0.25 is 9%. For H=0.5 there is an increase of 39% with respect to the finless duct, while for the case of H=0.75 the value of Nu is almost tripled, presenting an increase of 177%. A similar behavior is observed for Pr=7.

A notable fact that can be observed from the curves of Pr=7 is that for H=0 and H=0.25 the development of Nu presents fluctuations before reaching the asymptotic value. This fluctuating behavior is not present in the cases of H=0.5 and H=0.75, thus leading to the conclusion that large fins have a smoothing effect on the development of the local Nusselt number. This is attributed to the fact that the large fins confine the transversal movement of the fluid and reduce the secondary velocities. Although the mean axial velocity remains constant under the constant Dean number for the various cases of Fig. 3, the transversal flow field is less intense for large fins and a smooth solution of the local Nusselt number is obtained.

The dependence of the fully developed Nusselt number on De can also be seen in Fig. 4 where Nu is plotted against De for Pr=7 and aspect ratios b/a=0.8 and 0.5, while the various curves correspond to different fin heights. These plots show an essentially linear dependence between the two quantities for fins up to H=0.5. For H=0.75, however, the corresponding curves consist of an initial region with a steep inclination which fades after a certain value of De.

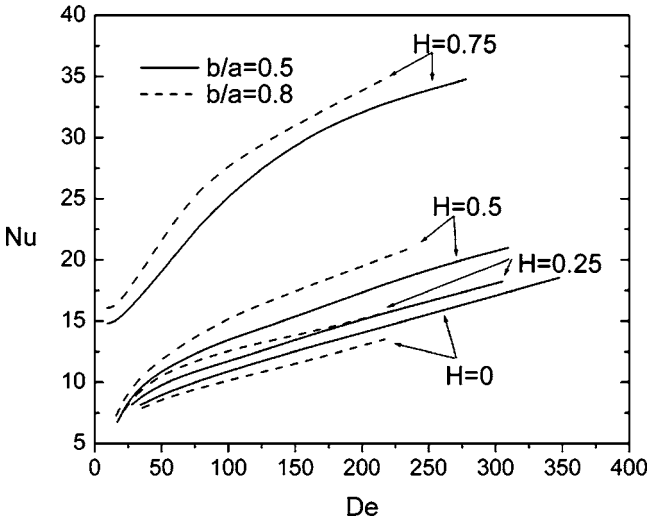

Fig. 4 Variation of the Nusselt number with De for Pr=7 and aspect ratio b/a=0.8 and 0.5

An important consideration concerns the effectiveness of the use of finned ducts in industrial applications. Some information has already been obtained from the observation that ducts with fins present a smaller thermal entrance length than finless ones. However, the most important factor is the efficiency to produce high heat transfer rates with the least possible friction losses. Figures 5(*a*), 5(*b*), and 5(*c*) show plots of the ratio of the Nusselt number to the friction product fRe against the fin height and the aspect ratio of the cross section. The diagram of Fig. 5(*a*), in particular, corresponds to a straight elliptic duct. It is observed that the use of fins is efficient only if their height ranges between H=0.75 and H=0.82. In that interval the ratio Nu/fRe is 0.238 and appears slightly increased compared to that of the finless duct which is approximately 0.229. The maximum ratio appears for aspect ratio b/a=0.5.

Figure 5(*b*) depicts the variation of the ratio Nu/fRe with height H and aspect ratio b/a for flow conditions of constant axial pressure gradient dP_a/dz=−40,000 constant curvature κ=0.1, and Prandtl number Pr=0.7. It is evident that in this case the finless duct is by far the most efficient flow passage. The ratio Nu/fRe for H=0 is almost doubled compared to the straight duct and ranges between 0.4 and 0.5 while for ducts with fins of medium and large heights the ratio Nu/fRe is 0.25.

A different behavior is observed in Fig. 5(*c*), where the plot of Nu/fRe corresponds to the same conditions dP_a/dz=−40,000 and κ=0.1, and Pr=7. Although the finless duct is still the most efficient passage with Nu/fRe reaching 0.47, the corresponding ratio for the cases of medium and large fins has increased significantly compared to the previous plot for Pr=0.7, reaching a value of 0.42. This observation leads to the conclusion that an important

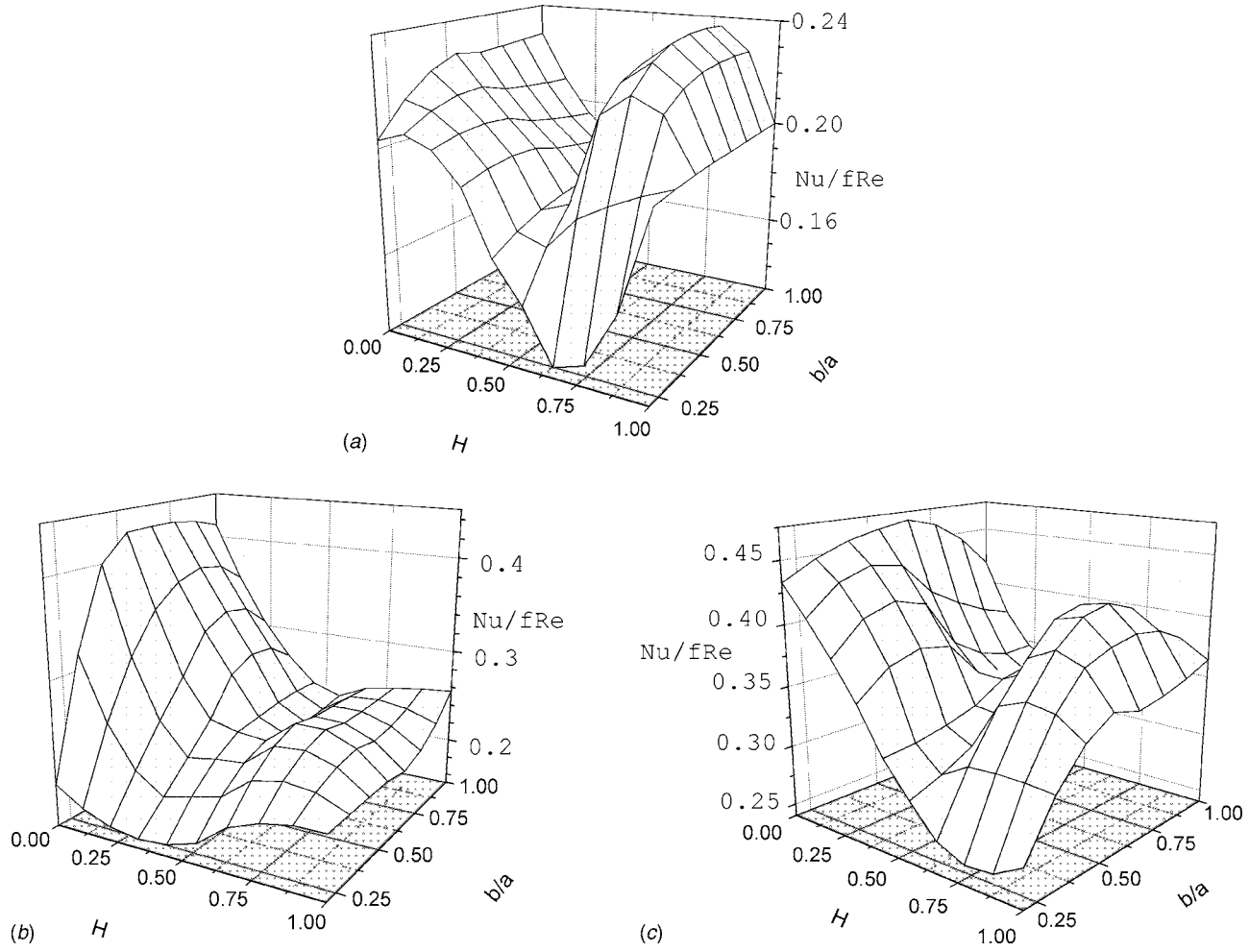

Fig. 5 Dependence of the ratio Nu/fRe on the fin height and the aspect ratio in: (*a*) a straight duct; (*b*) a curved elliptic duct with dP_a/dz=−40,000, κ=0.1, Pr=0.7; and (*c*) curved elliptic duct with dP_a/dz=−40,000, κ=0.1, and Pr=7

factor, which should determine whether a finned duct should be employed in an application, is the medium that will be used and particularly its Prandtl number. It is also concluded that the most preferable aspect ratio for the elliptic duct is $b/a=0.8$.

5 Conclusions

The present study examined the thermal flow in curved circular and elliptic ducts with internal fins. The results showed that the insertion of fins in a duct shortens the thermal entrance length by increasing the duct surface that contacts the fluid and smoothes the developing local Nu by confining the transversal movement of the fluid.

Concerning the benefits from the use of finned ducts, in terms of the ratio $\mathrm{Nu}/f\mathrm{Re}$, it was found that for straight ducts the optimum values of the aspect ratio and the fin height are $b/a=0.5$ and $H=0.78$, respectively. When the curvature was included in the computations, the results showed that finned pipes are preferable only for the mediums with high Prandtl numbers, over $\mathrm{Pr}=7$. The optimum duct dimensions in this case are $b/a=0.8$ and $H=0.75$.

Acknowledgment

This work is part of the "Karatheodoris" program, funded by the University of Patras Research Committee.

Nomenclature

D_h = hydraulic diameter
H = relative fin height $H=H_a/a=H_b/b$
J = Jacobian of transformation $J=x_\xi y_\eta - x_\eta y_\xi$
Pe = Peclet number (=RePr)
Pr = Prandtl number $(=\nu/\alpha)$
T = fluid temperature
u,v,w = dimensionless velocity components $(U,V,W)/(\nu/D_h)$
$\bar{U}, \bar{V}$ = contravariant velocities
w^* = normalized axial velocity $(=w/\bar{w})$
x,y,z = dimensionless coordinates $(X,Y,Z)/D_h$

Greek Symbols

θ = dimensionless temperature $(=(T-T_{\text{entrance}})/(T_{\text{surface}}-T_{\text{entrance}}))$
ν = kinematic viscosity

References

[1] Akiyama, M., and Cheng, K. C., 1971, "Laminar Forced Convection in the Thermal Entrance Region of Curved Pipes With Uniform Wall Temperature," Can. J. Chem. Eng., **52**, pp. 234–240.

[2] Kalb, C. E., and Seader, J. D., 1974, "Fully Developed Viscous-Flow Heat Transfer in Curved Circular Tubes With Uniform Wall Temperature," AIChE J., **20**(2), pp. 340–346.

[3] Kalb, C. E., and Seader, J. D., 1972, "Heat and Mass Transfer Phenomena for Viscous Flow in Curved Circular Tubes," Int. J. Heat Mass Transfer, **15**, pp. 801–817.

[4] Dong, Z. F., and Ebadian, M. A., 1992, "Effects of Buoyancy on Laminar Flow in Curved Elliptic Ducts," ASME J. Heat Transfer, **114**, pp. 936–943.

[5] Silva, R. J., Valle, R. M., and Ziviani, M., 1999, "Numerical Hydrodynamic Analysis of Laminar Flow in Curved Elliptic and Rectangular Ducts," Int. J. Therm. Sci., **38**, pp. 585–594.

[6] Prakash, C., and Liu, Y.-D., 1985, "Analysis of Laminar Flow and Heat Transfer in the Entrance Region of an Internally Finned Circular Duct," ASME J. Heat Transfer, **107**, pp. 84–91.

[7] Dong, Z. F., and Ebadian, M. A., 1991, "A Numerical Analysis of Thermally Developing Flow in Elliptic Ducts With Internal Fins," Int. J. Heat Fluid Flow, **12**, pp. 166–172.

[8] Papadopoulos, P. K., and Hatzikonstantinou, P. M., 2004, "Comparison of the CVP and the SIMPLE Methods for Solving Internal Incompressible Flows," *Proceedings of the 4th International Conference on Engineering Computational Technology*, B. H.V. Topping and C. A. Mota Soares, eds., Civil Comp Press, Stirling, Scotland, paper No. 82.

[9] Dravid, A. N., Smith, K. A., Meril, E. W., and Brian, P. L. T., 1971, "Effect of Secondary Fluid Motion on Laminar Flow Heat Transfer in Helical Coiled Tubes," Int. J. Heat Mass Transfer, **21**, pp. 1197–1206.

Thermal Radiative Properties of a Semitransparent Fiber Coated With a Thin Absorbing Film

Weixue Tian

Wei Huang

Wilson K. S. Chiu[1]
e-mail: wchiu@engr.uconn.edu

Department of Mechanical Engineering,
University of Connecticut,
Storrs, CT 06269-3139

This study presents the hemispherical model to predict the hemispherical total thermal radiative properties of a fiber coated with a thin film. The fiber is composed of semi-transparent media, such as fused silica. The film is made of strong absorbing media with thickness on the order of tens of nanometers. The film is assumed to be "locally flat" at the point of incidence for radiative transfer analysis because the thickness of the film is much less than the fiber radius. Wave optics is employed to calculate the reflectance and transmittance of the thin film while the ray tracing method is used for radiative transport analysis of the fiber. Effects of film and fiber substrate optical properties, film thickness and temperature on predicted thermal radiative properties are investigated. One of the applications of the proposed model is for studying the chemical vapor deposition of hermetic coatings on optical fibers, in which the thermal radiative properties of the fiber–film system heavily influence the fiber surface temperature and chemical reaction rate. [DOI: 10.1115/1.2717247]

1 Introduction

Carbon films grown by chemical vapor deposition (CVD) can be applied as a hermetic barrier for optical fibers used in harsh environments. In the CVD process, an optical fiber exiting the draw tower traverses through a chamber mixed with inert and reactant gas. The remnant heat from the draw tower decomposes the hydrocarbon precursor gas, and a layer of carbon approximately 50–100 nm thick is then deposited on the surface of the optical fiber. Because the temperature in the reaction chamber is very high (typically around 1000–2000 K), radiative heat transfer plays an important role in predicting the fiber surface temperature [1]. The thermal radiative properties of the thin film coated fiber is an important parameter that affects the transport phenomena and chemical reaction rate in the CVD process. The film's thickness and fiber temperature changes as the fiber traverses from the inlet to outlet, and the thermal radiative properties also change. Therefore, the objective of this study is to develop a numerical model to predict the thermal radiative properties of the thin film coated fiber and investigate how parameters such as temperature and film thickness affect the thermal radiative properties. Radiative properties of fibers with or without thin films can also be of interest for many other applications, such as insulation [2], photothermal radiometry [3], and optical fiber drawing [4,5].

Radiative transfer in semitransparent fibers of different size has been extensively studied. Comprehensive reviews of radiative transport in fibrous media can be found in Refs. [6,7]. Most previous studies in predicting thermal radiative properties of fibers are based on Mie scattering or Rayleigh scattering theory because the diameters of the fibers are comparable or smaller than the wavelength of interest [8]. Yamada [9] employed diffraction theory for a relatively large sized fiber. Although most researchers considered bare fibers in their study, the radiative properties of a fiber coated with a dielectric film were investigated to determine the effect of a thin film on insulation performance [2]. Most of these studies focused on predicting the scattering phase function and extinction (or absorption) cross section [10], but cannot be directly applied to predict the total hemispherical emittance or absorptance of thin film coated fibers. Although directional emittance for cylindrical geometries can be predicted by solving the radiative transfer equation [11,12], these models do not account for the thin film boundary and are more involved than the approach proposed in this study. Several book chapters [8,13–15] have been devoted to describe the ray tracing method and wave optics to calculate the optical properties of thin films. The effect of substrate properties on radiative properties of the thin film were investigated by Armaly and Look [16]. Taylor and Viskanta [17] investigated the radiative properties of thin film coated on a flat plate for solar energy utilization. Partial coherence theory was employed to study the thermal radiative properties of thin films by Chen and Tien [18] as well as Anderson and Bayazitoglu [19].

We use a ray tracing method [20,21] to model the radiative transfer in the fiber. The ray tracing method is valid for radiative transfer inside the fiber because the typical diameter of optical fiber is around 125 μm and much larger than the wavelength of interest for thermal radiation at high temperature (most radiative energy concentrates on 0.5–30 μm or less at 1000 K or higher temperature) as well as the coherence length (around 2 μm or less for temperature higher than 1000 K) of blackbody radiation. In the proposed model, the film radiative properties were calculated using wave optics because the thickness of the film is of tens of nanometers and interference needs to be accounted for. The above calculated directional spectral radiative properties need to be integrated over all wavelengths of interest and all solid angles in a hemisphere to obtain the total hemispherical properties, which can be employed in heat transfer analysis. The film deposited on a cylindrical substrate can be assumed be "locally flat" at the point of incidence when the film thickness is much smaller than the radius of the cylindrical substrate. Detailed description for methodology development in cylindrical geometry will be provided in the next section.

2 Problem Description and Analysis

A fiber–thin film structure shown in Fig. 1 is considered in this study. The fiber–film system is diffusively irradiated by a blackbody enclosure. Figure 1(*a*) shows the geometry and coordinate system used. The coordinates are locally defined, where θ is the polar angle defined by the angle of incidence with the local surface normal and ϕ is the azimuthal angle defined by the angle between the axial direction and the projection of the ray on the tangential plane, as shown in Fig. 1(*a*). Because radiation at any particular point on the film surface is the same (symmetry), the radiative properties of the fiber–film structure can be obtained by calculating reflection and attenuation of rays launched at any one particular point on the film surface with different θ and ϕ. In the following description, the name electromagnetic wave is used to describe the radiative energy propagation when the phase information of the radiative energy is of interest. When the phase information or interference is not of concern, ray tracing is used to describe the flow of radiative energy. As shown in Fig. 1(*b*), an electromagnetic plane wave from the source becomes reflected and refracted by the air–film interface (outer surface of the thin film). The refracted wave then propagates into the film and its

[1]Corresponding author.

Contributed by the Heat Transfer Division of ASME for publication in the JOURNAL OF HEAT TRANSFER. Manuscript received July 5, 2005; final manuscript received August 2, 2006. Review conducted by Yogendra Joshi. Paper presented at the 2005 ASME Summer Heat Transfer Conference (HT2005), San Francisco, CA, USA, July 15–22, 2005.

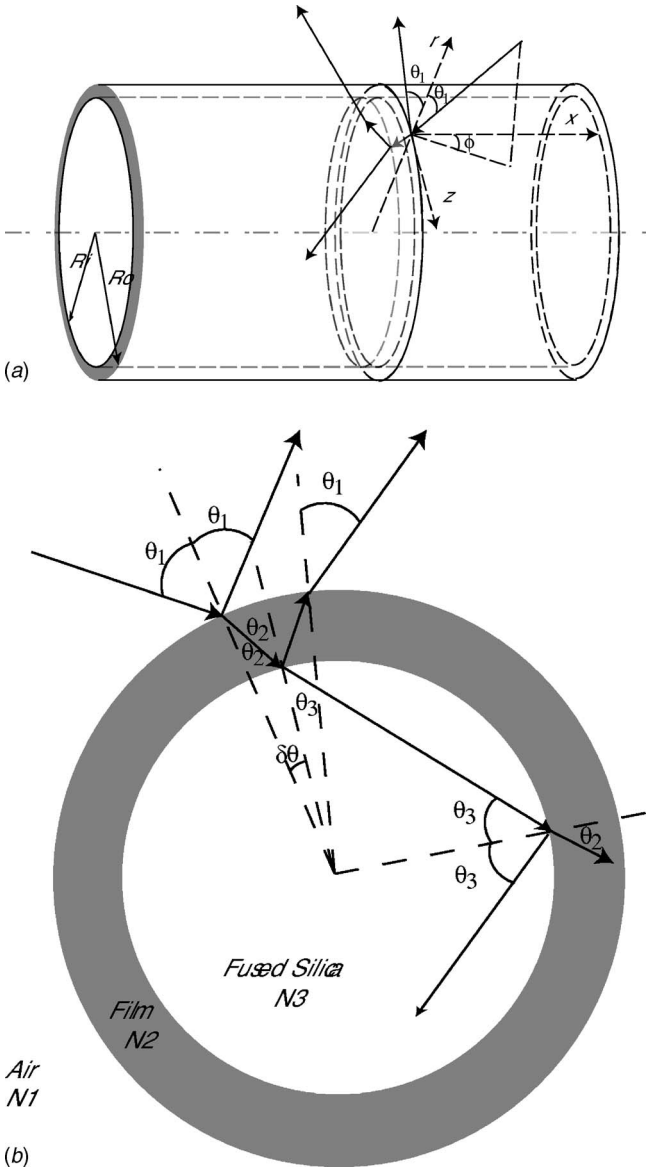

Fig. 1 Schematic of system geometry and coordinates for this study. To demonstrate the effect of thin film, drawing is not to scale. (*a*) Geometry and coordinates of the optical fiber-thin film structure; (*b*) Cross section view of the system, the incident wave is assumed to be aligned with the cross section.

amplitude decreases due to absorption of the film. When the wave reaches the film–substrate interface (inner surface of the film), it is again reflected and refracted. The semitransparent media in the fiber then further absorbs the radiative energy of rays penetrating into the fiber. The surviving wave is then reflected and refracted at the film–substrate interface again. For clarity of illustration, the Poynting vector (indicating the direction of wave propagation) shown in Fig. 1(*b*) is chosen to be aligned with the cross section in this particular case, i.e., the azimuthal angle of the Poynting vector $\phi=\pi/2$.

2.1 Optical Properties of the Film. The thin film coated on the fiber is assumed to be isotropic and homogeneous. The air–film and film–fiber interface is optically smooth because the thickness of a typical hermetic carbon film is roughly 50–100 nm, which is three orders of magnitude less than the diameter of a typical optical fiber. The path length of the electromagnetic wave in the film is therefore very small, compared with the fiber radius. The change of orientation of the local coordinates for defining angles, shown as $\delta\theta$ in Fig. 1(*b*), is very small and its effect on θ and ϕ can be neglected. Therefore, the refracted angle from the air–film interface equals the incident angle for the film–fiber interface. Both angles are denoted as θ_2 in Fig. 1(*b*). In other words, because the thickness of the film is much less than the radius of the optical fiber, the film can be assumed to be "locally flat" for calculating wave propagation in the film without introducing significant errors. The generalized Snell's law can be used to describe wave propagation at these two interfaces

$$N_1 \sin\theta_1 = N_2 \sin\bar{\theta}_2 = N_3 \sin\theta_3 \tag{1}$$

where N_1, N_2, and N_3 are complex refractive indices of air, film, and fiber, respectively. Air is almost transparent for all wavelengths of thermal radiation, therefore, the imaginary part of N_1 equals to zero, or $N_1=n_1$, where n_1 is the real part of N_1. For an absorbing film, both the real and the imaginary parts, are important in order to calculate the wave propagation at the interface, or $N_2=n_2+ik_2$. It is noted that $\sin\bar{\theta}_2$ is complex because N_2 has a complex component ik_2. Therefore, $\bar{\theta}_2$ does not represent the direction of the Poynting vector in the film. The substrate media is assumed to be weakly absorbing, i.e., the imaginary part of the refractive index is very small (k_3 is much less than 0.1 for fused silica at wavelength range 0.5–8 μm, while n_3 is approximately 1.5). Therefore it can be neglected in the film–fiber interface reflection and transmission calculations without causing significant error, or $N_3=n_3$.

For the electric vector perpendicular and parallel to the incident plane transverse electric (TE) and transverse magnetic (TM) waves, the reflectance and transmittance of the thin film can be obtained based on wave optics. It is not shown in this paper due to brevity and details can be found in Refs. [13] or [15].

2.2 Radiative Transfer in the Fiber. The radiative transfer in the fiber is calculated using the ray tracing method because the diameter of a typical optical fiber is much larger than the wavelength of interest and the coherence length of blackbody emission. As noted before, because the thickness of the film is much smaller than the radius of the fiber, the incident angle of the film–fiber interface is assumed to be equal to the refracted angle at the air–film interface, both shown as θ_2 in Fig. 1(*b*). It can also be found that the change of azimuthal angle is insignificant when the film thickness is small, i.e., the incident azimuthal angle at the film–fiber interface approximately equals the incident azimuthal angle at the air–film interface, shown as ϕ in Fig. 1(*a*). Details on the ray tracing method for cylindrical media can be found in Refs. [20,21]. The directional transmittance of the fiber can be derived as the following. The pathlength of a ray incident on the fiber and leaving the fiber can be written as

$$S = \frac{2R_f \cos\theta_3}{\cos\gamma} \tag{2}$$

where R_f is the radius of the fiber; and γ is the angle between the refracted ray and its projection on the cross section. From the geometry, it can be calculated using the following equation

$$\cos^2\gamma = \cos^2\theta_3 + \sin^2\theta_3 \sin^2\phi \tag{3}$$

The transmittance of the fiber is then

$$T_f = \exp(-\alpha_3 S) \tag{4}$$

2.3 Radiative Transfer in the Fiber–Film System. The overall radiative properties of the fiber–film system are modeled as a cylindrical fiber with the surface properties of the film. The radiative energy that is reflected and escaped from the fiber–film system is defined as "scattering" in the following discussion. The proportion of scattered radiative energy by the combined structure can be calculated as the summation of the reflectance of the thin film and the portion of radiative energy that penetrates into the

fiber and escapes from the air–film interface after multireflection in the fiber. It should be noted that θ_1 and ϕ defined based on the local coordinates are constant after multireflection because of axisymmetry. Therefore, the proportion of radiative energy scattered away by the fiber–film system can be written as

$$R(\theta_1,\phi) = R_w(\theta_1) + \sum_{j=1}^{\infty} R_j(\theta_1,\phi) \tag{5}$$

where R_w is the reflectance of the film. R_j is the proportion of energy leaving the fiber–film structure after the jth reflection from the film–fiber interface. To emphasize that these parameters are directionally dependent, their angular coordinates are given in parenthesis. R_j can be calculated by taking into account the transmittance of the fiber and transmittance and reflectance of the film

$$R_j = T_w^2 T_f (R_w T_f)^{j-1} \tag{6}$$

The incident wave from the blackbody is usually assumed to be randomly polarized in literature, therefore, the scattering proportion of energy by the film–fiber system is then the average of the TE and TM waves

$$R(\theta_1,\phi) = \tfrac{1}{2}[R_\perp(\theta_1,\phi) + R_\parallel(\theta_1,\phi)] \tag{7}$$

The incident irradiation is assumed to be diffusive, and the proportion of radiative energy scattered by the fiber–film system at the local hemisphere can be calculated as

$$\bar{R} = \frac{1}{\pi}\int_{2\pi} R(\theta_1,\phi)\cos\,\theta_1\, d\Omega \tag{8}$$

Due to energy conservation and the Kirchhoff's law, the directional and hemispherical emittance and absorptance of the fiber–film system can be calculated as

$$\alpha(\theta_1,\phi) = \epsilon(\theta_1,\phi) = 1 - R(\theta_1,\phi) \tag{9}$$

and

$$\bar{\alpha} = \bar{\epsilon} = 1 - \bar{R} \tag{10}$$

The total hemispherical absorptance and emittance are then calculated by integrating the spectral hemispherical emittance over wavelengths of interest for temperature T

$$\alpha_t(T) = \epsilon_t(T) = \frac{\int_0^{\infty} \bar{\epsilon}_\lambda e_{\lambda,T}(\lambda,T)d\lambda}{\sigma T^4} \tag{11}$$

The integration in Eq. (11) is carried out from 0.5 to 30 μm in this study. For thermal radiation, this wavelength range covers more than 99.5% of the radiation energy for temperature of 1000–2000 K.

3 Results and Discussion

Because of lack of radiative property data for a fiber–film system in the literature, the verification of the proposed model is carried out by comparing the results of the ray tracing method for plate geometry and wave optics results for free standing films separately with data in the literature [8,15,18]. These results show an exact match when the same methods are employed (data not shown).

To facilitate the discussion and parametric study, a baseline case is used in the following sections. The following optical parameters are used unless indicated otherwise in the discussion: fiber refractive index $N_3 = n_3 = 1.4$, fiber optical thickness $\tau_R = \alpha R_f = 0.675$, film refractive index $N_2 = 4 + 3.5i$, film thickness $L = 50$ nm, temperature of fiber–film system $T = 1000$ K, and $N_1 = 1$. According to the Kirchhoff's law, the effective emittance equals to the absorptance, therefore, the observed trends in predicted emittance or absorptance in the following discussion is explained using the emission or absorption or both, depending on the physics needed to explain the phenomena.

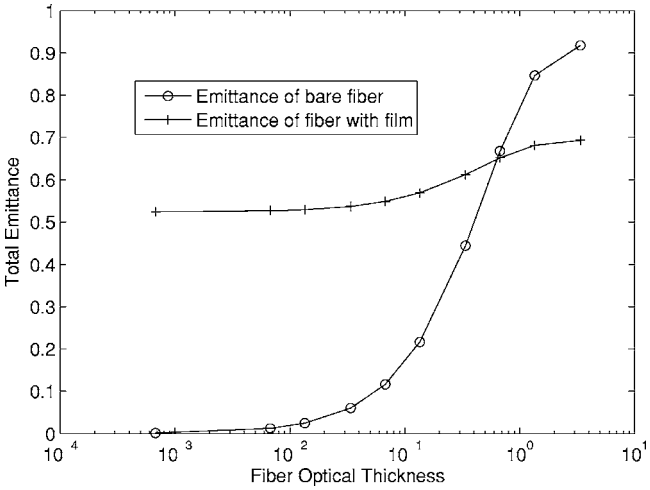

Fig. 2 Effect of the nondimensional fiber optical thickness τ_R on emittance of fiber–film system

3.1 Effect of Substrate Optical Properties. The effect of fiber optical thickness τ_R on total hemispherical emittance for a bare fiber and fiber–film system is demonstrated in Fig. 2. As one may expect, the emittance increases with increasing fiber optical thickness. However, the degree of emittance increase for a fiber–film system is not as substantial as for a bare fiber. This is because the reflectivity of the fiber–air interface is fairly small for a bare fiber, so the emission to the environment is highly dependent on the optical thickness of the fiber. For the fiber–film system, the film reflects and absorbs a substantial amount of energy before a ray reaches the fiber, therefore, the change of fiber optical thickness does not significantly change the absorptance or emittance. It is noted that the emittance of a bare fiber can exceed the emittance of a fiber with a film when the optical thickness of the fiber is high. It is because the reflectivity of the air–fiber interface is much less than that of the air–film interface, consequently, more radiative energy is able to penetrate into the bare fiber and yields higher absorptance than the film–fiber system when the fiber optical thickness is high.

3.2 Effect of Film Optical Properties. Figures 3 and 4 illustrate the effect of film optical properties on the hemispherical total emittance of the fiber–film system. The emittance and absorptance decreases monotonically when increasing the real part of film refractive index n_2. It is because the reflectance of the film increases monotonically with increasing n_2, as seen in Fig. 3. As a result, less radiative energy is able to penetrate into the fiber and leads to smaller absorptance when n_2 is higher. The effect of the imaginary part of the refractive index (extinction coefficient) κ_2 is more complicated. When the extinction coefficient of film is small compared with the real part of refractive index n_2, change of κ_2 does not have a significant effect on the film reflectance. However, the film becomes more absorbing as κ_2 increases. Therefore, the emittance and absorptance increases with increasing κ_2 within this range. As κ_2 becomes comparable with n_2, its effect on film reflectance becomes more significant. The film reflectance increases with increasing κ_2. Therefore, although the film becomes more able to absorb energy with increasing κ_2, less radiative energy is able to transmit into the film being absorbed. The absorptance and emittance decreases with increasing κ_2 within this range. Such a trend is more apparent when the fiber is transparent, or $\tau_R = 0$, as shown in Fig. 4. In such cases, the emission and absorption are purely from the film, therefore, the predicted emittance and ab-

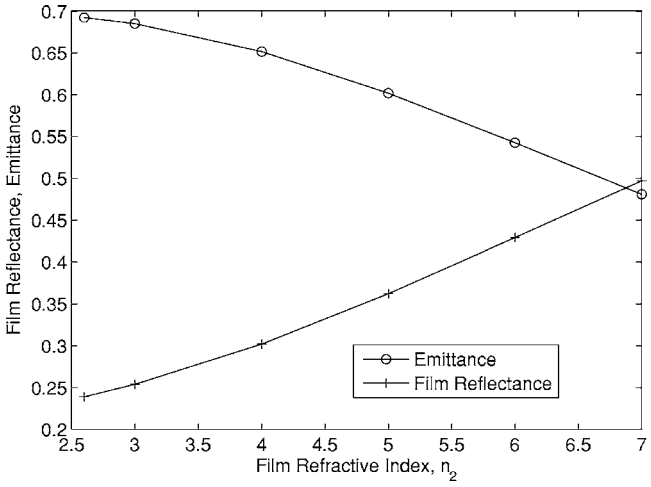

Fig. 3 Effect of real part of film refractive index on fiber–film emittance and film reflectance

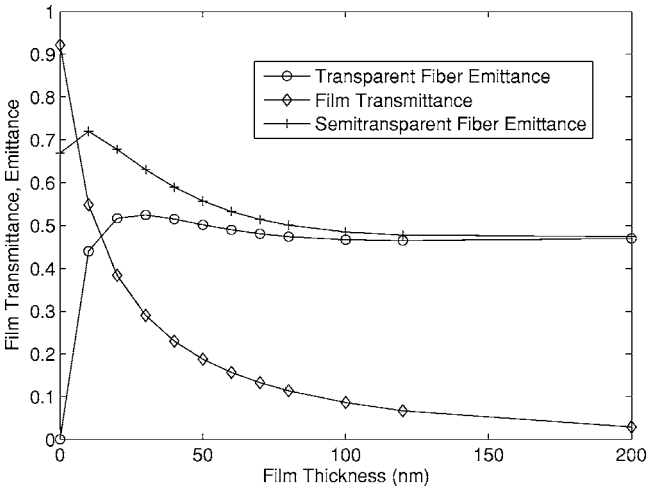

Fig. 5 Effect of film thickness on the emittance of fiber–film system and transmittance of film

sorptance are smaller than for a semitransparent fiber.

The effect of film thickness on emittance and absorptance is shown in Fig. 5. It can be seen from the figure that the emittance increases with film thickness in the initial stage, and start to decrease as the film grows further, until it reaches a constant value. The fiber–film emittance equals a bare fiber when the film thickness is zero. As the film starts to deposit on the fiber, an additional layer of absorbing and emitting material is added to fiber, therefore, the emittance starts to increase. For a transparent fiber with $\tau_R=0$, i.e., the fiber is not emitting, such a trend is more prominent. As the film thickness increases further, the transmittance of the film becomes smaller, the film becomes opaque, and the predicted emittance becomes dominated by the air–film interface. In fact, for the cases shown in Fig. 5, when the film thickness is larger than 100 nm, the film transmittance is small enough that the difference in the fiber substrate (transparent or semi-transparent) does not affect the predicted emittance significantly.

3.3 Effect of Temperature. Since the spectral emittance and absorptance is wavelength dependent, it is expected that the total emittance should be a temperature dependent property because the emissive power in Eq. (11) is both temperature and wavelength dependent according to Planck's law. Such a temperature dependence could be important for heat transfer analysis. Figure 6 presents the temperature dependent emittance of a bare fiber compared to a fiber with 50-nm-thick film. For the bare fiber, because the optical thickness is not wavelength dependent, the predicted spectral emittance is wavelength independent. Therefore, the total emittance is not temperature dependent, as seen from Eq. (11). For the fiber coated with a film, the dependence of total hemispherical emittance on temperature is almost linear, despite many complicated factors that affect the spectral emittance. Similar linearity is observed in predicted emittance of a weakly absorbing film on a strongly absorbing substrate [22]. However, because the film in this study is strongly absorbing, the trend of the linearity is exactly the opposite; the total hemispherical emittance is predicted to be decreasing with increasing temperature in this study. This can be explained by the almost linear increase of film reflectance with temperature. Although such a trend can be different when the optical properties of the film and fiber are wavelength dependent, in general, the spectral properties at small wavelengths have more weight on the total properties as temperature increases due to Planck's law.

4 Conclusions

In conclusion, the hemispherical total emittance and absorptance of a semi-transparent fiber coated with a thin absorbing film

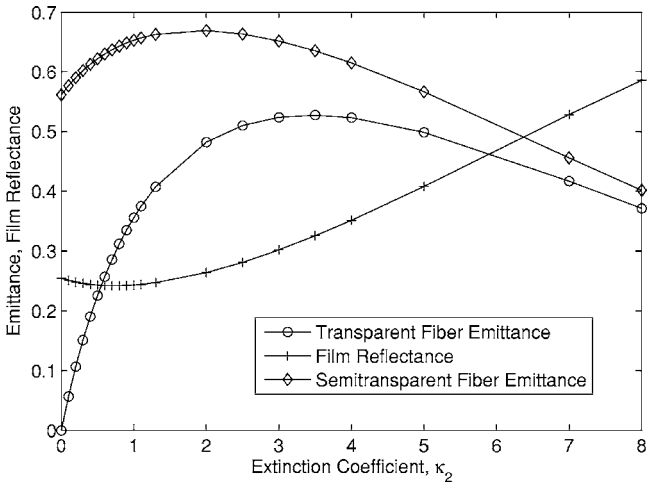

Fig. 4 Effect of imaginary part of film refractive index on fiber–film emittance and film reflectance

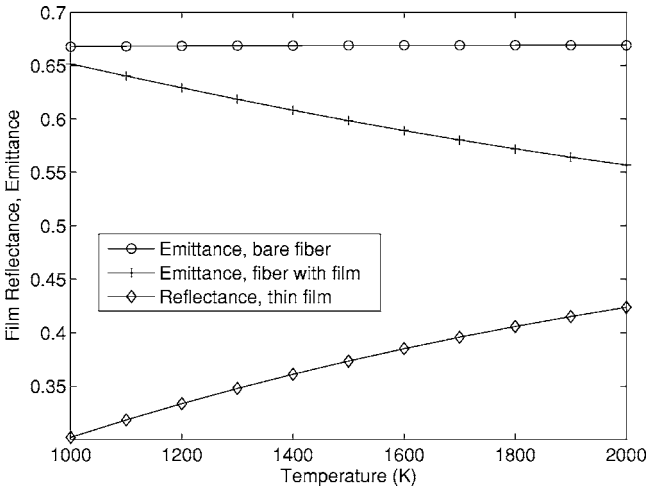

Fig. 6 Effect of temperature on emittance of a bare fiber and fiber–film system as well as reflectance of film

is investigated. Wave optics is used for thin film analysis while the ray tracing method is used for the fiber analysis. It is found that the presence of a thin absorbing film has profound effects on the predicted thermal radiative properties. For example, the emittance of a bare fiber can be higher than a fiber coated with a strongly absorbing film when the optical thickness of the fiber is large. The effect of fiber substrate and film optical properties and film thickness on predicted absorptance and emittance is investigated. It is found that the effects of these parameters are strongly interdependent. For example, the effect of substrate optical thickness can be very significant when the film thickness is small, and negligible when the film thickness is large, as seen in Fig. 5. The predicted total hemispherical emittance and absorptance are found to be dependent on temperature even for "gray media."

Acknowledgment

Financial support by National Science Foundation is gratefully appreciated. We also thank OFS Specialty Photonics Division and Srinath Charkravarthy for valuable discussions.

Nomenclature

e = hemispherical spectral emissive power, $W/m^2\ \mu m$
k = imaginary part of complex refractive index, extinction coefficient
L = film thickness, m
N = complex refractive index
n = real part of complex refractive index
R = reflectance
r = reflection coefficient
S = path length of a ray penetrating through a fiber, m
T = temperature, K, transmittance
t = transmission coefficient

Greek Letters

α = absorption coefficient, m^{-1}, absorptance
β = nondimensionalized parameter
ϵ = emittance
η = nondimensionalized film thickness
γ = angle between a ray and its projection on cross section
λ = wavelength, μm
θ = polar angle for direction
ϕ = azimuthal angle for direction
τ = optical thickness
σ = Stefan–Boltzmann constant

Subscripts

$1,2,3$ = media 1, 2, and 3
f = fiber
w = wave optics for film
g = geometry optics for film
t = total properties
λ = spectral property

References

[1] Iwanik, P. O., and Chiu, W. K. S., 2003, "Temperature Distribution of an Optical Fiber Traversing through a Chemical Vapor Deposition Reactor," Numer. Heat Transfer, Part A, **43**, pp. 221–237.
[2] Wang, K. Y., Kumar, S., and Tien, C. L., 1987, "Radiative Transfer in Thermal Insulations of Hollow and Coated Fibers," J. Thermophys. Heat Transfer, **1**(4), pp. 289–295.
[3] Borca-Tasciuc, T., and Chen, G., 1997, "Temperature Measurement of Fine Wires by Photothermal Radiometry," Rev. Sci. Instrum., **68**, pp. 4080–4083.
[4] Yin, Z., and Jaluria, Y., 2000, "Neck Down and Thermally Induced Defects in High-speed Optical Fiber Drawing," ASME J. Heat Transfer, **122**, pp. 351–362.
[5] Reeve, H. M., Mescher, A. M., and Emery, A. F., 2004, "Investigation of Steady-State Drawing Force and Heat Transfer in Polymer Optical Fiber Manufacturing," ASME J. Heat Transfer, **126**, pp. 236–243.
[6] Viskanta, R., and Menguc, M. P., 1989, "Radiative Transfer in Dispersed Media," Appl. Mech. Rev., **42**, pp. 241–259.
[7] Baillis, D., and Sacadura, J.-F., 2000, "Thermal Radiative Properties of Dispersed Media: Theoretical Prediction and Experimental Characterization," J. Quant. Spectrosc. Radiat. Transf., **67**, pp. 327–363.
[8] Siegel, R., and Howell, J. R., 2002, *Thermal Radiation Heat Transfer*, 4th ed., Taylor & Francis, New York.
[9] Yamada, J., and Kurosaki, Y., 2000, "Radiative Characteristics of Fibers with a Large Size Parameter," Int. J. Heat Mass Transfer, **43**, pp. 981–991.
[10] Tagne, H. T. K., and Baillis, D. D., 2005, "Radiative Heat Transfer using Isotropic Scaling Approximation: Application to Fibrous Medium," ASME J. Heat Transfer, **127**, pp. 1115–1123.
[11] Lin, J.-D., and Huang, J.-M., 1987, "Radiative Transfer within a Cylindrical Geometry with Fresnel Reflecting Boundary," J. Thermophys. Heat Transfer, **2**, pp. 118–122.
[12] Wu, C. Y., Sutton, W. H., and Love, T. J., 1988, "Directional Emmitance of a Two-Dimensional Scattering Media with Fresnel Boundaries," J. Thermophys. Heat Transfer, **3**, pp. 274–282.
[13] Heavens, O. S., 1991, *Optical Properties of Thin Solid Films*, Dover, New York.
[14] Bohren, C. F., and Huffman, D. R., 1983, *Absorption and Scattering of Light by Small Particles*, Wiley, New York.
[15] Born, M., and Wolf, E., 2002, *Principles of Optics*, 7th ed., Cambridge University Press, Cambridge, UK.
[16] Armaly, B. F., and Look, D. C., 1973, "Effect of Substrate on Radiative Properties of Thin Film," Appl. Opt., **12**(8), pp. 1904–1908.
[17] Taylor, R. P., and Viskanta, R., 1975, "Spectral and Directional Radiation Characteristics of Thin-Film Coated Isothermal Semitransparent Plates," Waerme- Stoffuebertrag., **8**, pp. 219–227.
[18] Chen, G., and Tien, C. L., 1992, "Partial Coherence Theory of Thin Film Radiative Properties," ASME J. Heat Transfer, **114**, pp. 636–643.
[19] Anderson, C. F., and Bayazitoglu, Y., 1996, "Radiative Properties of Film Using Partial Coherence Theory," J. Thermophys. Heat Transfer, **10**(1), pp. 26–32.
[20] Liu, L. H., Tan, H. P., and Yu, Q. Z., 2002, "Internal Distribution of Radiation Absorption in One-Dimensional Semitransparent Medium," Int. J. Heat Mass Transfer, **45**, pp. 417–424.
[21] Tian, W., and Chiu, W. K. S., 2006, "Radiative Absorption of an Infinitely Long Hollow Cylinder with Frensel Surfaces," J. Quant. Spectrosc. Radiat. Transf., **98**, pp. 249–263.
[22] Kovalev, V. N., 1983, "The Total Hemispherical Emissivity of the Surface in the System Metal-Thin Oxide Film," Heat Transfer-Sov. Res., **15**, pp. 80–90.